Observing planet formation: constraints on the spatial distribution and the growth of solids in protoplanetary disks

Marco Tazzari

München 2016

Observing planet formation: constraints on the spatial distribution and the growth of solids in protoplanetary disks

Marco Tazzari

Dissertation
an der Fakultät für Physik
der Ludwig–Maximilians–Universität
München

vorgelegt von
Marco Tazzari
aus Ravenna, Italien

München, den 30. September 2016

Erstgutachter: Prof. Dr. Barbara Ercolano

Zweitgutachter: Prof. Dr. Thomas Preibisch

Tag der mündlichen Prüfung: 20. Dezember 2016

To Agnese

Contents

List of Figures

List of Tables

List of Acronyms

CPU   Central processing unit

FFT   Fast Fourier transform

FT   Fourier transform

GPU   Graphics processing unit

ISM   Interstellar medium

MCMC   Markov chain Monte Carlo

PMS   Pre-main sequence

SED   Spectral energy distribution

SFR   Star forming region

TD   Transition disk

YSO   Young stellar object

Zusammenfassung

Die Entstehung von Planeten und Sternen ist eng miteinander verknüpft. Der Stern bildet sich im Zentrum einer rotierenden Materiescheibe. Die Planeten entstehen wiederum in der zirkumstellaren Scheibe. Das Kern-Akkretions-Modell beschreibt die allmähliche Entstehung von Planeten in folgender Weise: Interstellare Staubteilchen mit Größen im Submillimeterbereich wachsen durch Kollisionen auf eine Größe von Millimetern bzw. Zentimetern heran. Sie stoßen wieder zusammen und bilden im weiteren kilometergroße Planetesimale. Schließlich akkretieren die felsartigen Planetenkerne Gas und bilden dann, je nach akkretierter Gasmasse, einen erdähnlichen Planeten oder einen Gasriesen. Moderne Interferometer mit Wellenlängen von Submillimeter über Millimeter bis in den Radiobereich wie das Atacama Large Millimetre Array (ALMA) oder das Very Large Array (VLA) detektieren die thermische Emission von Staubkörnern und erlauben eine nie dagewesene Auflösung von protoplanetaren Scheiben bis auf Längenskalen, auf denen sich die Planetenbildung ereignet.

In den letzten Jahren haben ausführliche photometrische Studien im Submillimeter- und Millimeter-Wellenlängenbereich Hinweise auf Kornwachstum in Scheiben geliefert, allerdings nur gemittelt über die gesamte Scheibe. Zudem wurde die Ableitung der Staubeigenschaften vom beobachteten spektralen Index unter plausiblen, aber stark vereinfachenden, Annahmen durchgeführt. In Rahmen dieser Dissertation wurde eine Analysemethode entwickelt, die es zum ersten Mal erlaubt, gleichzeitig die Struktur der Scheibe und die Eigenschaften des Staubs durch eine Anpassung eines selbstkonsistenten, physikalischen Modells an die Beobachtungen in mehreren Wellenlängenbereichen zu ermitteln. Außerdem wird eine neue Version eines Computercodes präsentiert, die durch die Verwendung moderner Grafikkarten viel schneller ist. Das stellt einen Durchbruch in der Rechenleistung dar, der erforderlich ist, um die riesigen, aktuell verfügbaren Datenmengen zu bewältigen.

In der Anwendung der Multiwellenlängen-Analyse auf Beobachtungen dreier Scheiben in Sternentstehungsregionen der Sternbilder Stier (Taurus) und Schlangenträger (Ophiuchus) zeigt sich ein radialer Gradient in der Verteilung der Korngröße. Dabei sind große Körner von bis zu einem Zentimeter Größe auf die innere Scheibe beschränkt. Dagegen sind Körner, die viel kleiner sind als ein Millimeter, in der gesamten Scheibe zu finden. Ähnliche Ergebnisse betreffen eine andere analysierte Scheibe in HD 163296. Dort gilt zusätzlich, dass das Radialprofil der Korngröße ein Szenario unterstützt, in dem verstärktes Kornwachstum genau dort auftritt, wo der zweithäufigste, flüchtige Stoff in Scheiben, nämlich Kohlenmonoxid (CO), gefriert.

Das Computerprogramm, das im Rahmen der Dissertation entwickelt wurde, dient auch zur Beschleunigung der zwölf Analysen von hochaufgelösten Beobachtungen in Studien ganzer Populationen von Sternen mit protoplanetaren Scheiben. Konkret wurde das Programm auf mit ALMA beobachtete Scheiben in einer Sternentstehungsregion im Sternbild Wolf (Lupus) angewendet. Daraus wurde die physikalische Struktur von mehr als zwan-

zig Scheiben abgeleitet. Neben anderen physikalischen Parametern wurden ihre Größen und Staubmassen bestimmt. Bis jetzt ist dies die größte Anzahl von Scheiben aus der gleichen Sternentstehungsregion, die je einheitlich mit einem selbstkonsistenten Modell betrachtet wurde. Es ist bemerkenswert, dass dieser Satz an Scheiben im Massenbereich von 0,7 bis 1 Sonnenmassen und im Strahlungsfluss — integriert über den Submillimeterbereich — vollständig ist. Die Ergebnisse sind im Einklang mit vorherigen Arbeiten, die auf einfacheren Analysen beruhten. Allerdings zeigen sie auch einen klaren Unterschied in der Korrelation zwischen der Leuchtkraft und der Größe der Scheiben aus der älteren, ca. drei Millionen Jahre alten Region im Sternbild Wolf und der jüngeren, ca. 1-2 Millionen Jahre alten Population aus dem Grenzgebiet zwischen Stier und Fuhrmann (Auriga).

Die Anwendung der Analyse dieser Dissertation auf Multiwellenlängen-Beobachtungen einer großen Zahl von Scheiben, die mit ALMA beobachtet wurden, wird es erlauben, das Wachstum fester Körper im frühen Stadium vieler protoplanetarer Scheiben räumlich aufzulösen. Diese Messungen werden von zentraler Bedeutung sein, um theoretische Modelle der Planetenentstehung aufzustellen, zu testen und sie weiter zu verbessern.

Abstract

Planets are thought to form in the circumstellar disks orbiting young stars in formation. According to the core-accretion model, a candidate scenario for Earth-like planets, the interstellar sub-μm-sized dust particles grow thanks to collisions to mm/cm size and then form km-sized planetesimals via dynamical encounters. Eventually, the rocky planetary cores accrete gas and, depending on the total gas mass attained, a terrestrial planet or a gas giant forms. Modern sub-mm/mm/radio interferometers such as ALMA and VLA detect the thermal emission of dust grains and provide us with an unprecedented sharp view of protoplanetary disks at the spatial scales where planet formation occurs.

In recent years, evidence of grain growth in disks has been obtained by extensive sub-mm/mm photometric studies, but so far they only provided disk-averaged estimates of the dust properties. Moreover, the derivation of dust properties from the observed spectral index was done under reasonable - but simplifying - assumptions rather than with a proper modeling of the disk emission. The thesis presents an analysis method that enables - for the first time - the disk structure and the dust properties to be constrained simultaneously by fitting multi-wavelength observations with a self-consistent physical model. The thesis presents also an accelerated version of the computer code that uses modern graphics cards and provides the computational breakthrough needed to exploit the new wealth of information now available.

Applying the multi-wavelength analysis to observations of three disks in the Taurus and Ophiuchus star-forming regions, a key result is a radial gradient in the grain-size distribution, with large grains of up to $1\,\mathrm{cm}$ size confined to the inner disk and smaller grains of size $\ll 1\,\mathrm{mm}$ populating the whole disk. Similar results hold for another disk, HD 163296, where in addition the grain size radial profile supports the scenario of enhanced grain growth at the snowline location of the second most abundant volatile in disks, CO.

The tool developed in the thesis is also designed to accelerate the analysis of high-resolution observations for demographic studies. By applying the analysis tool to an ALMA disk survey in the Lupus star-forming region, the physical structure of more than 20 disks is obtained, in particular the disks's size and dust mass among other physical parameters. To date, this is the largest sample of disks of the same star-forming region fitted homogeneously with a self-consistent model. Remarkably, the sample is complete in the mass range of $0.7M_\odot$ to one $M_\odot$. The results are compatible with previous studies based on simpler analyses but also highlight a consistent difference in the disks's luminosity-size correlation between the older ($\sim 3\,\mathrm{Myr}$) Lupus and the younger ($\sim 1-2\,\mathrm{Myr}$ old) Taurus-Auriga region.

The application of the analysis developed in this thesis to multi-wavelength observations of large samples of disks with ALMA will allow us to spatially resolve the early growth of solids in numerous protoplanetary disks, and therefore to provide measurements that will be crucial to inform, test, and refine theoretical models of planet formation.

1

Introduction

One of the experiences that more than any other caused wonder and amazement in all generations across the history of human kind is the sight of the starry sky on a clear night. The silvery light that our eyes detect and - now - our telescopes can collect, has been source of inspiration for poets, painters and philosophers in an incredible number of civilizations from all over the world. Nowadays, the progress of scientific knowledge and technological capabilities allowed us to reveal the physical nature and to understand the origin of many phenomena that until some centuries ago were regarded as mysterious or barely known. Notwithstanding, the question about how our planet, the Earth, originated and whether a planetary system like our Solar System is common or not in the Universe have challenged mankind since the beginning.

Seven centuries ago, in its *Divine Comedy*, Dante Alighieri described the orderly shape of the Universe, already relating the inclination of the ecliptic on the celestial equator to the origin of seasons, which in turn makes life possible on the Earth thanks to the alternation of summer and winter:

Vedi come da indi si dirama   *See, how thence oblique[1]*
l'oblico cerchio che i pianeti porta,   *Brancheth the circle, where the planets roll*
per sodisfare al mondo che li chiama.   *To pour their wished influence on the world;*

Chè se la strada lor non fosse torta,   *Whose path not bending thus, in Heaven above*
molta virtù nel ciel sarebbe in vano,   *Much virtue would be lost, and here on earth*
e quasi ogni potenza qua giù morta;   *All power well-nigh extinct; or, from direct*

e se dal dritto più o men lontano   *Were its departure distant more or less,*
fosse 'l partire, assai sarebbe manco   *I' the universal order, great defect*
e giù e su de l'ordine mondano.   *Must, both in Heaven and here beneath, ensue.*

Dante Alighieri, *The Divine Comedy*, ca. 1300

In the 14th century, starting from the evidence that life has developed on Earth, Dante Alighieri asked himself what were the conditions that made life possible on our planet, attempting an empirical explanation related to the disposition of our orbit. In the present days, after modern observing facilities allowed us to discover a few thousands of planets outside the Solar System, we are asking ourselves the same question, but from the opposite perspective: we detect a planet or a planetary system and we aim at understanding whether it is hosting life or not.

What are the signatures of life? Is there life elsewhere in the Universe? How different or similar to ours is life in the Universe, if it exists? These deep, pressing questions have been the driver of many fields of research in the last century. They are still unsolved, and this is mostly due to the fact that we are not able yet to fully answer to the original question: what are the conditions that make life possible? We have criteria[2] that help us ruling out planets where life (as we conceive it) is impossible, and identifying good candidates on which to focus, but we are still far from the definition of reliable tracers of life. For many exoplanets, we have now several observational techniques (e.g., radial velocity, transit, direct imaging) that allow us to measure (or at least put limits on) their orbit, mass, size and average composition. In some cases we can also obtain high resolution measurements of the transmission spectrum from their atmospheres (Madhusudhan et al. 2014, and references therein) where we look for traces of organic compounds or other chemical signatures of life. Moreover, for each planet-hosting star, we can define an habitable zone as the orbital region where a terrestrial planet would have environmental conditions that could support life. The requirement that water can be found in liquid phase on an Earth-like planet is only one of the several additional stellar and planetary properties that determine the habitability of a planet (for a recent review on habitability, see Güdel et al. 2014). Out of the almost three thousands confirmed exoplanets[3], only 10% reside in a habitable zone[4], and just a handful of them fulfill all the other habitability criteria. Incidentally, the last Earth-like exoplanet in a habitable zone has been discovered very recently around the nearest star Proxima Centauri (Anglada-Escudé et al. 2016), but despite its closeness (4.2 light years) the study was not able to exclude the presence of liquid water on it.

The fundamental questions about the development of life on the Earth and in the Universe are now tackled by several disciplines, from biology to chemistry, from geophysics to astronomy, and with a broad range of techniques, from radioactive dating of asteroid samples to space based missions around comets (e.g., the ESA Rosetta mission). In any case, our direct experience shows that life develops on those rocky aggregates that we call planets. Before any question about how life has been triggered on the Earth, the first and foremost question suggested by our experience is about how the Earth and the other planets in the Solar System formed. Indeed, we can legitimately surmise that there is a strong connection between the properties deciding the habitability of a planet (or planetary sys-

---

[1]Planets move on the zodiac, the *oblique* circle that is inclined (by $\sim 23.4°$) on the celestial equator in such a way that living beings on the planets benefit from that. Indeed, if the zodiac were not thus inclined, it would not divide seasons as it now does, substantially all the advantageous conditions that make this portion of the Universe habitable would be in vain, and the potential qualities intrinsic to the matter would never come into being. Moreover, if the inclination between the zodiac and the celestial equator would be larger or smaller than its actual value, shortcomings and imperfections would arise everywhere.

[2]A set of conditions that we regard as *necessary* for life to develop.

[3]2951 total confirmed exoplanets, as of 24 September 2016, http://exoplanets.org.

[4]297 exoplanets are found in a habitable zone (as of 24 September 2016) defined as the orbital region where planets attain an equilibrium temperature between $180\,\mathrm{K}$ and $310\,\mathrm{K}$ and have an insolation between 0.25 and 2.2 times the insolation received by the Earth from the Sun. Source: http://exoplanetarchive.ipac.caltech.edu/.

tem) and the process that led to its formation. A detailed knowledge of the typical environment where (and time scales on which) planets are formed is essential to understand the demographics of planetary systems at birth and to evaluate the potential of forming habitable planets.

Planet formation is thought to occur in the accretion disks made of gas and dust that surround young stars during their early evolution (first 10 Myr of their life, see Section 1.1). The small μm sized grains that the disk has inherited from the parent interstellar cloud have to grow by at least 13 orders of magnitude in size on their way to become planets: Section 1.2 is dedicated to describing what are the physical mechanisms that can lead to the formation of planets.

It is now manifest that understanding how planets form requires a coordinated effort: on the theoretical side (e.g., with sophisticated numerical codes for bottom-up planet synthesis or with simplifying parametric studies), on the experimental side (e.g., with laboratory experiments able to reproduce the physical conditions where grain growth and molecular line emission occur), on the observational side (e.g., with more detailed observations of single sources, as well as with demographic studies of disk surveys). The new generation of modern mm/radio interferometers like the Atacama Large Millimeter and sub-millimeter Array (ALMA) and the Karl J. Jansky Very Large Array (VLA), accompanied by the advances in the optical with new high angular resolution imagers like VLT/SPHERE is delivering us unprecedented sharp views of planet-forming disks (see Figure 1.1).

Exploiting the wealth of information provided by these revolutionary observing facilities is crucial to determine the properties of the solids, building blocks of planets, and therefore to constrain the initial conditions of planet formation. To this extent, as I describe at length in Section 1.3, the major goal of this Thesis has been the development of the tools needed for the analysis of these multi-wavelength data sets and their subsequent application to existing observations to determine the dust properties in different disks.
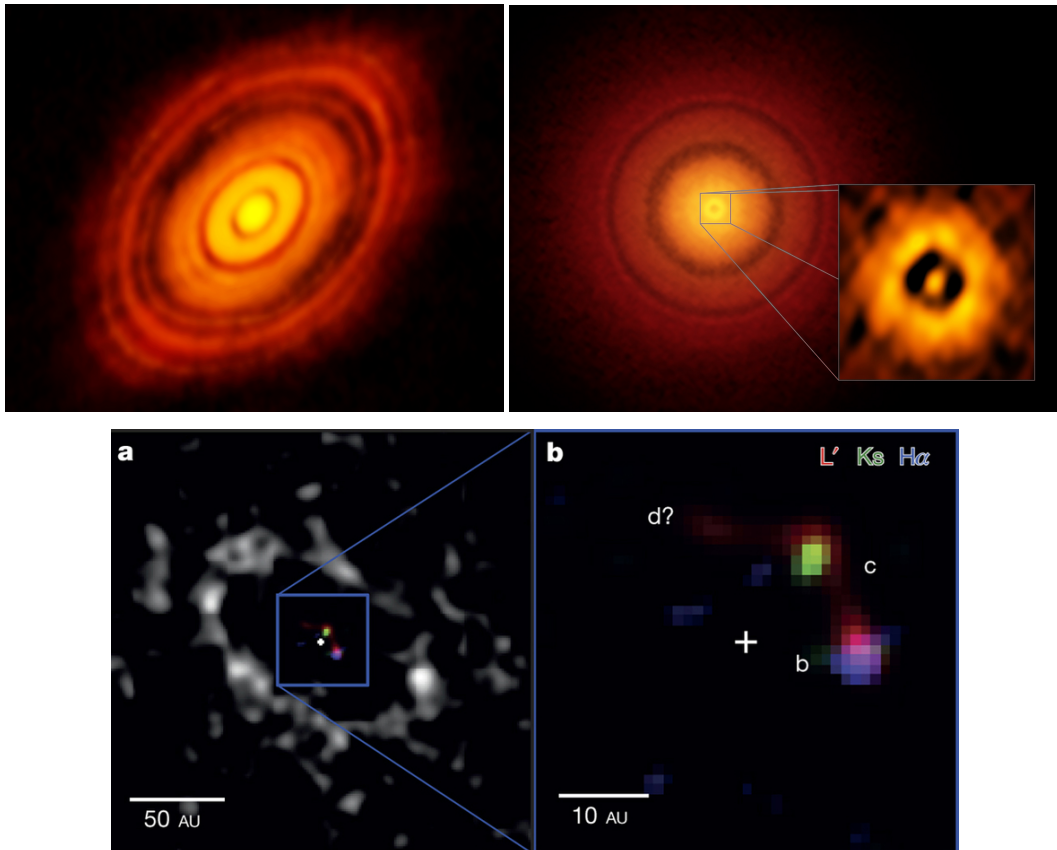
Fig. 1.1   *(top)*: ALMA reveals extraordinarily fine structures in the 890 μm dust continuum emission of the $\sim$ 1 Myr old HL Tau protoplanetary disk (left, ALMA Partnership et al. 2015), and of the $\sim$ 5−10 Myr old TW Hydrae disk (right, Andrews et al. 2016). While the HL Tau disk is surprisingly evolved for its young age (the gaps might be carved by forming planets, among other explanations), the older TW Hydrae disk is surprisingly smooth (the shallower gaps could be carved only by very low-mass planets), except for a hole in the inner $\sim$ 1 au (possibly cleared by photo-evaporation Ercolano et al. 2016).
(bottom): Panel (a) shows the VLA continuum image at 7 mm of the LkCa 15 protoplanetary disk (gray-scale, Isella et al. 2014) and the three candidate protoplanets detected in L' band with LBT and Magellan. Panel (b) shows a zoomed composite image of the detections (blue: Hα, green: KS, red: L'). Credit: Sallum et al. (2015)

1.1 From star forming regions to planet forming disks

Planets are forged in the circumstellar disks orbiting young stars in formation, which - thanks to their high density and relatively low temperatures - constitute an ideal environment for the growth of dust particles and the formation of dense clumps of gaseous material. While the two main scenarios usually employed to explain planet formation are presented in Section 1.2, here we focus on the environment where this process takes place.

The hypothesis of a Solar *nebula* as a way to explain the origin of the coplanar orbits found in the Solar System was formulated almost two centuries ago by natural philosophers (Laplace 1796) and subsequently assumed by astronomers (for a historical review, see Wood and Morfill 1988). Nowadays, the formation of a primordial disk out of which planets can be generated (i.e., the *nebula*) is reasonably well understood in the more general context of star formation. In the classical scenario of star formation (Shu et al. 1987), the disk structure naturally arises from the redistribution of angular momentum within a gravitationally collapsing molecular cloud core (Terebey et al. 1984). In the next paragraphs I will present the main phases of this process and the key observational probes that allow us to trace such evolutionary path.

The formation of low-mass stars begins with the fragmentation of a molecular cloud into one or more gravitationally bound cores, internally supported by the contribution of thermal pressure, magnetic fields and turbulence (phase 1 in Figure 1.2). During the evolution of the gravitationally bound core, further dissipation of energy and angular momentum can lead the core to become gravitationally unstable: it quickly collapses under its own gravity and forms one, or possibly more, protostars (phase 2). For clarity of this explanation, let us assume that only one protostar forms. At the center of the collapsed core a protostar enters its main accretion phase, with material being accreted directly from the infalling envelope as well as through the accretion disk that rapidly forms due to the conservation of angular momentum of the whole cloud. At this stage, the vigorous redistribution of angular momentum across the accretion disk (from the envelope to the disk, and from the disk inner edge to the stellar surface) is accompanied by the production of strong outflows and bipolar jets that eject a small fraction of the accreted material in a direction perpendicular to the disk plane and contribute to carrying away the excess angular momentum of the infalling material (phase 3). Once the protostar has reached most of its final mass it becomes a pre-main sequence (PMS) star (phase 4) and continues its evolution by accreting the material left in the circumstellar disk. Finally, once the gas in the accretion disk has been dissipated, the PMS star reaches its final mass and evolves at fixed mass towards the main sequence.

From an observational point of view, the evolutionary stages of young stellar objects (YSO) presented above (and illustrated in Figure 1.2) can be clearly identified from the slope of their spectral energy distribution (SED) in the near-/mid-IR window, between 2.2 and 20 μm: $\alpha_{\mathrm{IR}} = \mathrm{d}\log(\lambda F_\lambda)/\mathrm{d}\log\lambda$ (Lada and Wilking 1984; Lada 1987; Greene et al. 1994). The IR slope-based classification divides YSOs in three distinct classes, which can be interpreted in terms of an evolutionary sequence.

- Class I YSOs have $\alpha_{\mathrm{IR}} > 0.3$ and are generally interpreted as protostars with typical ages of $0.1 - 0.2\,\mathrm{Myr}$ Greene et al. (1994) surrounded by an accretion disk and embedded in a low-mass circumstellar envelope that is being rapidly dissipated.

- Class II YSOs start to be detectable in the optical (the PMS star is not embedded anymore in the envelope) and exhibit $-1.6 \leq \alpha_{\mathrm{IR}} \leq -0.3$: the thermal emission of the
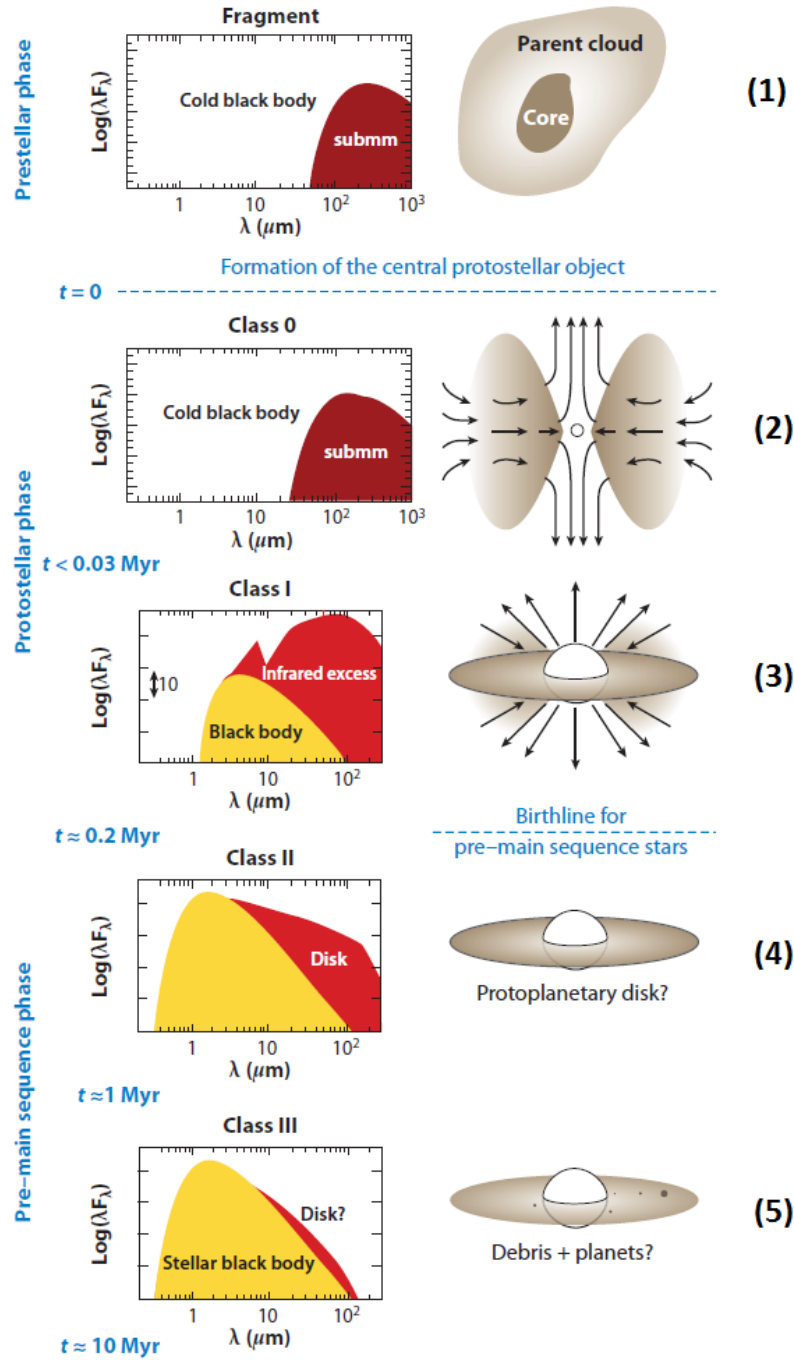
Fig. 1.2 Evolutionary stages of young stellar objects. For each stage, we show the observed SED *(left column)*, a schematic view of the spatial structure *(center column)*, and typical time scales. A molecular cloud undergoes gravitational collapse *(1)*, leading to the formation of a very dense core in which the protostar is getting assembled *(2)*. At its early stages, the protostar is still embedded in a dusty and optically thick cloud but exhibits powerful jets and outflows *(3)*. The protostar turns into a pre-main-sequence (PMS) star *(4)* and becomes visible at optical wavelengths. The dust in the surrounding accretion disk emits thermal radiation which appears as an IR/sub-mm/mm excess to the stellar photosphere black-body (BB) radiation. Finally, the PMS is surrounded by a planetary system and/or by a debris disk *(5)*. Credit: André (2002).

dust is detected as an IR excess w.r.t. the BB radiation from the stellar photosphere and becomes dominant at $\lambda > 20\,\mu$m. This is the stage in which planet formation is thought to occur as the circumstellar disk is still very massive (therefore has the potential of forming one or several planets) and very dense both in gas and dust. The disk is optically thick in the IR and (mostly) optically thin at (sub-)mm wavelengths.

- Class III YSOs are bright in the optical and exhibit very low or absent IR excess: the evolved PMS star has stopped accreting gas from the disk (which has been dissipated) and is (possibly) left with a surrounding planetary system and/or by a system of debris made of comets/asteroids and a distribution of smaller particles originated from the collisions between large bodies.

As soon as the observational capabilities allowed us to detect fainter sources, the classification has been extended to an earlier Class 0 phase, which comprehends deeply embedded sources with envelope mass larger than Class I sources, mostly invisible at IR wavelengths ($\lambda < \mu$m), but with strong emission at (sub-)mm wavelengths (Andre et al. 1993).

In this Thesis I will focus on the Class II phase of YSOs since it constitutes the evolutionary stage where planet formation has to take place. The presence of disks in Class II YSOs were first inferred from infrared excess and then confirmed in the millimetre with the first generation of interferometers. Beckwith et al. (1990) measured mm/radio fluxes that were incompatible with the observed optical extinctions unless a disk-like (as opposed to spherical) dust distribution was considered. These findings were confirmed by the high resolution optical images from the Hubble Space Telescope (HST) of several protoplanetary disks seen in silhouette in the Orion Nebula O'dell et al. (1993); McCaughrean and O'dell (1996). Subsequently, protoplanetary disks were targeted from a considerable number of surveys in different wavelength windows, from near- to far-IR (e.g., with the Spitzer Space Telescope, Evans et al. 2009) to (sub-)mm and radio (Dutrey et al. 1996; Andrews and Williams 2005; Andrews et al. 2009, 2013; Ricci et al. 2010b; Ansdell et al. 2016; Pascucci et al. 2016, among many others) which provided complementary multi-wavelength constraints that allowed us to reach a comprehensive view of their structure and fostered the development of models aimed at explaining the physical origin of their SED (see recent reviews by Dullemond et al. 2007; Williams and Cieza 2011; Testi et al. 2014; Andrews 2015).

The protoplanetary disks surrounding young stars during their Class II phase are flattened gaseous distributions enriched by a low-mass population (the dust to gas mass ratio is $\sim 1\%$) of dust particles with initial sizes around $1\,\mu$m. In the optical, the light emitted from the central star scatters on the small μm-sized grains, thus behaving as a tracer of the disk surface geometry. Recently, the advent of high angular resolution optical imagers (e.g., VLT/SPHERE) endowed with proper coronographs allows us to investigate the presence of forming (or already formed) planets by direct imaging. At IR wavelengths, the disk SED is dominated by the dust thermal emission which is optically thick and therefore acts as a *thermometer* for the disk surface layer. IR observations are typically used also to derive constraints on the dust properties and composition (e.g., from the 10μm spectral feature typical of astronomical silicates) and of the disk geometry (e.g., the disk flaring). How the temperature and the dust mass vary in the deeper regions of the disk cannot be determined with IR observations.

Sub-mm and mm observations exploit the fact that at these wavelengths the disk emission is optically thin and therefore have the unique capability of delivering us with a detailed view of the gas and dust distribution (building material for planets) in the disk. The
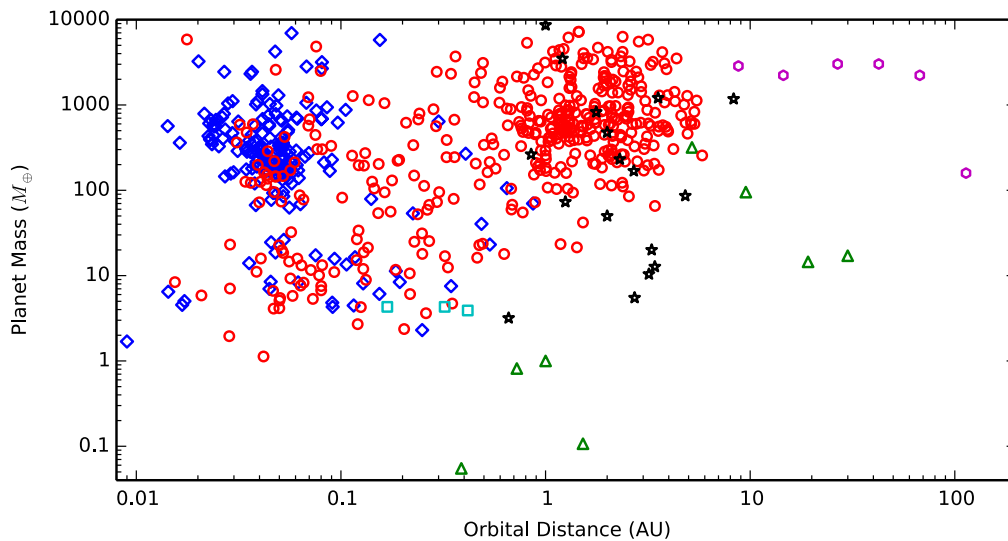
Fig. 1.3 Masses and orbital distances (semi-major axis) of exoplanets from the Exoplanet Orbit Database (Han et al. 2014, http://exoplanets.org) as of July, 2013. Exoplanets are colored according to the discovery method: radial velocity (red circles), transit (blue diamonds), imaging (magenta hexagons), gravitational microlensing (black stars), pulsar timing (cyan squares). Solar System planets are green triangles. Credit: Fischer et al. (2014).

development of modern radio interferometers like ALMA and VLA brought us the resolution needed to resolve the disk structure even at these long wavelengths (spatial scales $\sim$ au in the nearby SFRs). The gas is detected from the roto-vibrational transitions falling in the sub-mm/mm window and provide fundamental information not only on the mass distribution in the disk (recall that the gaseous mass is 100 times larger than the dust mass) which is useful to understand the dynamical evolution of the disk, but also on its velocity field from which we can probe its global kinematics (in many cases compatible with a keplerian motion). The dust is revealed through its thermal emission, which for most of the disk is in the Rayleigh-Jeans regime of the BB spectrum ($T_{\rm d} > 14$ K for observations at 1 mm) and one can therefore convert the mm continuum flux into a dust mass by a rather simple relation (see Eq. 2.9 in Chapter 2). By comparing observations at different (sub-)mm wavelengths we can gain information of the properties of the dust grains, such as their size and composition. As I will describe in Section 1.3, this is the main topic of the Thesis.

1.2   Mechanisms of planet formation

The last two decades have seen an extraordinary progress in the study of extrasolar planets, mainly thanks to the advances in the detection and in the characterization of their physical properties (Fischer et al. 2014, and references therein). The development of several detections methods (e.g., doppler measurements, transit observations, microlensing, astrometry, direct imaging) allowed us to explore parameter space regions (e.g., in the planet mass vs semi-major axis plane, see Fig. 1.3) that were unaccessible some years ago. The most prominent result of these planet-searching extensive studies has been to uncover the great diversity of the outcomes of the planet formation process, which is apparent in terms of planetary architectures as well as of physical properties of each planet Lissauer et al. (2014). Sizes, masses, average density and atmosphere composition of the observed exo-

planets place boundary conditions that are crucial to inform theoretical models of planet formation (Johnson et al. 2010; Howard 2013).

The variety in the physical properties that we currently observe in the exoplanet population can be hardly explained with a single, universal, mechanism. At a first order, we can divide the observed exoplanets into two morphological classes of planets: rocky (Earth-like) planets and gaseous (giant Jupiter-like or smaller sized Neptune-like) planets. Such differentiation is readily observed in our Solar System, with the inner planets being rocky (Mercury, Venus, the Earth, Mars) and the outer ones being gaseous (Jupiter, Saturn, Uranus, Neptune). Their different structure, size and mass imply that during their formation phase they have interacted in different ways with the gaseous disk where they were embedded. At the moment, theoretical models of planet formation are not able to constrain whether they formed *in situ* (i.e., in the location where we observe them today) or they formed outer in the disk and subsequently migrated reaching their current location at the time of the gas disk dissipation.

In the 20th century two main processes have been proposed to explain the formation of rocky and gaseous planets: the core accretion with subsequent gas capture model (Perri and Cameron 1974; Safronov 1972) and the disk instability model (Cameron 1978; Boss 1997). Both models have been developed to explain the formation of giant planets, however the core accretion model is also capable of explaining the formation of terrestrial planets (which can be thought as giant planets where a *runaway* gas accretion have not been triggered). In the next section I will outline the core accretion model and in Section 1.2.2 the gravitational instability model.

1.2.1 Core accretion

The fundamental idea behind the core accretion model for planet formation is that planets form through the progressive growth of solid particles, with the building blocks of planets to be identified in the sub-μm sized grains inherited from the parent ISM cloud (see Fig. 1.4). On their way to form a planet, the dust particles have to grow by at least 12 orders of magnitude in size via pair-wise interactions. As it will be apparent below, this dramatic growth needs the interplay of several physical mechanisms that become relevant at different growth stages and depend on the dynamical evolution of the disk.

In the first phase of planet formation the sub-μm sized grains are extremely well coupled to the gaseous disk via aerodynamic forces (gas drag). At this stage, grain growth is driven by coagulation (sticking in two body collisions), is favored by dust sedimentation (grain settling in vertical direction towards the disk midplane), is hampered by turbulence (who stirs up small solid particles preventing them from settling in the midplane), and is overall influenced by the radial drift toward the central star. All these processes determine the time and space evolution of the distribution of solids (micron to millimeter sized grains) in protoplanetary disks: observations able to constrain such distribution would provide us unique insight into the initial conditions of planet formation.

The second step of the core accretion model requires the grains to grow up to the formation of a population of *planetesimals*, bodies with 1-100 km radius whose orbital evolution is dominated by gravitational interactions rather than by interaction with the gaseous disks. Planetesimals are the building blocks of planets as they contribute to the formation the planetary (rocky) cores via two-body inelastic interactions. The process through which planetesimals can form is actually under debate, but there is general consensus about the fact that coagulation is not sufficient. Our knowledge of the coagulation (in terms of sticking efficiencies) and motion of solids in disks is based on theoretical models and limited
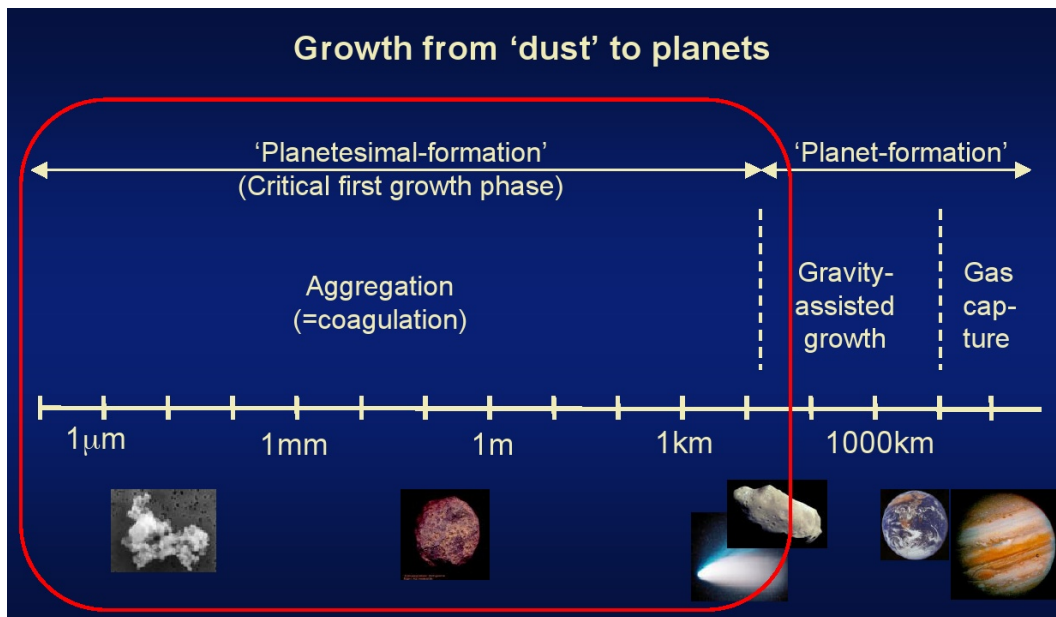
Fig. 1.4 Sketch of the core accretion model for planet formation. Planet formation starts with the build up of the planetesimals, bodies of 1-100 km in radius: the sub-μm sized ISM grains grow via coagulation up to $\sim$1 m, but further growth needs alternative mechanisms in which turbulence and gravity play important roles (see text). The planetary core is assembled from the planetesimals through gravity-assisted two-body inelastic encounters. If the protoplanet core is massive enough ($\sim 10 M_\oplus$) a rapid gas accretion is triggered and a gaseous planet is formed; otherwise, the a terrestrial planet with a rocky core and a tenuous atmosphere is formed. Credit: C. Dullemond.

laboratory experiments (for a review, see Blum and Wurm 2008): common evidence is that coagulation is able to produce dust agglomerates up to 1 m size in the inner disk but further growth by sticking of meter-sized boulders is rather difficult to conceive and impossible to reproduce in the laboratory.

In recent years several promising mechanisms have been proposed to explain the formation of planetesimals, and many of them are based on fluid instabilities forming dense clumps of dust particles (Chiang and Youdin 2010, and references therein). The process of grain growth via coagulation has an undoubted efficiency when the dust can be considered uniformly distributed throughout the disk: in this regime, the dust particles are subject to their mutual interactions and, since the total dust mass is much smaller (as low as 1%) than the total gas mass, they can be modelled in the gravitational field produced by the gas. However, a combination of vertical settling, radial drift and other effects (e.g., dust trapping, photoevaporation) might lead to local overdensities of dust that make its gravitational field not negligible anymore. In these conditions the dust comes to play a dynamical role in the disk evolution and new physical effects can become relevant.

In the classical model for planetesimal formation by Goldreich and Ward (1973), when the surface density of the dust particles (which have settled to the disk midplane) exceeds a critical value, a gravitational instability is triggered. At this point, dust particles collapse under their own gravity, thus leading to the prompt formation of planetesimals. This mechanism is extremely promising since the gravitational collapse is so fast that the it bypasses the potential issues involved in particle growth beyond the meter-scale regime. The role of turbulence in this mechanism is not clear yet. On the one hand, it seems to hamper the planetesimal formation: the velocity shear between the dust midplane (in Keplerian

motion) and the gas disk (in sub-Keplerian motion) undergoes Kelvin-Helmholtz instability that stirs up dust particles from the midplane and halts their collapse. On the other hand, recent numerical simulations (Cuzzi et al. 1993; Youdin and Goodman 2005) have shown that under certain conditions turbulence can be very effective in developing very dense clumps of solid material and therefore sustain the overall planetesimal formation.

Once a population of km sized planetesimals has formed in the disk, the planetary cores start to be formed via two-body inelastic collisions (aided by gravitational focusing) between the planetesimals. This leads to the growth of planetary cores up to a mass of the order of $1M_\oplus$. At this point, the maximum mass that a planetary core attains before the dissipation of the gaseous disk sets whether it will turn out in a terrestrial or in a gaseous planet. If the planetary core mass exceeds a critical mass (typically $\sim 10M_\oplus$ for fiducial disk parameters, but see more details in Pollack et al. 1996 and the heuristic derivation in Armitage 2010) then an hydrodynamic instability sets in and induces the rapid ($\sim 10^5$ yr) accretion of gas onto the protoplanet (Perri and Cameron 1974; Mizuno 1980). The amount of gas accreted depends on the supply from the disk which is in turn dependent on the gas density profile and on the disk dispersal time scale. This *runaway* accretion has the potential of forming gas giants like Jupiter or Saturn, as well as smaller gaseous planets like Neptune or Uranus, depending on the amount of gas available. If, conversely, the planetary core does not reach the critical mass (which is a function of the planetesimal distribution and of the gas cooling efficiency), it will terminate its evolution as a rocky planet with a tenuous atmosphere, similarly to our Earth. For this reason the core accretion scenario is the best candidate for the formation of terrestrial planets (Raymond et al. 2014, and references therein).

1.2.2 Disk instability

An alternative mechanism for giant planet formation is provided by the disk instability model, which was initially postulated by Cameron (1978) and only recently verified through exhaustive numerical simulations by Boss (1997). According to this model, if the protoplanetary disk is massive enough to be unstable under its own self-gravity, the giant planets are formed through the collapse of dense portions of the protoplanetary disk into gravitationally bound clumps. Unlike the core accretion scenario in which planetary cores are the outcome of a *bottom-up* grain growth process, in the disk instability model the formation of the cores is driven by the gas dynamics in which the dust *follows* the gas evolution and plays an indirect role by setting the opacity. For a recent review of disk instability applied to planet formation, see Helled et al. (2014).

The first necessary condition for planet formation through disk instability is the development of density perturbations in the disk. Through a linear stability analysis of the fluid equations governing the disk dynamics (for a derivation, see Armitage 2010) it can be shown that the disk becomes unstable to axisymmetric disturbances wherever

$$Q \equiv \frac{c_s \kappa}{\pi G \Sigma} < 1\,, \tag{1.1}$$

where $c_s \propto T^{1/2}$ is the sound speed, Σ is the gas surface density and κ is the epicyclic frequency (which equals $\Omega_{\mathrm{K}} = (GM_*/R^3)^{1/2}$ for Keplerian motion). The criterion above (Toomre 1964) has been developed for an infinitesimally thin disk and shows that pressure and shear have a stabilizing effect, while gravity tends to make the disk unstable. By means of numerous 2D and 3D numerical studies it has been verified (Durisen et al. 2007) that in the more realistic case of a disk with finite thickness and non-axisymmetric dis-

turbances, the stability criterion in Eq. (1.1) holds true, but instabilities develop for larger values of $Q \lesssim 1.7$ ($Q \lesssim 1.4$ for an isothermal disk, see Mayer et al. 2004). Wherever Q approaches the critical value, disk perturbations will grow exponentially forming density enhancements known as *spiral arms* that transport mass and angular momentum and dissipate through shocks (see Fig. 1.5, left panel).
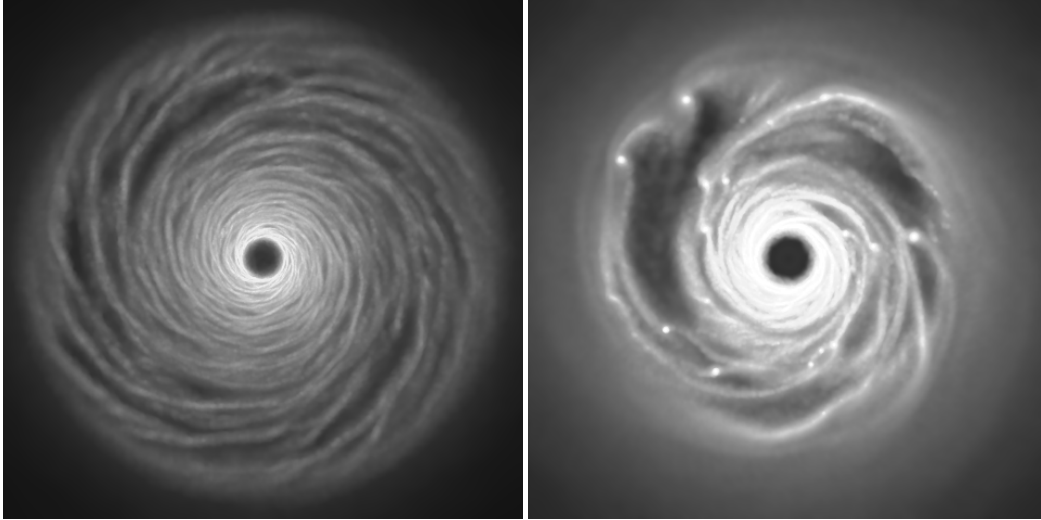
Fig. 1.5 Gas surface density of a massive ($M_{\mathrm{disk}} = 0.1 M_*$) self-gravitating disk. Spiral arms develop quickly at all radii into a quasi-steady state pattern *(left)*. Signs of fragmentation of the gaseous disk into gravitationally bound clumps are clearly visibile *(right)*. Credit: Rice et al. (2003).

Since the energy liberated by the spiral arms heats the gas and therefore contributes to the stabilization of the disk in a self-regulating mechanism, a second condition is necessary for disk instability to form giant planet cores. The additional destabilizing contribution is provided by the cooling mechanism, which has to counteract the heating contribution from the spiral arms dissipation. If t_{cool} is the cooling time scale and $t_{\mathrm{heat}} = 1/\Omega$ is the heating time scale (Ω is the angular gas velocity), it is useful to introduce the dimensionless ratio $\beta = t_{\mathrm{cool}}/t_{\mathrm{heat}} = t_{\mathrm{cool}}\Omega$ as an expression of the cooling efficiency. Gammie (2001) showed that a 2D disk fragments into gravitational bound clumps (see Fig. 1.5, right panel) if $\beta < \beta_{\mathrm{crit}}$, whereas it remains in a steady-state spiral pattern regime if $\beta > \beta_{\mathrm{crit}}$, where β_{crit} is a critical value which is function of the cooling law and typically varies between 6 and 12, depending on the adopted equation of state. The actual value of β_{crit} is currently under debate, as Meru and Bate (2011) showed that previous estimates based on 3D smoothed particle hydrodynamics (SPH) codes were not converging with numerical resolution. Recent revised estimates by Meru and Bate (2012) report β_{crit} as large as 20 or 30. Regardless the numerical intricacies of the disk instability mechanism and its non trivial dependence on the stellar properties and spectral energy distribution (SED), there is a general consensus that fragmentation is more likely to occur in the outer disk regions, and is positively favored if accretion from the molecular core onto the disk is still relevant.

The attractiveness of the disk instability model rests on its capability to form giant planets (mass $M_p \geq 1 M_J$) on a dynamical time scale, which is very short if compared to the viscous disk evolution. However, from a theoretical point of view, the effectiveness of this model in forming planets is still under heavy investigation: several uncertainties related to the cooling mechanism, to the role of metallicity and to the effects of stellar radiation have to be addressed with numerical simulations at higher resolution. From an

observational point of view, the increasing number of exoplanet detections is delivering us with an unprecedented sample that can be used to test the different physical ingredients of any planet formation model, e.g. through population synthesis studies (Mordasini et al. 2009). Furthermore, with the advent of ALMA, we have now the spatial resolution and the sensitivity to resolve spiral patterns in disks, which are expected to be detectable at (sub-)mm wavelengths and easily resolvable in disks in the closest star forming regions (Cossins et al. 2010; Dipierro et al. 2014, 2015).

1.3   Role of the Thesis: studying planet formation with multi-wavelength observations

The main topic of this Thesis is the characterization of the properties of the dust content in young circumstellar disks in order to provide robust constraints on the initial conditions for planet formation.

According to the core accretion scenario (Section 1.2.1), the formation of planets proceeds with the formation of rocky cores through the growth of dust aggregates from mm/cm to km sizes and the subsequent accretion of gas onto these cores to form the planetary atmosphere. The initial population of sub-micron sized dust particles coming from the ancestral interstellar cloud (Mathis et al. 1977) is processed by micro-physical interactions that determine the evolution of their shape, size, and structure (Testi et al. 2014 and references therein).

Determining the size distribution of dust grains in protoplanetary disks is of paramount importance in order to understand the initial conditions of planet formation. In the recent theoretical studies by Brauer et al. (2008) and Birnstiel et al. (2010) the evolution of dust grain populations have been modeled taking into account dust growth processes (coagulation and fragmentation) and the dynamical mechanisms responsible for the transport of dust grains (radial drift, vertical settling, turbulent mixing). According to these studies, radial drift effectively depletes the large grain population in disks within 1 Myr (see also Laibe 2014) unless it is halted by the occurrence of dust traps (Whipple 1972; Weidenschilling 1977; Klahr and Henning 1997; Pinilla et al. 2012) or a different aerodynamic behavior when the grains are extremely fluffy aggregates (Okuzumi et al. 2012; Kataoka et al. 2013).

The major limitation of theoretical grain growth studies is the lack of direct information on the actual size of dust grains occurring in the different regions of the protoplanetary disks. Observing a protoplanetary disk at different wavelengths allows different parts of the disk to be investigated (see Fig. 1.6). Optical, near-infrared, and mid-infrared observations show evidence of micron-sized dust grains in protoplanetary disks (Bouwman et al. 2001; van Boekel et al. 2003; Juhász et al. 2010; Miotello et al. 2012); however, they effectively trace the dust content only of the inner disk and its surface layer (both directly heated by the impinging stellar radiation). In order to study the disk midplane, where the bulk of the dust mass resides and planet formation is thought to occur, millimeter and sub-millimeter continuum observations are needed. At these longer wavelengths most of the disk becomes optically thin to its own thermal radiation and therefore directly probes the entire dust emitting volume. Moreover, by approximating the (sub-)mm dust opacity with a power law $\kappa_\nu \propto \nu^\beta$, changes in the spectral index β can be linked to changes in the dust properties (Stognienko et al. 1995; Henning and Mutschke 2010). In particular, Draine (2006) and Natta and Testi (2004) showed that β can be interpreted in terms of grain growth: large β-values are produced by small grains (μm to mm size), whereas small
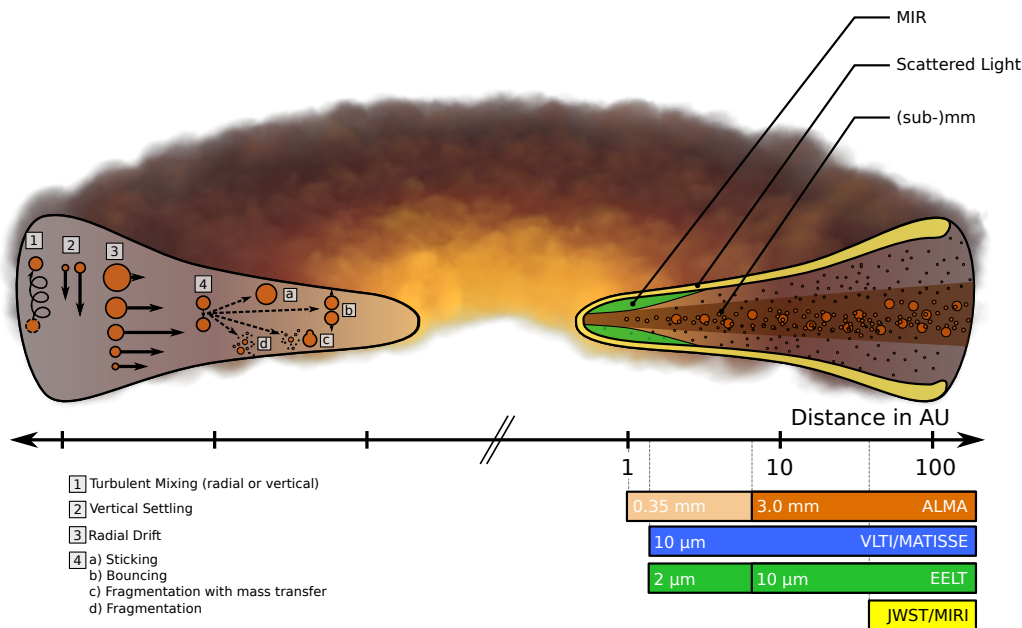
Fig. 1.6 Structure of a protoplanetary disk, with a summary of the grain evolution processes *(left side)* and an highlight of the regions probed by observations at different wavelengths *(right side)*. The left edge of the horizontal boxes indicate the spatial resolution attainable by different current (and future) observational facilities and instruments at different wavelengths for disks in the closest SFRs. Credit: Testi et al. (2014).

values $\beta \lesssim 1$ are a signature of dust grains larger than 1 mm.

From multiwavelength observations we can gain insight into the dust opacity spectral index, and therefore on the evolutionary stage of the dust in a protoplanetary disk. Past mm and sub-mm photometry studies of disks in several SFRs (Wilner et al. 2000; Testi et al. 2001, 2003; Rodmann et al. 2006) inferred disk-averaged β values which suggested that: (i) grain growth processes are particularly efficient, able to produce large grains (~ 1 mm) within relatively short timescales of $1 - 3$ Myr (Ricci et al. 2010a,b); (ii) local or global dust retention mechanisms must be occurring in disks in order to account for the observed presence of large grains in evolved disks (Testi et al. 2014).

In recent years, the improved observational capabilities offered by mm and sub-mm interferometers delivered - for the first time - spatially resolved observations that can be used to measure the dust properties as a function of the disk radius and to compare them with the theoretical predictions of grain growth models. Initial attempts using 1.3 and 3 mm observations showed hints of possible radial variation of the dust properties (Isella et al. 2010; Guilloteau et al. 2011) and recent studies have benefitted from extending the wavelength range to cm wavelengths using the Karl G. Jansky Very Large Array (VLA) (Banzatti et al. 2011; Trotta et al. 2013; Pérez et al. 2012; Menu et al. 2014; Andrews et al. 2014; Pérez et al. 2015). Azimuthal variations in the dust distribution have been recently discovered with ALMA early science observations in several disks and interpreted as dust traps, with the large grains being more concentrated than the small grains and the molecular gas (van der Marel et al. 2013, 2015; Fukagawa et al. 2013; Pérez et al. 2014; Casassus et al. 2015; Marino et al. 2015).

The main limitation of all the studies prior the beginning of my PhD is the lack of a self-consistent modeling of the multi-wavelength disk emission. Most of the studies

(except for Banzatti et al. 2011 and Trotta et al. 2013 who actually laid down the basis for the multi-wavelength fit that I have developed) fitted each wavelength separately, thus deriving a piece-wise solution made of disk models and dust populations of different grain sizes, each of them applying to different disk regions. The adoption of this piece-wise disk model reflected in the impossibility to interpret the results in terms of a global solution for the disk structure and a unique population of dust grains with a clearly defined maximum size distribution.

In my PhD I have therefore focused on developing the tools to investigate the dust properties in protoplanetary disks with a physically rigorous self-consistent modeling of the disk emission. The Thesis is organized as follows.

Chapter 2 – I present the disk model that I have employed to fit the multi-wavelength observations. I describe the main physical assumptions and the equations that are used to model the disk emission. I also explain the adopted dust model (grain composition, size, etc.) and the algorithm for computing the dust opacity.

Chapter 3 – I develop an analysis technique that allows us to constrain the disk structure (surface density and temperature profiles) together with the radial dust properties (maximum grain size profile). The analysis is based on the simultaneous fit of several observations at different wavelengths, spanning from 0.88 mm to 1 cm with a self-consistent disk model and a radially-dependent dust population. I apply the analysis to three protoplanetary disks and I use one of them to perform a (successful) benchmark of the technique against literature results. I obtain robust evidence that the grains are grown beyond $\sim$ cm sizes in the inner disk regions for all the disks, but the radial profiles are different for different disks. Understanding whether this reflects an evolutionary trend or an intrinsic scattering due to different initial conditions for the disk evolution requires to enlarge the sample to dozens of disks. With this study I have paved the way for applying this analysis to large samples of disks: the analysis is robust and computationally efficient, the interpretation of the results is robust as it rests on a self-consistent disk modeling, the exploration of degeneracies is thorough. This study sets the current state-of-the-art for the investigations of the dust properties from spatially resolved multi-wavelength radio observations.

Chapter 4 – I apply the multi-wavelength analysis technique developed in Chapter 3 to sub-mm, mm and cm observations of the protoplanetary disk around the Herbig Ae/Be star HD 163296. We assess the presence of large grains ($\gtrsim 1$ mm) in the inner disk region and smaller grains outside. For the first time, we observe that the radius where the grain size increases (≈ 100 au) interestingly matches the location of the CO snowline (which has been directly detected for this disk). Our findings provide observational support to the theoretical expectation that grain growth could be enhanced close to a snowline (e.g., due to changes in the grain sticking properties). Moreover, by applying the tool developed in Chapter 3 with a modified version of the two-layer disk model allowed us to discover the presence of a ring-like excess of emission exactly at 100 au from the central star. We could not pin down whether this excess is due to a local pressure maximum induced by the snowline or by local dust-retaining turbulent eddies, however we provided first evidence that grain growth might be influenced by the occurrence of gas snowlines.

Chapter 5 – I analyze the 890 μm continuum emission of more than 20 disks in the Lupus SFR which have been observed with ALMA at $\sim$0.3" ($\sim$50 au) resolution. The disks

have been fitted with the self-consistent disk model described in Chapter 2. Since we only have observations at one wavelength, we cannot constrain the radial dependence of the dust properties, but we derive for each disk its size and mass. The masses compare well with values derived with simpler methods, the discrepancy being due to the more refined determination of the temperature profile performed by our disk model. Moreover, I constrain the radial shape of the dust surface density and the disk inclination. The parameters derived with these fits provide structural constraints on a large set of disks that have been selected from a complete sample of Class II disks in the Lupus SFR. By studying the 890 μm integrated flux as a function of the disk size for the fitted Lupus disks I confirm the existence of a positive correlation that was initially claimed for disks in the younger Taurus-Auriga and Ophiuchus SFRs. Interestingly, I find an offset between the two correlations that is constant for disks of all sizes and might be a signature of the different mean ages of the different SFRs.

Chapter 6 – I develop a high performance computing tool that aims to accelerate the comparison of model predictions with interferometric observations at (sub-)mm wavelengths. With the huge enhancements in angular resolution and sensitivity delivered by modern radio interferometers such as ALMA and JVLA, the comparison of a model synthetic image with the observations becomes prohibitively intensive from a computational point of view since it involves several matrix operations (e.g., FFT, rotations, etc.) and interpolations (on non-uniformly spaced points). I therefore develop an accelerated library that leverages on the computing power of modern graphics processing units[5] (GPUs) which deliver stunning performances for matrix operations w.r.t. to the classical CPUs. I provide evidence of the speed-up that the library achieves under different working configurations. This GPU accelerated library constitutes the core engine of the code used in Chapter 3 to perform the multi-wavelength fits. The library is designed to work in parallel jobs on cutting-edge multi-CPU/multi-GPU architectures, thus allowing us to explore thoroughly even many-dimensional parameter spaces.

Chapter 7 – I draw the conclusions of this Thesis, highlighting the main findings and providing some prospective lines of research that this work suggests.

---

[5]Unlike central processing units (CPUs), which consist of a few cores designed for sequential processes, GPUs have a massively parallel architecture with thousands of smaller, but more efficient, cores optimized for the execution of multiple tasks simultaneously.

2

Modeling the (sub-)mm continuum emission of protoplanetary disks

In the last decade, the advent of modern radio interferometers such as ALMA and VLA allowed us to study the (sub-)mm/cm emission from protoplanetary disks at an unprecedented detail. The electromagnetic radiation emitted by protoplanetary disks provides us with a wealth of information about their geometrical and physical structure, however a proper modeling of their emission is needed in order to convert the observed flux into physical constraints. This task is usually performed with dedicated physical models that implement - at different degrees of accuracy - the several physical mechanisms that contribute to the continuum emission.

The role of this Chapter is to introduce the fundamental physics that we need to model the (sub-)mm spectral energy distribution (SED) of protoplanetary disks. In Section 2.1 I introduce the disk model based on the *two-layer* approximation that allows us to compute the disk emission in a simplified, yet physically rigorous, way and that constitutes the basis of the studies presented in Chapters 3, 4 and 5. In Section 2.2 I present the surface density profiles that are usually observed in disks. Finally, in Section 2.3 I present the model for the dust opacity and the algorithm for its computation.

2.1 Disk model

An accurate modeling of the physical structure (temperature and density distribution) of protoplanetary disks is needed in order to interpret their (sub-)mm emission in physical terms.

In this Thesis I adopt the *two-layer* disk model for passively irradiated disks, initially developed by Chiang and Goldreich (1997) and subsequently refined by Dullemond et al. (2001), so called because is a 1D model that resolves the radial structure of the disk assuming that its vertical structure can be reduced to two *layers*: the disk *surface* and the disk *interior*. These models proved successful in reproducing the continuum emission of protoplanetary disks in a wide range of wavelengths, from near-IR to sub-mm, and around stars ranging from low-mass brown dwarfs and T Tauri stars up to more massive Herbig AeBe stars (see Natta et al. 2007, and references therein). The advantage of using such
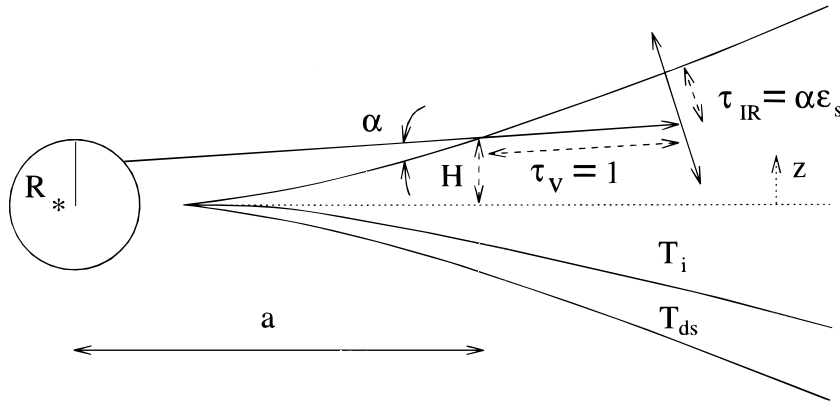
Fig. 2.1 Scheme of the two-layer disk model. Radiation from the star (left) impinges on the surface layer at an angle α and penetrates in the disk atmosphere until $\tau_* = 1$ (in the picture, the V in τ_V indicates that the stellar radiation is typically at visible wavelengths). Dust particles of the surface layer are heated and then re-emit the energy half away from the disk and half towards the disk midplane. The dust grains in the midplane are heated from this re-processed radiation and emit energy as black bodies at wavelengths much longer than visible, usually sub-mm/mm/cm. Credit: Chiang and Goldreich (1997).

models (as opposed to other disk models) is twofold: first, they provide us with a physically motivated disk structure which a parametric model would not be able to provide; second, as they are based on simple thermal balance arguments, they quickly converge to the solution, as opposed to models based on Monte Carlo calculations that are much more time-consuming.

The two layer disk model (see a scheme in Figure 2.1) is based on the fundamental assumption that the main source of heating for the disk is the stellar radiation (the disk is *passively* irradiated) and that the internal disk heating (e.g., due to the accretion process) is negligible at all radii (in the case this second heating dominates, the disk is said to be *active*). Further assumptions of the two layer model are hydrostatic equilibrium between gas pressure and stellar gravity and thermal balance between gas and dust. The two layer model neglects the disk self-gravity. In the following, we will assume that the disk is axis-symmetric and will make use of cylindrical coordinates (R, φ, z), where R is the distance from the star (located at the origin.

According to the model, the *surface* layer is defined as the region where the opacity to the stellar radiation is $\tau_s^{\mathrm{sur}} < 1$, while the disk *interior* (hereafter, *midplane*) is the region between the upper (at $z > 0$) and lower ($z < 0$) surface layers. Four inputs are needed for the computation of the two layer disk model: the stellar parameters (stellar luminosity L_*, mass M_*, effective temperature T_{eff}, distance d), the gas surface density profile $\Sigma_{\mathrm{g}}(R) \equiv \int \rho_{\mathrm{g}} \, \mathrm{d}z$, the dust properties (grain size distribution, grain composition, optical constants) and the gas-to-dust mass ratio $\zeta \equiv \rho_{\mathrm{g}}/\rho_{\mathrm{d}}$. The two layer disk model computes the thermal structure in an iterative way that converges when full thermal balance between surface and midplane layer is reached (within some accuracy) everywhere in the disk. At each iterative step, the model assumes that, at each radius, the surface layer absorbs a fraction of the impinging stellar radiation (striking the disk surface at a grazing angle α), heats up to a temperature T_{sur}, and then radiates half of the energy away from the disk and half towards the disk midplane. The dust grains residing in the disk midplane are then heated up to a temperature T_{mid} from this re-processed radiation and emit as black bodies at sub-mm/mm/cm wavelengths (here we neglect the surface layer absorp-

tion of this long-wavelength radiation). Following hydrostatic equilibrium, at each radius the midplane layer has a Gaussian vertical density distribution:

$$\rho(R,z) = \rho_0(R) \exp\left(-z^2/2H_p^2\right) , \tag{2.1}$$

where the scale height H_p is given by:

$$\frac{H_p}{R} = \left(\frac{T_{\mathrm{mid}}}{T_g}\right)^{1/2} \left(\frac{R}{R_*}\right)^{1/2} , \tag{2.2}$$

where $R_* = (L_*/4\pi\sigma_{\mathrm{SB}}T_{\mathrm{eff}}^4)^{1/2}$ is the stellar radius and $T_g = GM_*\mu m_p/k_{\mathrm{B}}R_*$ is the virial temperature at the stellar surface. The surface scale height H_s is then computed self-consistently from H_p, the grazing angle α, the surface density $\Sigma_{\mathrm{g}}(R)$ and the Planck mean opacity at the stellar temperature T_* (for the computational details, see Appendix A2 in Dullemond et al. 2001). We note that by imposing hydrostatic equilibrium the disk geometry turns out to be *flared*, i.e. the ratio H_s/R increases with radius[1].

A fundamental working condition for the two layer model is that the surface layer is optically thick to the stellar radiation, or, in other words, that the surface layer contains enough mass to reach $\tau_s^{\mathrm{sur}} = 1$. The optical depth of the surface layer is defined as $\tau_s^{\mathrm{sur}} = \kappa_\nu^{\mathrm{sur}}\Delta\Sigma$, where $\kappa_\nu^{\mathrm{sur}}$ is the opacity of the dust in the surface layer at the frequency ν, and $\Delta\Sigma$ is the surface density of the surface layer (computed as $\int \rho\, \mathrm{d}z$, with the line integral performed along the line of sight between the star and the surface element hit by the stellar radiation). Across the radial grid where the disk model is computed, it is possible that $\Delta\Sigma$ or $\kappa_\nu^{\mathrm{sur}}$ (or both) become so low that $\tau_s^{\mathrm{sur}} = 1$ is not reached anymore and the two layer model breaks down[2]. Let us call $\overline{R}$ the radius where this happens. In our implementation of the two layer model, to avoid the surface brightness of the disk falling off abruptly where the surface layer becomes optically thin, we assume a power-law behaviour for the midplane temperature such that:

$$T_{\mathrm{mid}}(R) = T_0(R/R_0)^{-k} , \tag{2.3}$$

where R_0 and T_0 are, respectively, the radius and the midplane temperature where the two layer model broke down and k is computed by fitting $T_{\mathrm{mid}}(R)$ in the region where the surface was still optically thick, around $R \approx R_0$.

Finally, following Isella et al. (2010) we impose a lower limit on the midplane temperature, namely the equilibrium temperature with the interstellar radiation field. We model this by adding an extra radiative flux impinging on the midplane $\sigma_{\mathrm{SB}}T_{\mathrm{ext}}^4$, where the temperature of the external radiation field $T_{\mathrm{ext}} = 7\,\mathrm{K}$. As a result, at each radius the midplane temperature is given by $[T_{\mathrm{mid}}^4(R) + T_{\mathrm{ext}}^4]^{1/4}$, where $T_{\mathrm{mid}}(R)$ is the temperature computed by the two-layer model for $R \leq \overline{R}$, and $T_{\mathrm{mid}}(R) \propto R^{-k}$ for $R > \overline{R}$. This additional flux contribution is negligible in the inner region of the disk and starts to be relevant only in the outer parts where T_{mid} becomes comparable to T_{ext}.

Once the surface and the midplane temperature profiles, respectively $T_{\mathrm{sur}}(R)$ and $T_{\mathrm{mid}}(R)$,

---

[1]Recent theoretical calculations of dust evolution show that in reality the disk geometry has to be flatter than the fully-flared one predicted by the two layer model (Dullemond and Dominik 2004). A reduced flaring allows mid- to far-IR fluxes as well as sub-mm spatially resolved observations to be better reproduced. In Chapters 4 and 5 we will employ far-IR observed fluxes to manually set a realistic flaring.

[2]$\Delta\Sigma$ is positively correlated with $\Sigma_{\mathrm{g}}(R)$, therefore with $\Sigma_{\mathrm{g}}(R)$ decreasing with radius, also $\Delta\Sigma$ decreases with radius. κ_ν^s can change with radius if the dust properties are radius-dependent (see Section 2.3).

are computed, the radial profile of the disk thermal emission at a given wavelength ν is given by:

$$I_\nu^{\text{tot}}(R) = I_\nu^{\text{sur}}(R) + I_\nu^{\text{mid}}(R) \, , \tag{2.4}$$

where

$$I_\nu^{\text{sur}}(R) = \frac{1}{d^2} \left\{ 1 + \exp \left[-\frac{\Sigma_{\text{d}}(R)\kappa_\nu^{\text{mid}}(R)}{\cos i} \right] \right\} B_\nu[T_{\text{sur}}(R)] \, \Delta\Sigma(R)\kappa_\nu^{\text{sur}} \, , \tag{2.5}$$

$$I_\nu^{\text{mid}}(R) = \frac{\cos i}{d^2} \left\{ 1 - \exp \left[-\frac{\Sigma_{\text{d}}(R)\kappa_\nu^{\text{mid}}(R)}{\cos i} \right] \right\} B_\nu[T_{\text{mid}}(R)] \, , \tag{2.6}$$

and $\Sigma_{\text{d}}(R) = \Sigma_{\text{g}}(R)/\zeta$ is the dust surface density, κ_ν^{sur} and $\kappa_\nu^{\text{mid}}(R)$ are respectively the surface and the midplane dust opacities, $B_\nu(T)$ is the blackbody brightness and i is the disk inclination ($i = 0°$ for a face-on disk). In the equations above we distinguish the surface and the midplane opacities (κ_ν^{sur} and κ_ν^{mid}, respectively) since they can be (and usually are) different: the disk surface hosts a population of small dust grains with sizes up to $1\,\mu\text{m}$ (thus providing a high optical depth at the visibile wavelengths), whereas the disk midplane is populated by the distribution of large grains (up to 1 mm or even 1 cm sized grains) representing the bulk of the dust mass (see Section 2.3 for more details). These equations hold for low disk inclinations (if the disk is seen at $i > 70°$ a proper ray tracing is needed to account for the optical depth induced by the vertical structure of the disk). The total disk emission can be computed by integrating over the disk surface:

$$F_\nu = 2\pi \int\limits_{R_{\text{in}}}^{R_{\text{out}}} I_\nu^{\text{tot}}(R) \, R\text{d}R \, , \tag{2.7}$$

where R_{in} and R_{out} are the inner and outer edges of the radial grid, respectively. In our modeling, $R_{\text{in}} = 0.1$ au, slighly larger than the dust sublimation radius (so that the dust is present everywhere in the disk region modeled), and $R_{\text{out}} \geq 600$ au, larger than the typical spatial extent of the sub-mm/mm emitting region.

Our two layer model implements the full equations and the iterative procedure described above, however, it is worth deriving here some simple relations that are typically used to convert the observed (sub-)mm flux into a disk mass. First, since $\Delta\Sigma \ll \Sigma_{\text{d}}$, the contribution from the disk midplane (eq. 2.6) to the total flux is much larger than the contribution from the disk surface (eq. 2.5). Moreover, since at (sub-)mm wavelengths the emission from the disk midplane is mostly optically thin, we can approximate the total flux as

$$F_{\text{mm}} \approx \frac{2\pi}{d^2} \int\limits_{R_{\text{in}}}^{R_{\text{out}}} \Sigma_{\text{d}}(R)\kappa_{\text{mm}}^{\text{mid}}(R)B_{\text{mm}}[T_{\text{mid}}(R)] \, R\text{d}R \, , \tag{2.8}$$

where it is apparent that the (sub-)mm continuum emission is a tracer of the dust mass (Σ_{d}), but the contribution of the mass to the observed flux is degenerate with the opacity and the temperature. In order to break this degeneracy it is necessary to gain independent information on the opacity (and, possibly, on its radial gradient) and on the temperature. This can be done, for example, by fitting simultaneously several observations at different

wavelengths, as we do in Chapter 3.

If we further assume that - at mm wavelengths - we are in the Rayleigh-Jeans regime of the spectrum ($T_{\mathrm{mid}} > 10$ K mostly everywhere in the disk), we obtain that the total flux can be approximated as:

$$F_{\mathrm{mm}} \approx \frac{M_{\mathrm{d}} \kappa_{\mathrm{mm}} <T>}{d^2} \, , \qquad (2.9)$$

where $<T>$ is the mass-averaged midplane temperature, M_{d} is the total dust mass and the opacity κ_{mm} has been assumed to be radially constant for this latter equation. This relation is usually employed to convert an observed (sub-)mm flux (F_{mm}) into a dust mass (M_{d}), however the uncertainties on the opacity and on the dust temperature constitute a major limitation of this simple conversion: the dust opacity can easily vary by one order of magnitude for not-so-much different grain size distributions or for slightly different grain composition, and the dust temperature varies by at least two orders of magnitude across the disk thus making it difficult to estimate its average value.

In the next Section we discuss possible choices for the surface density profile $\Sigma_{\mathrm{g}}(R)$ and in Section 2.2 describe the properties of the dust and the algorithm that allows us to compute its opacity κ_{ν}.

2.2   Disk surface density

In the previous section we have seen that the radial profile of the surface brightness of a protoplanetary disk at mm wavelengths has the following scaling (assuming that the emission is optically thin):

$$I_{\mathrm{mm}}(R) \propto \Sigma_{\mathrm{d}}(R) \kappa_{\mathrm{mm}}^{\mathrm{mid}}(R) B_{\mathrm{mm}} \left[T_{\mathrm{mid}}(R) \right] \, . \qquad (2.10)$$

Since most of the dust mass resides in the cold and dense disk midplane (Dullemond and Dominik 2004), this equation shows that observations at mm wavelengths can be used to trace the bulk of the dust mass in disks, provided that we have some constraint or make some assumption on the temperature profile and on the opacity: to obtain an estimate of the temperature profile $T_{\mathrm{mid}}(R)$ we can use a disk model (e.g., the one presented in the previous section), while for the dust opacity a common choice is to adopt a constant value throughout the disk, unless there is evidence for a radial gradient in κ (obtained, e.g., by comparing observations and multiple wavelengths)[3].

The total[4] surface density profile Σ is one of the most informative quantities describing the structure of a protoplanetary disk. Measurements of Σ are crucial to investigate both planet formation and disk evolution. By setting the mass distribution in the disk, the shape of Σ determines the initial orbits of the forming planets and influences their migrations. This is expected to leave important signatures in the properties of the exoplanet populations that we are now able to observe. Moreover, since Σ determines the angular momentum distribution in the disk, measuring it at a given time provides us with a direct measurement of the angular momentum flow in the disk and therefore a unique insight on its overall evolution (Hartmann et al. 1998).

---

[3]The absolute value of κ_{mm} depends on the actual properties of the dust grains emitting the (sub-)mm radiation (see next section). These properties (such as shape, size, composition of the grains) are unknown to us, however values typically used are $\kappa_{1\,\mathrm{mm}} \sim 2 - 3 \mathrm{\, cm}^2/\mathrm{g}_{\mathrm{dust}}$ (Beckwith et al. 1990).

[4]Where *total* means gas and dust. However, note that the dust mass is $\sim 1/100$ of gas mass.

For a geometrically thin disk in Keplerian rotation, the time (and space) evolution of Σ can be derived by solving the viscous equation (Lynden-Bell and Pringle 1974; Pringle 1981) which follows from the angular momentum conservation throughout the disk:

$$\frac{\partial \Sigma}{\partial t} = \frac{3}{R} \frac{\partial}{\partial R} \left[R^{1/2} \frac{\partial}{\partial R} \left(R^{1/2} \nu \Sigma \right) \right] , \qquad (2.11)$$

where $\Sigma = \Sigma(R, t)$ is a function of space and time and $\nu = \nu(R)$ is the kinematical viscosity. It can be shown[5] that the equation above has a diffusive nature, with viscosity being the driver of the diffusion: as time passes, the initial mass distribution $\Sigma(R, 0)$ spreads both inwards and outwards and is substantially accreted over a so called *viscous* time scale $t_\nu = R^2/\nu$.

The viscous equation can be solved analytically under simplifying assumptions on the viscosity and on its initial distribution. An important class of solutions is derived when the viscosity is assumed to have a simple power-law dependence which is constant with time, namely $\nu \propto R^\gamma$. In this case, the viscous equation has a similarity solution given by:

$$\Sigma(R, t) = \frac{C}{3\pi\nu_1} \left(\frac{R}{R_1} \right)^{-\gamma} \exp \left[-\frac{1}{\mathcal{T}} \left(\frac{R}{R_1} \right)^{2-\gamma} \right] \left(\frac{1}{\mathcal{T}} \right)^{1 + \frac{1}{2(2-\gamma)}} , \qquad (2.12)$$

in which R_1 is a radial spatial scale, C is a normalization constant and we have defined $\nu_1 = \nu(R_1)$. We have also introduced the dimensionless time $\mathcal{T}$:

$$\mathcal{T} = 1 + \frac{t}{t_\nu} , \qquad (2.13)$$

where the viscous time scale is given by:

$$t_\nu = \frac{1}{3(2-\gamma)^2} \frac{R_1^2}{\nu_1} . \qquad (2.14)$$

The global solution in Eq. (2.12) is often called *self-similar* solution of the viscous equation. For $t \ll t_\nu$ ($\mathcal{T} \sim 1$) we obtain that the initial mass distribution is

$$\Sigma(R, 0) = \Sigma_0 \left(\frac{R}{R_1} \right)^{-\gamma} \exp \left[-\left(\frac{R}{R_1} \right)^{2-\gamma} \right] . \qquad (2.15)$$

where we have substituted $\Sigma_0 = C/3\pi\nu_1$. This functional form is among the most used profiles to fit spatially resolved (sub-)mm observations of disks as it provides a smooth radial distribution with a clear physical interpretation. Thanks to the diffusive nature of the viscous equation, the self-similar solution in Eq. (2.15) is global (i.e., non-local) in the sense that links the time evolution of the inner disk (with power-law behaviour) to the one of the outer disk (which decreases with an exponential cut-off). The radial spatial scale R_1 is often called *characteristic radius* of the self-similar solution and can be regarded as a proxy for the disk size.

Another relevant spatial scale that follows from the angular momentum conservation

---

[5]By means of a change of variables such that $x = 2R^{1/2}$ and $y = \frac{3}{2}\Sigma x$, and assuming $\nu =$ const., Eq. (2.11) takes the shape of a prototypical diffusion equation $\partial y/\partial t = D\, \partial^2 y/\partial x^2$.

is the radius where the mass flux changes sign:

$$R_{\mathrm{T}} \equiv R_1 \left[\frac{\mathcal{T}}{2(2-\gamma)} \right]^{1/(2-\gamma)} . \tag{2.16}$$

At a given time, for $R < R_{\mathrm{T}}$ the fluid material moves inward and for $R > R_{\mathrm{T}}$ it moves outward; on the overall time evolution of the accretion disk, it is apparent from Eq. (2.16) that R_{T} moves outward. From the mass conservation we can also compute the time evolution of the total disk mass:

$$M(t) = M_0 \mathcal{T}^{-\frac{1}{2(2-\gamma)}} , \tag{2.17}$$

where $M_0 = 2\pi \int_0^\infty \Sigma(R, 0)\, R\, \mathrm{d}R$ is the initial disk mass.

2.2.1 Comparison with observations

In this section I illustrate some of the surface density profiles that are usually employed to interpret the spatially resolved continuum emission of protoplanetary disks. I also collect the main results obtained by past works in terms of measurements of disk sizes and spatial gradients of Σ.

The typical size of a protoplanetary disk is of the order of 100-500 au in radius, which corresponds to an angular size of $1'' - 3''$ at the distance of the closest low-mass star forming regions such as Taurus (140 pc) and Ophiuchus (125 au). At mm wavelengths this spatial resolution can be achieved only by means of interferometry (synthesis imaging), and this was one of the main motivations driving the development of modern (sub-)mm/cm interferometers such as ALMA and VLA.

The first millimetric survey targeting protplanetary disks was carried out by Dutrey et al. (1996), who observed more than 30 disks aroung young stars in the Taurus-Auriga star forming region. They fitted the mm observations with a simplified profile for the surface density, a truncated power-law:

$$\Sigma(R) = \begin{cases} \Sigma_0 \left(\dfrac{R}{R_0} \right)^{-p} & R \leq R_{\mathrm{out}} \\ 0 & \text{otherwise} \end{cases} \tag{2.18}$$

where $\Sigma_0 = \Sigma(R_0)$ and R_{out} is the disk radial size. This functional form has three free parameters: Σ_0, p and R_{out}, while R_0 can be kept fixed to an arbitrary value. Dutrey et al. (1996) obtained a distribution of values for R_{out} between 50 au and 300 au, but the angular resolution ($\sim 2''$, corresponding to 140 au in radius at the distance of Taurus-Auriga) was not good enough to obtain robust constraint on the radial gradient p. Using the power-law profile in Eq. (2.18) has the advantage of providing a simple phenomenological interpretation of the surface brightness: a monotonically decreasing (or increasing, for $p < 0$) surface density profile with a very clear definition of disk size (R_{out}). Nevertheless, the interpretation of the simple power-law profile in terms of accretion theory is less visibile w.r.t. the self-similar solution in Eq. (2.15).

More recently, Hughes et al. (2008) analyzed the dust and the gas emission at 890 μm and 1.3 mm of four young nearby disks finding that there is an apparent discrepancy between the gas and the dust outer radii (see also, de Gregorio-Monsalvo et al. 2013). By modeling the dust and the gas emission, Hughes et al. (2008) demonstrated that such dis-

crepancy cannot be solved by using a truncated power-law profile but rather with a similarity solution like the one given in Eq. (2.15). The main motivation for the success of the self-similar solution is in the exponentially-tapered edge, which allows a large enough gas column density to produce detectable CO 3-2 line emission, even though the drop off is significant enough that the dust continuum emission is negligible. The sharp outer edge of the power-law model, conversely, limits the extent of the CO emission to the region where dust continuum emission is present, which is in contrast with the observations.

Subsequently, the self-similar solution has been used in a number of studies that analyzed mm observations of Taurus-Auriga and Ophiuchus disks at sub-arcsecond angular resolution, allowing the disk size and the shape of Σ to be constrained more robustly (Isella et al. 2009, 2010; Andrews et al. 2009, 2010; Guilloteau et al. 2011). All these studies found a range of characteristic radii (proxy for the disk sizes) very similar: Isella et al. (2009) derived $R_c \sim 30 - 230$ au, while Andrews et al. (2009, 2010) obtained $R_c \sim 14 - 198$ au and Guilloteau et al. (2011) found $R_c \sim 10 - 180$ au. In terms of shape of Σ, the results are more assorted: Isella et al. (2009) reports γ between -0.8 and 0.8, Andrews et al. (2010) between 0.4 and 1.1, and Guilloteau et al. (2011) $\gamma \sim -0.2 - 1.6$. To understand whether the discrepancies between the shapes of Σ and the similarities in the disk sizes can be interpreted in terms of disk evolution, or are rather expression of the intrinsic scattering of the initial conditions of these disks, we need more complete and more uniform surveys of the closest star forming regions.

In the ALMA era, it is now possible to carry out high angular resolution ($< 0.3''$) and high sensitivity (rms $\sim 10\,\mu$Jy) observations for large samples of disks at multiple wavelengths, ranging from 890 μm to 3 mm. The first high-resolution surveys at 890 μm of protoplanetary disks in the closest star forming regions have been completed (Barenfeld et al. (2016), Upper Sco; Ansdell et al. (2016), Lupus; Pascucci et al. (2016), Chamaeleon). Leveraging on the power of statistical analysis, these observations have the potential of revealing scaling laws that we cannot investigate with the detailed modeling of single sources. To this extent, in Chapter 5 I show the application of the analysis tool that I have developed to the ALMA survey of the Lupus disks at 890 μ m, where I use the self-similar profile to derive constraints on the disk size and on the shape of Σ for 20 disks.

Throughout this Thesis, I always adopt the self-similar profile in Eq. (2.15) which allows the derived disk structure to be interpreted directly in terms of the evolution of accretion disks.

2.3   Dust model

In the previous section we recalled the fundamental equations of the two-layer disk model that is used throughout this Thesis. A key physical parameter that influences the continuum emission (especially at radio wavelengths) is the dust opacity κ_ν (see, e.g., Eq. 2.5 and 2.6), which depends on dust properties such as the grain size and shape distribution, the grain temperature, the chemical composition, the electric charge, etc. (see Chapters 22 to 25 in Draine 2011). Since all these properties must be specified in order to compute the bulk dust opacity κ_ν, we can use (sub-)mm observations (which are sensitive to κ_ν) to increase our knowledge of the dust properties in protoplanetary disks (Testi et al. 2001; Draine 2006). Observational constraints on the dust properties would be of paramount importance for theoretical models of planet formation as they would constitute a major input parameter setting the environment of the initial stages of planet formation (Armitage 2010; Testi et al. 2014).

2.3.1 Dust composition

Assessing the composition of dust grains from measurements of the wavelength-dependent opacity is not an easy task as it requires the simultaneous analysis of several tracers and an accurate modeling of the interaction between the grain and the radiation. Indeed many physical mechanisms (e.g., related to the thermal conditions where the dust grains live) as well as other dust properties may *pollute* the spectral features that can be used as signatures of particular dust compounds, thus making the determination of their abundances rather degenerate.

By collecting a wide range of astronomical data, the composition of primitive solar system bodies and solar elemental abundances, Pollack et al. (1994) derived a model for the composition and the abundances of grains and gaseous species in molecular cloud cores and accretion disks around young stars. The dust properties in protoplanetary disks are derived from those in molecular cloud cores assuming the cold dust in the outer disk has undergone minor processing (the dust in the cloud core is slightly processed from the shock occurring at the cloud-disk interface) and the dust of the inner disk has properties similar to those of the dust residing in the warm regions of cloud cores. The mass fractions of the most abundant grain species found by Pollack et al. (1994) are reported in Table 2.1.

Throughout this Thesis I assumed a simplified version of the Pollack et al. (1994) model assuming the three most abundant species: water ice, astronomical silicates (e.g., olivine) and refractory organics. Furthermore, since the process of grain growth in disks leads grains to form fluffy aggregates with fractal structures, the dust model I assume always considers a rescaled version of these abundances to account for a 30% vacuum in the grain composition (cf. the *Porous simplified version* in Table 2.1).

Table 2.1   Dust composition in protoplanetary disks

Species	Bulk Density (g/cm^3)	Pollack et al. (1994)		Simplified version	
		Mass fr. $\times 10^{-3}$	Volume fr. %	Compact Volume fr. %	Porous Volume fr. %
Water ice	0.92	5.55	59.46	65.99	46.2
Refractory organic	1.5	3.53	23.19	25.74	18.0
Olivine	3.49	2.64	7.46	8.27	5.8
Orthopyroxene	3.40	0.77	2.23	–	–
Troilite	4.83	0.77	1.57	–	–
Volatile organic	1.0	0.60	5.93	–	–
Metallic iron	7.87	0.13	0.16	–	–
Vacuum	–	–	–	0	30.0

Notes. Grain species in accretion disks around young stars, sorted by decreasing mass fraction, derived by Pollack et al. (1994). For each species, we report the mass and volume fractions found by Pollack et al. (1994) and the volume fractions for two simplified versions: for *compact* (0% vacuum) and *porous* (30% vacuum) grains. The latter version is adopted throughout this Thesis.

2.3.2   Shape

In the core accretion scenario, the coagulation of small sub-μm sized grains into larger aggregates is the first step towards planet formation. The complexity of the structures of the growing aggregates is determined by the dust composition, by the collision velocity between dust grains and by the relative size of the colliding grains (see Testi et al. 2014, and references therein). At low collision velocities the sub-μm sized aggregates develop fractal and fluffy structures (Kataoka et al. 2013), while as they grow and hit at higher velocities they are compactified and therefore can be better described as spherical grains with typical volume filling factor between 0.05 and 0.5 (Blum and Wurm 2008). Since the (sub-)mm emission is mostly produced by large mm-sized grains, for studies in this wavelength regime it is safe to assume that the dust grains have a spherical shape.

2.3.3   Grain size distribution

The distribution of dust grains in gas-free environments such as asteroid belts and debris disks is regulated by a so-called *collisional cascade* (Williams and Wetherill 1994): large bodies undergo collisions at extremely high velocities (order of km/s) which cause their fragmentation into smaller bodies which, in turn, collide and fragment further until they reach μm sizes and are removed by Poynting-Robertson drag (Wyatt et al. 1999). Dohnanyi (1969) computed the grain size distribution induced by such a collisional cascade and found that it is well represented by a power-law density distribution[6] $n(a) \propto a^{-q}$, where a is the grain radius and $q = 3.5$. Derived under the assumption that the collisions have self-similar outcomes, the slope of the power-law distribution found by Dohnanyi (1969) is primarily set by the mass dependence of cross section and is very weakly dependent on the mechanical details of the fragmentation process (Tanaka et al. 1996; Makino et al. 1998; Kobayashi and Tanaka 2010).

 Since the Dohnanyi (1969) distribution is in good agreement with size distribution of ISM grains (Mathis et al. 1977), it is normally used to describe the dust also in the gas-rich medium of protoplanetary disks. In the standard star formation scenario (Shu et al. 1987), protoplanetary disks are made out of the material of their parent cloud, therefore it is reasonable to assume that the building blocks available for planatesimal formation are the sub-μm sized grains typical of the ISM. However, in the gas-rich interior of protoplanetary disks, the grain motions are damped by the interaction with the gas and their relative velocity is greatly reduced. This leads to an enhanced probability of grain sticking in low-velocity encounters, and to an overall growth of grain size (Birnstiel et al. 2011). For a review of theoretical models of grain growth in protoplanetary disks see Birnstiel et al. (2016).

 Throughout this Thesis, we assume a power-law grain size distribution that captures both the aspects described above: in the disk atmosphere (i.e., the surface layer) we expect the grain size distribution to be dominated by small, sub-μm sized grains, therefore we will adopt a slope $q = 3.5$ (Mathis et al. 1977). Conversely, in the disk interior (i.e., in the midplane layer), we expect the grains to have grown in size and settled (Dullemond and Dominik 2004; Tanaka et al. 2005), therefore we will use a slope $q = 3.0$ which corresponds

---

[6]The distribution can also be stated as a function of grain mass: $n(m) \propto m^{-\alpha}$, with $\alpha = 11/6$.

to a population of larger grains. The grain size distribution can be summarized as follows:

$$n(a)^{\mathrm{sur}} = \begin{cases} a^{-3.5} & 10\,\mathrm{nm} \leq a \leq 1\,\mu\mathrm{m} \\ 0 & \mathrm{otherwise} \end{cases} \qquad \text{(for the surface)} \qquad (2.19)$$

$$n(a)^{\mathrm{mid}} = \begin{cases} a^{-3} & 10\,\mathrm{nm} \leq a \leq a_{\mathrm{max}} \\ 0 & \mathrm{otherwise} \end{cases} \qquad \text{(for the midplane)} \qquad (2.20)$$

where a_{max} is the maximum grain size in the midplane layer.

There is theoretical (Brauer et al. 2008; Birnstiel et al. 2009) and observational (Testi et al. 2003; Natta and Testi 2004; Rodmann et al. 2006; Ricci et al. 2010b) evidence that typical a_{max} in the disks midplane is (at least) $1\,\mathrm{mm} - 1\,\mathrm{cm}$, but these are disk-averaged values and a currently active area of research is the determination of the maximum grain size that can be reached in protoplanetary disks as a function of the location in the disk (Pérez et al. 2012; Tazzari et al. 2016). Indeed, many dynamical an micro-physical effects arising from the interaction with the gas hamper the growth of dust grains, resulting in several *barriers* that the grains have to overcome in order to reach the planetesimal size.

One of the main aims of this Thesis (cf. Section 1.3) is to determine the radial profile of a_{max} in protoplanetary disks: in Chapter 3 I develop a tool that allows us to constrain $a_{\mathrm{max}}(R)$ from multi-wavelength resolved (sub-)mm observations and in Chapter 4 I apply the method to the disk orbiting the Herbig AeBe star HD 163296.

2.3.4 Opacity calculation

In this section we compute the opacity κ_ν corresponding to the dust model specified in the previous sections. We therefore aim at computing the optical properties of a population of dust grains with size distribution $n(a)$, spherical shape and a mixed chemical composition.

First, we use the Bruggeman (1935) mixing theory that allows us to compute the optical properties of dust grains made of different chemical components by combining the optical properties of each component. The simplified version of the Pollack et al. (1994) dust model that we are using assumes dust grains made of water ice, refractory organics and olivine, with volume fractions of 46.2%, 18% and 5.8%, respectively, and account for a 30% of vacuum. The average density of a composite grain can be computed as:

$$\overline{\rho} = \sum_{j=1}^{N} f_j \rho_j \,, \qquad (2.21)$$

where f_j and ρ_j are the volume fraction and the bulk density of the $j-$th component, respectively, and N is the total number of components. For our dust model $\overline{\rho} = 0.9\,\mathrm{g/cm}^3$ and $N = 4$, vacuum being the fourth component having $f_4 = 0.30$.

It is useful to define the complex *refractive index* $m_j = n_j + ik_j$ and the *dieletric function*[7] $\epsilon_j = m_j^2$ of the $j-$th chemical component. Note that both these quantities are function of λ, the wavelength of the incident radiation, and vacuum has $\epsilon = 1$ by definition. Throughout this Thesis we use the measurements of the wavelength-dependent refractive index from Warren (1984) for water ice, from Zubko et al. (1996) for refractory organics and from Weingartner and Draine (2001) for astronomical silicates.

---

[7]Defined as the response of a material to an incident electric field $E = E_0 e^{-i\omega t}$.

According to the Bruggeman (1935) theory, we can derive an *effective* dielectric function $\epsilon_{\rm eff}$ for a composite material by solving the following *mixing rule* for $\epsilon_{\rm eff}$:

$$\sum_{j=1}^{N} f_j \frac{\epsilon_j - \epsilon_{\rm eff}}{\epsilon_j + 2\epsilon_{\rm eff}} = 0 \,. \tag{2.22}$$

Once $\epsilon_{\rm eff}$ is computed, to convert the dielectric function into an opacity estimate we use Mie theory[8] (Mie 1908; Debye 1909) which provides a solution to Maxwell's equations for spherical grains of size comparable to the wavelength of the incident radiation. Mie theory allows us to compute the wavelength dependence of the normalized absorption cross section $Q_{\rm abs}(\nu, a)$ for a grain of radius a. From the definition of opacity (Rybicki and Lightman 1986) we can thus compute the opacity of a single grain as:

$$\kappa_{\rm abs}(\nu, a) \equiv \frac{C_{\rm abs}}{m} = \frac{Q_{\rm abs}\pi a^2}{m} = \frac{3}{4a\overline{\rho}} Q_{\rm abs}(\nu, a) \,, \tag{2.23}$$

where $C_{\rm abs}$ is the absorption cross section and m is the grain mass. For a population of dust grains with size distribution $n(a)$, the overall opacity is obtained by mass-averaging $\kappa_{\rm abs}$ over the population:

$$\kappa(\nu) = \frac{1}{M} \int\limits_{m_{\rm min}}^{m_{\rm max}} \kappa_{\rm abs}(\nu, m)\, n(m) m \,{\rm d}m = \frac{4\pi\overline{\rho}}{3M} \int\limits_{a_{\rm min}}^{a_{\rm max}} \kappa_{\rm abs}(\nu, a)\, n(a) a^3 \,{\rm d}a \,, \tag{2.24}$$

where $m = \frac{4}{3}\pi\overline{\rho}a^3$ is the mass of a grain and M is the total mass of the dust population. At radio wavelengths the frequency dependence of κ can be well approximated with a power-law, therefore it is usually written as:

$$\kappa(\nu) = \kappa_0 \left(\frac{\nu}{\nu_0} \right)^{\beta} \,, \tag{2.25}$$

where κ_0 is a normalization factor and β is the spectral index. Opacity measurements at mm wavelengths for dust in the ISM exhibit a steep spectral index $\beta_{\rm ISM} = 1.7$ (Friesen et al. 2005), while in protoplanetary disks the observed values are smaller $\beta_{\rm disk} \simeq 1$ (Beckwith et al. 1990; Testi et al. 2003; Natta and Testi 2004; Ricci et al. 2010a,b).

While the absolute scale of κ indeniably depends on the grain structure (which sets the absorption and scattering cross sections), Draine (2006) showed that the small $\beta_{\rm disk}$ values that are commonly observed in disks can be safely interpreted as the result of an increased grain size $a \gtrsim 3$ mm. The mm spectral index β can be therefore used as a tracer for grain growth, and has been recently measured in a few protoplanetary disks as a function of the distance from the star (Pérez et al. 2012, 2015; Tazzari et al. 2016; Guidi et al. 2016): all these studies find $\beta \ll 1$ in the inner disk ($R < 100$ au) and a gradient towards larger $\beta \simeq \beta_{\rm ISM}$ in the outer disk, evidence that would confirm the size-sorting effect induced by radial drift (large grains, less coupled with the gas than small grains, drift inwards more quickly).

Finally, the theoretical dust opacity calculation described in this section allows us to convert the measurements of β in estimates of the maximum grain size: in Figure 2.2 we show that $\beta \lesssim 1$ is a clear signature of the presence of large grains with sizes $a_{\rm max} \gtrsim$

---

[8]A modern derivation of Mie theory is given in Stratton (1941) and in Chapter 9 of van de Hulst (1981).
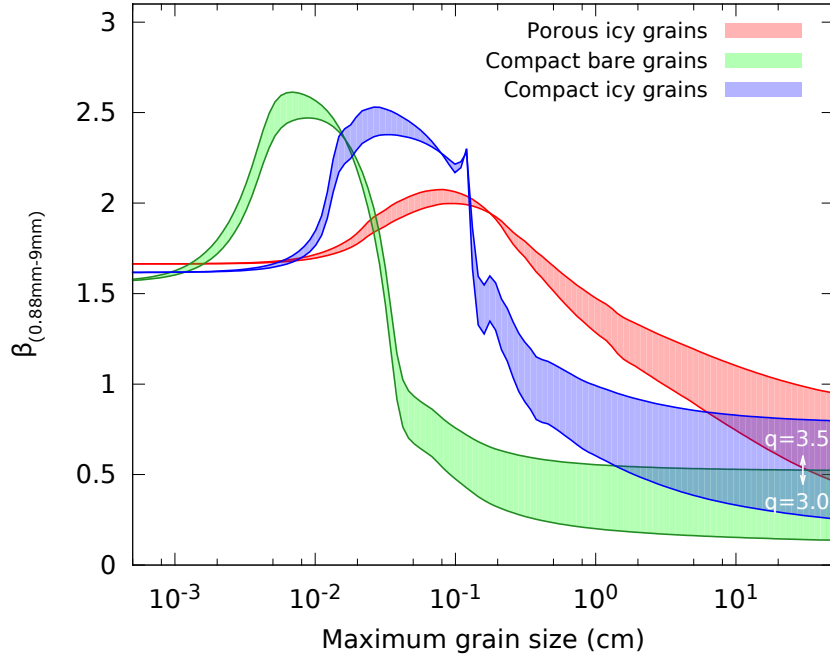
Fig. 2.2 Dust spectral index β as a function of a_{max} for a dust population with a power-law size distribution as in Eq. (2.19) and (2.20), for three different grain compositions. The colored bands show the range of β values produced for different power law indices q. $\beta \lesssim 1$ can be safely interpreted in terms of large grains ($a \gtrsim 1\,\mathrm{mm}$), regardless the composition. Credit: Testi et al. (2014).

1 mm, regardless the dust composition, porosity and size distribution (Testi et al. 2014). In Figures 3.1 (Chapter 3) and C.1 (Appendix C) I show the opacity $\kappa(\lambda)$ and the spectral index β as a function of a_{max} for the dust model that I adopt throughout this Thesis.

3

Multi-wavelength analysis for interferometric (sub-)mm observations of protoplanetary disks

The content of this chapter has been published in:

3.1   Need for a *forward-modeling* approach

The first multi-wavelength study that leveraged on a wide sub-mm/cm wavelength coverage was carried out by Pérez et al. (2012), who used interferometric observations between 0.88 and 9.8 mm to constrain the radial profile of the β index in the AS 209 protoplanetary disk. They fit each wavelength separately assuming a dust opacity constant with radius, and derived a disk temperature profile and an optical depth profile $\tau_\nu \propto \Sigma \kappa_\nu$ for each wavelength, where Σ is the dust surface density and κ_ν is the dust opacity. Then, given that the surface density must be wavelength independent, they ascribed the changes in τ_ν to variations in κ_ν (and therefore in the dust properties), thus deriving the $\beta(R)$ profile. They found $\beta \sim 0.5$ (mm- and cm-sized grains) in the inner disk region ($R \lesssim 50\,au$) and $\beta \gtrsim \beta_{\mathrm{ISM}} = 1.7$ (sub-mm-sized grains) in the outer disk. The main limitation of this study was the lack of a self-consistent modeling of all the fitted wavelengths with a single disk model with radially-dependent dust properties. The adoption of this piece-wise disk model reflected in the impossibility to interpret the results in terms of a global solution for the disk structure characterized by a unique population of dust grains with a clearly defined maximum size distribution.

Improving on the results of Banzatti et al. (2011), Trotta et al. (2013) carried out the first attempt of a self-consistent modeling of the disk structure and the dust properties

by fitting interferometric observations of the CQ Tau protoplanetary disk using a radius-dependent grain size distribution. With this model, they were able to fit observations simultaneously at 1.3, 2.6, and 7mm, finding evidence of dust grains ranging in size from a few cm in the inner disk ($<$ 40 au) to a few mm at 80 au. The work by Trotta et al. (2013) laid down the basis of the study we present here, where we have developed this multiwavelength fit technique further.

In this Chaper we present a data analysis procedure that exploits the wealth of information carried by multiwavelength (sub-)mm observations in order to characterize the disk structure and the level of grain growth in the disk in a self-consistent way. Previous studies fit observations at different wavelengths separately, inferring for each of them a different temperature and surface density profile. We note that the discrepancy in the temperature profile inferred from fitting two different wavelengths can be as large as a factor of 2, especially in the outer disk, see Figure C.2 in Appendix C). Then, making assumptions on the average temperature and surface density profile that should characterize the disk, these studies reconciled the wavelength-dependent discrepancies between the models by deriving a $\beta(R)$ profile. Adopting a more typical forward-modeling technique, the multi-wavelength analysis we present here derives a self-consistent disk model defined by unique temperature, surface density, and grain size profile that make it capable of reproducing the observed disk emission at all the wavelengths simultaneously. The multiwavelength nature of the analysis enables us to break the degeneracy between the disk temperature, the dust opacity, and the dust surface density and thus provides us with a self-consistent physical description of the disk structure.

With ALMA reaching full science and the major upgrade of the VLA, the improving quality of the (sub-)mm observational datasets in terms of angular resolution and sensitivity make such automated multiwavelength analysis an ideal tool to investigate the disk structure and the dust properties for a large number of disks.

The Chapter is organized as follows. In Section 3.2 we introduce the architecture of the analysis technique, describing the details of disk and of the dust models, and clarifying the Bayesian approach adopted for the analysis. In Section 3.3 the details of the observations are given. In Section 3.4 we present the results of the fit of FT Tau and in Section 3.5 fit results for the other disks. In Section 3.6 we compare and discuss the results obtained for the different disks. In Section 3.7 we draw our conclusions. In Appendices B and C we describe, respectively, the implementation of the Bayesian analysis and the results produced during the benchmarking of our analysis against previous results by Pérez et al. (2012).

3.2   Analysis technique

We developed a method for constraining the dust properties and the disk structure through the self-consistent modeling of sub-mm and mm observations. The method is based on the simultaneous *uv*-plane fit of several interferometric observations at different wavelengths. The strength of the method lies in the fact that it allows the derivation of a unique disk structure and dust size distribution capable of reproducing the observed flux at all the fitted wavelengths (forward-fit).

The method adopts a Bayesian approach and performs an affine-invariant Markov chain Monte Carlo (MCMC) method developed by Goodman and Weare (2010) to explore parameter space in an efficient way. The results of the fit provide probability distributions for the value of each free parameter, estimates of their correlations, and a best-fit model from which residual maps can be computed.

Furthermore, we designed the method to have a modular and flexible architecture. It is *modular* in the sense it allows the disk and the dust models to be changed independently of each other, making it suitable for studying disks with particular morphologies (e.g., with holes or asymmetries) or for testing different dust opacity models. It is *flexible* as it is designed to fit each observed $(u, v)-$point independently rather than binned values of deprojected visibilities (which would require an a priori knowledge of the disk center, inclination, and position angle). This makes the method ready to be applied to disks with non-axisymmetric surface brightness distributions and to be expanded in future to fit the disk inclination and position angle self-consistently with the disk structure.

It is worth noting that the major requirement of this method is the availability of a fast and efficient disk and dust model. Since the MCMC usually requires from one to two million model evaluations in order to converge, the speed and the efficiency of the model become extremely important and determine the overall computation time. For this, a huge effort was put into the optimization of the disk and the dust models and into the computation of synthetic visibilities. The average time required for one posterior evaluation[1] is approximately 30 seconds on an Intel® Xeon® CPU E5-2680 at 2.70GHz, thus implying that one million evaluations would require more than 1 year to be computed. However, since half of the model evaluations required by the affine invariant MCMC can be computed independently of each other at each step, the overall computation time can be shortened to 2 days by parallelizing the code and running it on hundreds of cores. We achieved an extremely good scalability of the code performance up to 200 cores using the implementation and parameters discussed in Section 3.2.3.

3.2.1 Disk model

We compute the disk structure and its thermal emission adopting the two-layer disk model of Chiang and Goldreich (1997) with the refinements by Dullemond et al. (2001). According to the two-layer approximation, the disk is modeled as a surface layer directly heated by the radiation of the central star and an internal layer – hereafter called midplane – heated by the radiation reprocessed by the surface layer. Accretion, if present, is another process that would contribute to the heating of the midplane. This internal heating is most efficient in the very inner regions of the disk and only if the accretion rate is very high (see, e.g., Dullemond et al. 2007, and references therein); however, for this particular study we neglect it. Assuming that the disk is vertically isothermal (separately in each layer) and in hydrostatic equilibrium under the gas pressure and the gravitational field of the star, the two-layer approximation allows us to compute the structure of the disk by solving the vertical radiative transfer equation at each radius. The disk model is computed over a logarithmic radial grid between an inner and an outer radius, respectively $R_{in} = 0.1\,au$ and $R_{out} \geq 300\,au$; the exact value of R_{out} is chosen to be much larger than the continuum emission observed for the particular object that is being fitted.

Once the surface and the midplane temperature profiles, respectively $T_{sur}(R)$ and $T_{mid}(R)$, are computed, the radial profile of the disk thermal emission (assumed to be optically thin)

---

[1] A posterior evaluation consists of an execution of the disk and the dust models; the computation of the synthetic visibilities through four fast Fourier transforms (FFT) (for the test case, we fit four wavelengths and the matrix sizes were 1024x1024, 1024x1024, 4096x4096, and 4096x4096, which are defined by the range of (u,v) distances sampled by the observed visibilities); and the sampling of the synthetic visibilities at the location of the antennas (for the test case we have approximately 2.5 million *uv*-points).

at a given wavelength ν is given by:

$$I_\nu^{\text{tot}}(R) = I_\nu^{\text{sur}}(R) + I_\nu^{\text{mid}}(R) \,, \tag{3.1}$$

where

$$I_\nu^{\text{sur}}(R) = \frac{1}{d^2} \left\{ 1 + \exp\left[-\frac{\Sigma_{\text{d}}(R)\kappa_\nu^{\text{mid}}(R)}{\cos i} \right] \right\} B_\nu[T_{\text{sur}}(R)] \, \Delta\Sigma(R)\kappa_\nu^{\text{sur}} \,, \tag{3.2}$$

$$I_\nu^{\text{mid}}(R) = \frac{\cos i}{d^2} \left\{ 1 - \exp\left[-\frac{\Sigma_{\text{d}}(R)\kappa_\nu^{\text{mid}}(R)}{\cos i} \right] \right\} B_\nu[T_{\text{mid}}(R)] \,, \tag{3.3}$$

and $\Sigma_{\text{d}}(R)$ is the dust surface density, κ_ν^{sur} and $\kappa_\nu^{\text{mid}}(R)$ are respectively the surface and the midplane dust opacities (see the next Section for details), $B_\nu(T)$ is the blackbody brightness, i is the disk inclination ($i = 0°$ for a face-on disk), $\Delta\Sigma$ is the surface density of the surface layer, and d is the distance to the disk. These equations are derived for a geometrically thin disk ($H/R \ll 1$) and for low disk inclinations (if the disk is seen at $i > 70°$ a proper ray tracing is needed to account for the optical depth induced by the vertical structure of the disk). We refer the reader to Dullemond et al. (2001) for a complete derivation of the above expressions .

To complete the definition of the model, a radial profile for the gas and the dust surface density must be specified. In continuity with previous studies (Andrews et al. 2009; Isella et al. 2010), we parametrize the surface density adopting a self-similar solution for an accretion disk (derived assuming viscosity is constant in time; Lynden-Bell and Pringle 1974; Hartmann et al. 1998)

$$\Sigma_{\text{g}}(R) = \Sigma_0 \left(\frac{R}{R_0} \right)^{-\gamma} \exp\left[-\left(\frac{R}{R_{\text{c}}} \right)^{2-\gamma} \right] \,, \tag{3.4}$$

where Σ_0 is a constant, R_0 is a scale radius that we keep fixed at $R_0 = 40\,\text{au}$, and R_c is the spatial scale of the exponential cutoff. Assuming a constant dust-to-gas mass ratio $\zeta = 0.01$ throughout the disk, the dust surface density is $\Sigma_{\text{d}} = \zeta \, \Sigma_{\text{g}}$. A fixed ζ across the disk is a commonly used simplifying assumption, which we also adopt in our models as we cannot independently constrain the gas and dust surface density profiles with our observations. It is expected (e.g., Birnstiel and Andrews 2014) that the gas and dust disk surface densities evolve differently over time. This is also confirmed by some observations that show extended, dust depleted outer gaseous disks (e.g., de Gregorio-Monsalvo et al. 2013). In addition, as discussed above, we assume that viscous evolution has been shaping the surface density profile, but that it is not important for the disk heating balance. This is a common approximation that generally describes the observations well; high spatial resolution observations reveal that these smooth surface densities are an approximation of the real dust distribution (e.g., ALMA observations of the HL Tauri disk, ALMA Partnership et al. 2015). In this study, considering the limited angular resolution of the observations we are analyzing, there is no need to adopt a more detailed radial profile.

We now discuss two fundamental modifications we implemented in the two-layer disk model for the present study. First, the two-layer model is applicable only if, at every radius, the disk absorbs all the impinging stellar radiation. However, due to the exponential tapering of the dust surface density, the outermost disk region will eventually become optically thin to the stellar radiation. In this outer region, instead of adopting the two-layer

Table 3.1   Stellar and disk properties.

Object	SpT	$L_\star$ $(L_\odot)$	$M_\star$ $(M_\odot)$	$T_\star$ (K)	i (°)	P.A. (°)	Ref.
AS 209	K5	1.5	0.9	4250	38	86	1
DR Tau	K7	1.09	0.8	4060	25^a	75^a	2
FT Tau	K6-M3.5[b]	0.38	0.85	5000	23	29	3

Notes For each disk we give the spectral type of the central star, its luminosity, mass, and surface temperature. We also provide the parameters defining the disk geometry, namely the inclination and the position angle (measured East of North). [a] From Eisner et al. (2014); [b] From Luhman et al. (2010a,b). **References.** (1) Andrews et al. (2009); (2) Ricci et al. (2010b); (3) Guilloteau et al. (2011); Kenyon and Hartmann (1995).

model (which becomes numerically unstable), we assume that the disk temperature decreases radially as a power law $T_{\mathrm{mid}}(R) \propto R^{-k}$, where k is obtained by fitting the T_{mid} profile in the optically thick disk region. Hereafter we call $R \geq \overline{R}$ the region where we apply this power law assumption. Second, following Isella et al. (2010) we impose a lower limit on the midplane temperature, namely the equilibrium temperature with the interstellar radiation field. We model this by adding an extra radiative flux impinging on the midplane $\sigma_{\mathrm{SB}} T_{\mathrm{ext}}^4$, where the temperature of the external radiation field $T_{\mathrm{ext}} = 10\,\mathrm{K}$ and σ_{SB} is the Stephan-Boltzmann constant. As a result, at each radius the effective midplane temperature is given by $[T_{\mathrm{mid}}^4(R) + 10^4]^{1/4}$, where $T_{\mathrm{mid}}(R)$ is the temperature computed by the two-layer model for $R \leq \overline{R}$, and $T_{\mathrm{mid}}(R) \propto R^{-k}$ for $R > \overline{R}$. This additional flux contribution is negligible in the inner region of the disk and starts to be relevant only in the outer parts where T_{mid} becomes comparable to $10\,\mathrm{K}$.

The geometry of the disk on the sky is defined by specifying the disk inclination i (the angle between the disk rotation axis and the line of sight, where $i = 90°$ corresponds to an edge-on view) and position angle *PA* (the angle between the disk semi-major axis as it appears on the sky and the north direction, measured east of north). In the present study i and *PA* are fixed parameters (see Table 3.1 for detailed references).

Furthermore, in our model we account for the possible contamination by emission from ionized gas, which is mostly relevant at longer wavelengths and is caused by thermal or non-thermal emission processes (e.g., free-free or gyro-synchrotron emission) from free electrons in the densest parts of a wind or the stellar corona (Rodmann et al. 2006; Ubach et al. 2012). We estimate and subtract this contamination by assuming that the emission is unresolved by our observations and dominates the long-wavelength emission at and beyond 3.6 cm. We estimate the maximum possible contamination extrapolating to millimeter wavelengths the flux density observed with the VLA at 6 cm (assuming that at these wavelengths there is no contribution from dust emission) and using an optically thick spherical wind approximation ($F_\nu \sim \nu^{0.6}$: Panagia and Felli 1975). This assumption is conservative in the sense that provides the maximum possible contamination at shorter wavelengths.

3.2.2   Dust model

In order to account for the settling of large grains toward the disk midplane, as predicted by the models and observed by the lack of large grains in the disk atmosphere (e.g., based on studies of silicate features; Natta et al. 2007 and references therein), we adopt two different dust size distributions for the surface and for the midplane, which result in two different
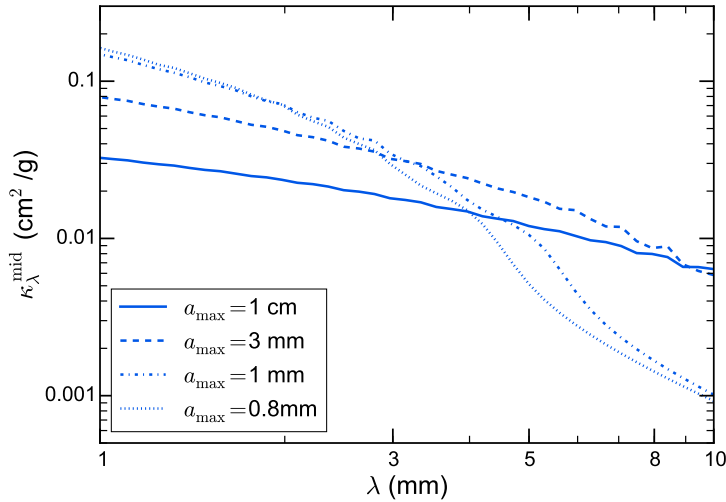
Fig. 3.1 Dust opacity (per gram of dust) for $a_{max} = 0.8, 1, 3$ mm, and 1 cm, computed for the midplane population of grains assuming the composition of 5.4% astronomical silicates, 20.6% carbonaceous material, 44% water ice, and 30% vacuum and a size distribution $n(a) \propto a^{-q}$ for $a_{min} < a < a_{max}$ with $q = 3.0$ and $a_{min} = 10$ nm.

opacities, κ_ν^{sur} and κ_ν^{mid}, respectively.

The choice of the dust grain size distribution aims at simply modeling a protoplanetary disk with a surface layer mainly composed of small grains and a midplane layer of larger pebbles (Dullemond and Dominik 2004; Tanaka et al. 2005). For both the surface and the midplane we adopt a power law distribution $n(a) \propto a^{-q}$ for $a_{min} < a < a_{max}$, where a is the dust grain radius and $q > 0$ is the power law index, choosing $a_{min}^{sur} = a_{min}^{mid} = 10$ nm, kept fixed throughout the disk. The particular value chosen for a_{min} does not affect our results as long as $a_{min} \ll 1 \, \mu m$ (Miyake and Nakagawa 1993). For the surface we assume $a_{max}^{sur} = 1 \, \mu$m constant throughout the disk, whereas for the midplane we allow a radial variation of a_{max}^{mid} modeled as

$$a_{max}^{mid}(R) = a_{max0} \left(\frac{R}{R_0} \right)^{b_{max}}, \tag{3.5}$$

where $R_0 = 40$ au and a_{max0} is a normalization constant. In the disk surface we choose $q = 3.5$ which describes well the size distribution of interstellar dust grains (Mathis et al. 1977; Draine and Lee 1984) out of which protoplanetary disks form, whereas for the disk midplane we assume $q = 3$, which accounts for an enhanced population of large grains. In Figure 3.1 we show the midplane dust opacity as a function of wavelength, computed for some a_{max} values ranging from 0.8mm to 1cm (which are representative values of the grain sizes we find in the analyzed disks, see below Section 3.4). The impact of the choice of q on the resulting β value can be seen in Figure 4 of Testi et al. (2014).

We assume the same dust composition in the surface and in the midplane. Similarly to Banzatti et al. (2011) and Trotta et al. (2013), we assume the following simplified volume fractional abundances from Pollack et al. (1994): 5.4% astronomical silicates, 20.6% carbonaceous material, 44% water ice, and 30% vacuum, thus implying an average dust grain density of 0.9 g/cm³. We choose the fractional abundances given above for continuity with previous studies on grain growth; however, we note that more recent estimates based on analysis of data from the Spitzer Space Telescope can be found in the literature

(e.g., Juhász et al. 2010).

Given the dust composition and the grain size distribution, we compute the dust opacity using the Bruggeman effective medium theory (Bruggeman 1935) to calculate the dielectric function of the composite spherical grain and Mie theory to derive the dust absorption coefficients. The complex optical constants used to compute the dielectric function are taken from Weingartner and Draine (2001) for silicates, Zubko et al. (1996) for carbonaceous material, and Warren (1984) for water ice.

3.2.3 Modeling methodology

We adopt a Bayesian approach, which provides probability distribution functions (PDFs) for the free parameters of the model using a variant of the MCMC algorithm family. Isella et al. (2010) provide a general description of the use of this methodology for modeling protoplanetary disks.

Our disk model is defined by the following free parameters: Σ_0, R_c, γ (to define the disk structure) and $a_{\mathrm{max}0}$, b_{max} (to define the dust distribution). In the present study the following parameters are kept fixed: the dust properties (e.g., composition, shape, porosity), the disk inclination i, the disk position angle PA, and the contaminating free-free flux density at each wavelength $F_{\mathrm{ff}}(\nu)$. We note, however, that in a more general approach these parameters could be added to the Bayesian analysis and derived consistently with the disk structure and the grain size distribution.

Given a set of values for these parameters, we compute the synthetic disk images (one per fitted wavelength), and then we sample their Fourier transform at the same $(u, v)-$plane locations of the observed visibilities. We finally compute the total χ^2 as the sum of the several partial χ^2_λ computed for each wavelength,

$$\chi^2 = \sum_\lambda \chi^2_\lambda = \sum_\lambda \sum_{j=1}^{N_\lambda} \left| V_{\lambda,j}^{\mathrm{obs}} - V_{\lambda,j}^{\mathrm{mod}} \right|^2 \cdot w_{\lambda,j}, \tag{3.6}$$

where $w_{\lambda,j}$ is the visibility weight[2], $V_{\lambda,j}^{\mathrm{obs}}$ and $V_{\lambda,j}^{\mathrm{mod}}$ are respectively the observed and the synthetic visibilities, and N_λ is the number of visibility points at the wavelength λ.

The posterior PDF is computed as the product of the likelihood of the observations given the model, namely $\exp(-\chi^2/2)$, by the prior PDF $p(\boldsymbol{\theta})$ (where $\boldsymbol{\theta}$ is a point in the 5D space of parameters). We assume a uniform prior for all the parameters, therefore $p(\boldsymbol{\theta}) = 1$ for $\boldsymbol{\theta} \in \Theta$ and $p(\boldsymbol{\theta}) = 0$ otherwise, where Θ is a 5D domain in the space of parameters defined by the ranges given in Table 3.2. In principle, the domain Θ can be

Table 3.2 Ranges defining the space of parameters explored by the Markov chain

Parameter	Min	Max	Unit
γ	-1	4	–
Σ_0	0.1	200	g/cm^2
R_c	5	300	au
$a_{\mathrm{max}0}$	0.001	100	cm
b_{max}	-5	2	–

---

[2]The visibility weights $w_{\lambda,j}$ are computed theoretically as described by Wrobel and Walker (1999) and then re-scaled in order to assign the same weight to each wavelength.

changed from disk to disk (e.g., the R_c interval can be changed depending on the disk size determined from observations); however, in this study we kept it fixed to the intervals given in Table 3.2, which are large enough to be suitable for different disks.

In addition to the disk structure and the dust size distribution, we also derive the precise position of the disk centroid by adding two *nuisance* parameters for each wavelength, $\Delta\alpha_0$ and $\Delta\delta_0$, that measure the angular offset between the disk centroid with respect to its nominal position (α_0, δ_0). This method allows the derivation of the correct center position for the model even without any prior information on the star proper motion or other systematic position offsets between the different wavelength observations.

The fit is performed using a variant of the MCMC algorithm (Goodman and Weare 2010), which allows the parameter space to be explored by several Markov chains at the same time (an *ensemble* of hundreds to thousands of *walkers*[3]), which interact with each other in order to converge to the maximum of the posterior. There are two advantages of using several chains simultaneously. On the one hand, it allows a more complete exploration of the parameters space (each chain starts from a different initial location); on the other hand, it allows the computation to be massively parallelized. We perform the MCMC using the implementation provided in the Python package *emcee* (Foreman-Mackey et al. 2013), which offers the possibility of running the computation in parallel on several cores and has been used for an increasing number of astrophysical problems in recent years. In this study, we perform MCMC with 1000 chains: they are initialized with uniform random distribution in the parameter space Θ, made evolve for a *burn-in* phase of some hundreds steps, and finally let sample the posterior for several hundreds steps (for a detailed explanation of the criteria used to assess the convergence of the chain, see Appendix B).

The outcome of the MCMC is a collection (a *chain*) of posterior samples out of which we can estimate the 1D and 2D marginal distributions of the free parameters (marginalization means that all but one or two parameters of the posterior are integrated over). From the 1D marginal distributions, we do a point estimate of each parameter using the median and we estimate the uncertainty as the central interval; i.e., from the 16th to the 84th percentile. These estimators give a good representation of the marginalized distribution, and reduce to the usual central credibility interval in the Gaussian case. For each fit, we present a *staircase* plot with the 1D and 2D marginalized distributions of the interesting physical parameters.

For this study, the optimization of the disk model and of the imaging routines allowed us to execute the fits efficiently on hundreds of cores (hosted at the Computational Center for Particle and Astrophysics, C2PAP) and thus to reduce the time needed to perform each multiwavelength fit to 1 or 2 days. For further details on the implementation, see Appendix B.

3.3   Observations

In this study we apply our method to three protoplanetary disks for which multiwavelength (sub-)mm observations are available: AS 209, DR Tau, and FT Tau. The AS 209 observations have already been presented by Pérez et al. (2012) and we refer the reader to that paper for their details. DR Tau and FT Tau observations from CARMA and VLA are now described in turn. A summary can also be found in Table 3.3.

---

[3]In this affine-invariant MCMC, the chains are also called *walkers*.

Table 3.3   Details of the observations used for the fits

Object	α (J2000.0)	δ (J2000.0)	Telescope	λ (mm)	F_λ (mJy)		Beam properties FWHM ($''$)	P.A. ($°$)	F_{ff} (μJy)	Ref.
AS 209	16 49 15.30	−14 22 08.7	SMA	0.88	580	±60	0.61×0.45	32.4	–	1
			CARMA	2.80	40	±60	0.93×0.63	−21.9	–	1
			VLA	8.00	1.1 ± 0.1		0.25×0.18	−77.0	80	1
			VLA	9.83	0.48± 0.1		0.30×0.20	−79.0	100	1
DR Tau	04 47 06.20	+16 58 42.8	CARMA	1.30	137	±20	0.25×0.22	−63.8	–	3
			VLA	7.05	1.4 ± 0.1		0.43×0.33	−54.2	‹122	3
			VLA	7.22	1.4 ± 0.1		0.45×0.34	−54.1	‹120	3
FT Tau	04 23 39.19	+24 56 14.1	CARMA	1.30	107	±10	0.52×0.39	−60.0	–	2
			CARMA	2.60	24 ± 2		1.13×1.02	−77.3	–	2
			VLA	8.00	1.1 ± 0.1		0.48×0.32	71.3	‹220	3
			VLA	9.83	0.7 ± 0.1		0.57×0.36	70.9	‹190	3

Notes. For each disk we give the coordinates and the properties of the observations: λ is the wavelength of the combined continuum data, F_λ is the integrated continuum flux density (with error), FWHM and PA are respectively the size and the position angle (measured east of north) of the synthesized beam, F_{ff} is the estimated free-free contamination upper limit.
References. Observations presented in: (1) Pérez et al. (2012) (2) Kwon et al. (2015) (3) this work.

3.3.1   CARMA observations of DR Tau and FT Tau

Observations of DR Tau at 1.3mm were obtained using CARMA between October 2007 and December 2011. Multiple array configurations (A, B, and C) provide a *uv*-coverage spanning 15-1290 kλ. Double-sideband single-polarization receivers were tuned to a LO frequency of 230 GHz in A configuration, 227.75 GHz in B configuration, and 228.60 GHz in C configuration. For optimal continuum sensitivity, the spectral windows in the correlator were configured to the maximum possible bandwidth per spectral window (0.47 GHz). The number of continuum spectral windows varied for different configurations: a total bandwidth of 1.9 GHz was available for the B and C configuration observations, while during the A configuration observations the total bandwidth was 8 GHz. Observations of complex gain calibrators (0530+135 and 0449+113) were interleaved with science target observations. Additionally, a strong quasar was observed to calibrate the complex bandpass. The absolute flux density scale was derived from observations of a secondary flux density calibrator (3C84 or 3C273), whose flux density was monitored by the CARMA observatory, resulting in a fractional uncertainty of $\sim 15\%$ in the absolute flux density calibration. Calibration was performed with the MIRIAD software package, with each dataset being calibrated separately. The 1 and 3 mm CARMA observations of FT Tau are presented in Kwon et al. (2015), to which we refer for the observational details. Here we give a brief description. The data were obtained over a period of about 2 years, between 2008 Oct 15 and 2011 Jan 5. For good *uv* coverage, multiple array configurations were employed: 1 mm observations in B and C configurations provide a *uv* coverage of 17.0–620 kλ, and 3 mm observations in A and C configurations gives a *uv* coverage from 4.1–727.6 kλ. MIRIAD (Sault et al. 1995) was used for the data calibration. The absolute flux density was obtained through observations of a reliable flux calibrator (Uranus) and resulted in fractional uncertainties of 10% and 8% for observations at 1.3 and 2.6 mm, respectively. The complex gains were obtained through observations of a nearby bright point source (3C111). In the case of the A configuration data at 3 mm the C-PACS (Pérez et al. 2010) was employed to remove short-period atmospheric turbulence. We note that while the images of Kwon et al.

(2015) are produced with a Briggs robust parameter of 0 (which produces images with a lower signal-to-noise ratio but better beam resolution), the images in this study use the natural weighting (which does not apply any density weighting function to the observed *uv*-points thus producing images with the best signal-to-noise ratio). Through the analysis procedure described in Section 3.2.3 we fit the flux measured at each *uv*-point, therefore we adopt the natural weighting scheme since is the most suitable to perform a direct comparison between the observed and the model data.

3.3.2   VLA observations of DR Tau and FT Tau

Observations of DR Tau and FT Tau using the Karl G. Jansky Very Large Array (VLA) of the National Radio Astronomy Observatory[4] were made as part of the Disks@EVLA project (AC982) between 2010 November and 2012 August. DR Tau was observed using the Q-band ($\lambda \sim$7mm) receivers with two 1GHz basebands centered at 41.5 and 42.5GHz in the C and B configurations, providing projected *uv*-spacings from 5 to 1500 kλ. FT Tau was observed using the Ka-band ($\lambda \sim$1cm) receivers with two 1GHz basebands centered at 30.5 and 37.5GHz in the C and B configurations, providing projected *uv*-spacings from 8 to 1300 kλ. For both targets the complex gain was tracked using frequent observations of J0431+2037 (in C configuration) or J0431+1731 (in B configuration), and the complex bandpass was measured using 3C84. The absolute flux density scale was derived from observations of 3C147 (e.g., Perley and Butler 2013), and its overall accuracy is estimated to be 10%. The data were calibrated, flagged, and imaged using a modified version of the VLA Calibration Pipeline[5]. At Ka-band the calibrator source J0431+2037 turned out to have multiple components that required the source to be modeled before being used to derive calibration solutions. In addition, because of the substantial time period covering the observations, corrections for source proper motion and/or other systematic position offsets between datasets (e.g., caused by the structure of J0431+2037) also had to be applied. The astrometry reported here corresponds to that derived from the B configuration data. The VLA observations shown in this study have been imaged using natural weighting.

Both sources were also observed with the C-band ($\lambda \sim$6cm) receivers in the most compact, D configuration of the VLA in 2010 July in order to evaluate any potential contamination from ionized gas at shorter wavelengths. Two 1GHz basebands were centered at 5.3 and 6.3GHz. Complex gain variations were tracked through observations of J0431+2037, the bandpass was measured using 3C84, and the absolute flux density scale was obtained through observations of 3C147. DR Tau was detected with an integrated flux density $F_{6cm} = 99 \pm 31\mu$Jy, while for FT Tau a 3σ upper limit on the 6cm flux density of 72μJy was obtained.

3.4   Results

For each disk, we give a set of statistical and physical results that we describe in turn. In this section we discuss in detail the results for FT Tau and in Section 3.5 we provide detailed plots for the other disks.

In Figure 3.2 we present a staircase plot showing the posterior PDF computed from the chain, after proper thinning; the fit needed 800 burn-in steps, and 500 further steps

---

[4]The National Radio Astronomy Observatory is a facility of the National Science Foundation operated under cooperative agreement by Associated Universities, Inc.

[5]See `https://science.nrao.edu/facilities/ vla/data-processing/pipeline/scripted-pipeline`.
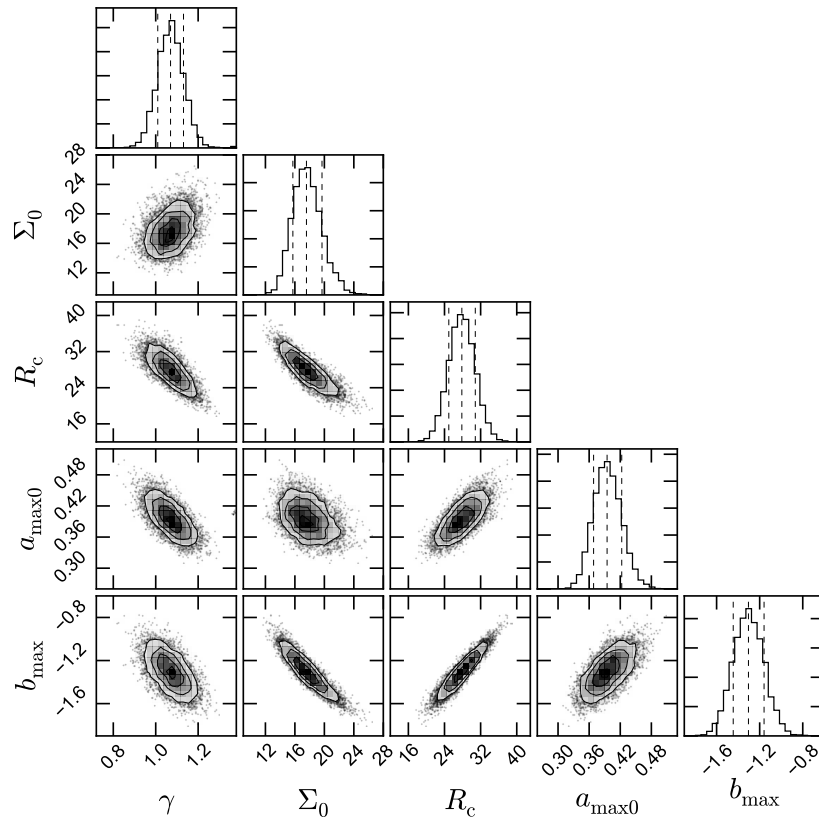
Fig. 3.2 Representation of the MCMC results for FT Tau. On the top diagonal, the 1D histograms are the marginalized distributions of the fitted parameters; the vertical dashed lines represent (from left to right) the 16th, the 50th, and the 84th percentiles. The 2D density plots represent the bi-variate distributions for each pair of parameters, with one dot representing one sample. The plot shows the posterior sampling provided by 500 steps of the 1000-walkers chain (800 burn-in steps were performed to achieve convergence). We note that in order to obtain an independent set of samples, the chain has been thinned by a factor equal to the autocorrelation time (~ 80 steps in this case).

Table 3.4   Fitted disk centroid positions

Object	Telescope	Epoch (UT)	α (J2000.0)	δ (J2000.0)	$\Delta\alpha, \Delta\delta$ mas	p.m. (α) mas/yr	p.m. (δ) mas/yr
AS 209	–	2000.0	16 49 15.30324	−14 22 08.6346	–	−7.69	−22.84
	SMA	2006-05-12	16 49 15.282	−14 22 08.77	0.005		
	CARMA	2009-12-10	16 49 15.303	−14 22 08.853	0.005		
	VLA	2011-05-20	16 49 15.298	-14 22 08.914	0.005		
DR Tau	–	2000.0	04 47 06.209	+16 58 42.81	–	12.6	−17.1
	CARMA	2011-12-06	04 47 06.219	+16 58 42.711	0.002		
	VLA	2012-08-08	04 47 06.217	+16 58 42.652	0.006		
FT Tau	–	2000.0	04 23 39.193	+24 56 14.11	–	10.3	−21.4
	CARMA	2008-10-15	04 23 39.193	+24 56 14.003	0.002		
	VLA	2011-03-28	04 23 39.196	+24 56 13.977	0.004		

Notes. For each object we give the astrometric coordinates at the reference Epoch 2000.0 with proper motion estimates from SIMBAD. For each interferometric dataset we give the coordinate of the disk center derived from the fit, with the estimated errors ($\Delta\alpha$ and $\Delta\delta$ are found to be approximately equal). These are the formal uncertainties of the fitting process and do not account for the uncertainties introduced by the phase calibration (position accuracy of the calibrator and potentially uncorrected phase offsets); we estimate that they contribute at the $0.1''$ level for our observations.

to sample the posterior. On the diagonal of Figure 3.2 we show the marginalized 1D distributions for each parameter, which display a Gaussian-like shape; off the diagonal we show the 2D marginalized distributions, which give an overview of the correlations between the parameters. For FT Tau we obtain the following parameter values:

$$\gamma = \quad 1.07 \pm 0.06$$

$$\Sigma_0 = \quad 18 \pm 2 \, \mathrm{g/cm^2}$$

$$R_c = \quad 28 \pm 3 \, \mathrm{au}$$

$$a_{\mathrm{max0}} = \quad 0.40 \pm 0.03 \, \mathrm{cm}$$

$$b_{\mathrm{max}} = \quad -1.3 \pm 0.1.$$

The errors are given by the central credibility interval of their marginalized distribution (i.e., the 16th and 84th percentiles). We note that the fit has some additional parameters, specifically four pairs of directional offsets (one pair ($\Delta\alpha_0, \Delta\delta_0$) for each wavelength), but for the clarity of the plot we do not show them. In Table 3.4 we list the derived position of the disk centroid (α, δ) determined by the fit, where $\alpha = \alpha_0 + \Delta\alpha_0$ and $\delta = \delta_0 + \Delta\delta_0$. For each disk, we also list (from the SIMBAD database) the star reference position at Epoch 2000.0 (from Hipparcos or 2MASS measurements), the proper motion estimates (from Hipparcos or US Naval Observatory Catalogs), and– for each interferometric dataset– the fitted disk center position with derived uncertainties. Within the uncertainties, the derived positions are consistent with the expected stellar positions based on the astrometric and proper motion measurements.

In Figure 3.3 we compare the observed and the model images at each wavelength, showing the residuals obtained by imaging the residual visibilities (obtained by subtracting the noise-free model visibilities from the the observed visibilities). The best-fit model represented in Figure 3.3 corresponds to the model with median values of the marginalized
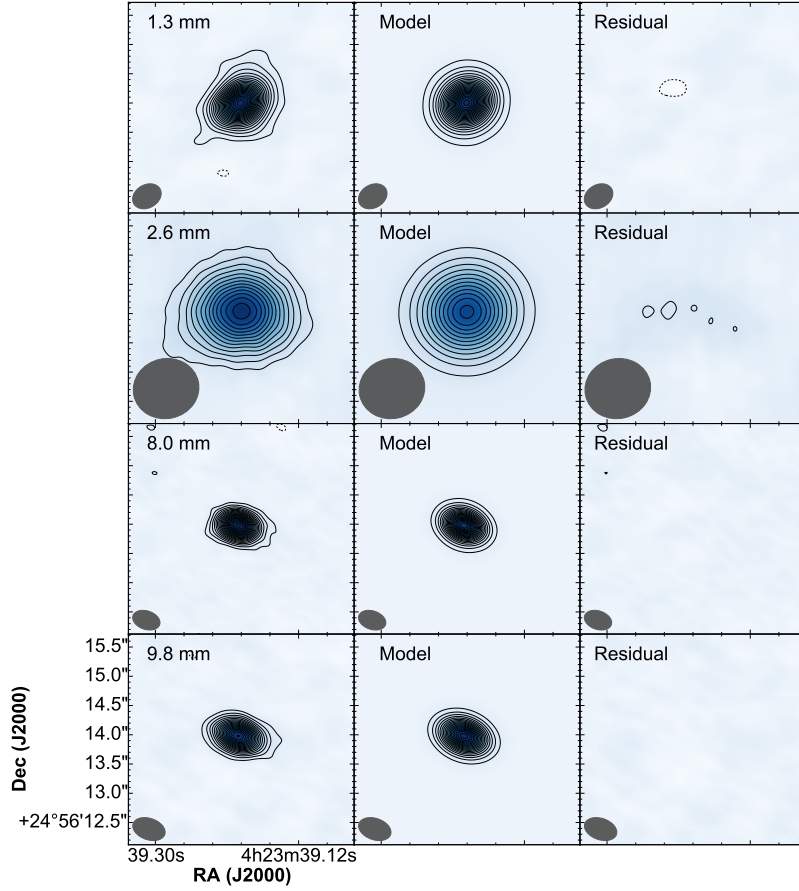
Table 3.3 Comparison between the observed and the best-fit model images at different wavelengths of the FT Tau protoplanetary disk. The best-fit model is defined by the following parameters: $\gamma = 1.07$, $\Sigma_0 = 18\,\mathrm{g/cm^2}$, $R_c = 28\,\mathrm{au}$, $a_{\mathrm{max0}} = 0.4\,\mathrm{cm}$, $b_{\mathrm{max}} = -1.3$. The observed images are shown in the left panels, the model images in the center panels, the residuals in the right panels. The positive and negative contour levels are spaced by 3σ (starting from -3σ) and are the same in all the panels. The synthesized beam FWHM is represented as a gray ellipse in the bottom-left corner of each map.

distributions ($\gamma = 1.07$, $\Sigma_0 = 18\,\mathrm{g/cm^2}$, $R_c = 28\,\mathrm{au}$, $a_{\mathrm{max0}} = 0.4\,\mathrm{cm}$, $b_{\mathrm{max}} = -1.3$) and we have verified that it is among the models with lowest reduced $\tilde{\chi}^2 \simeq 1.01$. To produce the maps we have applied the CLEAN algorithm (Clark 1980) with natural weighting. The residuals are small at all the wavelengths, with one negative 3σ residual left at 1.3mm, a few 3σ residuals left at 3mm, and no residuals within $\pm 3\sigma$ left at 8.0 and 9.8 mm.

Figure 3.4 shows the comparison between the probability distribution of the model visibilities and the observations as a function of the deprojected baseline length (*uv*-distance). Each panel corresponds to one wavelength, with the upper frame showing the real part $\mathrm{Re}(V)$ and the lower frame showing the imaginary part $\mathrm{Im}(V)$. The declining profile of $\mathrm{Re}(V)$ with increasing *uv*-distance shows that the disk is spatially resolved at all the wavelengths. Furthermore, we note that the visibility profile at longer wavelengths has a steeper decline with increasing baseline than the visibility profile at shorter wavelengths, thus confirming the rather general observational feature that the size of the (sub-)mm emitting region is anticorrelated with the observing wavelength (Pérez et al. 2012; Testi et al. 2014).

The models fit the observations with a very good agreement at the shortest wavelength
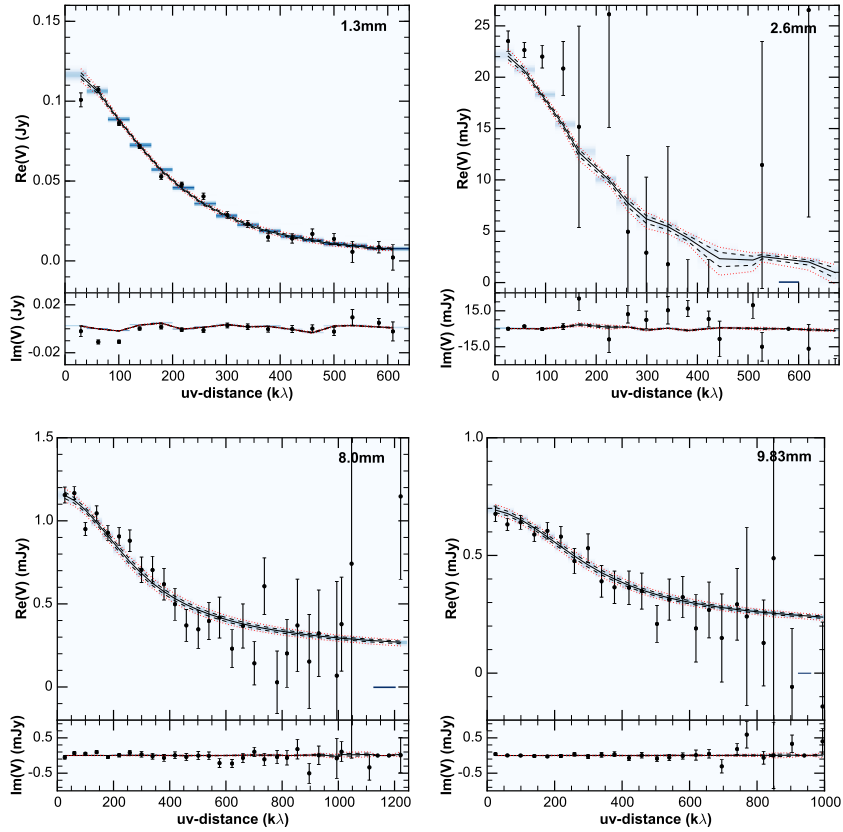
Fig. 3.4   Comparison between the model and the observed visibilities as a function of deprojected baseline length (*uv*-distance) for FT Tau. The data are binned in 40kλ bins. Black dots represent the observed data and the colored boxes represent the probability distribution of model visibilities for each *uv*-distance bin. The *x*-axis extent of each box is the bin size, while the *y*-axis extent is not fixed as it depends on the probability distribution of the model at that particular *uv*-distance bin; in some cases they are very close to each other. The color scale represents the density of the distribution. The solid black curve is the median, the dashed black lines are the 16th and 84th percentiles, and the red dotted lines are the 2.3th and 97.7th percentiles.
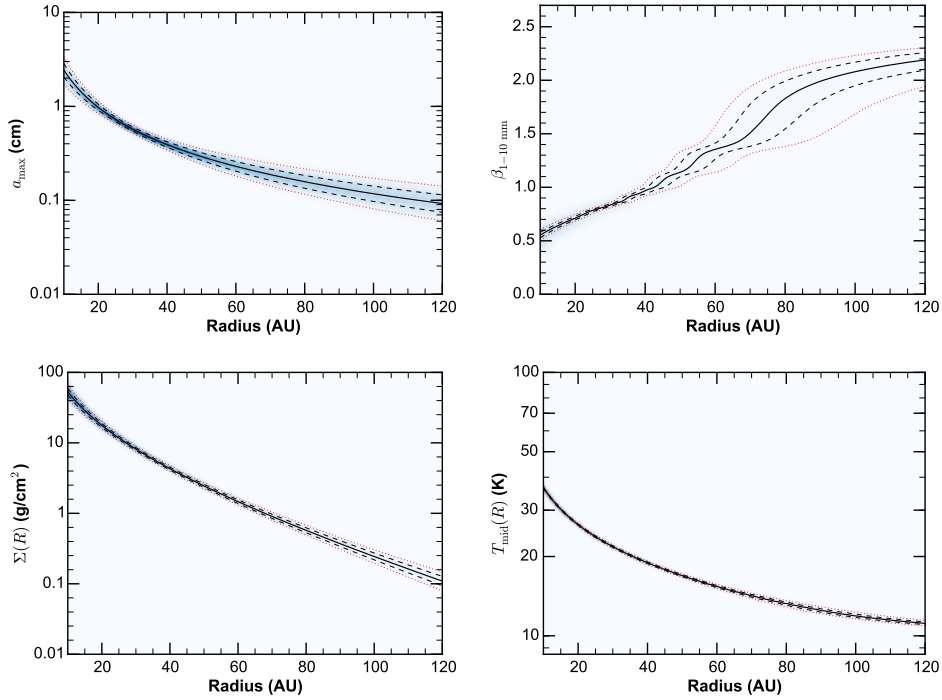
Fig. 3.5 Results of the FT Tau fit. *Top:* in the left panel, the posterior PDF of the maximum dust grain size a_{max} as a function of the disk radius; in the right panel, the posterior PDF of the dust spectral radial profile $\beta(R)$ between 1 and 10 mm. *Bottom:* in the left panel, the posterior PDF of the gas surface density; in the right panel, the posterior PDF of the midplane temperature. Line conventions are the same as those in Fig. 3.4.

(1.3 mm), and a lower degree of agreement at longer wavelengths. This should not be a surprise for two main reasons: first, the observations at the shorter wavelength also have higher signal-to-noise ratio and therefore have more weight in the fit; second, we are modeling all the wavelengths simultaneously and so the resulting best-fit models are not necessarily the models that best fit each wavelength separately. We note, however, that although the VLA observations at 8.0 and 9.83 mm have a worse signal-to-noise ratio, the models are still able to reproduce the observed total flux density (short *uv*-distances) and the average flux density at the longer spatial frequencies extremely well. In the case of FT Tau, the observations at 2.6 mm have a very low signal-to-noise ratio compared to those at 1.3, 8.0, and 9.8 mm.

The top-left panel of Figure 3.5 shows the posterior PDF of the maximum dust grain size a_{max} as a function of the disk radius. The maximum dust grain size is larger in the inner disk than in the outer disk, changing by one order of magnitude from 1 cm at 20 au to 1 mm at 120 au. We note that the smoothness of the $a_{\mathrm{max}}(R)$ profile follows from the power-law parametrization in Eq. 3.5. The 2σ error bars (given in terms of the 2.3-97.7% credibility interval) are smaller than 10% at all radii and allow us to conclude that there is a clear signature of a radial gradient in the maximum dust grain size throughout the disk. In the top-right panel of Figure 3.5 we present the posterior PDF of the dust spectral index radial profile $\beta(R)$ between 1 and 10 mm, computed given the $a_{\mathrm{max}}(R)$ posterior PDF

Table 3.5   Parameters derived from the fits

Object	γ	Σ_0 (g/cm^2)	R_c (au)	$a_{\mathrm{max}\,0}$ (cm)	b_{max}
AS 209	$0.91^{+0.03}_{-0.03}$	$7.0^{+0.4}_{-0.4}$	78^{+3}_{-3}	$0.62^{+0.02}_{-0.02}$	$-1.17^{+0.07}_{-0.07}$
DR Tau	$1.10^{+0.08}_{-0.1}$	20^{+3}_{-3}	21^{+3}_{-3}	$0.24^{+0.03}_{-0.02}$	$-1.8^{+0.2}_{-0.2}$
FT Tau	$1.07^{+0.06}_{-0.06}$	18^{+2}_{-2}	28^{+3}_{-3}	$0.40^{+0.03}_{-0.03}$	$-1.3^{+0.1}_{-0.1}$

Notes. For each parameter of the fit we list the median value; the error bars are given by the 16th and 84th percentiles.

according to

$$\beta(R) = \frac{\partial \log \kappa_\nu(R)}{\partial \log \nu} \,. \tag{3.7}$$

The spectral index β increases with radius: the small values $\beta < 1$ for $R < 50$ au signal the presence of dust grains that have reached sizes comparable to 1 mm or more (Natta and Testi 2004), whereas in the outer disk the spectral index approaches $\beta \gtrsim \beta_{\mathrm{ISM}} = 1.7$, a signature of the presence of smaller grains. The fact that in the outer disk we obtain $\beta \gtrsim \beta_{\mathrm{ISM}}$ for grains somewhat larger ($a_{\mathrm{max}} \approx 1$ mm) than the usual ISM dust grains ($a_{\mathrm{max}} \approx 1 - 10\,\mu$m) is consistent with the observations at different wavelengths; these observations give us information on different spatial scales in the disk and they are all fit well by a model with the a_{max} profile shown in Figure 3.5. The bottom plots in Figure 3.5 present the physical structure derived for FT Tau: the gas surface density (bottom-left panel) and the midplane temperature (bottom-right) profiles. The surface density profile monotonically decreases with a power-law index $\gamma = 1.07 \pm 0.06$, a normalization value $\Sigma_0 = 18 \pm 2\,$g/cm^2 at 40 au, and a cut-off radius $R_c = 28$au. The midplane temperature profile decreases from 40K in the inner disk to 11K in the outer region.

The AS 209 and DR Tau protoplanetary disks have been fit with the same analysis presented here and the results are shown in Section 3.5. For both these disks the fit performed well, as can be seen from the maps of the residuals and the comparison between the model and the observed visibilities at all the wavelengths. We note that the observations of DR Tau at 1.3 mm display an asymmetry (in the NE region) that an axisymmetric disk model like the one we are using here is not able to account for. In Table 3.5 we summarize the results of the fits for the FT Tau, AS 209, and DR Tau protoplanetary disks. In all disks we find sharply decreasing dust grain sizes, with $a_{\mathrm{max}} \approx 0.5$ cm at $R \lesssim 40$au, with a radial power law slope $-1.8 \leq b_{\mathrm{max}} \leq -1.17$. We also note that AS 209, DR Tau, and FT Tau are fit with $\gamma > 0$ and $b_{\mathrm{max}} < 0$. A degeneracy between γ and b_{max} is also apparent from the bi-variate distributions in Figure 3.2 (bottom-left panel) and was already observed by Trotta et al. (2013).

In Table 3.6 we list the physical quantities derived from the models: the total mass of the disk M_{disk} (computed as the sum of the dust and the gas mass), the radius R_{90} containing 90% of the disk mass, and the radius $\overline{R}$ within which the temperature is computed using the two-layer approximation (see Section 3.2.1). It is reassuring that for all the disks, $\overline{R}$ is larger than or comparable to the radius containing 90% of the mass, thus implying that the assumption of a power-law temperature profile in the region $R > \overline{R}$ has minimal influence on the computation of the total flux density. We observe that the disk masses that we

Table 3.6   Models: physical quantities

Object	M_{disk}	R_{90}	$\overline{R}$
	$(10^{-3}\,M_\odot)$	(au)	(au)
AS 209	$14.9^{+0.4}_{-0.4}$	161^{+5}_{-3}	155^{+5}_{-4}
DR Tau	14^{+4}_{-1}	52^{+3}_{-3}	65^{+4}_{-2}
FT Tau	15^{+1}_{-1}	69^{+6}_{-4}	99^{+7}_{-6}

Notes. For each disk we list the total disk mass M_{disk}, the radius R_{90} within which 90% of the disk mass resides, and the radius $\overline{R}$ within which the disk temperature is computed with the two layer disk model.

obtain with our multiwavelength analysis are comparable within a factor of 2 (or 4 in the worst case) with those derived by previous single-wavelength studies. The Andrews et al. (2009) analysis of AS 209 found $M_{\text{disk}} = 28 \times 10^{-3}\,M_\odot$ ($\gamma = 0.4$, $R_c = 126$ au), the Isella et al. (2010) analysis of DR Tau found $M_{\text{disk}} = 63 \times 10^{-3}\,M_\odot$ ($\gamma = -0.3$, $R_c = 41$ au), and the Guilloteau et al. (2011) analysis of FT Tau found $M_{\text{disk}} = 7.7 \times 10^{-3}\,M_\odot$ ($\gamma = -0.17$, $R_c = 43$ au). We note that in two cases (DR Tau and FT Tau) we obtain $\gamma > 0$, whereas past analyses obtained $\gamma < 0$. Furthermore, in all the cases we obtain γ values larger than the previous single-wavelength studies. As noted by Trotta et al. (2013), this can be understood by looking at the anticorrelation between γ and b_{max}, clearly visible in the bottom-left frame in the staircase plot in Figure 3.2: single-wavelength studies (that adopt an opacity constant with radius and therefore $b_{\text{max}} = 0$) obtain smaller γ values than a multiwavelength analysis, where b_{max} and γ are constrained simultaneously.

3.5   Fits results

As anticipated in Section 3.4, here we present the results of the multiwavelength fits for AS 209 and DR Tau. For each disk we present staircase plots with the 1D and 2D marginalized posterior PDFs, maps of the residuals at each wavelength (obtained subtracting the best-fit model from the observations), and a comparison between the observed and the model visibilities at each wavelength. We also present the physical structure derived for each disk: the gas surface density and the midplane temperature profile. In Figures 3.6, 3.7, and 3.8 we present the results of the fit for AS 209 showing respectively the comparison of model and observed visibilities, the residual maps and the posterior PDFs, and the derived disk structure. In Figures 3.9, 3.10, and 3.11 we present the same plots for DR Tau.
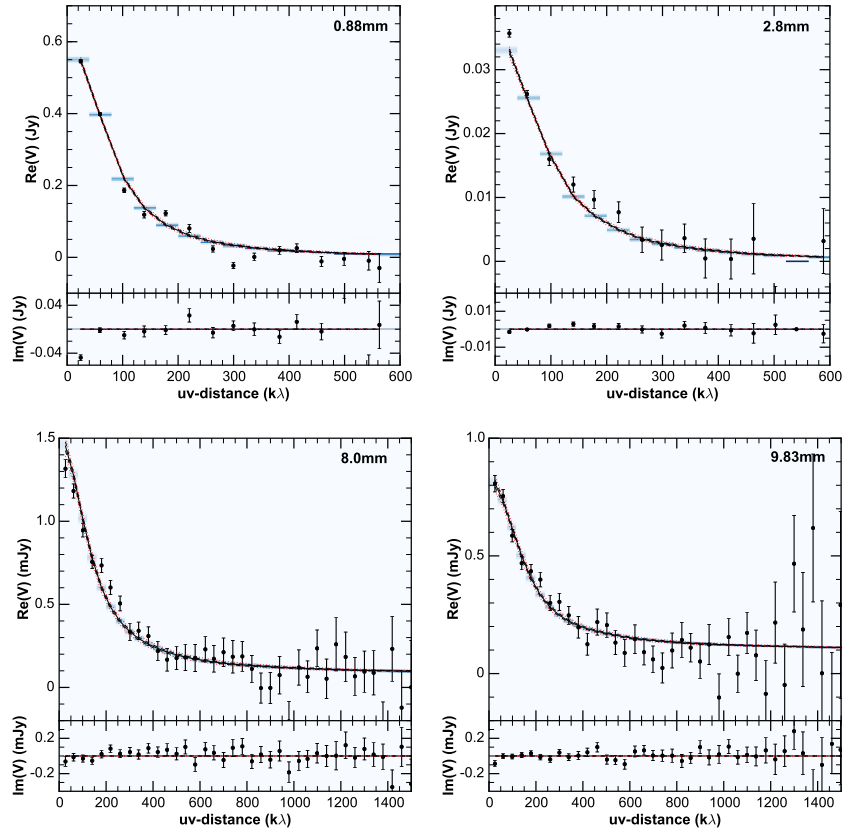
Fig. 3.6 AS 209 bin-averaged visibilities as a function of deprojected baseline length (*uv*-distance). Black dots represent the observed data, the colored area represents the density of models for each *uv*-distance bin, and the lines are defined as in Figure 3.5.
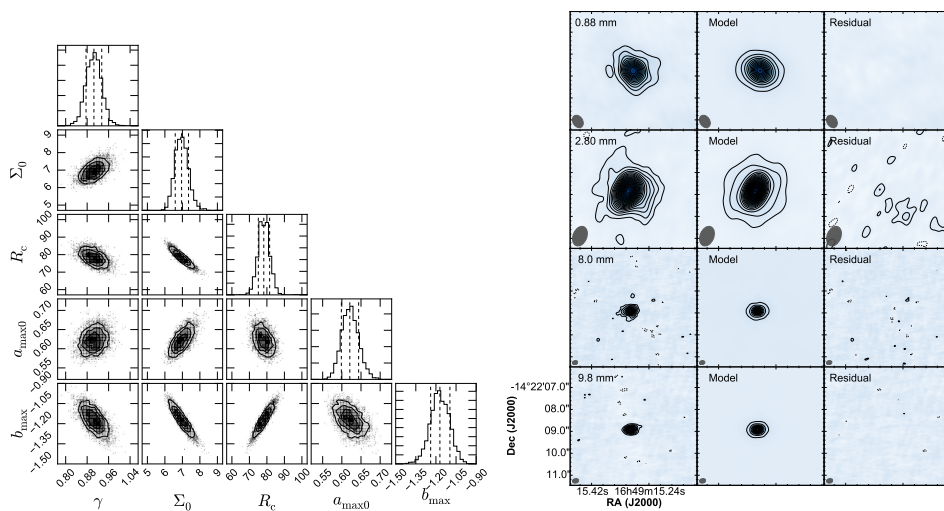
Fig. 3.7 *Left panel:* Staircase plot showing the marginalized and bi-variate probability distributions resulting from the fit for AS 209. *Right panel:* AS 209 maps of the residuals at the fitted wavelengths.
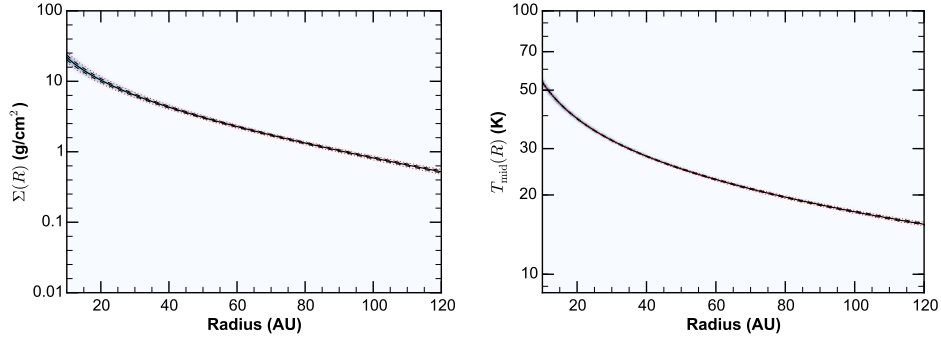
Fig. 3.8 Results of the AS 209 fit. *Left panel:* posterior PDF of the gas surface density. *Right panel:* posterior PDF of the midplane temperature. Line conventions are the same as those in Fig. 3.4.
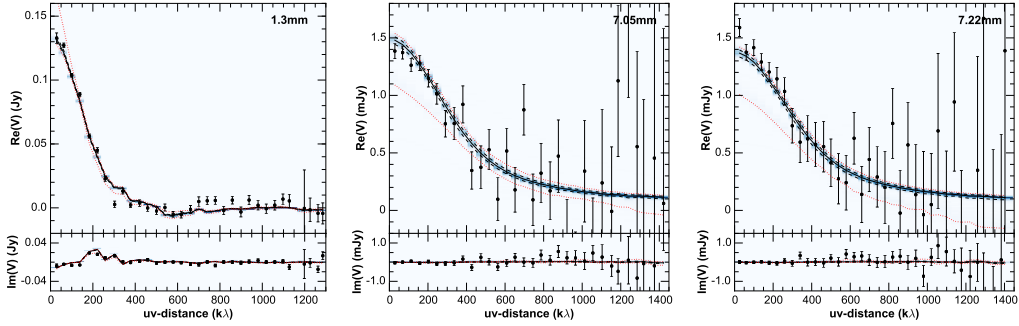
Fig. 3.9 DR Tau bin-averaged visibilities as a function of deprojected baseline length (*uv-distance*). Color and line conventions are defined in Figure 3.5.
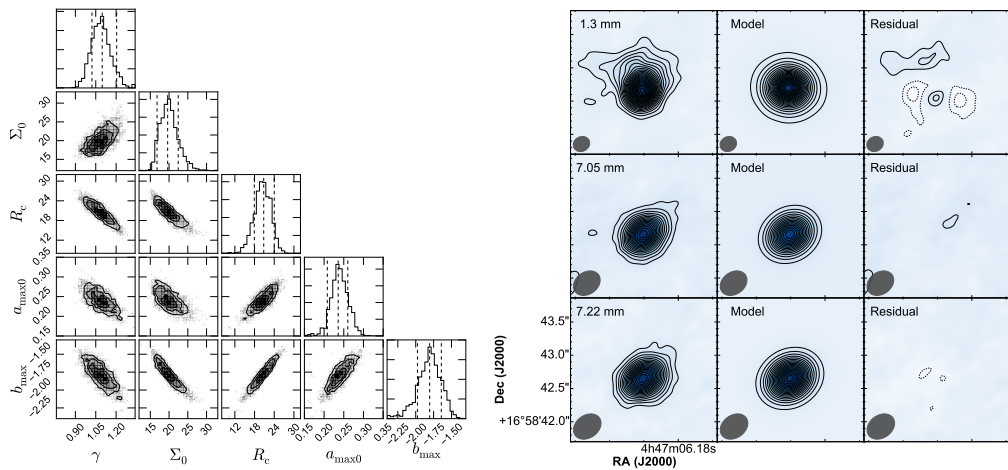
Fig. 3.10 *Left panel:* Staircase plot showing the marginalized and bi-variate probability distributions resulting from the fit for DR Tau. *Right panel:* DR Tau maps of the residuals at the fitted wavelengths.
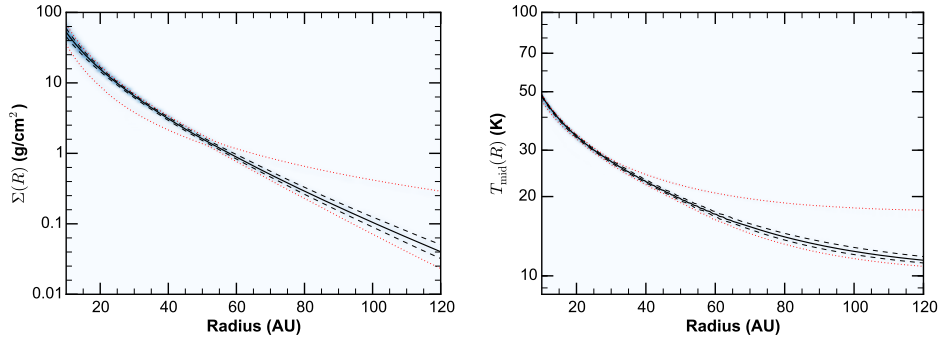
Fig. 3.11   Results of the DR Tau fit. *Left panel:* posterior PDF of the gas surface density. *Right panel:* posterior PDF of the midplane temperature. Line conventions are the same as those in Fig. 3.4.

3.6   Discussion

In the previous section we show how our new multiwavelength fitting technique allows us to simultaneously constrain the disk structure and the radial variation of the maximum dust grain size. This is the most important difference between our method and previous attempts to use multiwavelength observations to constrain the dust properties. We derive a unique, yet simplified disk physical structure that describes the emission at all the observing wavelengths and at the same time we obtain a self-consistent distribution of particle sizes that we assume to be a continuous function. Previous analyses have either assumed a non-self-consistently derived temperature distribution across the disk (Guilloteau et al. 2011) or have used different disk physical structure fits at different wavelengths to infer from their differences a constraint on the dust properties (Banzatti et al. 2011; Pérez et al. 2012). The method we developed, extending the work of Trotta et al. (2013), improves on previous results by attempting a self-consistent modeling of the disk structure and dust radial stratification. Our models produce results that are in qualitative agreement with previous studies (larger grains in the inner disk than in the outer disk), but do show some quantitative difference even when using the same assumptions about the dust composition.

We used the AS 209 protoplanetary disk to perform a detailed comparison of the results from our multiwavelength analysis with those of Pérez et al. (2012), who constrained the disk structure and the dust radial distribution fitting each wavelength separately. The details of the comparison are given in Appendix C, while here we briefly summarize the main results. Adopting the same disk model and the same dust properties as Pérez et al. (2012) we fit the AS 209 protoplanetary disk separately at each wavelength and found an extremely good agreement with the disk structure obtained by Pérez et al. (2012). Then, we performed a multiwavelength fit again using the same disk model and dust prescriptions used by Pérez et al. (2012) and we compared the resulting $a_{max}(R)$ and $\beta(R)$ profiles. The two techniques provide $a_{max}(R)$ profiles in good agreement almost throughout the disk, with some differences in the inner region where the emission is not spatially resolved. The main differences between the two approaches arise from the different derivation of the dust temperature profile. The modeling by Pérez et al. (2012) produces independent temperature profiles at different wavelengths, whereas our multiwavelength fit derives a unique temperature profile for the disk midplane that holds at all wavelengths (which is made possible by imposing a fixed parametrization of the maximum grain size with radius,
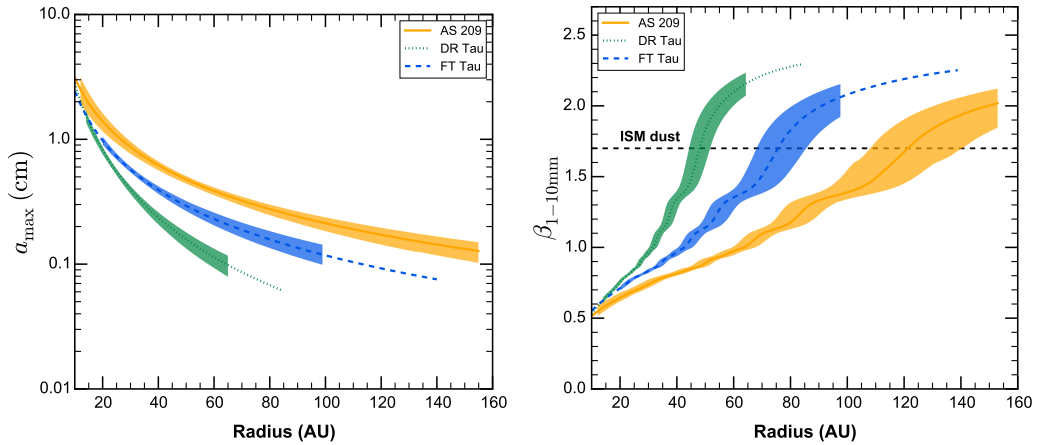
Fig. 3.12 *Left panel:* radial profile of the maximum dust grain size a_{max} constrained from the multiwavelength fits. *Right panel:* radial profile of the dust opacity spectral slope $\beta(R)$ between 1 mm and 10 mm. The dashed black horizontal line at $\beta_{\mathrm{ISM}} = 1.7$ represents the typical value of β for small ISM dust grains. *In both panels:* the thick lines represent the median (i.e., the best-fit) model, and the shaded areas represent the 1σ credibility intervals. The best-fit model lines are plotted wherever the signal-to-noise ratio is higher than 3 (computed for the observation displaying the most extended disk emission); the shaded areas are truncated at half the average beam size (inner regions) and at $R = \overline{R}$ (outer regions).

in our case a power law[6]). Obtaining an accurate estimate of the temperature in the outer disk is difficult due to the low optical depth to the stellar radiation and the low temperature reached by the disk midplane (moreover, other external heating effects possibly start to play a role). Because we expect –within the range of wavelengths at which we observe– that the major contribution of the emission always comes from the midplane dust, modeling this emission with a unique temperature profile is more physically founded than using several different temperature profiles that apply in different disk regions. This consideration is the main motivation for the development of our joint multiwavelength analysis.

In the left panel of Figure 3.12 we compare the radial profiles $a_{\mathrm{max}}(R)$ obtained for the disks in the sample. The observed declining profile of $a_{\mathrm{max}}(R)$ with radius is in line with the expected outcome of the viscous evolution of disks according to which the smaller dust particles (closely coupled with the gas) are brought to large stellocentric distances, whereas the larger dust grains (less coupled with the gas and more sensitive to the gas drag) drift inwards (Weidenschilling 1977; Brauer et al. 2008; Birnstiel et al. 2010; Armitage 2010). In both figures, we plot the best-fit models as lines and the 1σ credibility intervals as shaded areas. The best-fit models are truncated at the radius where the signal-to-noise ratio of the observations becomes lower than 3, computed for the observation displaying the most extended disk emission. The shaded areas are truncated in the inner region at half the synthesized beam size to give a visual representation of the average angular resolution of the observations, and in the outer regions at $R = \overline{R}$. All the objects support evidence of large grains in the inner disk ($a_{\mathrm{max}} \approx 1\,\mathrm{cm}$) and smaller grains in the outer disk ($a_{\mathrm{max}} \lesssim 3\,\mathrm{mm}$), with changes in size of at least one order of magnitude. Given the constrained $a_{\mathrm{max}}(R)$ profiles, we compute the dust spectral index $\beta(R)$ profiles (shown in the right panel of Figure 3.12), which grow accordingly from $\beta \approx 0.5$ in the inner disk to $\beta \gtrsim 1.7$ in

---

[6]This choice is justified by the outer disk maximum grain size distribution derived by other authors and by simple fits to the predictions of global dust evolution models, e.g., Birnstiel et al. (2012).

the outer disk. These findings confirm the earlier evidence of $\beta(R)$ increasing with radius obtained by Pérez et al. (2012), Banzatti et al. (2011), and Guilloteau et al. (2011) with different techniques, and by Trotta et al. (2013) with an initial implementation of this joint multiwavelength analysis.

The $a_{\max}(R)$ radial profiles derived for the three disks tend towards similar values $a_{\max}(R) \simeq 2$ cm in the innermost spatially resolved region $10\,\mathrm{au} < R < 20$ au, but display apparent differences in the slope with AS 209, FT Tau, and DR Tau showing respectively an increasing steepness. The differences we observe in the slopes may be due to several factors: different disk ages (grain growth processes can lead to time-dependent grain size distributions), different initial grain size distributions of the primordial material out of which the disks formed, different dust compositions, and/or different disk morphologies. The limited sample of disks analyzed here clearly does not enable us to investigate in detail these effects on the dust size distribution, but the overall similarity between the profiles is remarkable. The three disks –AS 209, FT Tau, and DR Tau– appear to have progressively more concentrated large grains. Extension of our analysis to a larger sample of objects will possibly allow us to understand what drives these differences in the overall distribution of grain sizes in disks. Our work here lays down the methodology for this type of study.

3.7   Conclusions and outlook

This study presents the architecture and the capabilities of a new multiwavelength analysis designed to constrain the structure and the dust properties of protoplanetary disks through a simultaneous fit of interferometric (sub-)mm observations at several wavelengths. The analysis adopts a Bayesian approach and performs a fit in the *uv*-plane. It requires models for the disk thermal emission and the dust opacity. The architecture of the analysis is highly modular (the disk and the dust models can be changed independently of each other) and therefore is particularly suitable for testing other models for the dust opacity or the disk structure (e.g., disks with holes or with non-axisymmetric morphology).

For this study, we modeled the disk with a two-layer disk approximation (Chiang and Goldreich 1997; Dullemond et al. 2001) and the dust opacity with Mie theory. We applied the fit technique to three protoplanetary disks (AS 209, DR Tau, and FT Tau) for which sub-mm, mm, and cm observations are available. We combined observations from the CARMA, SMA, and VLA interferometers with different angular resolution and signal-to-noise ratios. Despite the heterogeneity of the observations, the analysis technique has proven to be effective in simultaneously fitting all the datasets available for each object, as the visibility comparisons and the residual maps show. Furthermore, the convergence of the Markov chain Monte Carlo was assessed through careful statistical checks. The strength of our method lies in the fact that it allows us to derive a unique and self-consistent disk structure $(\Sigma(r), T(r))$ that is applied to all wavelengths to derive the overall variation of the maximum grain size with radius under the simplifying assumption that the radial profile $a_{\max}(R)$ can be approximated with a smooth power law, which is a realistic assumption given the angular resolution of the observations we are analyzing here.

In the three disks analyzed here, we find a common trend of larger (cm-sized) grains in the inner disks (R<30-40 au) and smaller (mm-sized) grains in the outer disks, but different slopes of $a_{\max}(R)$ for different disks. A natural question that arises is whether this is an evolutionary trend (caused by dust growth processes) or an intrinsic variability of disk properties. It is not possible to answer this question with the very limited sample we have analyzed here, but the analysis method is ready to be performed on larger samples that

will have the potential of giving us some insight into possible correlations and intrinsic variability.

The highly modular architecture of the analysis makes it suitable for testing other dust opacity and disk models with relatively little coding effort. From this perspective, it will become important to develop new models that are on the one hand more computationally efficient, and on the other hand refined enough to describe the complex structures now seen in the dust and gas distribution of protoplanetary disks (e.g., ALMA Partnership et al. 2015). The versatility of the method makes this kind of multiwavelength analysis suitable for tackling many interesting questions about the dust and the gas evolution in protoplanetary disks.

4

Dust properties across CO snowline in the HD 163296 disk

The content of this chapter has been published in:

> *"Dust properties across CO snowline in the HD 163296 disk from ALMA and JVLA observations"*
> Guidi, G., **Tazzari, M.**, Testi, L., de Gregorio-Monsalvo I., Chandler, C. J., Pérez, L., Isella, A., Natta, A., Ortolani, S., Henning, T., Corder, S., Linz, H., Andrews, S., Wilner, D., Ricci, L., Carpenter, J., Sargent, A., Mundy, L., Storm, S., Calvet, N., Dullemond, C., Greaves, J., Lazio, J., Deller, A., Kwon, W., 2016, A&A **588**, A112.

4.1 Connecting grain growth with gas properties

It was realized already four decades ago that aerodynamical friction may effectively prevent grain growth (Weidenschilling 1977). The process of rapid radial migration and fragmentation sets an upper limit to the grain sizes as a function of radius and a very rapid evolutionary timescale for dust particles in disks (Brauer et al. 2008; Birnstiel et al. 2012). These theoretical expectations are at odds with direct observations of dust properties in the outer disks from millimeter observations (Ricci et al. 2010b; Birnstiel et al. 2010). This is a general result, although some authors have shown that disks with peculiar growth processes (e.g., Laibe et al. 2014; Drążkowska et al. 2014) or specific dust properties (Okuzumi et al. 2012) may retain large particles more efficiently. To overcome the general inconsistency between models and observations, the most commonly accepted scenarios involve local grain growth and trapping in small regions, with sizes close to or smaller than the local disk scale height (Klahr and Henning 1997; Pinilla et al. 2012; Testi et al. 2014; Johansen et al. 2014).

The regions in the disk midplane that correspond to the *snowlines*[1] of major volatiles are particularly interesting. The presence of a snowline may locally promote efficient grain

---

[1]For a given molecule, the *snowline* radius marks the region where the species is in gaseous phase (at radii smaller than the snowline) and the region where the species condenses into ices (at radii larger than the snowline).

growth through recondensation across the snowline or by changing the sticking properties of ice-coated grains and, in addition, the local release of volatiles from the ices may induce a local pressure bump that could trap large grains (e.g., Supulver and Lin 2000; Wada et al. 2009; Ros and Johansen 2013; Gundlach and Blum 2015).

It is now becoming possible to investigate observationally the effect of the CO snowline on grain growth. Indeed, on the one hand, recent multi-wavelength studies by Pérez et al. (2012); Tazzari et al. (2016) (see Chapter 3) are able to provide robust constraints on the radial variations of the dust properties; on the other hand, the CO snowline has been clearly identified in several nearby disks (Mathews et al. 2013; Qi et al. 2013, 2015) by studying its effects on DCO^+ and N_2H^+ abundances. Since the CO abundance in protostellar ices is found to be about 30-40% of H_2O (Öberg et al. 2011), the CO snowline is one of the most important snowlines to be studied after water's one.

In this work we focus on the Herbig Ae star HD 163296, a bright and isolated object at a distance of 122^{+17}_{-13} parsec (van den Ancker et al. 1998) with a relatively massive disk ($\sim 0.1 M_\odot$: Qi et al. 2011; Isella et al. 2007) and an excellent prototype for gas- and dust-rich protoplanetary disks. An estimated age of 5 Myr was obtained from the comparison between Hipparcos astrometric measurements and pre-main sequence evolutionary models by van den Ancker et al. (1998). The stellar parameters computed by Natta and Testi (2004) are $M_* = 2.3 M_\odot$, $L_* = 36 L_\odot$, $T_{eff} = 9500 K$. To study the dust properties in the protoplanetary disk around HD 163296, we re-analyse the ALMA Science Verification observations (de Gregorio-Monsalvo et al. 2013; Mathews et al. 2013; Rosenfeld et al. 2013) and for the first time discuss the continuum emission in Band 6, combined with new VLA observations from the Disks@EVLA collaboration. In Section 4.2 we describe the observational data, in Section 4.3 we report the main new results of our analysis, in Section 4.4 we present the result of our disk modeling, and in Section 4.5 we discuss the main implications for grain properties.

4.2   Observations

4.2.1   ALMA observations

The ALMA observations of HD 163296 (also known as MWC 275) were part of the ALMA Science Verification Program 2011.0.000010.SV[2]. Band 6 observations were performed on 2012 June 9, June 23, and July 7 using a set of configurations comprising 20, 21 and 19 antennas, respectively. The total integration time was 3.14 hours (1.4 hours on the science source), the field of view was $\sim$20"onds and the baselines ranged from 20 to 400 meters, corresponding to spatial scales of 1600 au to 80 au at the distance of the object. The flux density calibrator for the three execution blocks were Juno, Neptune, and Mars, while the phase calibrator was J1733-130 and the bandpass calibrator J1924-292. The correlator was set with four spectral windows in dual polarization mode, two spectral windows in the upper side band and two in the lower side band. Two spectral windows, #0 (216.2 - 218 GHz) and #3 (233.1 - 234.9 GHz), were used to observe the line-free continuum with channel widths of 488 kHz; while at higher resolution (244 kHz) spectral window #1 (219.5 - 220.4 GHz) included the $C^{18}O(2-1)$ line at 219.560 GHz and the $^{13}CO(2-1)$ line at 220.398 GHz, and spectral window #2 (230.5 - 231.5 GHz) covered the $CO(2-1)$ line at 230.539 GHz. Imaging of the continuum emission of HD 163296 was performed

---

[2]The ALMA Science Verification data can be found at: `https://almascience.eso.org/alma-data/science-verification`

excluding the above-mentioned lines (see Rosenfeld et al. 2013; Klaassen et al. 2013). Data was calibrated using version 4.1.0 of the Common Astronomy Software and Application (CASA), self calibration was applied making use of the line-free channels, and using robust weighting during the CLEAN deconvolution, we were able to reach a resolution of $0.74'' \times 0.60''$ with a rms of 0.37 mJy/beam (see Table 4.1).

Band 7 observations were made on 2012 June 9, June 11, and June 22 with the same antenna configurations as for Band 6. Collectively, the five datasets covered an integration time of 3.9 hours, with 2.3 hours on the science target. The flux density calibrators were Juno and Neptune, while the bandpass and phase calibrators were the same as those used for Band 6. The two spectral windows in the lower side band were #2 ($345.56 - 346.03$ GHz) and #3 ($346.52 - 347.47$) with channel widths of 122 and 244 kHz, respectively. The ones in the upper side band were #1 ($356.50 - 356.97$ GHz) with 122 kHz channel width and #0 ($360.11 - 360.23$ GHz) at a high spectral resolution of 30.5 kHz; these included the emission lines: CO($3 - 2$) at 345.796 GHz (#2), $HCO^+(4 - 3)$ at 356.734 GHz (#1), $H^{13}CO^+(4 - 3)$ at 346.998 GHz (#3) and $DCO^+(5 - 4)$ at 360.160 GHz (#0). A detailed analysis of these spectral lines has been published by Mathews et al. (2013), de Gregorio-Monsalvo et al. (2013), and Rosenfeld et al. (2013). In this work we focus on the imaging of the continuum emission, obtained with the task CLEAN applying a robust weighting with Briggs parameter 0.5 and achieving a synthesized beam of $0.57'' \times 0.37''$ and a rms of 0.18 mJy/beam (see Table 4.1).

4.2.2 VLA observations

Observations of HD 163296 were made using the Karl G. Jansky Very Large Array (VLA) of the National Radio Astronomy Observatory[3] as part of the Disks@EVLA project (AC982) in 2011 May and June in the BnA and A configurations. The Ka-band ($\lambda \sim$1cm) receivers were used with two 1GHz basebands centered at 30.5 and 37.5GHz, providing projected uv-spacings from 25 to 3,800 kλ. The complex gain was tracked via frequent observations of J1755$-$2232, and the spectral shape of the complex bandpass was determined through observations of 3C279. The absolute flux density scale was derived from observations of 3C286 (Perley and Butler 2013, e.g.,), and its overall accuracy is estimated to be 10%. The data were calibrated, flagged, and imaged using a modified version of the VLA Calibration Pipeline[4] with CASA. The astrometry reported here corresponds to what was derived from the A configuration data.

In addition, HD 163296 was observed with the C-band ($\lambda \sim$6cm) receivers in the DnC configuration in September 2010, in order to evaluate any potential contamination from ionized gas at shorter wavelengths. Two 1GHz basebands were centered at 5.3 and 6.3GHz. Complex gain variations were tracked through observations of J1820$-$2528, and the bandpass and absolute flux density scale was obtained through observations of 3C286. The data were calibrated, flagged, and imaged using the CASA data reduction package. HD 163296 was detected with integrated flux density $F_{5.2cm} = (410 \pm 57)\mu$Jy.

---

[3]The National Radio Astronomy Observatory is a facility of the National Science Foundation operated under cooperative agreement by Associated Universities, Inc.

[4]See https://science. nrao.edu/facilities/vla/data-processing/pipeline/scripted-pipeline

4.3 Observational results

4.3.1 Continuum maps

In Figure 4.1 we show the continuum intensity maps obtained from the line-free channels at three different wavelengths: ALMA Band 7, ALMA Band 6, and the combination of the two VLA frequency ranges at 30.5 and 37.5 GHz. The parameters of the images are listed in Table 4.1.
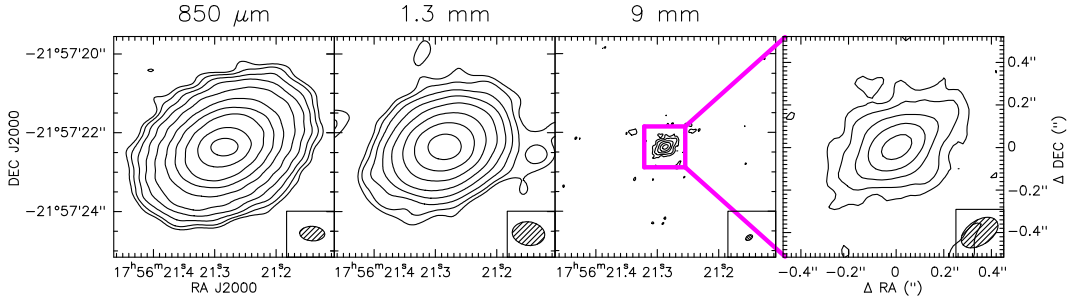
Fig. 4.1 Continuum maps at different wavelengths, from the left: 850 μm, 1.3 mm, and 9 mm, the last obtained from the combination of VLA 8.0 mm and 9.8 mm bands. The contour levels correspond to -3 (dashed), 3, 6, 12, 24, 48, 100, 200, 400, 800, 1600 σ. The bottom right of every panel shows the synthesized beam (see Table 4.1).

Table 4.1 Parameters for the deconvolved images displayed in Fig. 4.1 and for the images obtained from the single VLA frequencies of 30 and 37 GHz.

	λ [mm]	ν [GHz]	F_{int} [mJy]	F_{peak} [mJy/beam]	rms [mJy/beam]	CLEAN beam [FWHM]	Beam P.A. [°]
ALMA B7	0.85	352.9	213 ± 21	440	0.18	$0.57'' \times 0.37''$	86.5
ALMA B6	1.33	225.3	600 ± 60	220	0.37	$0.74'' \times 0.60''$	77.3
VLA Ka	9.00	34.0	1.83 ± 0.02	0.847	0.013	$0.18'' \times 0.11''$	-49.4
VLA Ka	8.00	37.5	2.02 ± 0.2	0.928	0.024	$0.16'' \times 0.10''$	-56.1
VLA Ka	9.83	30.5	1.65 ± 0.2	0.806	0.015	$0.19'' \times 0.12''$	131.5

In agreement with previous work (de Gregorio-Monsalvo et al. 2013; Natta and Testi 2004), we observe more compact emission at longer wavelengths, obtaining at 850 μm a projected radius of $\sim2.4''$ at a three-sigma level, corresponding to about 290 au, while the outer radius of the emission is ~260 au at 1.3 mm, and ~40 au at 8-10 mm. We note that the low signal-to-noise of the VLA data at 8 and 10 mm can lead to underestimating the extent of the emission at these wavelengths, and it is critical to consider the visibility function for a proper analysis of the disk structure. We use $44°$ for the disk inclination and $133°$ for the disk position angle (from Qi et al. 2011) and plot the normalized real and imaginary part of the visibilities in Figure 4.2.

These plots show that the real part of the visibilities declines more steeply at the shorter wavelengths (ALMA 850 μm and 1.3 mm) than at longer wavelengths (VLA 8 mm and 9.8 mm), demonstrating that the millimeter wavelength emission is intrinsically considerably more extended than the centimeter wavelength emission (a point source would be a constant 1.0 as a function of uv-distance in this plot). The integrated flux density above the 3σ level at 850 μm is $F_{850\mu m} = 2.13 \pm 0.02$ Jy, similar to the value found
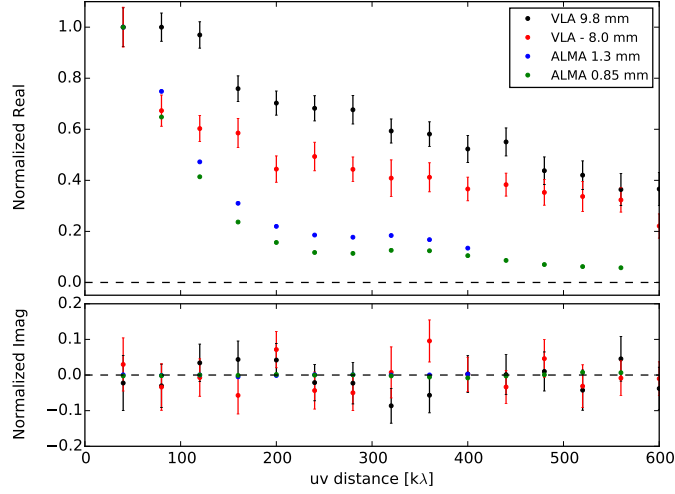
Fig. 4.2 Real and imaginary parts of the measured visibilities as a function of uv-distance, deprojected assuming PA=133°, i=44°and bin-averaged every 40 kλ. Visibilities at each wavelength have been normalized by the average value at 40 kλ and error bars display the standard error of the mean, negligible for ALMA observations.

by Isella et al. (2007) and de Gregorio-Monsalvo et al. (2013), while in Band 6 we find $F_{1.3mm} = 0.59 \pm 0.06$ Jy. At the longer wavelengths, the flux density decreases by almost 3 orders of magnitude, with $F_{8mm} = 2.0 \pm 0.2$ mJy and $F_{10mm} = 1.6 \pm 0.2$ mJy. We include a calibration error of 10% in the measurements of the flux densities. We find a smoothly decreasing intensity profile at all wavelengths, consistent with the disk temperature and surface density decreasing with radius.

4.3.2 Proper motions

We checked whether the position of the star at the two different epochs of our observations was consistent with the proper motions reported in the literature: applying a gaussian fit with to the images we find that the positions of the peaks fall within the 3σ error ellipse from the predicted position based on the Hipparcos astrometric mission measurements (J1991.25). For the ALMA observations (2012), we used Band 7 data because of its better signal-to-noise, with the peak position of the images obtained from the calibrated dataset before the self-calibration was applied. Figure 4.3 displays the estimated positions of the central star, and the astrometric error for interferometric observations is affected, among other things, by the phase calibration and depends on several factors (weather conditions, the separation between the target and the calibrator, etc.). We assume here that the absolute astrometry of the ALMA data is 0.1″[5], while for the VLA in A configuration, it is expected to be $\sim$ 0.02″[6]. The proper motions derived from a least-squares interpolation between our peaks at the two different epochs and the J1991.25 Hipparcos position are consistent with the latest reduction of the Hipparcos data (van Leeuwen 2007) within the errors and are listed in Table 4.2. The main difference we find is in the right ascension,

---

[5]https://help.almascience.org/index.php?/Knowledgebase/Article/View/153/6/what-is-the-astrometric-position-accuracy-of-an-alma-observation

[6]https://science.nrao.edu/facilities/vla/docs/manuals/oss/performance/positional-accuracy
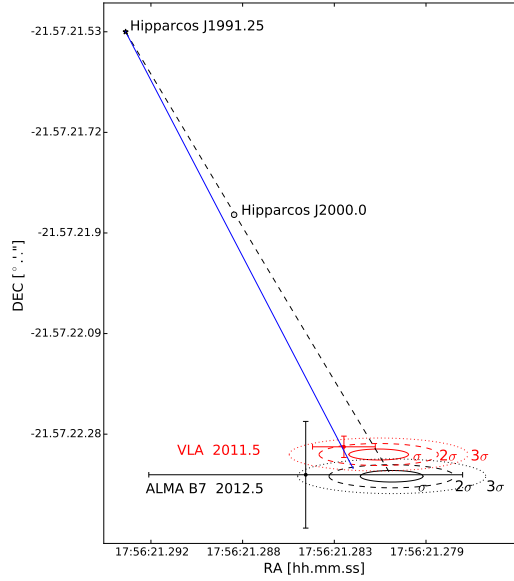
Fig. 4.3   Position of HD 163296 at the different observing epochs. The dashed line represents the proper motions from the Hipparcos measurement (J1991.25) to 2012, with respective proper motion error ellipses at 1, 2, and 3 σ from the predicted positions. The black dot indicates our position estimate for the star at epoch 2012.5 based on the peak of the image in Band 7, while the red dot is the peak of the VLA image at 9 mm in 2011.5. The error bars are given by the astrometric accuracy of 0.1" for ALMA and 0.02" for VLA. The blue solid line represents the proper motions calculated from a least-squares regression between Hipparcos measurements and the observations.

where our best fit would imply a smaller proper motion. Nevertheless, the difference is still well within the uncertainties.

Table 4.2   Coordinates of HD 163296 at different epochs

	RA [$hh : mm : ss$]	DEC [$° . ' . ''$]
Hipparcos J1991.25	17:56:21.293	-21.57.21.527
VLA 2011.5	17:56:21.283	-21.57.22.30
ALMA 2012.5	17:56:21.285	-21.57.22.36

4.3.3   SED and free-free contribution

The integrated flux densities measured within a three-sigma level in our observations and the spectral energy distribution predicted by our model (see Section 4.4) are plotted in Figure 4.4. Our model is consistent with the observed flux densities in the literature (Natta and Testi 2004; Isella et al. 2007). At submillimeter and millimeter wavelengths, the continuum emission is due to the dust in the colder regions of the disk midplane, while at centimeter wavelengths the emission may also arise from free electrons in the stellar wind. Since this contribution is thought to come from a region in the inner part of the disk, we examined the longest baselines ($\geq$1500 kλ) in the VLA 8.0 and 9.8 mm observations and we estimate an upper limit of 0.3 mJy for this wind emission, corresponding to the asymptotic value reached at the higher uv-distances by the real part of the visibilities. We fit a power law for the free-free emission by performing a least squares interpolation between

Table 4.3   Proper motions of HD 163296

	pm-ra [*mas/yr*]	pm-dec [*mas/yr*]	error ellipse [*mas mas*]
Hipparcos	-7.98	-39.21	[0.94 0.51]
This work	-6.8	-38.5	[1.0 1.0]

our estimates at 8 and 10 mm and other VLA measurements at 3.6 cm (Natta and Testi 2004) and 5.2 cm (see Section 4.2). The resulting power law is $F_\nu \propto \nu^{-0.19\pm0.11}$, and is shown in Figure 4.4 (where we plot νF_ν as a function of λ). According to this estimate, the free-free component at wavelengths shorter than 7 mm is negligible (see also Natta and Testi 2004).
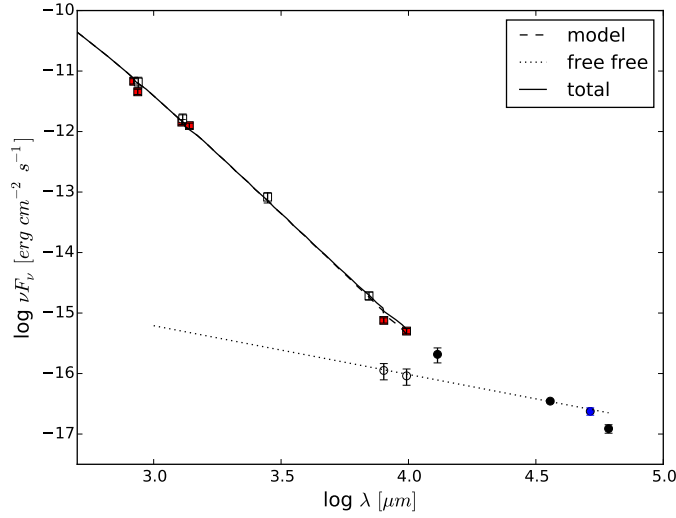
Fig. 4.4   HD 163296 spectral energy distribution. Our measurements are represented in red filled squares, the white empty squares are taken from the literature (Isella et al. 2007; Natta and Testi 2004), and the longer wavelength measurements used to evaluate the free free contribution are shown with full black circles (Natta and Testi 2004) and a blue full circle (Disks@EVLA collaboration). Empty circles show the value of 0.3 mJy for the free free emission estimated in this work. The dashed curve shows the best fit model from this work (see Section 4.4), the dotted line is the estimated free-free emission, and the solid line the sum of the two.

4.3.4   Excess emission at 850 μm

In Figure 4.5 we show the intensity profile of the image at 850 μm: as the disk is inclined by 44° from the line of sight, the best angular resolution is reached using only the data along the projected disk major axis. We considered the pixels inside one beam across the major axis, each point corresponding to a pixel of 0.1 ″ in the image (the points are therefore not all independent). The vertical spread is due to the shape and position angle of the synthesized beam, and to estimate the error when averaging on bins (Fig. 4.5, second panel) we weighted the points for the number of correlated pixels, i.e., $\sigma = \sqrt{(M-1)\Sigma_i(x_i - \mu)^2/(NM)}$, where M is the number of correlated points and N the number of averaged pixels.

A simple analysis of the profiles reveals a bump in the emission between 80 and 150 au: fitting a simple polynomial to outline a smooth profile does not produce an accurate fit (see Fig. 4.6). The degree of the polynomial was chosen as the lowest degree that would provide a reasonable fit to the intensity profile. To characterize the properties of this bump we fitted a combination of a 3rd degree polynomial plus a gaussian curve to our flux density profile (see Fig. 4.6, right panel): subtracting the polynomial from the data leaves a gaussian-shaped residual (see Fig.4.5, second panel) centered at about (106 ± 4) au, with a full width at half maximum (FWHM) of (71 ± 18) au and a peak at $(67 \pm 29)\%$ of the smooth polynomial profile. An estimate of the maximum spatial extent of the feature can be derived from deconvolving our best fit Gaussian with the synthesized beam ($\sim 0.5''$ in Band 7), resulting in an upper limit of ~ 40 au in FWHM. These values depend on the choice of the pixel size of the image and the tolerance we use for the points on the major axis, and thus are useful only for giving a rough estimate of the spatial scale of this unresolved emission excess. An independent analysis of this excess, obtained from modeling the visibilities directly, is shown in Section 4.

The feature cannot be clearly identified in Band 6 intensity profiles: we find an indication of a faint excess in the radial profiles along the disk projected major axis, but its detection depends on the small variation in the position angle and inclination parameters, making its characterization unreliable. This is consistent with the lower angular resolution of the Band 6 SV data: if we image the Band 7 dataset with a restoring beam equal to Band 6 resolution, the feature is diluted and cannot be reliably separated from the smooth disk emission (see Figure 4.7).

Table 4.4　　Best fit parameters of the polynomial fits

	a_0	a_1	a_2	a_3
Polynomial	(4.2 ± 0.1)e-01	(-5.6 ± 0.3)e-03	(2.7 ± 0.2)e-05	(-4.8 ± 0.6)e-08
	a_0	a_1	a_2	a_3
Polynomial	(4.6 ± 0.2)e-01	(-7.3 ± 0.9)e-03	(4.0 ± 0.7)e-05	(-7.4 ± 1.6)e-8
+ Gaussian	α [Jy/beam]	μ [AU]	σ [AU]	
	(3.4 ± 1.5)e-02	(1.06 ± 0.04)e+02	(3.0 ± 0.8)e+01	

Best fit parameters with associated standard deviations, obtained from the least-square interpolation of the data along the major axis using a 3rd-degree polynomial ($y = a_0 + a_1x + a_2x^2 + a_3x^3$) and a polynomial plus a Gaussian curve ($y = a_0 + a_1x + a_2x^2 + a_3x^3 + \alpha \, exp(-(x - \mu)^2/2\sigma^2)$), where x is in au and y in Jy/beam.

4.3.5　DCO$^+$ emission

We extracted the DCO$^+$ (J = 5−4) emission lines at 360.160 GHz from the ALMA Band 7 observations in order to compare the dust continuum radial profile with a potential molecular tracer of the CO snowline (Mathews et al. 2013, see). We used the CASA task "clean" with natural weighting to produce an integrated map of the DCO$^+$ emission in the velocity range 0.8-10 km/s, and the resulting synthesized beam is $0.62'' \times 0.42''$. We find a ring-like structure, similar to the one reported by Mathews et al. (2013), with a central radius of ~ 110 au and a total extent of the DCO$^+$ emission (detected at greater than 3σ) of 200 au in radius. In Fig. 4.5 (top panel), we show the radial profile of the integrated DCO$^+$ emission along the disk projected major axis: we note a symmetry between the southeast and the northwest directions, both displaying a double peak at a distance of ~ 60 au and ~ 140 au from the central star. We also point out that the minimum between the two peaks on both
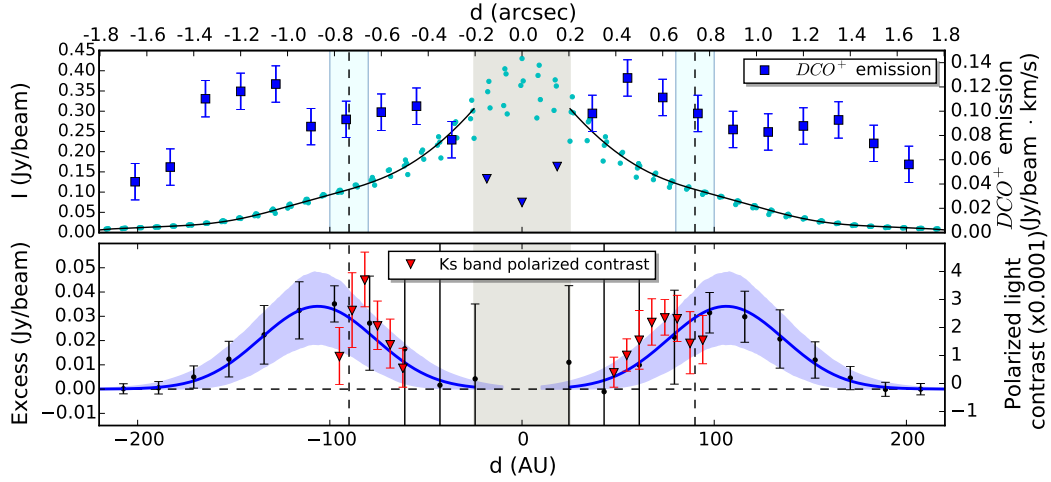
Fig. 4.5 *Top panel*: flux density at 850 μm along the disk major axis from SE (left) to NW (right). The solid line represents the fit (polynomial profile + a Gaussian for the excess) performed excluding the inner 0.2" of the disk (gray shaded area). The vertical dashed line corresponds to the CO snowline at 90 ± 10 au (from Qi et al. (2015)). DCO^+ emission in blue squares binned by 0.15", the blue triangles show the upper limit of DCO^+ emission in the inner 0.2" region of the disk, where we are limited by resolution. *Bottom panel*: residuals obtained by subtracting the polynomial fit from the data are shown with black dots binned by 0.15"onds. The blue solid line represents the Gaussian that best fits the excess (see Table 4.4), with the shaded area showing the 1σ fit uncertainty. The red triangles are the polarized light contrast in the Ks band (from Garufi et al. 2014, the scale is on the right side vertical axis).
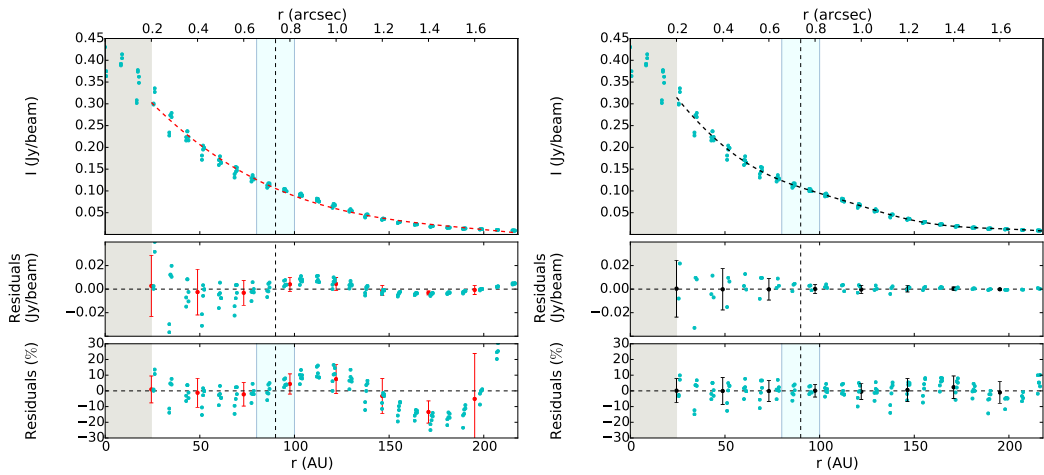
Fig. 4.6 *Left:* flux density across the disk major axis with a polynomial fit of degree 3 (dashed line in the upper panel). The second and third panels show the absolute residuals and the percentage residuals respectively. *Right:* the same intensity profile fitted with a 3rd-degreee polynomial plus a Gaussian (see Table 4.4 for the best fit parameters).

sides appears to fall at the position of the excess in the continuum emission at 850 μm ($\sim$110 au). The signal-to-noise ratio of the DCO^+ image is very low, so this result is very tentative and should be verified with higher sensitivity observations.
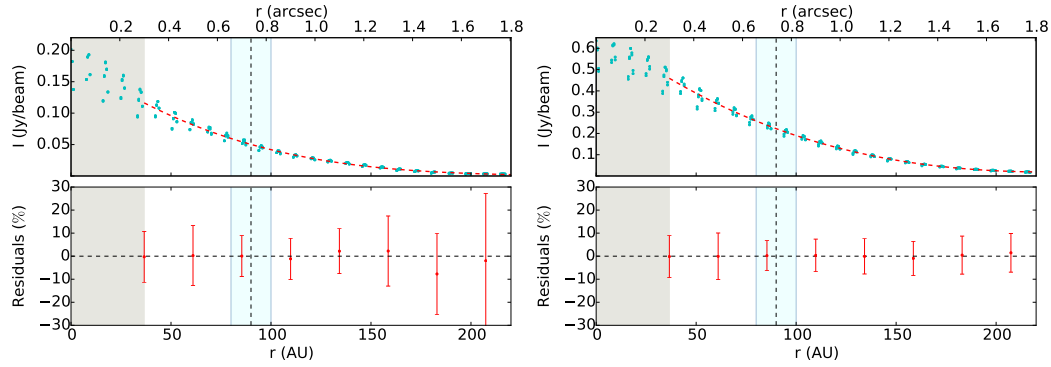
Fig. 4.7   *Left:* radial profile at 1.3 mm across the disk major axis, with the dashed curve resulting from the polynomial fit of the data. Bottom panel: absolute residuals with respect to the polynomial interpolation. The excess emission found at $850\,\mu$m is not visible in Band 6. *Right:* radial profile of the image at 850 μm restored with the same beam as Band 6 ($0.74''\times0.60''$, PA 77.3°).

4.3.6   Spectral index profiles

The dust opacity at millimeter and submillimeter wavelengths is usually approximated by a power law, $\kappa_\nu \propto \nu^\beta$ (e.g., Hildebrand 1983). The emission properties depend on the details of the composition, geometry, and size distribution of dust grains, most of which are very difficult to constrain. A general conclusion, however, is that in the conditions expected for dust in the densest regions of cores and disks, larger grain sizes correspond to lower values of the β index (e.g., Miyake and Nakagawa 1993; Stognienko et al. 1995; Natta and Testi 2004; Draine 2006). Even though directly connecting a value of β to the detailed properties of the dust population is not possible, measurements of β have been successfully used to infer the growth of dust in disks for many years (e.g., Beckwith and Sargent 1991; Wilner et al. 2000; Testi et al. 2001, 2003; Rodmann et al. 2006; Ricci et al. 2010b; Kwon et al. 2015).

Previous measurements of the dust opacity power law between 0.87 and 7 mm (Isella et al. 2007) and between 1.3 and 7 mm (Natta and Testi 2004) have already shown that grain growth occurs in the disk around HD163296. With the high resolution of ALMA it is now possible to extend these studies and constrain the radial behavior of the opacity spectral index β (see, e.g., Pérez et al. 2012, 2015; Tazzari et al. 2016), not just its average value across the disk. We recall here that the emission from the disk midplane is generally optically thin, and at these wavelengths the Rayleigh-Jeans regime is a good approximation. To verify these assumptions, we compared the brightness temperature derived from our observations with the temperature profile of our best-fit model (see Sect. 4.4), in order to estimate the optical depth τ of the emission as $\tau \simeq -ln(1 - T_b/T_{model})$. We found τ increasing toward the central regions, as expected, with values <0.6 for the emission at 850 μm, and <0.5 for the emission at 1.3 mm outside a inner region of ~30 au (see Fig. 4.8 for the 850 μm optical depth profile). At longer wavelengths, we estimate a lower optical depth with values of $\tau < 10^{-1}$ at both 8 and 10 mm. The assumption of optically thin continuum emission is therefore consistent with our data, and we expect a linear relation between flux density and dust opacity.

The flux density emitted from a ring dr at a given radius can be written as

$$F_\nu(r) \propto \Sigma(r) \cdot B_\nu[T(r)] \cdot \nu^{\beta(r)}, \tag{4.1}$$
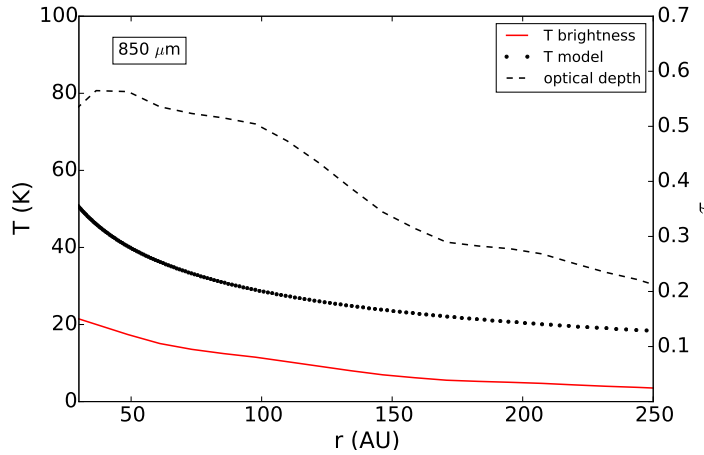
Fig. 4.8 Temperature profile of the best fit model (see Sect.4.4) in black dots and brightness temperature from the observations at 850 μm (red solid line) plotted in function of the distance, starting from 30 au to have a reliable estimate considering the resolution of the observations. On the right axis, the optical depth from the comparison of the two temperatures, plotted as the dashed line.

where $T(r)$ and $\Sigma(r)$ are the midplane temperature and surface density at the distance r from the star, and B_ν is the Planck function. In the Rayleigh-Jeans regime we therefore have $F_\nu(r) \propto \Sigma(r) \cdot T(r) \cdot \nu^2 \cdot \nu^{\beta(r)}$. Producing matched images (same beam, pixel size and centered on the peak of the emission) at different wavelengths and measuring the ratio of the flux densities as a function of distance from the star allows the spectral index, α (where $F_\nu \propto \nu^\alpha$), to be determined. Then, given the assumptions noted above, the power-law dependence of the dust opacity, β, can be derived as $\beta = \alpha - 2$ and does not depend on temperature or surface density. As discussed in Sect. 4.3.3, the observation at 8 and 10 mm includes gas emission from the stellar wind that needs to be subtracted to study the dust emissivity. The VLA maps used to compute the spectral index were produced by subtracting a point source at the center of the system with a flux density of 0.3 mJy from the calibrated visibilities (see Sec. 4.3.3).

In the lefthand panel of Figure 4.9 we show the intensity maps at 850 μm and 9 mm with a circular beam of 0.5″, the corresponding averaged radial intensity profiles and the derived α profile. The intensity-averaged values (and consequently the spectral index) are plotted as long as they stay above the 1σ level. We see an increasing trend in the spectral index α from $\sim$2.5 in the inner regions to $\sim$3.5 at 150 au. The profiles are displayed starting from and sampling every half resolution element of the images, corresponding to $\sim$30 au; the large error associated with this spectral index profile is dominated by the limited signal-to-noise ratio of the VLA images. With the same procedure we computed the spectral index between the ALMA Band 6 and 7 images, with a matching circular beam of 0.6″, and obtained the profile shown in the righthand panel of Figure 4.9. In this case the profile is sampled every 0.3″ ($\sim$40 au). In spite of the high signal-to-noise of the ALMA images, the large uncertainties are caused by the small wavelength leverage between the ALMA Band 6 and 7 observations. In propagating the uncertainty on α, we used a 10% calibration error for each flux, which in the case of $\alpha(850\mu m - 1.3mm)$ represents a pessimistic estimate, because the two ALMA observations were carried out with the same phase calibrator and with Neptune as flux calibrator. Within the uncertainties the α profile seems

to be consistent with the measurements between 850 μm and 9 mm. The spectral index remains below the value of 3 beyond 50 au, corresponding to a $\beta < 1$ under the assumptions mentioned above, this indicates the presence of grains that have grown to at least 1 mm in size (using the dust opacity curves computed by Testi et al. 2014). We find no features in the α (and by implication, β) profiles across the CO snowline, as would be expected for localized grain growth, but it should be noted that the resolution of the spectral index maps is limited by the lower resolution of Band 6 observations ($\sim 0.6''$), which would not be sufficient to detect small scale variations of the emission (see Section 4.3.4). We return to the estimate of $\beta(r)$ in Sect. 4.5.

4.4 Modeling results

In Section 4.3.4 we have shown that the surface brightness radial profile for the continuum emission at 850 μm is compatible with having an excess peaked around 110 AU, with deconvolved FWHM $\leq$ 40 AU. To assess the robustness of this result, we performed a direct fit of the interferometric data (i.e., the visibilities) using the fitting scheme described by Tazzari et al. (2016) to which we refer for the analysis details. To estimate the disk thermal emission at 850 μm, we used a classical two layer disk model (Chiang and Goldreich 1997) with refinements by (Dullemond et al. 2001) and a reduced disk flaring that adequately describes the observed far-infrared flux (from Tilling et al. 2012). The resulting vertical scale height for the surface layer at $R > 50$ AU is $h/R \sim 0.08$. Moreover, we assumed a constant dust to gas mass ratio $\zeta = 0.01$ and the following gas surface density profile:

$$\Sigma_{\mathrm{g}}(R) = \Sigma_0 \left(\frac{R}{R_0} \right)^{-\gamma} \exp \left[-\left(\frac{R}{R_{\mathrm{c}}} \right)^{2-\gamma} \right] , \tag{4.2}$$

where $R_0 = 10$ AU is a fixed scale length and Σ_0, R_c, and γ are free parameters to be fitted. To compute the disk emission, the dust opacity is calculated using Mie theory (see Trotta et al. 2013, for details of the computation) assuming the same dust composition throughout the disk, given by the following fractional abundances adapted from Pollack et al. (1994): 5.4% astronomical silicates, 20.6% carbonaceaous material, 44% water ice, and 30% vacuum. Furthermore, we assume a power-law grain size distribution $n(a) \propto a^{-q}$ for $a_{\min} \leq a \leq a_{\max}$, where a is the grain radius. To model the expectation that in the disk midplane there are larger grains than on the surface (Testi et al. 2014), we used different parametrization for the grain size distribution in these two regions: $q = 3.5$, $a_{\min} = 10$ nm, $a_{\max} = 100$ μm in the surface and $q = 3$, $a_{\min} = 10$ nm and $a_{\max} = 0.8 * (R/10 \text{ au})^{-1.025}$ mm in the midplane, where this variable maximum grain size is chosen to reproduce the $\beta(R)$ profiles found in Sect. 4.3.6. The modeling methodology is based on a Bayesian approach and employs an affine-invariant Markov Chain Monte Carlo (MCMC) ensemble sampler (Foreman-Mackey et al. 2013) to explore the parameter space and find the best-fit models (Tazzari et al. 2016).

In panel (a) of Figure 4.10 we show the comparison between the observations at 850 μm and the best-fit model (obtained running a MCMC with 500 chains) that corresponds to the following median values:

$$\gamma = 0.882 \pm 0.002 \, ,$$

$$\Sigma_0 = (13.40 \pm 0.03) \, \text{g/cm}^2 \, ,$$
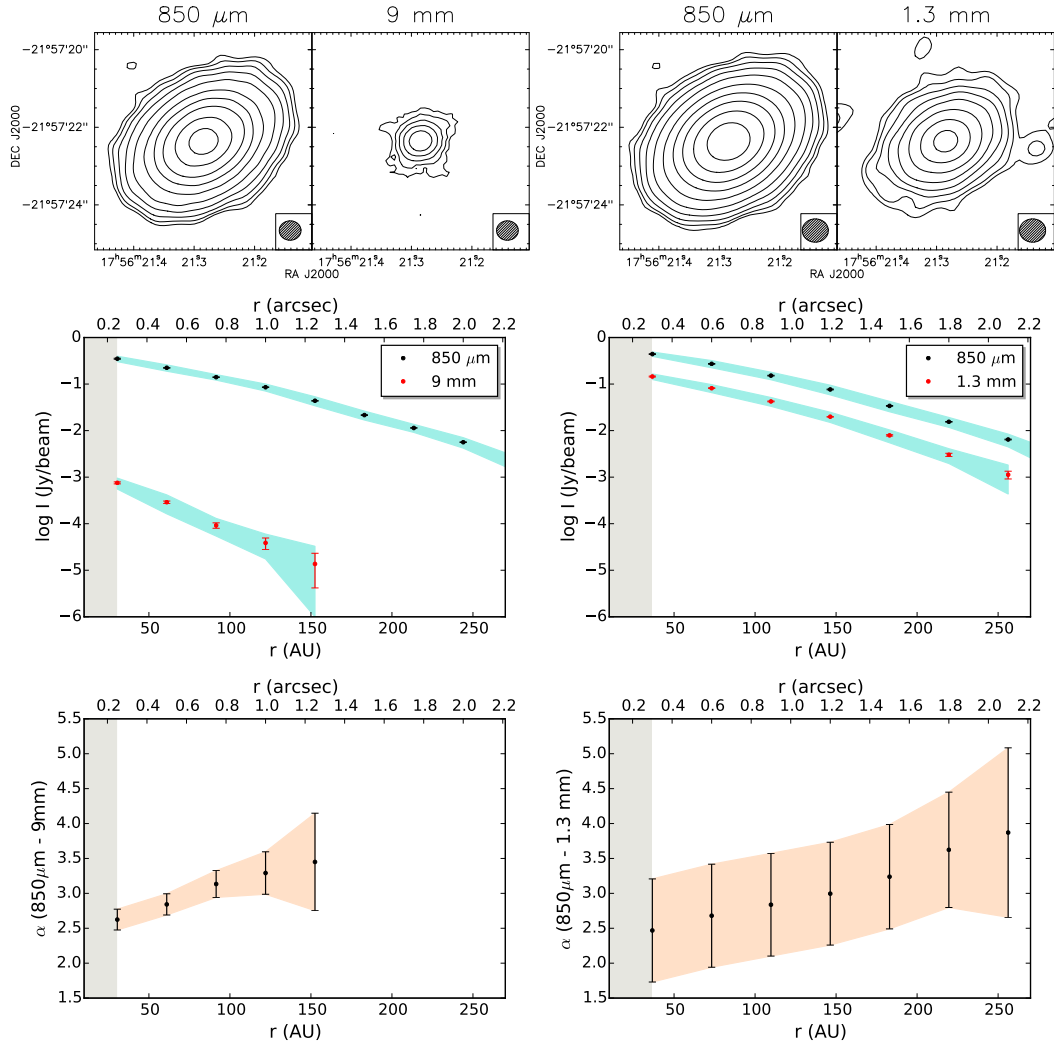
Fig. 4.9 *Left*: Flux density maps (top panel) at 850 μm and 9 mm with contour levels at -3 (dashed), 3, 6, 12, 24, 48, 100, 200, 400, 800, and 1600 σ. Disk surface brightness profiles (middle panel) used to compute the spectral index, plotted on a logarithmic scale. The shaded region shows the dispersion of the individual data points in the images, while the error bars show the uncertainty on the mean for each bin. The flux density spectral index (bottom panel) was calculated between 850 μm and 9 mm as a function of radial distance. The profiles were averaged on ellipses of semi major axis r (shown in" and au in the top and bottom axes, respectively). The shaded region indicates the uncertainty of the measurement, resulting from the noise of the deconvolved images and the systematic calibration uncertainty; the low signal-to-noise ratio in the VLA map dominates the uncertainty on the spectral index determination beyond $\sim$100 au. *Right*: as above, but for the two ALMA datasets at 850 μm and 1.3 mm.

$$R_c = (118.7 \pm 0.2)\, \text{au}\,.$$

We note that the model with median values also gives the minimum χ^2, with a reduced $\chi^2_{\text{red}} =1.853$. The ring-shaped residuals are clearly visible in the righthand plot of panel (a), and this show that a simple two-layer disk model with a monotonically decreasing surface density (and thus surface brightness) is not sufficient to completely account for the observed flux density profile.
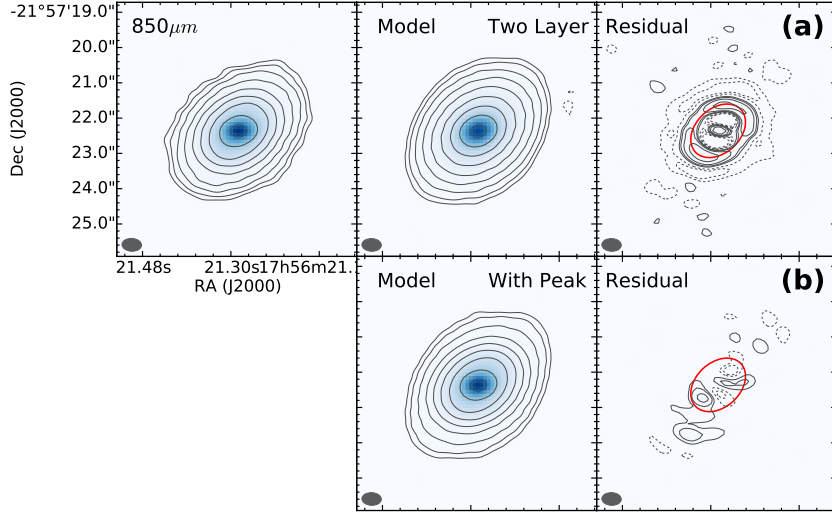
Fig. 4.10   Continuum maps at 850μm showing the results of the fits of the visibilities. The top left panel shows the observations, the two panels in the center the best-fit model, and the two panels on the right the residuals. The red solid curve represents the CO snowline at 90 au. Panel (a): we use a classical two-layer disk model that implements a monotonically decreasing surface brightness. Ring-shaped residuals are clearly visible. Panel (b): we use the two layer disk model with an additional Gaussian peak. We fit the peak location ($R_p = 96$ AU) and width $\text{FWHM}_p = 58$ AU. The residuals are substantially reduced. The parameters used for the CLEAN are the same as discussed in Section 4.2, and the contour levels are the same as those used in Figs. 4.1 and 4.9.

To assess whether the residuals can be explained by adding a simple ring-like peak or whether they need a more complicated treatment, we performed another fit with a modified version of the two-layer model. This modified two-layer disk model implements an additional ring-like structure in the 850 μm emission, with a disk surface brightness $I'(R)$ as follows:

$$I'(R) = I_{2\text{L}}(R) + I_p I_{2\text{L}}(R_p) \exp\left[-\frac{(R - R_p)^2}{2\sigma_p^2}\right] , \qquad (4.3)$$

where $I_{2\text{L}}(R)$ is the brightness computed by the classical two layer model, R_p the peak center, σ_p the peak width, and I_p the peak intensity (in units of the brightness in the vicinity of the peak, namely $I_{2\text{L}}(R_p)$). This new model therefore has six free parameters: three of them for the two-layer model (γ, Σ_0, R_c) and another three to define the peak (R_p, σ_p, I_p). We performed the fit with the Tazzari et al. (2016) modeling tool discussed above, with the results shown in panel (b) of Figure 4.10. The best-fit model ($\chi^2_{\text{red}} = 1.830$) is described by $\gamma = 1.32 \pm 0.01$, $\Sigma_0 = (24.6 \pm 0.3)$ g/cm^2, $R_c = (111.3 \pm 0.8)$ au, which correspond to a radial profile that is slightly steeper than the simple power-law model but has a similar cut-off radius. For the Gaussian peak, we find that is described by $R_p = (96 \pm 1)$ au, $\sigma_p = (24.9 \pm 0.5)$ au and $I_p = 128 \pm 20\%$. This modified disk model is able to reproduce the observations with an extremely good agreement, as confirmed by the considerably smaller residuals (right plot of panel (b), Figure 4.10). The midplane temperature is computed at every radius according to the two-layer approximation: in Figure 4.8 (Section 4.3.6) we show the temperature profile of this best-fit model.

In conclusion, the peak inferred from the direct fit of the visibilities is evidence of a

ring-like structure centered at 96 AU with a FWHM$= 2\sqrt{2\ln 2} \cdot \sigma_p \approx (58 \pm 3)$ AU, compatible with the upper limit resulting from the simple polynomial+Gaussian fitting of the continuum surface brightness in Section 4.3.4.

4.5 Discussion

In Section 4.3 we derived spatially resolved spectral index profiles for the dust emission from the HD 163296 protoplanetary disk and we identified and characterized an unresolved excess 850 μm emission centered at $\sim$110 au. The presence of this feature has also been confirmed through a detailed modeling of the visibilities in Sect. 4.4. In this section we analyze these results and their possible implications for the growth of grains in the HD 163296 disk.

4.5.1 $\beta(r)$ profiles and grain growth

In Section 4.3.6 we derived the radial distribution of the spectral index as measured combining the ALMA 850 μm image with the ALMA 1.3 mm or the VLA 10 mm images. Under the assumptions of optically thin emission and Rayleigh-Jeans regime, the spectral index profiles can be directly converted into opacity power-law index profiles by subtracting a constant value of 2.0. Our modeling of the disk (Sect. 4.4) and the comparison of the measured brightness temperature with the expected temperature profile from our model (Sect. 4.3.6) confirm that the emission is optically thin throughout the disk, with the exception of the very inner region that is not resolved by the ALMA and VLA observations. On the other hand, the Rayleigh-Jeans approximation is not fully justified in the outer regions of the disk, especially for the ALMA Band 7 data. To estimate the value of the opacity power-law index as a function of radius we thus used (see Eq. 4.1)

$$\beta(r) = \left[\log\left(\frac{\nu_1}{\nu_2}\right)\right]^{-1}\left[\log\left(\frac{F_{\nu_1}(r)}{F_{\nu_2}(r)}\right) - \log\left(\frac{B_{\nu_1}(T(r))}{B_{\nu_2}(T(r))}\right)\right] \tag{4.4}$$

where $T(r)$ are the temperature profiles derived from our models. In Fig. 4.11 we show the profiles of $\beta(r)$ obtained from Eq. 4.4 using the intensity profiles shown in Fig. 4.9.

Our analysis of the continuum emission at three different frequencies shows in the first place a decreasing spatial extent with increasing wavelength, confirming the presence of dust processing and radial transport in this disk, as already shown by the comparison between the size of the dust and gas disk by de Gregorio-Monsalvo et al. (2013) and confirm and extend the results of Natta and Testi (2004); Natta et al. (2007), who showed the presence of large grains in the HD 163296 disk from integrated spectral indices and suggested a possible spectral index variation within the disk.

The $\beta(r)$ profiles are qualitatively consistent with the results of similar analyses performed in other classical smooth disks (Guilloteau et al. 2011; Banzatti et al. 2011; Pérez et al. 2012, 2015; Trotta et al. 2013; Menu et al. 2014; Tazzari et al. 2016), with a significant variation of β throughout the disk ($\Delta\beta > 1$), indicating a maximum grain size a_{max} decreasing with the distance from the star. The ALMA and VLA data provide for the first time the combination of signal-to-noise ratio, angular resolution and image fidelity to successfully perform an analysis in the image plane. Unfortunately, the ALMA Band 6 science verification data do not have the angular resolution to probe the dust properties in a localized region across the CO snowline. Similarly, the VLA data do not have a high enough signal-to-noise ratio at 100 au and beyond to derive strong constraints in the outer disk.
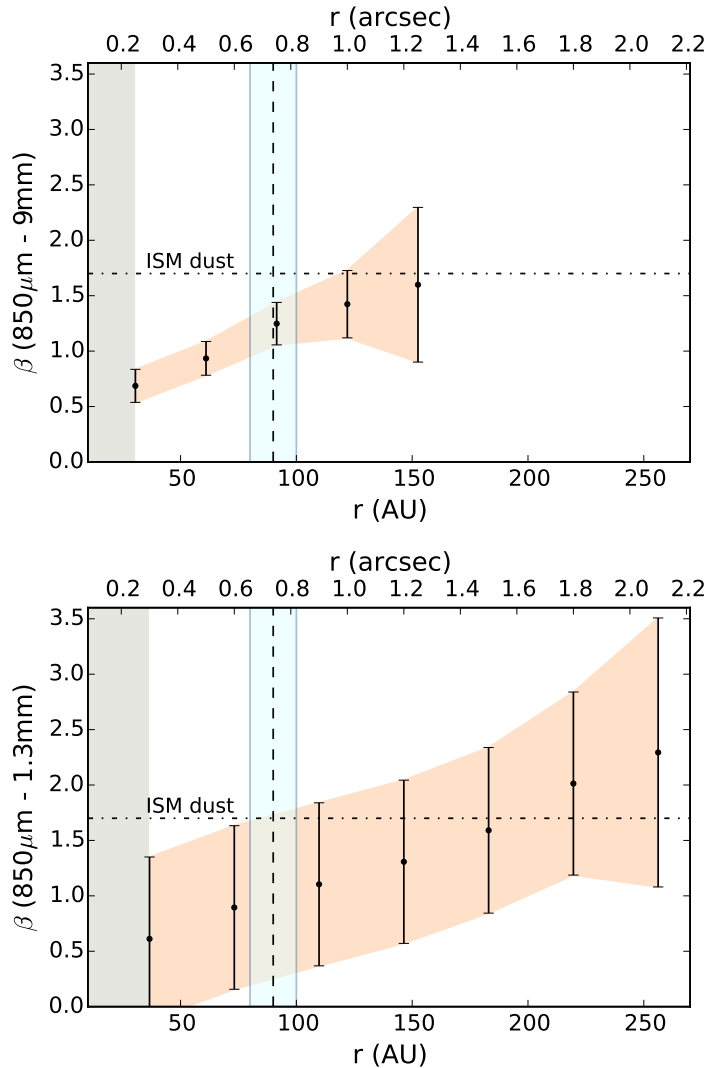
Fig. 4.11   Dust opacity power-law index (β) profiles derived using Eq. 4.4. $\beta(r)$ is computed between 850 μm and 9 mm in the top panel and between 850 μm and 1.3 mm in the bottom panel. The uncertainties are propagated from the surface brightness profiles presented in Fig. 4.9. The derived values of $\beta(r)$ in the top panel are dominated by the low signal-to-noise in the VLA image from $\sim$100 au and are very uncertain beyond this radius. The CO snowline at 90$\pm$10 au from Qi et al. (2015) is pictured as the dashed vertical line.

The conclusion that we can draw from the $\beta(r)$ profiles is that there is convincing evidence of large grains inside the CO snowline, but at $\sim$70 au resolution the profile appears to be smooth with no features. The data are consistent with significant grain growth throughout the inner 150-200 au of the disk. As discussed by many authors (see, e.g., Testi et al. 2014, and references therein), deriving a direct constraint on the level of grain growth from the β values is not trivial, because it requires assumptions on the dust structure and composition, which cannot be constrained outside the solar system. Nevertheless, a very broad range of reasonable assumptions on the grains properties imply that β values lower than 1 in the millimeter to centimeter regime can only be produced by grains and pebbles larger than a millimeter in size, and can be significantly larger under reasonable assump-

tions for grain porosity (Natta and Testi 2004). As an example, if we adopt an educated guess for the grain composition based on the constraints from our own Solar System (e.g., Natta and Testi 2004), combined with a fraction of vacuum of ∼50%, we derive maximum grain sizes as large as ∼ 1 cm at the CO snowline and even exceeding ∼ 10 cm in the inner ∼50 au of the disk (see Fig. 4 of Testi et al. 2014).

4.5.2 The nature of the 850 μm excess

We found an excess emission at 850 μm located at about 105-115 au from the star with a full width along the disk major axis of ≤ 40 au. This excess appears to be located very close to the CO snowline at 90 au as measured by Qi et al. (2015), who resolved the N_2H^+ emission in this disk with ALMA. The N_2H^+ molecule is thought to be a robust tracer of CO condensation fronts, because of the strong correlation between its abundance and gas phase CO depletion (see also Qi et al. 2013).

An analogous excess ring was found in the images of scattered light from HD 163296 taken with VLT/NACO (Garufi et al. 2014): polarized light images in Ks band displayed a "broken" ring feature with an excess along the major axis between ∼0.5 and 1", corresponding to 60 and 120 au, respectively (shown in Figure 4.5, middle panel). The upper limit on the extent of the excess we found corresponds to a total radial extent of $\lesssim$40 au, while the dimension of the resolved ring found in infrared polarized light by Garufi et al. (2014) measured 0.45″ on the east side and 0.6″ on the west side, corresponding to 60 au and 73 au, respectively.

The interpretation of the ring in Ks band polarized contrast given by Garufi et al. (2014) was the effect of self-shadowing of the disk created by a puffed-up inner region, with the outer disk emerging from the shadow at the location of the polarized emission. Garufi et al. (2014) could not exclude other effects that are possibly related to the CO snowline, but could not reach a conclusion as the polarized infrared light is tracing the τ ∼1 (at 2 μm) surface of the disk atmosphere at much higher altitudes in the disk than the cold midplane where the CO snowline (and the bulk of the disk material) is located.

Our result provides an important contribution, since it shows that the excess is not purely a disk surface feature. The detection of the excess at the two different wavelengths, tracing two different vertical regions of the disk, suggests the presence of a structure that concerns the whole vertical extent of the disk. At millimeter wavelengths we are probing the disk midplane, and the emission is proportional to the surface density, the dust properties, and the temperature profile (see Sect. 4.3.6). In principle any localized change of one (or more) of these properties can explain the excess emission that we find in our images.

The lack of sensitivity or angular resolution in the VLA and ALMA Band 6 data do not allow us to probe the spectral index of the excess detected in Band 7. Future ALMA and/or VLA observations may allow us to probe the presence of large grains at the location of the excess emission. The possibility of large grains at the snowline may also be connected with a local increase in the surface density (or temperature), which could also explain the observed excess.

This is indeed expected from the simulations of grain growth across snowlines (e.g., Ros and Johansen 2013). We note that the effect of snowlines on grain growth is still poorly understood theoretically and much work is still needed. Recent simulations (Stammler, priv. comm.) show that, as grains maintain the (water) ice mantles across the CO snowline, this does not produce a discontinuity in the coagulation and fragmentation properties. The only effect would be a drop in the mass of solid particles inside the snowline because a fraction of the mantles is released in the gas. Such a variation in the surface density

distribution across the snowline may produce an effect similar to the one we observe in the brightness profile and possibly also explain the effects on the disk surface observed in the near infrared.

Another mechanism that has been proposed to explain emission rings near snowlines in disks is sintering (Okuzumi et al. 2016): this process brings icy grains to bond at temperatures close to the sublimation temperature. As a consequence, these aggregates can easily fragment by collisions close to the snowline leading to the accumulation of smaller fragments, which are less affected by radial drift. Clearly more theoretical work is needed before a detailed comparison of our observations with models can be done.

An alternative explanation for this excess emission, which is not connected to the presence of the CO snowline, could be that particles are trapped by zonal flows (Dittrich et al. 2013, e.g.,) or by vortices (e.g., Klahr and Henning 1997). Such a mechanism has been invoked to explain the presence of annular dust confinement in some transitional disks (e.g., Pérez et al. 2014). Future higher angular resolution mm observations of the dust and gas will allow this possibility to be tested.

4.6   Summary

We have re-analyzed HD 163296 ALMA Science Verification data at 850 μm and 1.3 mm, and VLA data at 8 and 10 mm to study the radial behavior of dust properties in this disk. Our goal was to combine high resolution observations to derive the profile of the dust opacity spectral index, which is ultimately related to the size of grains throughout the disk, and look for evidence of grain growth across the CO snowline.

Our analysis shows, in the first place, more compact emission moving to longer wavelengths, confirming that dust processing and radial migration are taking place in this disk. A significant conclusion is that the dust opacity spectral index varies with radius and decreases toward the center to values ≤ 1, indicating the presence of large grains (≥ 1 mm) in the inner regions of the disk (inside 100 au). Our $\beta(r)$ profiles agree with those found in other resolved disks (Guilloteau et al. 2011; Pérez et al. 2012, 2015; Tazzari et al. 2016, e.g.,).

For this particular source, where a direct measurement of the location of the CO snowline is available, our analysis supports a scenario where the grains outside the snowline have not grown significantly, while the inner disk is populated by large grains. This general distribution would be consistent with an enhanced production of large grains at the CO snowline and subsequent transport to the inner regions. The alternative explanation of a smooth distribution of the grain sizes due to growth and transportation processes unrelated to the CO snowline is also consistent with the observed $\beta(r)$ profile.

A second important finding is the evidence of an excess in the continuum emission at 850 μm near the location of the CO snowline and approximately at the same position of the excess in Ks band polarized light as found by Garufi et al. (2014). Our finding confirms that the infrared excess emission is not only related to a disk surface layer effect, but also has more profound roots in the disk midplane, which is responsible for the 850 μm emission. The possible causes for this bump could be a local increase in the dust surface density due to dust trapping, for example caused by a local pressure maximum at the location of the snowline (Armitage 2010) or by turbulent eddies that can retain grains in their interior (Klahr and Henning 1997).

It is not clear whether the dust at this location has a different opacity spectral index β

with respect to the bulk of the dust, since we lack the spatial resolution and/or sensitivity at 1.3 mm and $\sim$10 mm to clearly detect the excess emission.

To conclusively probe whether this excess is a local change in the dust density and properties due to an effect of the CO snowline or another dust-trapping process, ALMA high resolution and sensitivity observations at mm wavelengths are needed, as well as higher sensitivity VLA measurements. As a future development, with ALMA longer baselines we might be able to resolve the iceline of the most important volatile, H_2O, and investigate the role of snowlines in grain growth more extensively.

5

ALMA survey of Lupus protoplanetary disks II: structure of disks

The content of this chapter has to be included in:

> *"ALMA survey of Lupus protoplanetary disks II: structure of disks"*
> **Tazzari, M.**, Testi, L., Williams, J. P., van Dishoeck, E., Ansdell, M., Manara, C., Miotello, A., Natta, A., et al., to be submitted to A&A.

The investigation of the fundamental properties of protoplanetary disks can be done either with dedicated studies on single objects or with statistical studies on large samples. The latter has the unique potential of revealing scaling laws that are key to understand how disks evolve on their way to form planets. In this chapter I analyze the ALMA observations of protoplanetary disks in the Lupus star forming region presented in Ansdell et al. (2016), which is a near complete (96% completeness) survey of Class II disks in the Lupus I-III clouds.

The chapter is organized as follows. In Section 5.1 I present the sample selection, in Section 5.2 the modeling details and in Section 5.3 the modeling results. I also provide a comparison with previous results by Ansdell et al. (2016). The results are discussed in Section 5.4 and in Section 5.5 I draw the conclusions.

5.1 Observations and sample selection

The bandwidth-weighted average frequency of the continuum observations is 335.8 GHz (890 μm). The flux calibration error of these observations is estimated to be 10%. For details on observational setup and data reduction we refer to Ansdell et al. (2016).

We carry out the analysis of the disk structure for a sub-sample of the 61 sources that have been detected in the continuum observations by Ansdell et al. (2016). The sample in Ansdell et al. (2016) contained a near complete (96% completeness) census of the sources with Class II or Flat IR spectra in the Lupus star forming region (I to IV clouds, whereas V and VI host Class III disks). We selected the sub-sample from the total sample of 61 objects excluding the edge-on disks (J16070854-3914075), the disks with clearly resolved gaps or holes (J16083070-3828268, RY Lup, Sz 111), the sources with irregular

shapes (J16090141-3925119, Sz 74, J16070384-3911113, Sz 118), the resolved and unresolved binaries (V856 Sco, Sz 123A) and two sources (J15450634-3417378, J16011549-4152351) for which we do not have information on the stellar parameters. We also exclude 14 sources with an integrated flux $F_{\text{cont}} < 4 \, \text{mJy}$ (Sz 106, J16002612-4153553, J16000060-4221567, J16085529-3848481, J16084940-3905393, V1192 Sco, Sz 104, Sz 112, J16073773-3921388, J16080017-3902595, J16085373-3914367, J16075475-3915446, J16092697-3836269, J16134410-3736462): such a low signal-to-noise ratio does not allow a robust estimate of their disk structure. We end up with a sub-sample of 33 sources. In addition, we also analyze the Band 7 observations of IM Lup that have been taken by another observing program (Cleeves et al., in prep.). Table 5.1 provides a list of the 34 sources (with stellar properties) analyzed in this work.

In Figure 5.1 we summarize the properties of the sub-sample in comparison to the complete sample from Ansdell et al. (2016). In the left panel, we show the distribution of stellar masses, ranging between $0.1 \, M_\odot$ and $3 \, M_\odot$. In the right panel we present the integrated continuum flux at 890 μm as a function of stellar mass for all the sources detected in the Ansdell et al. (2016) sample. In particular, we differentiate the sources considered in this analysis (blue dots) from the sources that we excluded (black symbols). The red dots represent the disks that were initially included in our analysis but turned out to be too faint to enable us to constrain their structure.

Finally, it is noteworthy that the sub-sample is complete (i.e., we apply our analysis to all the sources with stellar mass) in the $0.7 - 1 \, M_\odot$ mass bin: in this and in future plots the sources in this bin are highlighted as blue circled dots.

5.2 Modeling

To study the structure of the disks we fit their continuum emission with a disk model that is based on the two-layer approximation (Chiang and Goldreich 1997; Dullemond et al. 2001). In the following we introduce the fundamental quantities that are needed to compute the disk emission and for more details we refer to Tazzari et al. (2016) and Chapter 2.

5.2.1 Disk model

Under the basic assumptions that, at each radius, the disk is vertically isothermal and in hydrostatic equilibrium, the two-layer approximation allows us to compute the disk continuum emission given the properties of the central star, a surface density profile and a dust grain size distribution.

Following previous studies (Andrews et al. 2009; Trotta et al. 2013; Tazzari et al. 2016), we parametrize the gas surface density with a self-similar solution for an accretion disk (Lynden-Bell and Pringle 1974; Hartmann et al. 1998):

$$\Sigma(R)_{\text{g}} = \Sigma_0 \left(\frac{R}{R_0} \right)^{-\gamma} \exp \left[- \left(\frac{R}{R_c} \right)^{2-\gamma} \right] , \tag{5.1}$$

where Σ_0 is a normalization factor, R_0 is a characteristic radius that we keep fixed to 10 AU, γ is the power-law slope and R_c is the exponential cut-off radius. The dust surface density is given by:

$$\Sigma_{\text{d}}(R) = \zeta \, \Sigma_{\text{g}}(R) , \tag{5.2}$$
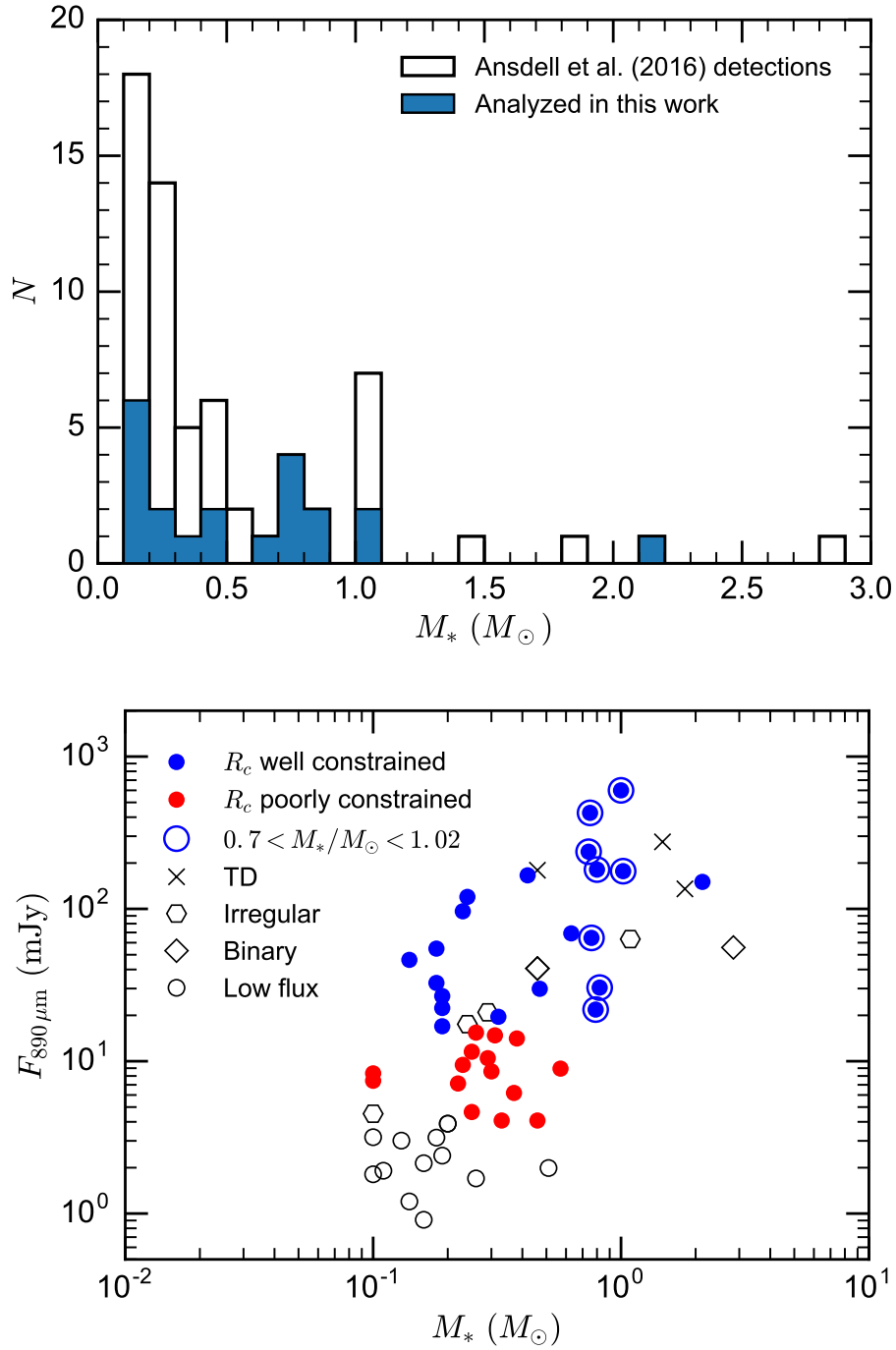
Fig. 5.1 *Left panel:* distribution of stellar mass for the full Lupus sample from Ansdell et al. (2016) (white bars) and for the sub-sample analyzed in this work (blue bars). In the $0.7 - 1.02\,M_\odot$ mass bin the sub-sample is complete. *Right panel:* integrated continuum flux at $890\,\mu$m measured from Ansdell et al. (2016) as a function of stellar mass. Blue and dots represent sources that have been analyzed in this work. In this and subsequent plots, the circled blue dots identify sources in the $0.7 - 1.02\,M_\odot$ mass bin where the sub-sample is complete. The "x" symbols represent the transition disks (TD), i.e. disks with resolved inner holes, hexagons the sources with irregular shape, diamonds the binary sources, empty circles the sources with integrated flux $F_{\rm cont} < 4$ mJy.

Table 5.1   Source properties

Name	RA (J2000)	Dec (J2000)	d	M_*	L_*	SpT	T_{eff}
			(pc)	$M_\odot$	$L_\odot$		(K)
Sz 65	15:39:27.75	-34:46:17.56	150	0.76	0.832	K7	4060
J15450887-3417333	15:45:8.85	-34:17:33.81	150	0.14	0.058	M5.5	3060
Sz 68	15:45:12.84	-34:17:30.98	150	2.13	5.129	K2	4900
Sz 69	15:45:17.39	-34:18:28.66	150	0.19	0.088	M4.5	3197
Sz 71	15:46:44.71	-34:30:36.05	150	0.42	0.309	M1.5	3632
Sz 73	15:47:56.92	-35:14:35.15	150	0.82	0.419	K7	4060
IM Lup	15:56:9.18	-37:56:6.12	150	1.0	1.65	M0	3850
Sz 83	15:56:42.29	-37:49:15.82	150	0.75	1.313	K7	4060
Sz 84	15:58:2.5	-37:36:3.08	150	0.18	0.122	M5.0	3125
Sz 129	15:59:16.45	-41:57:10.66	150	0.8	0.372	K7	4060
J16000236-4222145	16:00:2.34	-42:22:14.99	150	0.24	0.148	M4	3270
MY Lup	16:00:44.5	-41:55:31.27	150	1.02	0.776	K0	5100
Sz 133	16:03:29.37	-41:40:2.14	150	0.63	0.07	K2	4900
Sz 90	16:07:10.05	-39:11:3.64	200	0.79	0.661	K7	4060
Sz 98	16:08:22.48	-39:04:46.81	200	0.74	2.512	K7	4060
Sz 100	16:08:25.74	-39:06:1.63	200	0.18	0.169	M5.5	3057
Sz 108B	16:08:42.86	-39:06:15.04	200	0.19	0.151	M5	3125
J16085324-3914401	16:08:53.22	-39:14:40.53	200	0.32	0.302	M3	3415
Sz 113	16:08:57.78	-39:02:23.21	200	0.19	0.064	M4.5	3197
Sz 114	16:09:1.83	-39:05:12.79	200	0.23	0.312	M4.8	3175
J16124373-3815031	16:12:43.73	-38:15:3.4	200	0.47	0.617	M1	3705

Notes. Distances: for stars in the Lupus I, II and IV clouds $d = 150\,\text{pc}$, while for stars in the Lupus IV cloud $d = 200\,\text{pc}$ (see Comerón 2008). Stellar parameters L_*, T_{eff} and SpT are derived from X-Shooter measurements by Alcalá et al. (2014). Stellar masses are the same used in Ansdell et al. (2016), obtained using evolutionary tracks by Siess et al. (2000).

where ζ is the dust-to-gas mass ratio, assumed to be constant and equal to the typical ISM value $\zeta = 0.01$. The choice of the profile in Eq. (5.1) and of a constant dust-to-gas ratio are a clear simplification of reality, in which we expect ζ to change across the disk from both observational (de Gregorio-Monsalvo et al. 2013) and theoretical (Birnstiel and Andrews 2014) arguments. However, since in this study we are only analyzing the dust continuum emission (we cannot pose any constraint on the actual gas-to-dust variations in the disks), these choices are useful as they provide us with a simple parametrization of the dust distribution that we can directly compare to other studies. As a result, there are three free parameters describing the surface density: Σ_0, γ and R_c.

To compute the continuum emission we compute the dust opacity of the grain population using the Mie Theory (which allows us to compute the emissivity of a single spherical grain) and the Bruggeman mixing theory (Bruggeman 1935, which allows us to compute the effective dielectric constants for composite grains). For both the disk surface and midplane we use a MRN-like grain size distribution (Mathis et al. 1977), i.e. a number density $n(a) \propto a^{-q}$ for $a_{\min} \leq a \leq a_{\max}$ and $n(a) = 0$ otherwise, where a is the grain radius. In the surface layer we use $a_{\min} = 10\,\mathrm{nm}$ and $a_{\max} = 1\,\mu\mathrm{m}$ with $q = 3.5$, typical of a population of small grains (this ensures that the surface layer is optically thick to the stellar radiation). In the disk midplane, where dust coagulation and settling are expected to occur (Dullemond and Dominik 2004), we use $a_{\min} = 10\,\mathrm{nm}$ and $a_{\max} = 1.023\,\mathrm{cm}$ with $q = 3.0$, which corresponds to a population of larger grains and reproduces the same opacity (per gram of dust) used by Ansdell et al. (2016), namely $\kappa_{890\,\mu\mathrm{m}} = 3.37\,\mathrm{cm}^2/\,\mathrm{g}$. Similarly to Trotta et al. (2013) and Tazzari et al. (2016), we assume spherical grains and we adopt the simplified volume fractional abundances found by Pollack et al. (1994): 20.6% carbonaceous materials, 5.4% astronomical silicates, 44% water ice and 30% vacuum, for an average grain density of $0.9\,\mathrm{g}/\,\mathrm{cm}^3$.

Finally, the disk appearance on sky is set by the disk inclination along the line of sight, defined as $i = 0°$ for a face-on disk and $i = 90°$ for an edge-on disk, and by the disk Position Angle, defined East-of-North from $P.A. = 0°$ to $P.A. = 180°$.

5.2.2 Disk flaring

Computing a realistic dust temperature profile is key for a reliable estimate of their sub-mm continuum emission and therefore of their mass. The self-consistent fully-flared models based on the two-layer approximation (Chiang and Goldreich 1997; Dullemond et al. 2001) are typically too vertically thick and do not properly reproduce the spectral energy distribution in the far-IR. This is confirmed by theoretical and observational studies (refs) that require a reduced disk flaring (i.e., some degree of dust settling) in order to reconcile the far-IR and the sub-mm fluxes. Daemgen et al. (2016) use the ratio between the far-IR and the J-band[1] fluxes as a proxy for the disk flaring. With a spectroscopic study of disks around very low mass T Tauri stars and brown dwarfs they find that the dust temperature strongly depends on the disk flaring (in addition to stellar luminosity), and to a lesser degree on the disk mass and other disk properties. In this work we use the spectral slope between the far-IR and the J-band to obtain a rough estimate of the disk flaring that characterizes the disks in our sample. Since the spectroscopic measurements are not available for all the sources in our sample, we derive an average disk flaring reduction factor that we use for all the fitted sources.

To this purpose, we use Herschel/PACS measurements at 70, 100 and 160 μm from

---

[1]A good proxy for the stellar photospheric emission.
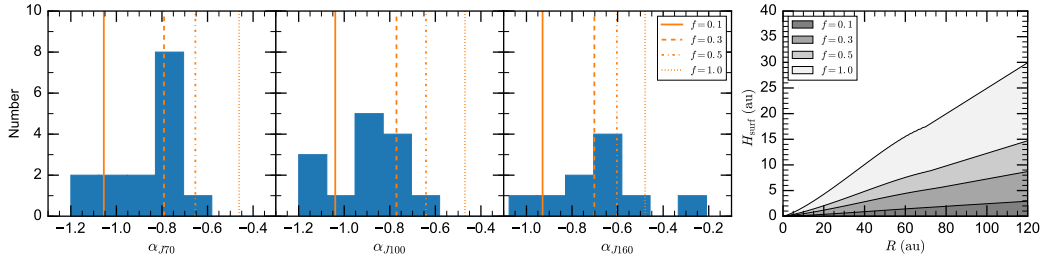
Fig. 5.2 *Left:* spectral indices for the sources in our sample measured between J-band (2MASS, 1.235 μm) and, respectively, 70 μm, 100 μm, 160 μm (Herschel/PACS) using the definition in Eq. (5.3). The vertical lines show the spectral indices obtained with our disk model for different values of the flaring parameter iflar, from a fully-flared model ($f = 1$, dotted line) to less flared models ($f = 0.5, 0.3, 01.$, respectively dash-dotted, dashed and solid line). *Right:* scale-height of the disk surface layer computed by the model.

(refs). We compute the spectral slope between the Herschel/PACS bands and the 2MASS J-band (1.235 μm) as (Adams et al. 1987; Daemgen et al. 2016):

$$\alpha_{\lambda_1 \lambda_2} = \frac{\log(\lambda_1 F_{\lambda_1} / \lambda_2 F_{\lambda_2})}{\log(\lambda_1 / \lambda_2)} \, , \tag{5.3}$$

which provides a model-independent estimate of the far-IR dust emission. In Figure 5.2 we present the histograms of the computed spectral slopes. On the same histograms the orange vertical lines represent the spectral slopes computed from our disk model for different values of the flaring reduction parameter f. By varying this parameter we can manually reduce the disk flaring from a fully-flared profile ($f = 1$), which produces flatter spectral slopes ($\alpha \geq -0.5$), to progressively less flared models ($f < 1$), which produce progressively steeper spectral slopes ($\alpha \leq -0.5$). By comparing the synthetic and the observed spectral slopes we find that a disk flaring reduced by a factor ≈ 3 ($f = 0.3$) gives a good representation of the slopes at all the three bands simultaneously. We adopt this value for all the fits that we perform in this study.

5.2.3   Modeling methodology

We perform the fits with a bayesian approach, which produces probability distribution functions (PDFs) for the free parameters of the model by means of a Markov Chain Monte Carlo (MCMC) algorithm. The free parameters are seven: Σ_0, γ and R_c which define the surface density, i and $P.A.$ which define the disk appearance, $\Delta\alpha$ and $\Delta\delta$ which define the (R.A., dec) offset of the disk center with respect to the phase center of the observations. We consider these last two parameters as *nuisance parameters*: for each disk we fit the disk center to achieve a better matching between model and observations, however the information encoded in such offset is not relevant for the aims of this study[2].

Following the implementation developed by Tazzari et al. (2016), for a given set of values of the free parameters the model produces a synthetic image of the disk that is then Fourier-transformed and sampled in the same $(u, v)-$locations of the observed visibilities.

---

[2]In principle it is possible to relate the fitted offsets to the proper motion of each single object as shown in Tazzari et al. (2016), but this is beyond the scope of this chapter.

We finally compute the χ^2 as:

$$\chi^2 = \sum_{i=0}^{N} w_i |V^{\mathrm{obs}}(u_i, v_i) - V^{\mathrm{mod}}(u_i, v_i)|^2 \,, \tag{5.4}$$

where V^{obs} and V^{mod} are the observed and the synthetic visibilities, respectively, w_i is the weight associated to the observed visibilities at the (u_i, v_i) location[3], and N is the total number of (u, v)−locations. The posterior PDF is computed as $\exp(-\chi^2/2)$ within a rectangular domain in the parameter space (the region of interest), and zero outside such domain. The ranges defining the domain of exploration of the parameter space are detailed in Table 5.2.

Table 5.2   Parameter space explored by the Markov chains.

Parameter	Min	Max
γ	-2	2
Σ_0	$0.05\,\mathrm{g/\,cm^2}$	$400\,\mathrm{g/\,cm^2}$
R_{c}	2 au	400 au
i	$0°$	$90°$
$P.A.$	$0°$	$180°$
$\Delta\alpha$	-2"	+2"
$\Delta\delta$	-2"	+2"

The region of interest in the 7-dimensional parameter space is explored using an ensemble of Markov chains that evolve simultaneously according to the affine-invariant MCMC algorithm by (Goodman and Weare 2010). Two of the main advantages of using this algorithm are: first, the several chains are initialized in random locations across the domain of interest, thus ensuring that the PDFs that we derive after they have converged do not depend on their initialization. Second, the algorithm enables a massive parallelization of the computation[4]: in a reasonable amount of time it allows us to achieve a rather solid sampling of the posterior PDF out of which we can derive reliable PDFs for all the parameters.

In this study, we perform the fits using one hundred chains, which is a reasonable number for a seven-dimensional parameter space (approx. 10-20 walkers[5] per parameter). We initialize the chains in random positions in the domain of interest, making sure that they are not initialized too close to the borders in order to avoid computational issues. After initialization, we let the chains evolve for a burn-in phase of 1000-1500 steps (the actual number varies from source to source) and then we take 4000-5000 steps to achieve a good sampling of the posterior PDF. This results in approximately 500-700 thousands evaluations of the posterior for the fit of each disk.

---

[3]Following Tazzari et al. (2016), the weights are calculated from theoretical arguments according to Wrobel and Walker (1999) and then re-scaled to ensure that $\sum_i w_i = 1$.

[4]The evolution of half of the chains can be computed simultaneously, thus implying that a single step of the whole ensemble takes just twice as long as the time needed to evolve one chain (provided that the fit is executed on a number of processes at least equal to half the number of chains).

[5]In the MCMC terminology for the ensemble sampling Goodman and Weare (2010), a *walker* is one of the Markov Chains of the ensemble.

The product of a MCMC fit is the chain that results from collecting the locations of all the walkers throughout their evolution. Each element of the chain represents a sample of the posterior PDF. Therefore, to give an adequate representation of the results of the fit we always provide a plot of the chain, projected in the various dimensions. By marginalizing[6] the chain over one parameter we obtain an estimate of its PDF, out of which we derive its value as the median and uncertainty as the central interval (between 16% and 84% percentiles). By marginalizing the chain over two parameters of interest we obtain the 2D distribution of the samples from which we can study their correlation.

To perform the fit we use the implementation of the MCMC algorithm provided by the Python package ᴇᴍᴄᴇᴇ (Foreman-Mackey et al. 2013), which allows us to exploit the massively parallel nature of the algorithm by running the fits on many cores simultaneously. For this study, we use the computing facilities hosted at the Computational Center for Particle and Astrophysics (C2PAP).

5.3   Modeling results

In this section we present the results of the fits. Here we show the results for Sz 71 to present the analysis that we performed for each disks, while the detailed plots of all the other fits are reported in the Appendix D.

The staircase plot in Figure 5.3 shows the Markov chain resulting from the fit of Sz 71. On the main diagonal we show the histograms of the marginalized distribution, with vertical dashed lines indicating the 16th, 50th and 84th percentiles. The distributions are single-peaked, with profiles very close to Gaussians. For Sz 71 we find the following best fit parameters: $\gamma = 0.27 \pm 0.01$, $\Sigma_0 = 16.2 \pm 0.25\,\mathrm{g/cm^2}$, $R_c = 85 \pm 1\,\mathrm{au}$, $i = 40.8 \pm 0.7°$ and $P.A. = 37.5 \pm 0.1°$. The off-diagonal 2D plots represent the bivariate distributions between each pair of parameters which provide an immediate estimate of their correlation. The red lines highlight the location of the best-fit model, which has been chosen among the models with lowest chi-square.

A description of the physical structure of the best fit model for Sz 71 can be found in Figure 5.4, where we plot the gas surface density and cumulative mass (left panel), the midplane temperature (middle panel) and the optical depth of the disk midplane at the observing wavelength (right panel) as a function of the distance from the star. In all plots, we highlight the radius containing the 95% of the mass as a vertical dotted red line. The disk model for Sz 71 has a very flat ($\gamma \sim 0$) surface density profile in the inner disk and a sharp exponential cut-off at $R_c \sim 85\,\mathrm{au}$, with 95% of the mass contained within 150 au. The disk is optically thin at 890 μm almost everywhere, except in the inner $R < 2.6$ au region which, anyway, gives a negligible contribution to the total mass. The midplane temperature decreases monotonically from 325 K in the innermost disk region ($R \sim 0.1$ au) to ~ 10 K at 100 au and then levels to 7 K, which is the minimum temperature allowed in the model, chosen to give a simple realization of the typical interstellar radiation field.

Figure 5.5 is a visual representation of how the distribution of models (i.e. the posterior samples shown in Figure 5.3) compare with the observations. The top (bottom) panel shows the Real (Imaginary) part of the deprojected observation and model visibilities as a function of baseline length. The observation and model visibilities have been centered on the disk centroid (according to the fitted offsets $\Delta\alpha$ and $\Delta\delta$) and then de-projected assuming the fitted values of i and $P.A.$. Of the model visibilities we show the posterior PDF (as

---

[6]Integrating over all but the one (the two) parameter (parameters) of interest.
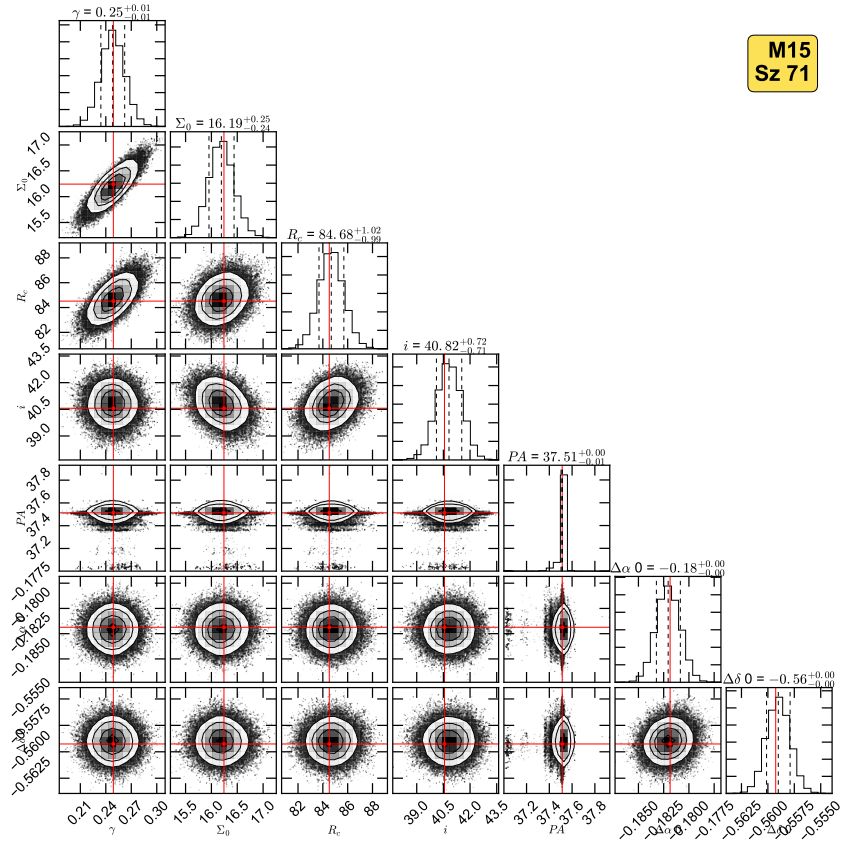
Fig. 5.3 Staircase plot of the chain resulting from the MCMC fit of Sz 71. The histograms on the main diagonal are the marginalized distributions of each parameter (from left to right, γ, Σ_0, R_c, i, $P.A.$, $\Delta\alpha$, $\Delta\delta$, respectively) with vertical dashed lines indicating the 16%, 50% and 84% percentiles. The off-diagonal 2D plots show the correlation between each couple of parameter, with contour lines showing 0.5σ increments. The red solid lines highlight the coordinates of the best-fit model.
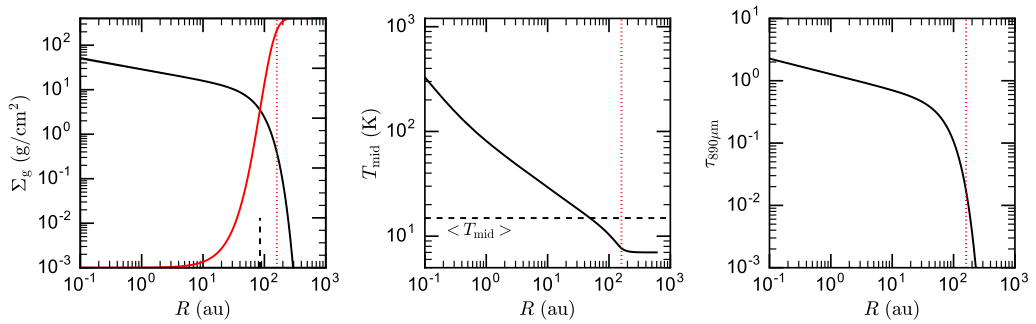
Fig. 5.4 Physical structure of the best-fit model describing Sz 71. *(left)*: surface density profile $\Sigma_g(R)$, with the dashed vertical line highlighting the cut-off radius $R_c \simeq 85\,\mathrm{au}$. *(middle)*: dust temperature profile $T_{\mathrm{mid}}(R)$ derived self-consistently at each radius given the stellar properties and $\Sigma_g(R)$. The dashed horizontal line represents the mass-averaged dust temperature $< T_{\mathrm{mid}} > \simeq 14\,\mathrm{K}$. *(right)*: optical depth of the disk midplane at the observing wavelength: the sub-mm continuum emission is expected to be optically thick only in the inner most $R < 2\,\mathrm{au}$ (highlighted by the dashed line).
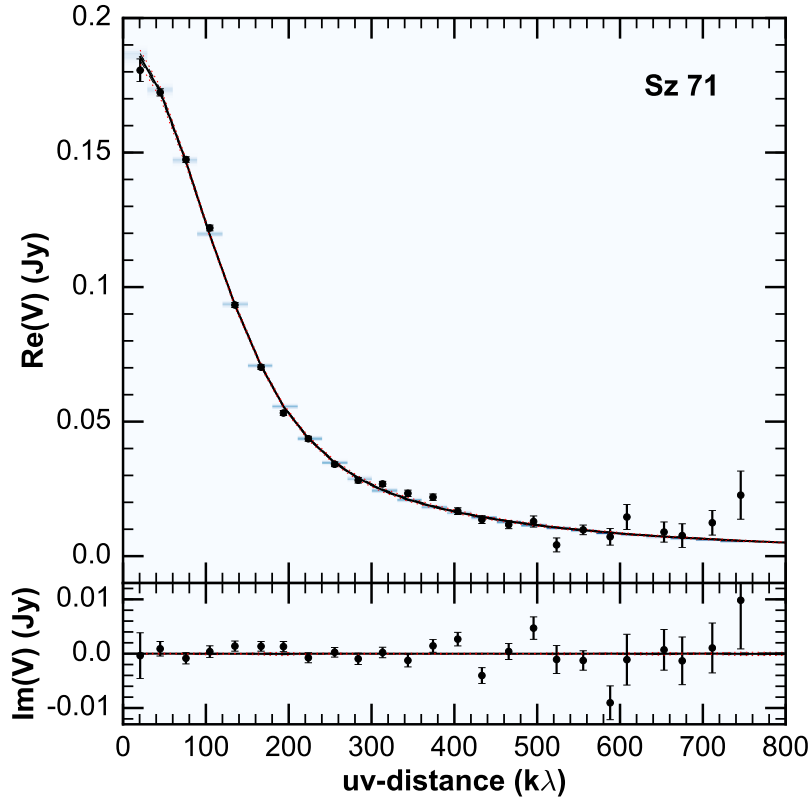
Fig. 5.5 Comparison between model and observed visibilities of Sz 71 as a function of deprojected baseline length (uv-distance). The panel above (below) shows the Real (Imaginary) part of the visibilities. Black dots show the observed visibilities (binned every 30kλ), the blue density indicators represent the PDF of the model visibilities in each uv-bin. The black solid line corresponds to the median of the model visibilities PDF, the black dashed lines the 16th and 84th percentiles, the red dotted lines the 2.7th and 97.7th percentiles.

the blue density indicator for each uv-bin), the median (black solid line), the 1σ central interval (the black dashed lines) and the 2σ central interval (the red dotted lines). In the case of Sz 71 the posterior PDF of the model visibilities has a very narrow peak, therefore these lines are very close to the median (cfr. with the broader model visibilities PDF derived for some disks in Appendix D). The Real part of the observation and model visibilities match almost perfectly up to 300 kλ and are compatible within 2σ at higher uv-distances. The Imaginary part of the model visibilities is on average 0 (as it should be for a centered azimuthally symmetric surface brightness distribution) with a residual oscillating behaviour at very low signal to noise level, probably due to some sort of asymmetry in the disk that cannot be described by our axis-symmetric disk model.

In Figure 5.6 we compare the observation to the best-fit model images. The three panels illustrate the images of the observations, of the model and of the residuals, derived from the respective visibilities with the CLEAN algorithm (Clark 1980) and a natural weighting scheme using the software CASA 4.5.0. The best-fit model (whose location in the parameter space is highlighted in Figure 5.3) reproduces the observations extremely well (the residuals being lower than the 3σ level).

In Table 5.3 we report the values of the parameters derived for Sz 71 and for all the
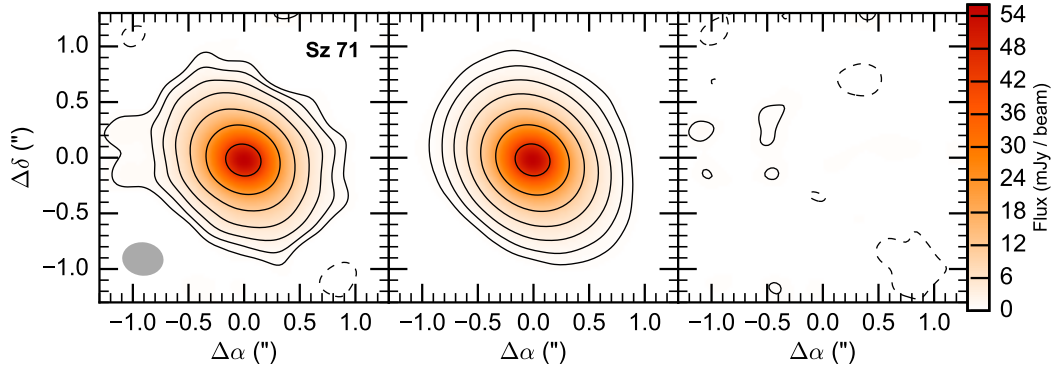
Fig. 5.6 Comparison between the observed *(left)* and the best-fit model *(middle)* images for Sz 71. Residuals are shown in the right panel. The best-fit model has the following parameters γ... The three images have been produced by applying the CLEAN deconvolution algorithm with natural weighting to the observed, best-fit model and residual visibilities, respectively. Contour levels refer to -3, 3, 6, 12, 24, 48, 50, 100, 150, etc. multiple of the rms, which here is $\sigma = 0.3$ mJy/beam. The FWHM of the synthesized beam is shown as a grey ellipse in the left panel.

other disks. For each disk, we provide estimates of the free parameters γ, Σ_0, R_c, i and $P.A.$, derived from the Markov chains as described in Section 5.2.3. From the chains, we also compute some derived quantities such as the disk outer radius R_{out}, defined as the radius containing 95% of the model flux, and the total dust mass M_{dust}, computed by integrating the dust surface density:

$$M_{\mathrm{dust}} = \int\limits_{R_{\mathrm{in}}}^{R_{\mathrm{out}}} \Sigma_d(R)\, 2\pi R\, \mathrm{d}R\,, \tag{5.5}$$

where $R_{\mathrm{in}} = 0.1$ au is the inner edge of the radial grid of the model (fixed for all the disks). The derived quantities are estimated in two steps: first, we build a PDF of the derived quantity by computing it for each sample of the Markov chain and then we estimate it as the median of its distribution, assigning an uncertainty that corresponds to the central interval between the 16th and 84th percentile.

For all the 21 disks in the sample the Markov chains converged to single-peaked distributions with moderate to absent degeneracy. In all these cases, the best-fit model has usually a normalized chi-square of 1.0 ± 0.2 and the residuals are at very low signal-to-noise levels. We note, however, that two disks (IM Lup and Sz 98) display a significant level of ring-shaped residuals that cannot be explained by our model. Ring-like structures might be produced by several processes, either linked to the dynamics of the disk (e.g., planet formation) or to the physical conditions in the disk (e.g., gas condensation). For these disks, a more detailed analysis is required to assess the physical process that originates such structures (Guidi et al. 2016).

5.3.1 Comparison with Ansdell et al. (2016)

We now compare our results with those by Ansdell et al. (2016), who derived dust masses and disk inclinations with a simplified method.

First, in Figure 5.7 we compare the dust masses: the plot shows the ratio between the masses derived from our fits and those derived by Ansdell et al. (2016) by converting the

Table 5.3   Value of free parameters and derived quantities for all the disks.

Name	γ	Σ_0 g/cm^2	R_c au	i °	$P.A.$ °	R_{out} au	M_{dust} $M_\oplus$
Sz 65	0.12 ± 0.24	20.71 ± 2.95	28.03 ± 0.56	61.46 ± 0.88	108.63 ± 0.37	42.39 ± 2.96	16.07 ± 0.61
J15450887-3417333	-0.72 ± 0.70	104.05 ± 42.70	16.13 ± 1.08	36.30 ± 5.56	2.41 ± 2.53	23.43 ± 1.23	32.19 ± 7.86
Sz 68	-0.39 ± 0.27	188.99 ± 80.18	14.04 ± 0.96	32.89 ± 3.32	175.78 ± 3.13	23.03 ± 0.40	40.05 ± 12.32
Sz 69	0.72 ± 0.21	50.24 ± 18.02	9.11 ± 2.00	43.53 ± 8.65	124.28 ± 17.10	18.04 ± 1.60	7.59 ± 1.84
Sz 71	0.25 ± 0.01	16.19 ± 0.24	84.68 ± 1.00	40.82 ± 0.71	37.51 ± 0.01	127.14 ± 1.12	80.21 ± 1.01
Sz 73	1.00 ± 0.17	10.94 ± 1.10	43.47 ± 7.43	49.76 ± 3.95	94.71 ± 5.17	79.41 ± 19.36	9.32 ± 1.20
IM Lup	0.65 ± 0.00	22.25 ± 0.10	431.74 ± 6.81	48.40 ± 0.11	144.37 ± 0.00	504.01 ± 0.00	439.46 ± 3.76
Sz 83	0.40 ± 0.09	151.83 ± 28.03	36.18 ± 1.32	3.31 ± 2.90	163.76 ± 5.94	64.42 ± 1.12	160.76 ± 11.49
Sz 84	-0.98 ± 0.20	3.04 ± 0.46	40.57 ± 1.10	73.99 ± 1.56	167.31 ± 0.77	52.26 ± 2.26	13.83 ± 0.54
Sz 129	-0.33 ± 0.02	18.43 ± 0.38	50.25 ± 0.39	31.74 ± 0.75	154.94 ± 0.43	70.29 ± 1.23	70.94 ± 0.56
J16000236-4222145	-0.20 ± 0.02	6.13 ± 0.16	89.60 ± 0.91	65.71 ± 0.36	160.45 ± 0.02	129.38 ± 2.26	72.56 ± 0.75
MY Lup	-0.59 ± 0.06	9.85 ± 0.66	60.67 ± 0.62	72.98 ± 0.35	58.94 ± 0.12	85.14 ± 0.74	86.05 ± 2.06
Sz 133	-0.17 ± 0.16	14.25 ± 6.01	66.77 ± 2.39	78.53 ± 0.65	126.29 ± 0.09	108.68 ± 4.78	91.73 ± 11.82
Sz 90	-0.68 ± 0.80	6.36 ± 2.73	29.07 ± 2.21	61.31 ± 5.34	123.00 ± 4.86	38.18 ± 5.23	8.31 ± 0.46
Sz 98	0.11 ± 0.01	5.06 ± 0.10	198.93 ± 2.80	47.10 ± 0.70	111.58 ± 0.06	278.62 ± 4.86	153.91 ± 2.75
Sz 100	-1.52 ± 0.01	1.31 ± 0.03	59.99 ± 0.65	45.11 ± 0.97	60.20 ± 0.06	74.06 ± 1.29	42.53 ± 0.61
Sz 108B	-0.06 ± 0.52	9.08 ± 2.57	40.12 ± 4.93	49.09 ± 5.34	151.76 ± 6.05	55.55 ± 10.59	15.64 ± 0.88
J16085324-3914401	0.20 ± 0.86	46.56 ± 49.69	15.76 ± 3.76	60.72 ± 4.00	100.31 ± 5.47	25.57 ± 3.18	14.60 ± 11.15
Sz 113	-0.16 ± 0.59	81.09 ± 38.54	14.96 ± 1.85	10.78 ± 9.19	147.36 ± 14.20	22.24 ± 1.37	19.95 ± 4.61
Sz 114	0.23 ± 0.03	21.01 ± 0.54	60.71 ± 0.87	15.84 ± 3.39	148.73 ± 6.87	89.71 ± 1.56	58.30 ± 0.73
J16124373-3815031	0.65 ± 0.83	24.85 ± 15.94	21.85 ± 4.32	43.69 ± 7.39	22.99 ± 8.85	37.52 ± 7.64	11.44 ± 3.67

Notes. For disks in bold-face the marginalized distributions are single-peaked and allowed us to estimate the parameter values and a reliable best-fit model. For disks not in bold-face we are not able to derive some of the free parameter values. Columns 1-5: quantities directly estimated from the marginalized distribution of each parameter: the value is the median, the error bars represent the extent of the central interval between 16th and 84th percentiles. Columns R_{out} and M_{dust} report two derived quantities: the disk outer radius (defined as the radius containing 95% of the model flux) and the total dust mass (computed as in Eq. 5.5), respectively.
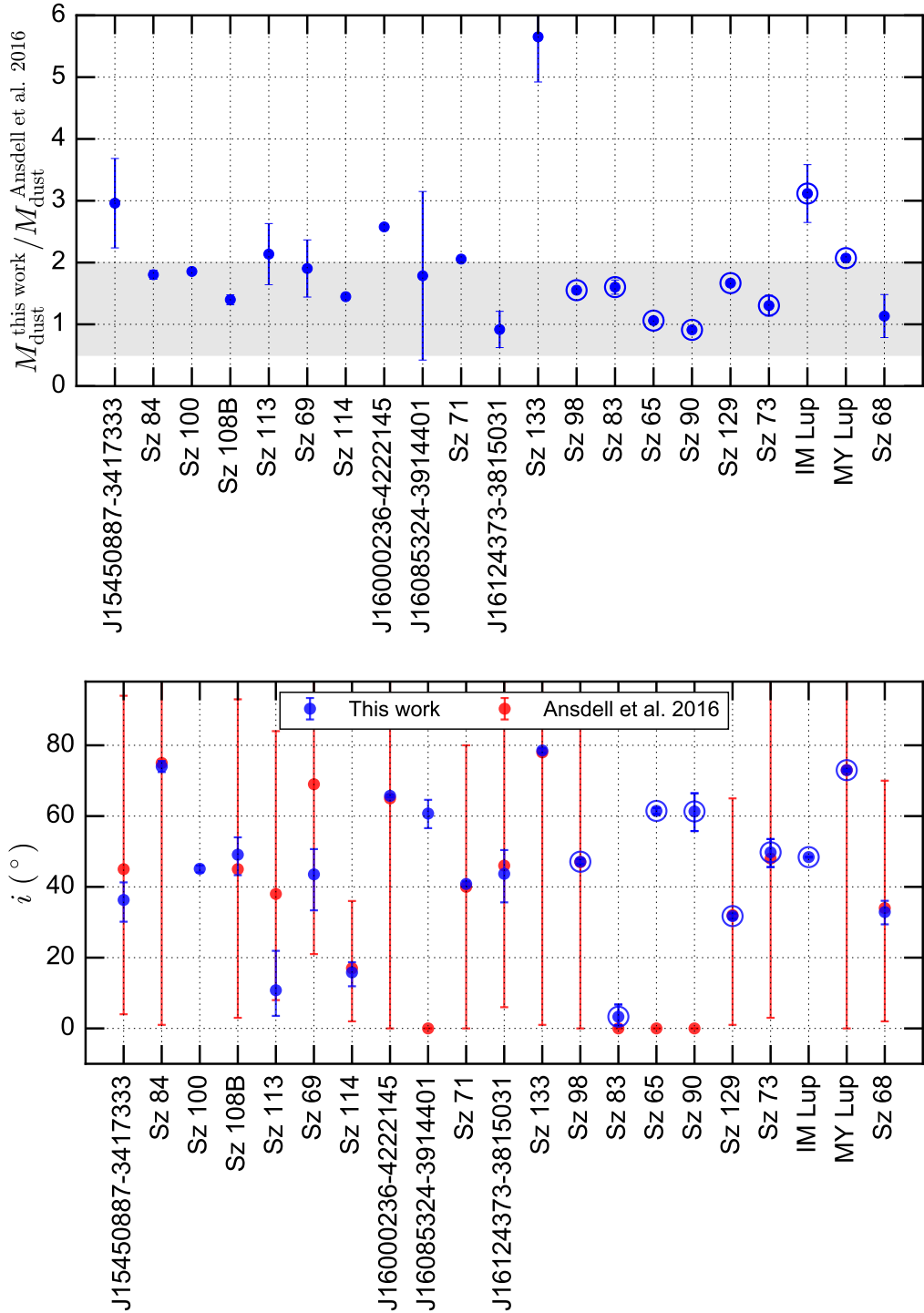
Fig. 5.7 *(top)*: Ratio between the dust masses derived in this work and those derived by Ansdell et al. (2016). Although derived with very different methods (for a detailed description, see the text), the masses are within a factor of 2 for the vast majority of disks. The disks are sorted from left to right by increasing stellar mass. *(bottom)*: Comparison between the disk inclinations i (along the line of sight) obtained in this work and those derived by Ansdell et al. (2016). The disks are sorted from left to right by increasing stellar mass.

spatially-integrated sub-mm continuum flux F_ν into dust mass:

$$M'_{\mathrm{dust}} = \frac{d^2 F_\nu}{\kappa_{890\,\mu\mathrm{m}} B_\nu(T_{\mathrm{d}})} \,, \tag{5.6}$$

where d is the distance, $\kappa_{890\,\mu\mathrm{m}} = 3.37\,\mathrm{cm}^2/\mathrm{g}$ (per gram of dust) is the dust opacity, $B_\nu(T)$ is the black-body brightness at the temperature T, and $T_{\mathrm{d}} = 20\,\mathrm{K}$ is the dust temperature.

Figure 5.7 shows that the dust masses obtained with our fits are in rather good agreement with those obtained by Ansdell et al. (2016). It is remarkable that the simple conversion in Eq (5.6) yields dust masses that are accurate within a factor of 2 at a 1σ level for the majority of disks (15 out of 20).

From Figure 5.7 it is also clear that our mass estimates are systematically larger than those by Ansdell et al. (2016). This discrepancy is not caused by a different dust opacity, as in our fits we assumed exactly the same opacity used by Ansdell et al. (2016). Rather, we interpret the discrepancy to be originated from a different assumption on the dust temperature: while Ansdell et al. (2016) assumed a disk average temperature of 20 K for all the disks in the sample (regardless the spectral type, the mass and the luminosity of the central star), in our fits we use a physical model (based on the two layer approximation, see Section 5.2.1) that takes into account the stellar properties and accurately derives the radial profile of the midplane temperature $T_{\mathrm{mid}}(R)$ by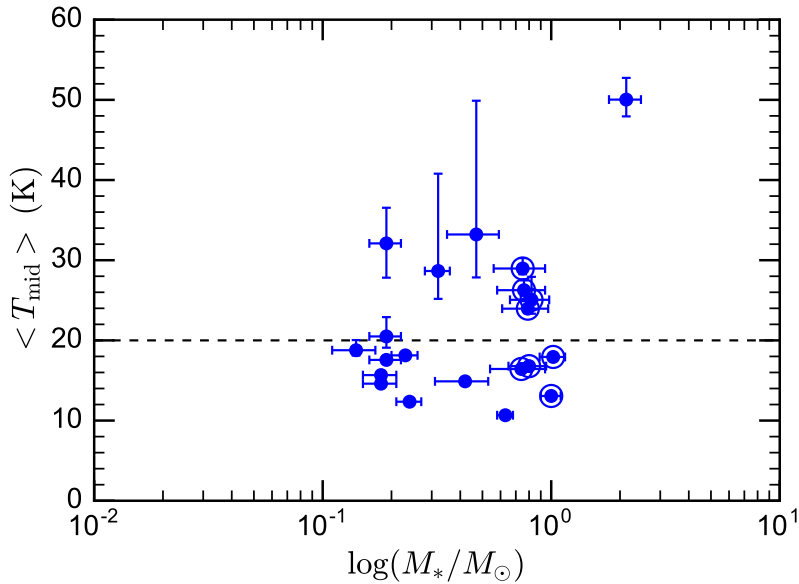 solving the energy balance at each radius. By checking the temperature profiles resulting from our fits, we observe that in many cases (see Figure 5.8) the disk-averaged temperature derived by our physical model is smaller than 20 K (but never smaller than 7 K by definition), thus explaining the tendency towards larger masses that characterizes our estimates.

Fig. 5.8 Mass-averaged midplane temperature as a function of stellar mass for the twenty disks for which we derive a reliable disk structure. Errorbars on the y-axis reflect the distribution of models obtained from the fits. In more than half disks we find a disk temperature smaller than $T_{\mathrm{d}} = 20\,\mathrm{K}$ used by Ansdell et al. (2016) (red dashed line).

In right panel of Figure 5.7 we compare the inclinations derived for all the disks. In

all the cases for which Ansdell et al. (2016) provide a measurement of inclination, their estimate is in complete agreement with ours. Moreover, in substantially all the cases we are able to put a more stringent constraint on the disk inclination, as shown by the much smaller error bars. The improvement in the estimate of the disk inclination is likely due to the fit procedure, which in the case of Ansdell et al. (2016) is based on the CASA procedure *uvmodelfit* with the assumption of a gaussian bightness profile, while in our case benefits of a more extended exploration of the parameter space.
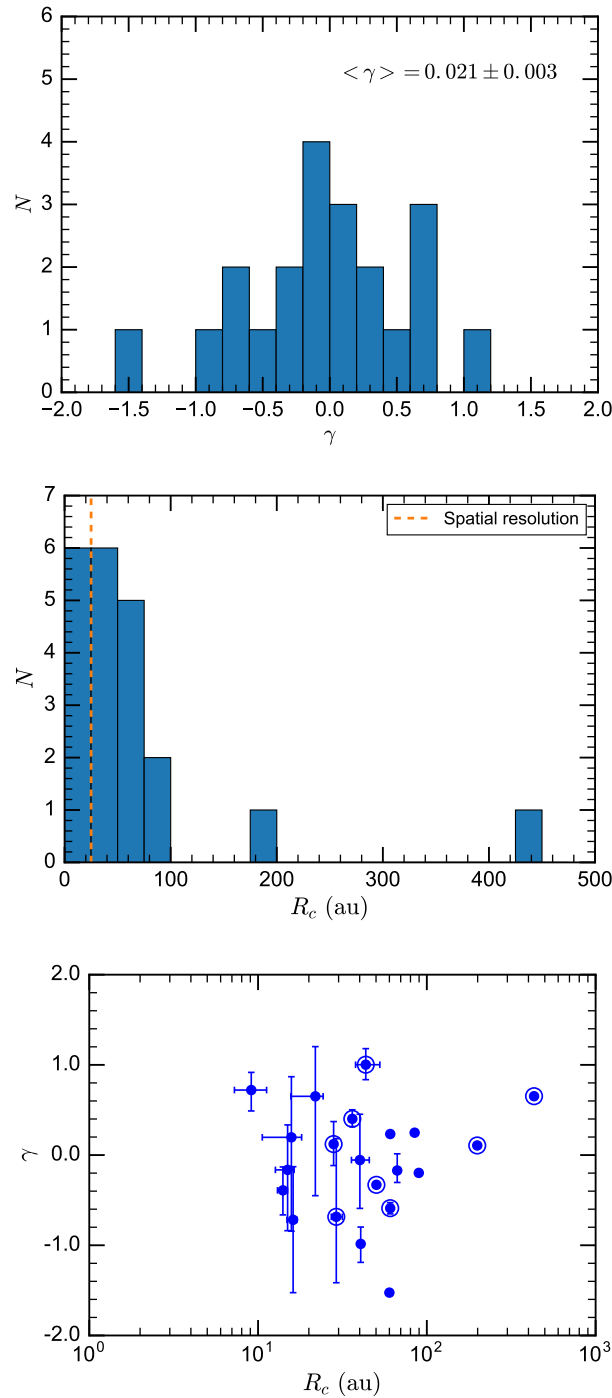
5.3.2 Distribution of slopes and radii

In Figure 5.9 we show the distribution of the cut-off radii R_c (left panel), disk sizes R_{out} (central panel) and slopes γ (right panel) obtained from our fits. The distribution of cut-off radii R_c derived from our fits counts 6 disks with $R_c < 25$ au, 12 disks with 25 au $\leq R_c \leq 75$ au and two much larger disks with $R_c \sim 200$ au (Sz 98) and $R_c \sim 430$ au (IM Lup). The distribution of their sizes (R_{out}) reflects that of R_c: 4 disks are compatible with being unresolved (the inferred size is smaller than the spatial resolution), 14 disks have a size between 25 au and 125 au, the two disks Sz 98 and IM Lup have a size of ~ 280 au and ~ 500 au, respectively. The range of values of R_c that we find is line with the findings of Andrews et al. (2009, 2010) in Ophiuchus (14 au $\leq R_c \leq 200$ au) and Isella et al. (2009) in Taurus-Auriga (30 au $\leq Rc \leq 230$ au) who fitted sub-mm observations of several disks using an exponentially-tapered power law surface density profile as we do here.

The distribution of γ (Figure 5.9, left panel) is centrally peaked around $\gamma = 0$ and has a standard deviation of 0.6. In the right panel of Figure 5.9 we show the distribution of γ as a function of R_c obtained for each disk, showing that there is not any particular trend between these two quantities. We notice that 10 disks are compatible with $\gamma > 0$ and other 10 disks with $\gamma < 0$. Interestingly, among the disks with negative γ, several of them are characterized by large cut-off radii ($40 - 70$ au) that could be a signature of a large cavity.

These findings compare well with the trend that has been emerging in last years thanks to the significant improvement in the observational capabilities in the (sub-)mm window (Williams and Cieza 2011): while low angular resolution observations were usually compatible with large and positive γ values (e.g., $\langle \gamma \rangle \sim 0.9$, Andrews et al. 2009, 2010; $\gamma \sim 0.9$, Hughes et al. 2008) mostly set by the fall-off of the outer disk (the only part clearly spatially resolved by such observations), higher angular resolution observations (capable of resolving the inner 100 au region) reveal that smaller γ values ($\langle \gamma \rangle \sim 0.1$, Isella et al. 2009; $\gamma \sim 0.1$, de Gregorio-Monsalvo et al. 2013) are required in order to reproduce the radial profile of the continuum brightness distribution consistently in the inner and in the outer disk.

It is worth noticing that the surface density profiles have been determined assuming a dust opacity κ_λ that is constant with radius, this choice being justified by the lack of a direct evidence that would call for a different treatment. Since a combination of grain growth and radial drift are expected to produce a size-sorting effect in the grain radial distribution (Birnstiel et al. 2010) with a consequent gradient in the dust opacity, the slope of $\Sigma(R)$ derived here might be shallower than the real one (see the discussion in Trotta et al. 2013). As shown by Tazzari et al. (2016), such degeneracy can be broken by forward-modeling spatially resolved multi-wavelength observations.

Fig. 5.9 Distribution of surface density slopes γ *(top)*, exponential cut-off radii R_c *(middle)* and the correlation between them *(bottom)* derived for the disks in the sample. The vertical dashed line in the top and middle panels gives a visual representation of the spatial resolution of the observations, estimated as half of the synthesized beam size (in our case ~ 25 au at a distance of 150 pc). There is no apparent correlation between γ and R_c. Several disks with negative γ values have large cut-off radii, and this might indicate the presence of a large inner cavity.
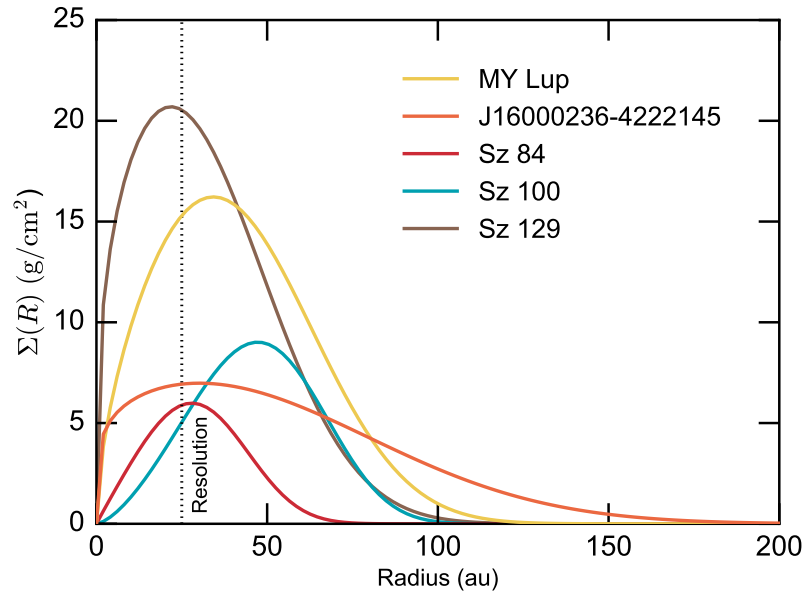
Fig. 5.10 Surface density profiles of the five disks having $\gamma < 0$ at a significance level larger than 3σ. The vertical dashed line gives a visual representation of the spatial resolution of the observations (25 au at 150 pc).

5.3.3 Transition disks

Transition disks are protoplanetary disks that exhibit inner cavities or gaps in their dust and gas distribution. In the observations by Ansdell et al. (2016) three disks already classified as TD were detected with clearly resolved gaps in the continuum emission (2MASS J16083070-3828268, RY Lup, Sz 111), three other sources (Sz 123A, Sz 100 and 2MASS J16070854-3914075) showed marginal evidence for cavities with diameter of 0.4" and six sources (Sz 84, MY Lup, Sz 112, 2MASS J16011549-4152351, 2MASS J16102955-3922144, and 2MASS J16081497-3857145) previously classified as TD did not exhibit any cavity or hole.

As explained in Section 5.1, we decided not to fit the three disks with clearly resolved gaps as we are already sure that their continuum emission cannot be explained with a simple model based on the two-layer approximation. For Sz 100, one of the three sources with possible cavities, we obtain a robust fit with $\gamma = -1.52$ that confirms the presence of an inner hole with radius $R_{\text{hole}} \approx 60$ au. Unlike Sz 100, the other two sources with possible cavities Sz 123A and 2MASS J16070854-3914075 were excluded from our sample, the former because is a binary, the latter because is edge-on. Finally, four out of the six disks classified as TD but with no evidence of cavities in the continuum maps were included in our sample: for Sz 84 and MY Lup we derive a surface density profile with a clear hole ($\gamma = -0.98$ and $\gamma = -0.8$) located respectively at $R_{\text{hole}} \approx 41$ au and $R_{\text{hole}} \approx 60$ au, for 2MASS J16102955-3922144 the fit is more uncertain (marginal evidence of a cavity at $R_{\text{hole}} \approx 60$ au) and for 2MASS J16081497-3857145 we obtain a structure that is compatible with being unresolved. The other two disks classified as TD (Sz 112 and 2MASS J16011549-4152351) were excluded from our sample due to a low integrated flux (below 4 mJy) and due to the lack of stellar parameters, respectively.

In addition to these disks, we also find evidence for the presence of holes in other two
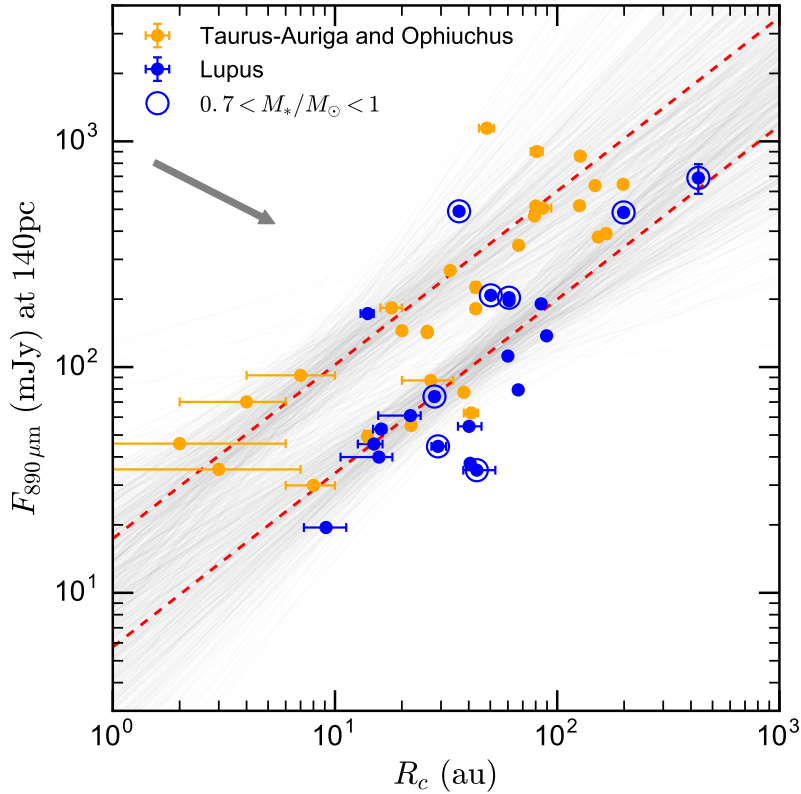
Fig. 5.11   Luminosity-size correlation. For each disk, we plot the flux at 0.88 mm normalized at the common distance of 140 pc. The fluxes $F_{1.3\,mm}$ from literature results have been re-scaled to 0.89 mm assuming an average spectral index $\alpha = 3$. Yellow circles are from the compilation in Andrews (2015). The red dashed lines indicate the correlation found by the bayesian linear regression and the gray lines represent the posterior density of models.

disks not classified as TD (2MASS J16000236-4222145 and Sz 129) for which we find robust estimates of negative γ values, respectively $\gamma = -0.2 \pm 0.02$ and $\gamma = -0.33 \pm 0.02$, and hole sizes of $R_{hole} = 30$ au and $R_{hole} = 20$ au (comparable with the spatial resolution of the observations). The surface density profiles corresponding to such γ values imply the presence of inner holes but the depletion factor inside R_{hole} is expected to be not as high as for $\gamma \leq -1$. We thus conclude that for these two disks the evidence for an inner hole is tentative and to be confirmed with higher angular resolution observations. For a visual representation of the surface density profiles of these disks, see Figure 5.10.

5.4   Discussion

In recent years, (sub-)mm observations of protoplanetary disks at an angular resolution high enough to resolve their structure ($\sim 0.75''$ for nearby SFRs) seem to suggest that fainter disks are also more compact (Andrews et al. 2010; Andrews 2015; Piétu et al. 2014). In order to check if this trend is verified also in the Lupus disks, in Figure 5.11 we show the disk 890 μm integrated flux (rescaled to the common distance of 140 pc) as a function of the disk cut-off radius, which is a direct proxy of the disk size. We compare the results from our fits (blue) with those by Andrews (2015) (yellow), which collected the fits of spatially

resolved (sub-)mm observations of disks in Taurus-Auriga and Ophiuchus from Andrews et al. (2009, 2010); Isella et al. (2010); Guilloteau et al. (2011); Piétu et al. (2014). The first evidence is that the Lupus disks that we fitted in this study are generally characterized by larger cut-off radii and smaller integrated fluxes. This behaviour seems to be consistent throughout the range of cut-off radii between 10 and 200 au. The disks in the $0.7 - 1.0\,M_\odot$ mass range (circled blue dots) in which our sample is complete appear to be distributed randomly, with no clear signs of correlation.

To assess whether the discrepancy between the Lupus and the Tarus-Auriga/Ophiuchus is statistically relevant, we use the Kelly (2007) Bayesian linear regression algorithm[7], which allows us to include uncertainties on both quantities in the computation. Figure 5.11 shows the resulting density of solutions as gray lines and the overall correlation determined by the regression algorithm as red dahsed lines. We infer the following correlations:

$$\log F_{890\,\mu m} = (0.77 \pm 0.18) \log R_c + (0.76 \pm 0.3) \qquad \text{(Lupus)}$$

$$\log F_{890\,\mu m} = (0.77 \pm 0.2) \log R_c + (1.24 \pm 0.2) \qquad \text{(Taurus-Auriga/Ophiuchus)}$$

Remarkably, the presence of an offset in the luminosity-size plane between the two populations is statistically significant at a 2σ level. This is particularly interesting if we consider that the two disk populations have mean ages differing by 1-2 Myr (Lupus being older) and recall that disks evolve by viscous spreading (cfr. Section 2.2): the total disk mass, and therefore the integrated mm flux, decreases with time as it is accreted by the central star, while the outer radius of the disk moves outwards. For the self-similar solutions adopted in this study (Eq. 5.1), it results that the two quantities evolve such that, at any given time, $M_d \propto R_c^{-1/2}$ (combine Eq. 2.16 and 2.17). The gray arrow in Figure 5.11 highlights the slope of the resulting viscous evolutionary track. Since the typical e-folding time of a viscously evolving accretion disk is 5-7 Myr (see Fig. 14 in Hernández et al. 2007), it follows that a difference of 1-2 Myr could induce relevant changes in the disk structure (mass, size). The results that we obtain here provide tentative evidence of these changes, as it seems that the older (3 Myr old) Lupus disks are more *evolved* than the younger (1-2 Myr old) Taurus-Auriga/Ophiuchus disks.

The analysis that we perform on each disk allows their structure (surface density and temperature) to be determined with a self-consistent disk model. Our fits analyzed observations at one wavelength only, therefore a certain degree of degeneracy between these two quantities and the dust opacity chosen is unavoidable[8], however the temperature is derived via a self-consistent resolution of the energy balance within the disk (given the properties of the central star and the local disk properties). This enables us to use the derived surface density profiles to obtain a physically motivated estimate of the total dust mass. In Figure 5.12 we report, for each fitted disk, the dust mass as a function of the cut-off radius (blue circles). To investigate the presence of a correlation between these two quantities we perform the same Bayesian linear regression by Kelly (2007) that we used above. We find a moderate/high correlation ($r = 0.75$) and a best-fitting curve $\log(M_{\text{dust}}) = (0.91 \pm 0.2) \log(R_c)$. The intrinsic scattering of the data is $\sigma = 0.13 \pm 0.05$. In Figure 5.12 the fitted correlation is shown as a red dashed line, while 400 posterior samples (gray lines) give a visual representation of the posterior PDF. In Appendix D (Figure D.1) we report the detailed staircase plot of the complete MCMC chain resulting from

---

[7]We use the linmix Python package which implements Kelly (2007) and is available here: https://github.com/jmeyers314/linmix.

[8]The incoming ALMA observations at 1.3 and 3 mm will help in breaking this degeneracy.
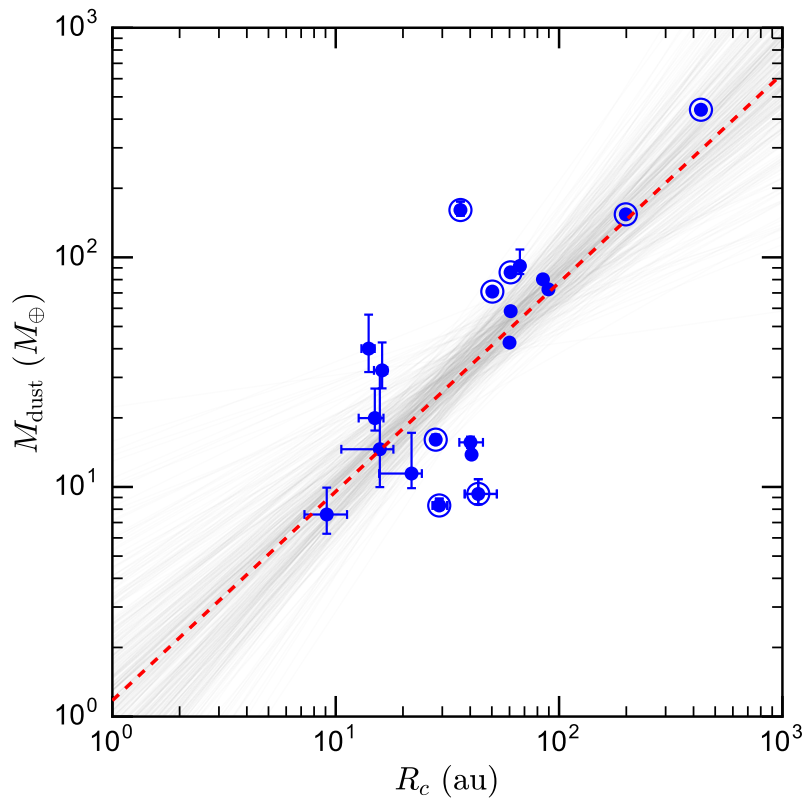
Fig. 5.12 Disk dust mass as a function of cut-off radius. The dust masses are computed from the modeling results by integrating the dust surface density profile. The red dashed line represent the correlation $M_{\rm dust} \propto R_c^{0.91\pm0.20}$ fitted by applying a Bayesian linear regression algorithm (Kelly 2007) to the data. The gray lines are 400 posterior samples and give a visual representation of the posterior PDF.

the Bayesian regression. The correlation that we find is less steep than the $M_d \propto R_c^{1.6\pm0.3}$ found by Andrews et al. (2009, 2010) in Ophiuchus. The difference between the two correlations is significant at a 3σ level and could be due to the different evolutionary stages of the Lupus and Ophiuchus disks. In order to assess whether viscous evolution can explain the discrepancy, further investigations with theoretical models of disk populations are needed.

Finally, in Figure 5.13 we collect the surface density profiles (and cumulative distribution) obtained for all the fitted disks. We compare these profiles with the minimum mass solar nebula (MMSN, Weidenschilling 1977) with the Solar System normalizations by Hayashi (1981). The green curves highlight Σ_g of the disks orbiting stars with stellar mass in the $0.7 - 1\,M_\odot$ range. We note that these curves can thus be directly compared to the MMSN curve, which has been obtained for the primordial disk orbiting around the Sun. In general, the Lupus disks seem to be less massive than the MMSN, only a few of them having a comparable mass. Interestingly, a comparison with the surface density profiles found in Taurus-Auriga/Ophiuchus and collected by Andrews (2015) confirms that the Lupus disks are also less massive than the Taurus-Auriga/Ophiuchus disks, many of them being more massive than the MMSN[9]. This finding would be consistent with the above interpretation of Lupus disks being more viscously evolved, i.e. less massive and more diffused. From these results we conclude that planet formation in the Lupus disks either has already taken place (which would explain the mass depletion) or will be unlikely to occur (most of disks do not seem to have enough mass to produce Solar-System like planets).

5.5 Conclusions

In this chapter we have analyzed the $890\,\mu$m continuum emission of than 20 disks in the Lupus SFR which have been observed with ALMA at $\sim$0.3" ($\sim$50 au) resolution (Ansdell et al. 2016). We have fitted the disk emission the a self-consistent disk model based on the two layer approximation and a realistic dust opacity computation.

For each disk, we derive the dust surface density profile, the temperature profile, and we constrain the disk inclination and position angle. The masses compare well with values derived with the simple flux conversion obtained by by Ansdell et al. (2016). The residual discrepancies are due to the more refined determination of the temperature profile enabled by our model-based analysis. The parameters derived with these fits provide structural constraints on a large set of disks that have been selected from the complete sample of Class II disks in the Lupus SFR. By studying the $890\,\mu$m integrated flux as a function of the disk size we obtain evidence of a correlation. Comparing the derived Lupus luminosity-size relation with the one obtained for Taurus-Auriga/Ophiuchus (Andrews 2015), we find a remarkably consistent offset between the two. This result, obtained in the context of viscous disk evolution, positively correlate with the differing mean ages of Lupus and Taurus-Auriga/Ophiuchus. Finally, we evaluate the potential for planet formation in the Lupus disks: we find them mass-depleted w.r.t. Taurus-Auriga/Ophiuchus, suggesting that either planets have already formed or they are unlikely to form.

The incoming ALMA observations at 1.3 and 3 mm will enable the multi-wavelength analysis developed in Chapter 3 to be appliedL: this will allow us to remove the degeneracies in the physical modeling and a more robust determination of the fundamental properties of the Lupus disks.

---

[9]Note, however, that the Taurus-Auriga/Ophiuchus sample collected by Andrews (2015) tends to select bright sources, while our Lupus sample is a sub-selection of a complete Class II survey.
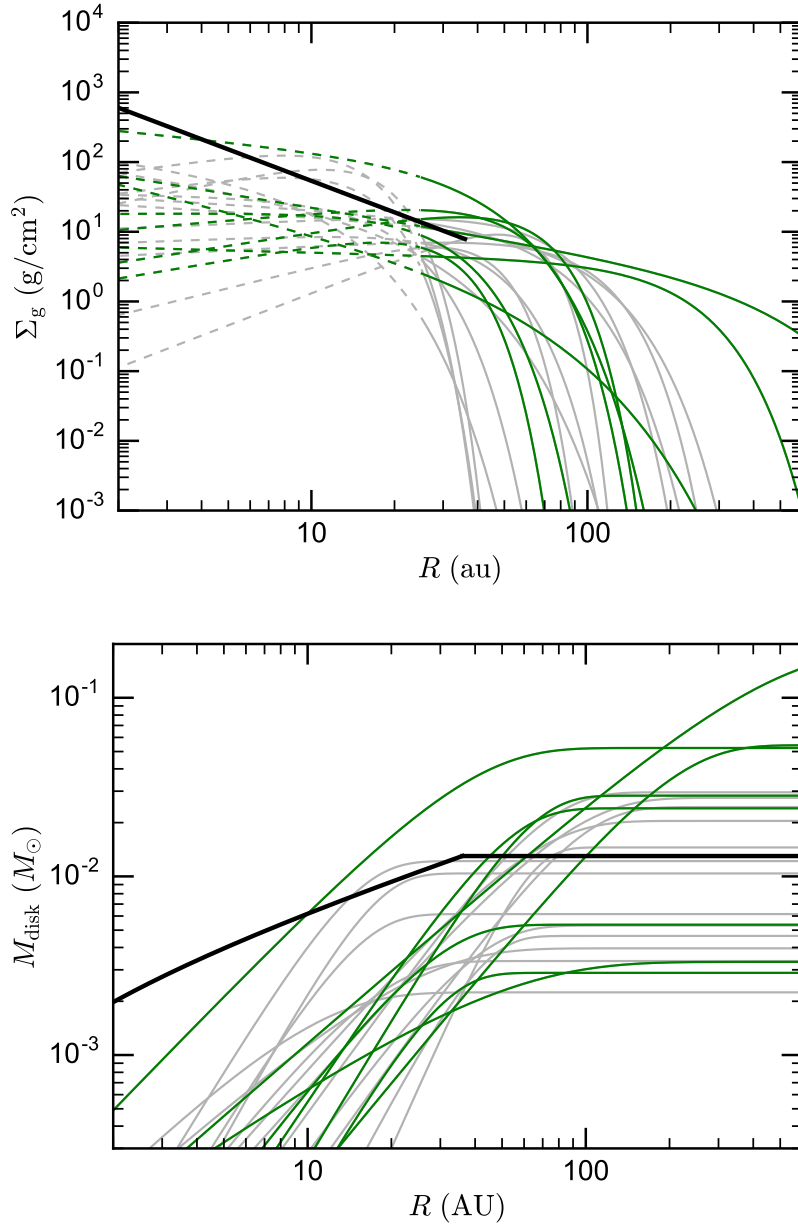
Fig. 5.13 *(top)*: Gas surface density profiles for the disks in the sample (gray curves) compared to the Hayashi (1981) surface density model for the solar system (black thick line). The green curves correspond to the sources in the 0.7-1 $M_\odot$ stellar mass bin. The inferred surface density profiles are dashed where they are not spatially resolved, i.e. for $R < 25$ au. *(bottom)*: The same curves as above, bust expressed in terms of cumulative distribution.

6

GPU-accelerated library for the analysis of interferometric observations

The content of this chapter has to be included in:

> "pyvfit: *a GPU-accelerated library for the analysis of interferometric observations*"
> **Tazzari, M.**, Testi, L., Beaujean, F., to be submitted to A&A.

6.1 Introduction

The advent of modern radio interferometers such as the Atacama large millimeter and submillimeter array (ALMA) and the upgraded Karl J. Jansky Very Large Array (JVLA) have rapidly transformed the landscape of interferometric observations in the sub-mm to cm wavelength window. By combining huge improvements in angular resolution and dramatic enhancements in terms of sensitivity, in the last few years these advanced radio telescopes have been delivering data that transformed many fields of astronomy ranging from protoplanetary disks and signatures of life to gravitational lenses, from the interstellar medium to galaxy clusters.

These new observational facilities offer unprecedented capabilities to investigate - with a very high signal-to-noise ratio - the structure of many sources that only a few years ago appeared as point-like. This is particularly true for protoplanetary disks, the field of research that motivated the development of the tool presented in this chapter and in which we are witnessing new discoveries about the spatial structure of disks on an almost daily basis.

The extreme angular resolution that is now achievable even at mm wavelengths (tens of mas) reveals sources with complex spatial structures that cannot be modeled anymore with a (combination of) simple two-dimensional Gaussians. Rather, it is now apparent that a comparison between the observations and physics-motivated models with varying level of details is the only way to fully exploit the wealth of information encoded in such spatially resolved observations. In the last years this *forward-modeling* technique has been

used with success in an increasing number of studies. The models that are used usually depend on a (preferably small) set of free parameters whose best-fit values are determined either manually (if the model is particularly expensive in computational terms) or by means of dedicated tools such as χ^2 optimizers or Markov Chain Monte Carlo (MCMC) samplers. In all these analyses the depth of exploration of the parameter space depends roughly on three factors: (i) the number of free parameters, (ii) the exploration algorithm, and (iii) the computational effort required to calculate the model and to compare it to the observed data (namely, to compute the likelihood of the data for a given set of values of the free parameters). It is worth noting that, in most cases, the overall time needed to obtain a statistically robust fit is largely set by the time taken by the computation of the likelihood which usually has to be calculated between $\sim 10^4$ to $\sim 10^6$ times (provided that the number of free parameters is not very large - e.g., less than 50 - and the likelihood distribution is well behaved). It follows that a fast and efficient likelihood computation is a crucial requirement for almost any algorithm of parameter space exploration to produce a result on a reasonable time scale.

While single dish telescopes measure the sky brightness directly, interferometers take measurements of its Fourier transform. The fit of interferometric data can be performed either in the *image* or in the *Fourier* plane. In the first case, the synthetic image produced of the model is compared to the image of the sky, which has to be reconstructed from the measurements of its Fourier transform with nonlinear deconvolution algorithms. In the second case, the only image to be processed is the synthetic image of the model, which is Fourier transformed and sampled in the same Fourier space locations where the measurements are available.

When fitting interferometric observations in the Fourier plane, the computation of the likelihood involves a compute-intensive image processing that consists of operations on large matrices and arrays; e.g., the Fourier transform operation, the sampling of the Fourier transformed model brightness in the locations where the measurements are available, etc. If the codes used so far have been able to deal with the complexity set by the size of the current interferometric data sets, there are two major challenges that radio astronomy faces in the next years. A first challenge is provided by the extreme angular resolution achieved by an ever growing number of observations, which translates into the demand for modeling larger and larger portions of the Fourier plane at the same time, which in turn requires the usage of larger and larger matrices and arrays. In addition, the data rate achieved by modern instrumentation is so high that much information delivered by the interferometers has to be time-integrated (e.g., on temporal bins of $\sim$30 s) before it can be handled. A second major challenge is set by the requirements for a multi-wavelength analysis that combines not only the dust continuum emission (Tazzari et al. 2016) but also the gas molecular lines. Indeed, modern receivers mounted on radio interferometers provide us with unprecedented sensitivity and spectral resolution in several wavelength windows allowing us to resolve not only the spatial distribution of the dust and gas content but also their velocity field. The observations taken in the thousands of spectral channels featured by the receivers encode a lot of information about the physical structure of the emitting sources, which however can be constrained only by comparing adequate physical models to such observations.

The observational capabilities of modern radio interferometers put researchers in the condition to address for the first time several specific physics questions, provided that the predictions of the models can be tested against the data in a time-effective way. As long as the observations allow to unveil new structures and new physical effects that were pre-

viously unseen, the complexity of the models has to increase accordingly. This inevitably results in a larger computational effort required to obtain model predictions, which adds to the even more demanding requirements set by the improved observations. It is thus evident that a breakthrough in the computational capabilities is needed in order to deal with the challenges posed by modern radio interferometry and to be able to fully exploit the abundance of information offered by the observations. To this end, in this chapter we provide a way to accelerate the comparison of model predictions to the data, and we do so by leveraging the performances offered by modern computing devices.

In this chapter we develop a computational tool called `pyvfit` that accelerates the calculation of the likelihood in the context of the analysis of interferometric observations. The tool is designed as a library that can be easily imported to accelerate already existing codes and provides a *drop-in* replacement for the function that computes the χ^2 given the synthetic image computed by the model and the interferometric data set. The acceleration is achieved by executing the image processing required by the likelihood computation on graphical processing units (GPUs)[1]. Thanks to their massively parallel architecture, GPUs perform operations on large arrays and matrices much more efficiently than CPUs and therefore constitute the ideal devices to accelerate the imaging processing tasks. In this tool we implement the imaging algorithms using the NVIDIA CUDA specifications that allow the code to run on NVIDIA GPU cards. Platform-independent alternatives are available on the market (OpenACC) but we favored NVIDIA CUDA for two main reasons: first, because nearly all high performance computing (HPC) clusters mount NVIDIA cards; second, because we also need to have fine-grained control on the code for optimum performance.

The acceleration of the likelihood computation achieved by `pyvfit` showcases the advantages of GPU-accelerated computing. This modern computing pattern consists of offloading the compute-intensive routines to the GPU, while the rest of the code is still executed on the CPU. In Section 6.3 we demonstrate that GPU accelerated computing is needed to deal with the challenges in terms of angular resolution and extreme multi-wavelength data sets that radio interferometry is now facing. As an example, we show that using the GPU version of `pyvfit` allows a multi-wavelength data set with 100 wavelengths to be fit by a single GPU (controlled by 16 CPU cores) on the same timescale on which the CPU version (executed on 100 CPU cores) fits a 5 wavelength data set.

Nowadays an increasing number of worldwide computing clusters are designed with hybrid architectures (e.g., the Oak Ridge National Laboratory's TITAN, the Swiss National Supercomputing Centre's Piz Daint, etc.) hosting nodes equipped with many CPU cores (usually 16 or 32) and 1 or 2 GPUs each. Such hybrid architecture and the usage of GPU-accelerated computing allows the clusters to optimize the usage of the resources (with CPUs dedicated to serial tasks and GPUs to massively parallel tasks) as well as the energy consumption. On a smaller scale, in the last years GPU cards have become more accessible in terms of price and selection, thus making it easier to equip single servers with one or two GPUs. In this multi-faceted context, `pyvfit` is a highly flexible tool that is designed to work in a multi-CPU/multi-GPU context. It can be used effortlessly both on a single server or on several nodes, and it automatically exploits the power of all the GPUs that are available on the machines.

The chapter is organized as follows. In Section 6.2 we describe the basic definitions and equations used by `pyvfit`. We also detail the implementation of the GPU version of

---

[1]As opposed to CPUs which consist of a few cores designed for sequential processing, GPUs have a massively parallel architecture that consists of thousands of smaller but more efficient cores designed for executing multiple tasks simultaneously.

the code. The results of the performance tests, with comparison between the CPU and GPU versions, are reported in Section 6.3. In Section 6.4 we draw our conclusions and in Appendix E we give additional details on the code implementation.

6.2   Description of `pyvfit`

Synthesis arrays, or *interferometers*, such as ALMA and JVLA allow us to make images of the sky by measuring the components of its Fourier Transform (FT), usually called *complex visibilities*. The output of an interferometer is a discrete set of samples of the FT of the sky brightness. A model can be fitted to interferometric data in two ways: (a) in the image plane, or (b) in the Fourier plane.

Approach (a) requires to perform the inverse Fourier transform of the complex visibilities by means of nonlinear deconvolution algorithms such as CLEAN (Clark 1980) that allow the image of sky to be reconstructed even though the visibilities are irregularly distributed. This approach is probably more intuitive (it works in the image plane), but is affected (to a non quantifiable extent) by the nonlinear effects introduced by the deconvolution algorithms. Basically, the synthetic brightness produced by a physical model is compared to a *model* of the measurements rather than to the measurements themselves.

Approach (b) embodies a more *forward-modeling* technique: the synthetic brightness produced by the model is Fourier transformed and sampled in the same Fourier-plane locations where the measurements are available so that the resulting comparison between the synthetic visibilities and the observed ones is a proper comparison between model and measurements. In addition to this intrinsic difference, approach (b) should be preferred over approach (a) because the noise of adjacent image pixels is inevitably correlated due to the finite extent of the point-spread-function (PSF) (and therefore requires an adequate consideration of the off-diagonal elements of the covariance matrix), whereas the noise of complex visibilities can be fairly considered uncorrelated (Wrobel and Walker 1999) (thus ensuring that the covariance matrix is diagonal).

In this study we adopt approach (b), namely the fitting in the Fourier domain. We develop a tool to accelerate the computation of the χ^2 between a model image and the observed interferometric data. Before introducing the tool, we recall the fundamental equations of synthesis imaging and define the relevant quantities used in the code.

6.2.1   Basic equations of Synthesis Imaging

To derive the response of an interferometer we first introduce some definitions and a system of coordinates, following standard conventions as in Thompson (1999). Let us call $\vec{b}$ the baseline vector connecting two antennas on the ground and $\vec{s}$ the unit vector (the same for all the antennas) pointing towards the source. It is useful to rewrite $\vec{s} = \vec{s}_0 + \vec{\sigma}$, where $\vec{s}_0$ represents the *phase center* of the synthesized field of view. It is possible to show (Thompson 1999) that the response of the interferometer to a source of brightness I is:

$$V_{\text{obs}}(\vec{b}) = \int_{\Omega_S} \mathcal{A}(\vec{\sigma})I(\vec{\sigma})e^{-2\pi i \nu \vec{b}\cdot\vec{\sigma}/c}\,\mathrm{d}\Omega\,, \tag{6.1}$$

where $\nu = c/\lambda$ is the radiation frequency, $\mathcal{A}(\vec{\sigma})$ is the normalized antenna reception pattern and Ω_S is the angular size of the source as it appears on sky Eq. (6.1) defines the *complex visibility* of the source. The brightness I is a flux density and is therefore measured

in Jy/ sr or Jy per beam area[2]; the visibility V_{obs} is a flux and is measured in Jy. Eq. (6.1) has been derived under the assumption that the brightness I is constant within the bandwidth $\Delta\nu$ of the observations, and that the source is in the far field of the interferometer and is spatially incoherent (i.e., that the contribution to the brightness I from different regions of the source can be considered uncorrelated).

It is useful to define a system of coordinates for the baseline vector (u, v, w), where u points towards the East, v towards the North and w towards $\vec{s}_0$, all of them being measured in units of the observing wavelength λ. Positions on sky have coordinates (l, m), which are the direction cosines computed w.r.t. the u and v axes. An image in the (l, m) plane can be regarded as the projection of the celestial sphere onto a plane tangent to the sphere in $(l, m) = (0, 0)$.

In the assumption of small field imaging it is possible to rewrite Eq. (6.1) as:

$$V_{\mathrm{obs}}(u, v) = \int\limits_{-\infty}^{+\infty} \int\limits_{-\infty}^{+\infty} I(l, m)e^{-2\pi i(ul+vm)}\mathrm{d}l\,\mathrm{d}m\,, \tag{6.2}$$

where we have made the fair assumption that for the primary beam $\mathcal{A}(l, m) \approx 1$ where $I(l, m) \neq 0$ and zero otherwise.

Interferometers measure the visibility function $V_{\mathrm{obs}}(u, v)$ in a discrete set of locations (u_k, v_k), with $1 \leq k \leq M$. In the following, we shall refer to these locations as *sampling points*.

In order to compare a synthetic, or model, brightness $I_{\mathrm{mod}}(l, m)$ produced by a model to the interferometric data we need to compute the synthetic visibilities V_{mod} according to Eq. (6.2):

$$V_{\mathrm{mod}}(u, v) = \int\limits_{-\infty}^{+\infty} \int\limits_{-\infty}^{+\infty} I_{\mathrm{mod}}(l, m)e^{-2\pi i(ul+vm)}\mathrm{d}l\,\mathrm{d}m \tag{6.3}$$

and then to sample $V_{\mathrm{mod}}(u, v)$ at the same sampling points (u_k, v_k) where the observations were taken. Finally, once the synthetic visibility function has been sampled, we can compare it to the measurements by computing the χ^2:

$$\chi^2 = \sum_{k=1}^{M} |V_{\mathrm{obs}}(u_k, v_k) - V_{\mathrm{mod}}(u_k, v_k)|^2\, w_k^2\,, \tag{6.4}$$

where w_k is the theoretical weight associated to the visibility measurement in (u_k, v_k) and is assumed independent from the fit parameters.

We conclude this theoretical section recalling a basic property of the Fourier Transform that becomes particularly useful to fit the location of a source on sky, that is, to find the angular offsets $\Delta\alpha$ and $\Delta\delta$ (right ascension and declination, respectively) between the actual source location and the phase center (α_0, δ_0). In particular, the behaviour of the Fourier Transform under translations allows us to perform a translation in the image plane $I(l, m) \rightarrow I(l - \Delta l, m - \Delta m)$ by simply multiplying the complex visibilities by a phase factor $\exp\left[-2\pi i\left(u\Delta l + v\Delta m\right)\right]$, where $\Delta l = \sin(\Delta\alpha)$ and $\Delta m = \sin(\Delta\delta)$ for sufficiently small imaging fields.

---

[2]The effective area of the synthesized beam.

```python
from package import libgpu_dp  # double precision

# model image
# in this example: point source
Nx = 1024  # matrix size
I_mod = np.zeros((Nx, Nx), dtype='complex128')
I_mod[Nx/2, Nx/2] = 1.0  # [Jy/sr]
cell = 0.01  # cell angular size [arcsec]

# observational data
# u, v: arrays [wavelength]
# Re, Im: arrays [Jy]
# w: array

# angular offsets (optional)
Delta_alpha =  0.5  # [arcsec]
Delta_delta = -2.5  # [arcsec]

# identifier for this execution (optional)
rank = 0

# execution
chi2_dp = acc_lib_dp.chi2(I_mod, cell,
                          u, v, Re, Im, w,
                          Delta_alpha, Delta_delta,
                          rank)
```

Fig. 6.1   Example usage of pyvfit

6.2.2   Usage of pyvfit

pyvfit can be installed via the common pip command and imported as a common Python package, with its functions offering a simple interface to the GPU accelerated routines. Following Figure 6.1 where we show an example usage of the tool, let us analyze the steps needed to execute the chi2 function:

1. We import the double precision version libgpu_dp from the package (to import the single precision one just replace _dp with _sp).

2. For this example, we create a mock model image I_{mod} in a square matrix of size $N_x \times N_x$ and double precision values. We choose the simplest model, i.e. a point source located at the image center. In an actual application, I_{mod} can be whatever brightness distribution the model predicts in the form of an image. I_{mod} has dimensions of a flux density, therefore is measured in Jy/sr. We also specify the cell angular size $\Delta\theta_x$ (in arcsec) to be 0.01 arcsec.

3. The observational data consist of two arrays with the u_k and v_k coordinates of each sampling point (in units of the observing wavelength), two arrays containing the real and imaginary part of the observed visibilities $\mathrm{Re}\, V_{\mathrm{obs}}$ and $\mathrm{Im}\, V_{\mathrm{obs}}$ (in Jy), and an array with the associated weight w_k.

4. As optional parameters, we provide angular offsets $(\Delta\alpha, \Delta\delta)$ (in arcsec) by which the model image has to be translated: if not provided to the chi2 function, they are assumed to be both zero, therefore no translation is executed.

5. Finally, as an additional optional parameter, we specify the rank for this computation, namely an integer number acting as an identifier of this chi2 execution. The

rank parameter is useful when running multi-CPU code on machines with more than one GPU, as it allows to balance the workload on all the available GPUs with minimum programming effort. As an example, for a multi-CPU application using the MPI technology, if rank is set to be equal to the MPI rank, then the package automatically takes care of distributing the parallel executions of chi2 to all the available GPUs. Alternatively, the rank parameter can be used to restrict the chi2 execution to one specific GPU among those available.

Basic requirements for the inputs are as follows. The image of the model brightness $I_{\mathrm{mod}}(l, m)$ has to be provided in the form of a square matrix of size $N_x \times N_x$, with N_x a power of 2 to allow the FFT algorithm to be used. N_x and $\Delta\theta_x$ must be chosen carefully so that the computation of the visibility function V_{mod} on a matrix of same size properly resolves the smallest angular scales (largest spatial frequencies) probed by the observations and encompasses the whole field of view (smallest spatial frequency) covered by the observations. The first condition is met if $\Delta\theta_x \leq 1/\max_k\{(u_k^2 + v_k^2)^{1/2}\}$, and the second if $N_x \geq \max_k\{(u_k^2 + v_k^2)^{1/2}\}/\min_k\{(u_k^2 + v_k^2)^{1/2}\}$, where the maximum and the minimum uv-distances are computed from the coordinates of the M sampling points. Note that, given N_x and $\Delta\theta_x$, in the Fourier space the $N_x \times N_x$ matrix covers an extent given by $|u| < 1/(2\Delta\theta_x)$ and $|v| < 1/(2\Delta\theta_x)$, with the origin of the (u, v) plane located at the pixel coordinate $(N_x/2, N_x/2)$. In order to avoid aliasing effects, it is important to bear in mind such conversions and ensure that the sampling points do not fall close to the matrix borders.

The (u_k, v_k) coordinates of the sampling points have to be expressed in units of the observing wavelength λ and the complex visibilities V_{obs} in Jy ($1\,\mathrm{Jy} = 10^{-23}\,\mathrm{erg\,s}^{-1}\,\mathrm{cm}^{-2}\,\mathrm{Hz}^{-1}$).

The angular offsets $(\Delta\alpha, \Delta\delta)$, if provided, need to be expressed in arcseconds.

6.2.3   Implementation

The package `pyvfit` is written in C++ 11 and uses NVIDIA CUDA to make the code executable on NVIDIA GPUs. NVIDIA CUDA is a platform and a programming model designed for parallel computing, particularly suitable for accelerating scientific applications (Nickolls et al. 2008): it provides tools to execute custom algorithms on GPUs and, through the NVIDIA CUDA Toolkit, it offers application programming interfaces (APIs) to high performance routines for scientific computing, e.g. linear algebra (`cuBLAS`) and FFT (`cuFFT`) among many others.

For the development of `pyvfit` we exploit the power of the already existing CUDA APIs and we write custom kernels (algorithms to be executed on GPUs) to implement more specific operations that are not available in the NVIDIA Toolkit. `pyvfit` provides *out-of-the-box* not only a GPU-accelerated version, but also a CPU-accelerated one that uses the OpenMP technology (Dagum and Menon 1998) to distribute the workload on multiple CPU cores. Indeed, the latest improvements in the NVIDIA CUDA technology allows the code of the numerical core functions to be executed both on GPUs and CPUs without needing to be modified. This ensures that the data is processed in the same way in the two versions, thus dramatically enhancing the versatility of the library, and making it relevant even for users without direct access to GPU-hosting machines.

Finally, for ease of use and greater flexibility, `pyvfit` is wrapped in a Python package that makes both the GPU- and CPU-accelerated routines accessible with a unique straightforward interface.

6.2.3.1   Algorithm and details of GPU implementation

We now turn to illustrate the structure of the algorithm of the `chi2` function which implements the synthesis imaging equations presented in Section 6.2.1 and computes the χ^2 given some interferometric data and a model image. In the following, we refer to the visual representation given in Figure 6.2.
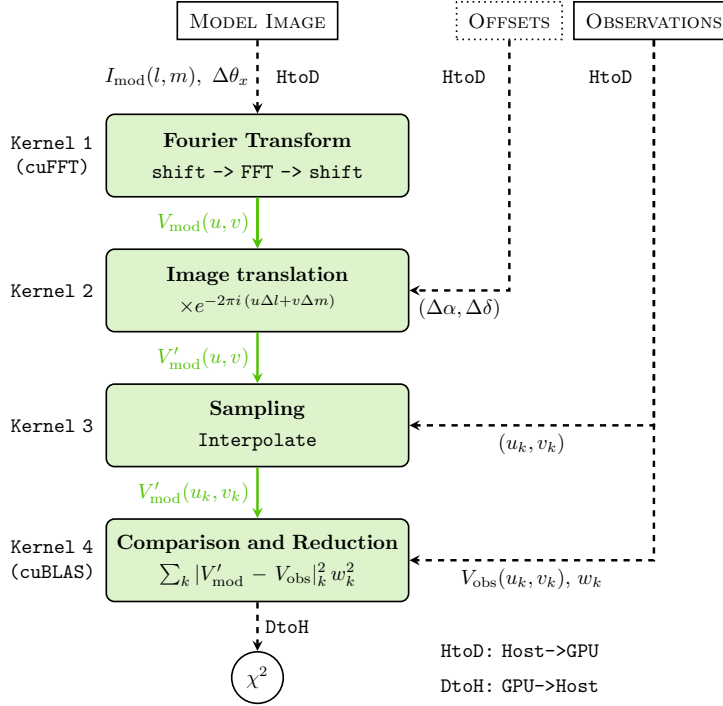
Fig. 6.2   Flow chart of the algorithm, proceeding from top to bottom. White boxes indicate inputs: the image of the model brightness, the observational data set, and (optional) the angular offsets. The only output is the χ^2. Green boxes represent the kernels that are performed on the GPU (device) and provide an elementary description of the operations they perform. Green arrows indicate data flow between kernels and black dashed arrows highlight memory transfers from host to GPU (host to device, HtoD) and viceversa (DtoH).

The two mandatory sources of input (white boxes in Figure 6.2) are

1. the MODEL IMAGE: an image of the model brightness $I_{\mathrm{mod}}(l, m)$ and the corresponding cell angular size $\Delta\theta_x$;

2. the OBSERVATIONS: an interferometric data set, i.e. a set of visibility samples $V_{\mathrm{obs}}(u_k, v_k)$ with weights w_k (for $1 \le k \le M$).

Optionally, it is possible to specify the right ascension and declination OFFSETS $(\Delta\alpha, \Delta\delta)$ by which the model image $I_{\mathrm{mod}}(l, m)$ has to be translated.

Following Figure 6.2, the algorithm is organized in five parts (kernels) that we now describe in turn.

Kernel 1 - Fourier Transform As a first step, following Eq. (6.3) the model brightness $I_{\mathrm{mod}}(l, m)$ is Fourier Transformed to obtain the visibility function $V_{\mathrm{mod}}(u, v)$.

First, we need to prepare the model image for the FFT algorithm. While the image has its center in the $(N_x/2, N_x/2)$ pixel, the FFT algorithm assumes the image center to be in the $(0, 0)$ corner. To correct for the differing definitions we apply to the image a `shift`

function that divides the image in four quadrants and swaps the upper-left quadrant with the lower-right one and the lower-left quadrant with the upper-right one. We implement this `shift` function as a CUDA C++ kernel. Note that our solution has been obtained independently from Abdellah (2014). For more details, see the `shift` implementation in Appendix E.

Second, we apply the FFT algorithm to the shifted image. To achieve the best performances, we exploit the implementation provided by the NVIDIA `cuFFT` library, which is a high performance implementation of the FFT algorithm (Cooley and Tukey 1965) and is freely available in the NVIDIA CUDA Toolkit[3]. The `cuFFT` library offers a simple interface to the many implementations of the FFT algorithm, namely the Real-to-Complex, the Complex-to-Complex, and the Complex-to-Real variants. All these functions are available both in single or double precision accuracy. In our code, even though the model image $I_{\mathrm{mod}}(l, m)$ is real-valued by definition, we decide to use the general Complex-to-Complex transform `cuFFT_Z2Z` (and its single precision version `cuFFT_C2C`), which allows the input and output data to have the same data layout. Conversely, the Real-to-Complex transform, which theoretically is faster, requires manipulation of the input data before it can be applied.

As a third and last step of this kernel, we apply the `shift` function again to the output of the FFT algorithm in order to bring the (u, v) plane origin (by definition assigned to the $(0, 0)$ pixel of the transform) back to the matrix center $(N_x/2, N_x/2)$. The resulting matrix contains N_x^2 samples of $V_{\mathrm{mod}}(u, v)$ evaluated at the regularly spaced pixel centers.

Kernel 2 - Image Translation If any angular offset $(\Delta\alpha, \Delta\delta)$ is provided, the model image $I_{\mathrm{mod}}(l, m)$ is translated accordingly. The image translation is performed with a custom CUDA C++ kernel that applies a phase shift to the visibility function $V_{\mathrm{mod}}(u, v)$ as explained in Section 6.2.1.

Kernel 3 - Sampling The output of Kernel 2 is a matrix containing N_x^2 samples of the visibility function, distributed on a regularly spaced grid. In order to evaluate the visibility function in the non-uniformly distributed sampling points (u_k, v_k) we implement a CUDA C++ kernel that performs a bilinear interpolation (Press et al. 2007) for each sampling point. The output of this kernel is a set of M samples $V_{\mathrm{mod}}(u_k, v_k)$.

Kernel 4 - Comparison and Reduction Following Eq. (6.4), the computation of the final χ^2 involves a reduction (summation) of the square discrepancies over all the M samples. To ensure high performances on the reduction operation we rely on the `cuBLAS` library[4] which offers an implementation of the highly optimized BLAS[5] routines for NVIDIA GPUs. The operation in Eq. (6.4) can be viewed as the Euclidean norm of an M-dimensional complex number, whose k-th component is given by $|V_{\mathrm{obs}}(u_k, v_k) - V_{\mathrm{mod}}(u_k, v_k)|^2 \, w_k$. We thus use the `cublasDznrm2` (`cublasScnrm2`) function that computes the Euclidean norm of an M-dimensional complex number with double (single) precision.

One of the most relevant bottlenecks that usually affect GPU applications is the memory transfer from host to device[6] (HtoD) and viceversa (DtoH), the main reasons being: (i) the much larger latency of the device memory w.r.t. the host memory (**e.g. numbers**), (ii) the limited memory bandwidth (usually smaller than 8GB/s). During the design of the code, we paid much care in reducing the HtoD and DtoH memory transfers to the absolute minimum. As an example, to this extent the behaviour of Fourier Transform under trans-

---

[3]For the development and testing of the code we used the NVIDIA CUDA Toolkit versions 6.0, 7.0 and 7.5, available here: https://developer.nvidia.com/cuda-toolkit

[4]cuBLAS is freely available in the NVIDIA CUDA Toolkit.

[5]Basic Linear Algebra Subprograms, http://www.netlib.org/blas/.

[6]In this context, the CPU represents the host system, while the GPU is the device.

lations is particularly useful as it allows us to perform the image translation directly on the GPU, with no need to move the data. As a result, Figure 6.2 shows that we have three HtoD memory transfers to upload the input data to the GPU, and only one DtoH transfer, to retrieve the result of the computation from the GPU. No other memory transfers are executed throughout the computation of Kernels 1 to 4. Moreover, wherever possible we preferred *in-place* operations that, avoiding the creation of intermediate copies of the data, help to reduce the overall amount of memory actually needed.

The current version of the code executes all the HtoD transfers at the beginning, i.e. immediately before `Kernel 1` execution, which makes the code more easily readable and debuggable. It is worth noting that possible speed improvements could be attained with H2D asynchronous transfers, which would allow the data to be transferred immediately before it is needed.

6.3   Performance

The performance tests that we report here have been executed on a local server with 28 physical CPU cores, 56 logical CPU cores and 1 NVIDIA Tesla K40.

In Figure 6.3 we show the comparison of the execution time on GPU and CPU of the `chi2` routine as a function of matrix size, for single e double precision. We perform the same measurements also for different number of sampling points, respectively 10^3 and 10^6, as to represent data sets of different size. For reference, in Table 6.1 we report the actual execution time measurements plotted in Figure 6.3.
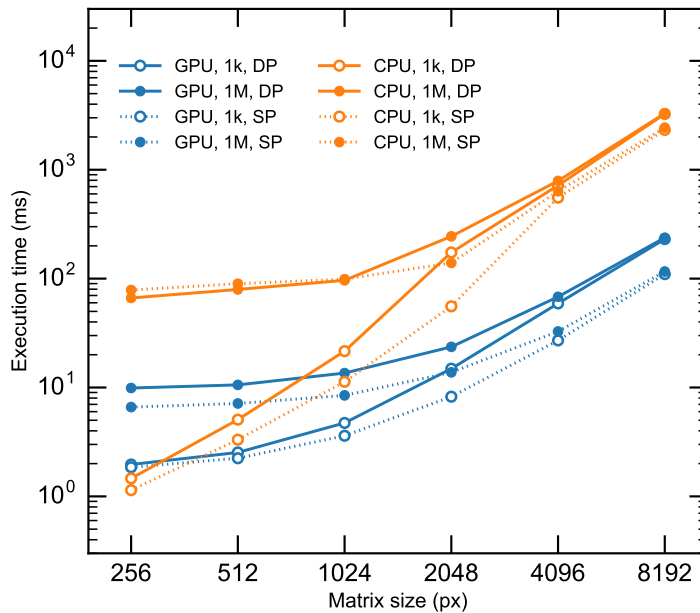
Fig. 6.3   Comparison of the execution time of `chi2()` on GPU (blue lines) and CPU (orange lines), as a function of matrix size. We report the execution time for double (solid lines) and single (dotted lines) precision, for 1 thousand (empty circles) and 1 million (filled circles) sampling points. For matrix sizes larger than 2048x2048 pixels, the GPU outperforms the CPU by a factor larger than 10x (20x) for the double (single) precision cases. Performance may vary based on OS version and motherboard configuration.

Table 6.1   Execution times of `chi2()` on CPU and GPU.

| Size	Double Precision		Single Precision	
	Time GPU	Time CPU	Time GPU	Time CPU
(px)	(ms)	(ms)	(ms)	(ms)
256	9.9	66.4	6.6	78.6
512	10.6	79.5	7.1	89.8
1024	13.6	96.5	8.5	99.0
2048	23.6	244.5	13.8	139.4
4096	68.1	789.7	32.7	634.4
8192	237.6	3294.8	116.3	2434.6

Notes – Times in the table refer to the case with 1 million sampling points.

Figure 6.3 displays that the execution of `chi2()` on the GPU allows a speedup around 10x, factor that is almost constant for matrix sizes larger than 1024x1024. The single precision versions are faster than the double precision ones, but the difference is almost negligible for CPUs, and not larger than a factor of two for GPUs. Interestingly, the number of sampling points has a major impact on performances at small matrix sizes (<1024x1024, in particular for the CPU version), whereas it becomes almost negligible for matrix sizes larger than 4096x4096. For small matrix sizes the translation and the sampling operations (through interpolation) dominate the computing time, which is somehow expected since the FFT routines are highly optimized. However, the typical matrix sizes used in fits of real ALMA and VLA observations are at least 1024x1024, in many cases 4096x4096 as soon as observations at medium-high (0.1"-0.2") angular resolution are considered. The plot confirms that in the working regime of our interest, the considerable speedup delivered by the GPU library will allow us to fit observations at an angular resolution 4-8 times higher (matrix size $\sim$ 8192x8192) than what the CPU version would allow.

In Figure 6.3 we compare the execution times of *one* single call of the *chi*2() function, in the CPU and GPU versions. Here, we study the execution times in a multi-wavelength working regime. In Figure 6.4 the execution times of *chi*2() are plotted as a function of matrix size, for different number of fitted wavelengths $N_\lambda = 2, 5, 10, 20, 50, 100$. We also represent the computing times for different number of CPU cores used: for the CPU version, 8, 16, and 32 computing cores; for the GPU version, 8 and 16 cores. For the GPU version, the number of cores indicates how many processes are controlling the GPU at the same time.

The most remarkable feature arising from the results in Figure 6.4 is the enormous computing power of the GPU card: if we compare the GPU execution times at $N_\lambda = 2$ and $N_\lambda = 10$, we see that they are substantially identical, and they start to increase very slowly at $N_\lambda > 50$. The GPU computing times are double for $N_\lambda = 100$ in comparison to those at $N_\lambda = 2$. If we repeat the comparison for the CPU execution times at the same N_λ values, we observe a much steeper increase. As a result, for small $N_\lambda \leq 5$, CPU runs are more convenient than GPU-accelerated runs, but as soon as the data to be processed increases ($N_\lambda \geq 10$), the GPU runs are as fast as before while CPU runs are rapidly outperformed. We can understand this behaviour[7]. if we consider that the GPU runs are affected by much

---

[7]The actual numbers could depend on the particular GPU used (for this test, we used the latest generation
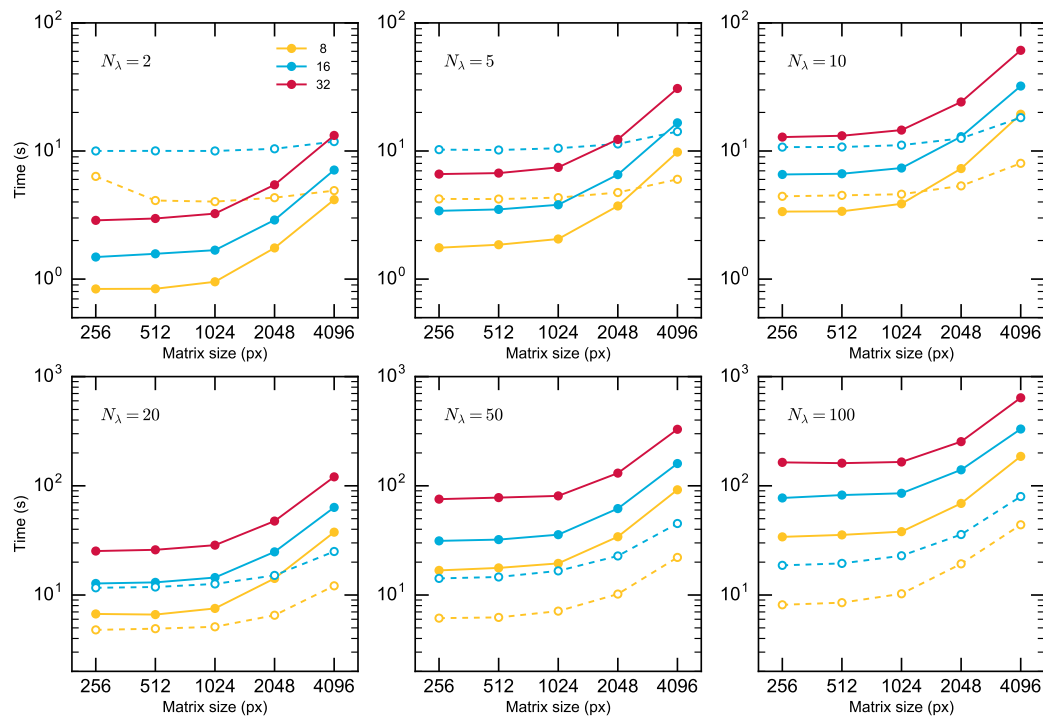
Fig. 6.4 Comparison betewen CPU (solid) and GPU (dashed) execution times for different matrix sizes and number of cores, 8 (yellow), 16 (blue), 32 (red). The six plots show how the execution times change as a function of the number of wavelengths fitted simultaneously N_λ. It is apparent that for small N_λ the CPU version is more efficient, but for N_λ approaching 100, the GPU version allows a speedup larger than 10x.

larger memory latency (compared to that of the RAM used by CPUs) and include memory transfer overheads, which CPU runs do not require. The main result of this analysis is that, while CPUs can be preferred for fitting a small number of wavelengths simultaneously, GPUs are definitely required to tackle the next generation multi-wavelength analysis of high resolution observations.

6.4   Conclusions

We have presented `pyvfit`, a Python package that offers a simple interface to high performance routines for comparing interferometric data sets with the predictions of a model. The main feature of the package is its capability to be executed on NVIDIA graphical processing units (GPUs), many-core devices designed to deliver extreme performances for parallel tasks.

The package has been designed as a general purpose tool whose usage can be easily implemented in already existing codes with minimal programming effort (as we demonstrate in Section 6.2.2). The package allows the user to exploit the power of modern NVIDIA GPU cards when computing Fourier Transforms and the other matrix operations involved in the likelihood computation. The package uses latest NVIDIA CUDA technologies to ensure the optimal usage of GPU resources and data consistency.

Thanks to the flexibility of the NVIDIA CUDA specifications, the numerical routines implemented in `pyvfit` can be compiled effortlessly for CPU as well as for GPU. We therefore provide also a full version of `pyvfit` that can be run on CPU. We remark that the only core routines that differ between the GPU and the CPU versions are the FFT implementations, for which we relied, respectively, on the well tested NVIDIA CUDA cuFFT library and on the widely used FFTW 3 library. Such code flexibility has the additional advantage of allowing the user to choose the device on which to run the code just by changing one import statement. More remarkably, `pyvfit` is suitable also for users who do not have direct access to machines with GPUs: thanks to the support of the OpenMP technology, the CPU version of `pyvfit` reaches very good performances even when it is executed on CPU (see Figure 6.3).

We have tested the performances of the GPU vs the CPU version. From a strong scaling perspective, the GPU-accelerated code achieves a >20x speedup for a single likelihood evaluation as compared to the multi-core CPU version. From a weak scaling perspective, the GPU library is particularly promising as it allows the simultaneous fit of many more wavelengths (up to 100) compared to the CPU version.

The GPU-accelerated library is designed to work in parallel environment, on multi-CPU/multi-GPU hybrid architectures, both on local servers and large clusters. Thanks to the flexibility and to the performances delivered, the GPU-accelerated routines offered in `pyvfit` are ideal tools to develop the next generation multi-wavelength analysis of observations at high angular resolution.

NVIDIA Tesla K40), but the embarrassingly parallel nature of the operations that we perform in the chi2() function ensures that very good performances should be attained on *any* modern GPU.

7

Conclusions and Outlook

In this chapter I summarize the main findings of the Thesis and I discuss some follow-up investigations suggested by this work.

In recent years, evidence of grain growth in disks has been obtained by extensive sub-mm/mm photometric surveys, but so far they only provided disk-averaged estimates of the dust properties. Moreover, these past studies derived the dust properties from the observed spectral index under simplifying assumptions (e.g., that the emission is optically thin and in Rayleigh-Jeans regime) rather than with a proper modeling of the disk emission.

In this Thesis I have developed an analysis method that enables - for the first time - the disk structure and the dust properties to be constrained simultaneously by fitting multi-wavelength observations with a self-consistent physical modeling. The fit is performed directly in the visibility (Fourier) domain. The usage of realistic models has allowed me to fit the observations with a physical interpretation of the detected disk emission, deriving the disk surface density and the temperature profiles, as well as the radial profile of the maximum grain size. Moreover, the novel method of fitting simultaneously observations at several wavelengths proved successful in breaking the degeneracy between the terms contributing to the (sub-)mm emission, namely surface density, temperature and dust opacity. This analysis sets the current state-of-the-art for the analysis of spatially resolved multi-wavelength radio observations.

I have applied the multi-wavelength analysis to observations between 0.88 mm and 1 cm of three disks in the Taurus and Ophiuchus star forming regions (SFRs). First, this allowed me to test the analysis method against literature studies, obtaining a positive result. Second, for all these disks I derived the radial profiles of their grain size distributions: they are all compatible with large grains (up to 1 cm) in their inner regions and small grains ($\ll$ 1 mm) populating the whole disks (which agrees with theoretical expectations of grain growth models), but at the same time they also show non negligible differences.

A natural continuation of this work would be to extend the analysis to a larger sample of disks, which would allow me to understand whether the differences reflect an evolutionary trend or an intrinsic scattering due to different initial disk conditions. To this extent, I am leading an international team who has been awarded ALMA time to conduct the largest survey to date at 3 mm of Class II disks belonging to the same star forming region (Lupus). By combining the incoming 3 mm observations with those at 0.87 mm (analyzed in this

Thesis) and at 1.3 mm (data being delivered at the moment of writing), I will carry out the most extensive analysis (30 disks) of multi-wavelength observations with a self-consistent modeling. The disk structures and grain size profiles that I will derive will be the first in terms of completeness of the sample and homogeneity of the analysis. This study will provide unique and statistically sound observational benchmarks useful to inform and refine any theoretical model of planet formation and disk evolution.

The study of grain growth will be carried out also with another recently approved ALMA observing program at 1.3 and 3 mm that follows up the VLA observations at 8 and 10 mm taken within the Disks@EVLA project. Constraints on the level of dust processing in the 18 disks targeted by the program will be derived with the analysis tool that I developed. As part of this project, I have applied the analysis tool to ALMA and VLA observations of the disk around the Herbig AeBe star HD 163296. Employing a modified disk surface brightness profile, the analysis tool has allowed me to reveal the presence of a strong ring-like excess peaked at 100 au. Interestingly enough, 100 au is also the location of the CO snowline[1] and this seems to support the theoretical expectation for which in the vicinity of a snowline grain growth could be enhanced, thus rapidly leading to the formation of grains beyond mm sizes. The angular resolution of the observations was limited, therefore we could not conclusively pin down whether the 100 au excess is due to such snowline effect, to local dust-retaining turbulent eddies, or to a dynamical effect (e.g., due to the presence of a giant planet). To address this question, I am part of an international collaboration that has been awarded time both at ALMA and VLA to execute high sensitivity observations of the HD 163296 disk at 1.3, 3, 8, 9.8 and 36 mm: with such an exceptional wavelength coverage and high spatial resolution ($\sim$ 10 au, which is the typical disk scale height at 100 au) we will probe the distributions of grains ranging between 1 and 10 mm out to a distance from the star $\gtrsim$ 140 au which will give crucial observational constraints for assessing the origin of the ring-like excess.

The tool developed in this Thesis has been designed also to accelerate the analysis of high resolution observations for demographic studies. I have used the analysis tool to fit observations of an ALMA Class II disk survey in the Lupus SFR. I have fitted the physical structure of more than 20 disks, obtaining their size and dust mass (among other physical parameters). To date, this is the largest sample of disks of the same SFR fitted homogeneously with a self-consistent modeling. Remarkably, the sample is complete in the $0.7M_\odot$-$1M_\odot$ mass range. The results are compatible with previous studies based on simpler analyses but also highlight a consistent difference in the disks luminosity-size correlation between the older ($\sim$3 Myr) Lupus and the younger ($\sim$1-2 Myr old) Taurus-Auriga region (data from literature results). In the next future, the study will be extended with the application of the same analysis to follow-up ALMA observations for complete samples of Class II disks in other SFRs (e.g., Taurus-Auriga, Ophiuchus, Upper Sco). By comparing results in SFRs with different mean ages, this follow-up study has the potential of revealing scaling laws (and their dependence on time and environmental parameters) that could have profound connections with the star and planet formation processes.

Finally, I have developed an accelerated version of the code that achieves the computational breakthrough needed to exploit the new wealth of information offered by modern sub-mm/radio interferometers. With the huge enhancements in angular resolution and sensitivity delivered by ALMA and VLA, the comparison of a model synthetic image with the observations becomes prohibitively intensive. I have therefore developed an accelerated library that leverages on the computing power of modern graphics processing units

---

[1]Location in the disk where CO freeze-out occurs.

(GPUs) which deliver stunning performances for matrix operations w.r.t. to the classical CPUs. From a strong scaling perspective, the GPU-accelerated code achieves a >20x speedup for a single likelihood evaluation as compared to the multi-core CPU version. From a weak scaling perspective, the GPU library is particularly promising as it allows the simultaneous fit of many more wavelengths (up to 100) compared to the CPU version. A natural case study that would benefit from the usage of the GPU-accelerated library is the simultaneous analysis of several spectral channels. Such analysis would allow not only the gas spatial distribution, but also its velocity field, to be constrained in a self-consistent way. This would open new opportunities to study the gas kinematics with proper modeling, thus allowing us to search for signatures of forming planets, to estimate the impact of accretion on the energy balance in the disks, and to assess the amount of gas turbulence.

Throughout the Thesis I have greatly benefitted from the multi-disciplinary environment that characterizes the Excellence Cluster *Universe*. On the one hand, it provided opportunities and a fertile ground for the development of skills at the interface between theoretical and observational astrophysics that revealed crucial to achieve the goals of the Thesis. On the other hand, I have been able to take advantage of its facilities, e.g. the computational center for particle and astrophysics (C2PAP), where I was awarded computing time in 2015 and 2016 and on which I executed all the fits performed in the Thesis.

In the last years we are witnessing an explosion of high resolution observations that are quickly revolutionizing protoplanetary disks studies. We can now legitimately say that the new field of *observational* planet formation has born. In this Thesis I have developed the tools that pave the way for an effective exploitation of the incoming wealth of data and make our analysis capabilities ready to advance our knowledge of the planet formation process.

A

Physical and astronomical constants

Physical constants

Speed of light	c	2.998×10^{10}	cm	s^{-1}	
Gravitational constant	G	6.673×10^{-8}	$cm^3\,g^{-1}$	s^{-2}	
Planck constant	h	6.626×10^{-27}	erg	s	
Proton mass	m_p	1.673×10^{-24}	g		
Boltzmann constant	k_B	1.381×10^{-16}	erg	K^{-1}	
Molar gas constant	$\mathcal{R}$	8.314×10^7	erg	$mol^{-1}K^{-1}$	
Stefan–Boltzmann constant	σ_{SB}	5.670×10^{-5}	erg	$cm^{-2}\,K^{-4}$	s^{-1}
Thomson cross-section	σ_T	6.653×10^{-25}	cm^2		

Astronomical constants

Solar mass	$M_\odot$	1.989×10^{33}	g
Jupiter mass	M_J	1.899×10^{30}	g
Earth mass	$M_\oplus$	5.974×10^{27}	g
Solar radius	$R_\odot$	6.963×10^{10}	cm
Jupiter radius	R_J	7.149×10^9	cm
Earth radius	$R_\oplus$	6.371×10^8	cm
Solar luminosity	$L_\odot$	3.846×10^{33}	erg s^{-1}
Astronomical Unit	1 au	1.496×10^{13}	cm
Light year	1 ly	9.419×10^{17}	cm
Parsec	1 pc	3.086×10^{18}	cm

B

Bayesian analysis: MCMC details and implementation

The tool developed in Chapter 3 and used in Chapters 4 and 5 is based on the Bayesian inference, which allows us to estimate the consistency of the model with its parameters against a given dataset by encapsulating the notion of degree of belief in terms of probability. In explaining how the tool works we will refer to Fig. B.1.

The interferometric observations are fitted directly in the $uv-$plane (i.e., the Fourier space) in order to avoid the nonlinear disturbances introduced by the CLEAN deconvolution algorithm. Quantitatively, the Bayes's Theorem can be written as follows:

$$p(\vec{x} \,|\, D) = \frac{p(D \,|\, M(\vec{x}))p(\vec{x})}{p(D)} \,, \qquad \text{(B.1)}$$

where M is the model, $\vec{x} = (\vec{x}_1, \ldots, \vec{x}_n)$ are the model parameters and D is the data. On the left-hand side $p(\vec{x} \,|\, D)$ is the *posterior probability* (hereafter *posterior*), representing our degree of belief on the parameter values *after* observing the data. On the right-hand side $p(D \,|\, M(\vec{x}))$ is the *likelihood* and represents the probability of observing the data D given the model $M(\vec{x})$; $p(\vec{x})$ is the *prior probability distribution* (hereafter *prior*) that represents our initial knowledge on the parameter values (it contains all previous information coming from other studies, constraints, etc.). Finally, $p(D)$ is a normalization factor, usually called *evidence*: while for our purposes (parameter estimate) is negligible, it becomes useful for model selection (i.e. to discriminate the goodness of different models).

Bayesian Fitting Tool

1. Disk model
computes disk emission at different wavelengths (for given i)

Fourier Transform

2a. Synthetic multi-wavelength visibilities sampled at the P.A.

2b. Observed multi-wavelength visibilities

3. posterior $\propto \exp(-\chi^2/2)$

Fig. B.1 Sketch of the Bayesian tool developed to fit multi-wavelength interferometric data sets (for more details, see Chapter 3).

In our case, the data D is constituted by the interferometric observations at different wavelengths, the model M is given by the disk and the dust models, the set of parameters $\vec{x}$ is given by the following free parameters: three for the surface density Σ_0, R_c, γ, and two
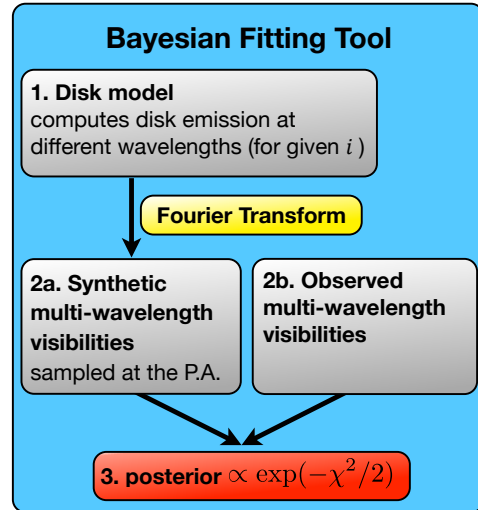
for the dust grain size distribution $a_{\text{max}0}$ and b_{max}, namely:

$$\vec{x} = (\Sigma_0,\ R_{\text{c}},\ \gamma,\ a_{\text{max}0},\ b_{\text{max}}) \,. \tag{B.2}$$

According to Eq. (B.1), the posterior is computed as the product of the likelihood and the prior (as explained above, we neglect $p(D)$). The prior can encapsulate our previous knowledge about the parameter values, if there is any. In our case, since we do not have any particular insight for their actual value, we adopt a *uniform* prior for all of them, namely $p(\vec{x}) = 1$ for $\vec{x} \in \mathcal{D}$ and $p(\vec{x}) = 0$ everywhere else, with $\mathcal{D}$ given by:

$$\mathcal{D} = [-1, 2]_{\gamma} \times [0.1, 200]_{\Sigma_0} \times [5, 300]_{R_{\text{c}}} \times$$

$$\times\ [0.001, 100]_{a_{\text{max}0}} \times [-5, 2]_{b_{\text{max}}} \,, \tag{B.3}$$

that is a rectangular five-dimensional domain and is equivalent to restricting the fitting algorithm to research within $\mathcal{D}$.

To compute the likelihood we proceed as follows. Let us call $\{\lambda_\ell\}_{\ell=1}^{L}$ the collection of L wavelengths we are fitting simultaneously. For each wavelength λ_ℓ, let $\{V_{\ell,j}^{\text{obs}}\}_{j=1}^{N_\ell}$ be the set of the observed visibilities. Given the parameter values $\vec{x}$, at each wavelength λ_ℓ:

1. the disk and the dust models compute the radial profile of the disk thermal emission (eq. 3.2, 3.3);

2. given the disk inclination (i) and Position Angle (*PA*), an intensity map is computed;

3. the model visibilities $\{V_j^{\text{mod}}\}_{j=1}^{N_\ell}$ are computed by taking the Fourier Transform (FT) of the intensity map and sampling it at the same $(u, v)-$plane locations of the observed visibilities.

Then, since the errors on the visibilities can be treated as gaussian (Wrobel and Walker 1999), we can use the χ^2 as an estimator for the likelihood, namely

$$p(D \,|\, M(\vec{x})) \propto \exp\left(-\chi^2/2\right) , \tag{B.4}$$

with

$$\chi^2 = \sum_{\ell=1}^{L} \sum_{j=1}^{N_\ell} \left| V_{\ell,j}^{\text{obs}} - V_{\ell,j}^{\text{mod}} \right|^2 \cdot w_{\ell,j} \,, \tag{B.5}$$

where $w_{\ell,j} = 1/\sigma_{lj}^2$ is the visibility weight.

To efficiently compute the posterior distributions for all the free parameters (the five physical parameters that define the disk model plus two offset parameters per each fitted wavelength) we use a variant of the MCMC algorithm (Mackay 2003; Press et al. 2007), which proved to be effective in finding global maxima for a wide range of posteriors. We adopt an affine-invariant ensemble sampler for MCMC proposed by Goodman and Weare (2010), which is designed to simultaneously run several Markov chains (also called *walkers*) interacting with each other to converge to the maximum of the posterior. For unimodal posteriors (i.e., posteriors that exhibit only one global maximum) this algorithm is efficient at avoiding getting stuck in local maxima and allows the computation to be massively parallelized over the walkers. According to our experience, we have always observed unimodal posteriors, thus making this algorithm particularly suitable for our purpose.

In this study, we let the MCMC (usually of 1000 walkers) evolve for an initial *burn-in* phase, which is needed to allow the MCMC to perform a reasonable sampling of the parameter space and to find the posterior maximum (which is usually achieved after ten *autocorrelation times*[1]). After the burn-in phase, we let the MCMC run for several other autocorrelation times (3-4) to get a sufficient number of independent posterior samples. Since two consecutive steps in the MCMC are correlated (Goodman and Weare 2010), in order to extract a set of independent posterior samples out of the whole MCMC we need (1) to discard the samples of the burn-in phase and (2) to thin the remaining chain, i.e., to consider only steps separated by one autocorrelation time and to discard all the steps between them[2]. For completeness, we note that to estimate the chain convergence we also analyzed the *acceptance ratio*, i.e., the ratio of accepted over proposed moves, verifying that it is within the acceptable range between 0.2 and 0.5 in all cases. The number of steps needed to achieve convergence varies from disk to disk and depends on several factors, thus making it not predictable a priori; for the disks analyzed here, we needed at most 2000 steps including burn-in. With 1000 walkers, 2000 steps, and an acceptance fraction of $\sim 0.2-0.5$, we note that the method requires the computation of several million models and likelihoods, hence it is necessary to exploit the efficient Message Passing Interface (MPI) parallelization of the computation by advancing several hundred walkers in parallel.

As explained in Section 3.2.3, in addition to the disk structure and the dust size distribution, we also fit the position of the disk centroid by adding two *nuisance* parameters for each wavelength, namely $\Delta\alpha_0$ and $\Delta\delta_0$. To implement these offset parameters we exploit the fact that a translation in the real space corresponds to a phase shift in the conjugate (Fourier) space. Therefore, to shift the disk emission computed by the model by $(\Delta\alpha_0, \ \Delta\delta_0)$ on the sky, we multiply the model visibilities $V_j^{\mathrm{mod}}(u, v)$ by the phase-shift $\exp\left[2\pi i(u\Delta\alpha_0/\lambda + v\Delta\delta_0/\lambda)\right]$, with $\Delta\alpha_0$ and $\Delta\delta_0$ given in radian units and λ in meters.

From the computational point of view, the main architecture of the analysis is written in Python and delegates the most demanding tasks, like the disk model evaluation or the visibility sampling, to C- and Fortran-compiled external libraries. Writing the main architecture of the analysis in Python allows us to use the affine-invariant MCMC algorithm implemented in the Python-based *emcee* package[3] which enables a massive parallelization of the overall computation. By far the most costly part of the sampling is the evaluation of the posterior, which *emcee* allows us to do simultaneously for half the walkers (it exploits the Message Passing Interface (MPI) protocol to distribute the computation to several cores). In our case, we ran the fits on hundreds of cores hosted at the Computational Center for Particle and Astrophysics (C2PAP), decreasing the overall computational time to approximately one or two days. After a careful profiling of the analysis method, we noted that the bottleneck of the posterior evaluation (i.e., the single walker computation) is given by the several Fourier transform computations[4] (one for each wavelength that is being fit) and by their sampling at the discrete locations where the antennas sampled the sky.

---

[1]The autocorrelation time of a MCMC is an estimate of the number of posterior PDF evaluations needed to produce a large number of independent samples of the target density.

[2]In our case, since the autocorrelation time is usually observed to be smaller than 100 steps, the thinning does not reduce the effective sample size, but allows us to save a lot of computational time during post-processing, e.g., when producing the *uv*-plots that show the comparison between the observed visibilities and the density of synthetic visibilities.

[3]The code can be found at https://github.com/dfm/emcee.

[4]To compute the Fourier transforms we use the numpy implementation.

C

Grain growth in AS 209: comparison with previous study

We present the results of the comparison between our analysis and the previous one by Pérez et al. (2012). As described below, the comparison is performed using the same observational datasets, the same disk model and the same dust opacity used by Pérez et al. (2012).

As presented in Section 3.2.3, our analysis consists of a self-consistent modeling of the disk structure and the radial distribution of the dust grains that provides us with a unique model that is capable of reproducing the multiwavelength observations simultaneously. In this framework, the radial profile of a_{max} is constrained from observations at several wavelengths. Then, from the resulting $a_{\mathrm{max}}(R)$ profile we derive the corresponding $\beta(R)$ profile through the dust opacity model.

The analysis of Pérez et al. (2012) consists of two steps: first, assuming a constant a_{max} throughout the disk, they separately fit the observations at different wavelengths and obtain radial profiles of the disk temperature and the optical depth $\tau_\lambda(R)$; then, assuming that the disk surface density Σ is unique, they interpret the wavelength dependence of τ_λ in terms of radial variations of β. In the end, they provide constraints on $a_{\mathrm{max}}(R)$ by fitting the $\beta(R)$ profile with a dust opacity model. In order to check whether we recover the results of Pérez et al. (2012) we first fit each wavelength separately. Subsequently, we perform a multiwavelength fit with the same disk and dust model and compare the results.

We perform single-wavelength fits of each observation of the AS 209 protoplanetary disk using the same setup for the disk model and the dust properties used by Pérez et al. (2012). For the disk model, we use the two-layer model described by Isella et al. (2010), which assumes the following surface density profile (Hartmann et al. 1998),

$$\Sigma(R) = \Sigma_{\mathrm{T}} \left(\frac{R}{R_{\mathrm{T}}} \right)^{-\gamma} \exp \left\{ -\frac{1}{2\,(2-\gamma)} \left[\left(\frac{R}{R_{\mathrm{T}}} \right)^{2-\gamma} - 1 \right] \right\} , \tag{C.1}$$

where R_{T} is the radius at which the radial component of the gas velocity changes sign (gaseous material at $R < R_{\mathrm{T}}$ moves inwards, at $R > R_{\mathrm{T}}$ moves outwards). The dust size distribution is defined with the parametrization in Eq. (3.5), with $a_{\mathrm{min}}^{\mathrm{mid}} = a_{min}^{sur} = 10\,\mathrm{nm}$, $a_{\mathrm{max}}^{\mathrm{mid}} = 1.3\,\mathrm{mm}$ constant throughout the disk ($b_{\mathrm{max}}^{\mathrm{mid}} = 0$), and $q_{\mathrm{mid}} = q_{\mathrm{sur}} = 3.5$. The dust
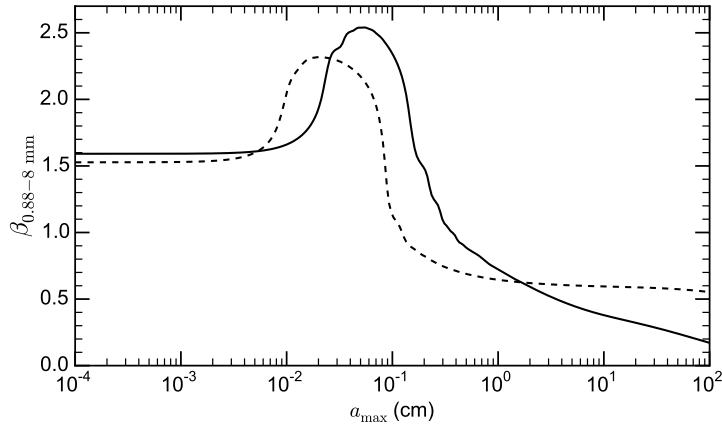
Fig. C.1   Dust opacity spectral index β between 0.88 and 8 mm as a function of the maximum dust grain size a_{max}. The solid line refers to our dust composition ($q = 3$, 5.4% astronomical silicates, 20.6% carbonaceous material, 44% water ice, and 30% vacuum), whereas the dashed line refers to the dust composition used by Pérez et al. (2012) ($q = 3.5$, 7.7% astronomical silicates, 29.5% carbonaceous material, 62.8% water ice).

grains are assumed to be compact spherical grains made of astronomical silicates (7.7%), carbonaceous material (29.5%), and water ice (62.8%) with an average dust grain density 0.9 g/cm^3 (the correct value should be 1.3 g/cm^3, but we adopt 0.9 g/cm^3 in order to have the same setup used by Pérez et al. 2012). The dust opacity is computed through Mie theory as described in Section 3.2.2 using the same optical constants. In Figure C.1 we show a comparison between the $\beta(a_{\mathrm{max}})$ profile for the dust we used in our joint multiwavelength fits (presented in Section 3.4) and the dust used by Pérez et al. (2012).

In Table C.1 we list the comparison of the single wavelength fits. The agreement between our results and those by Pérez et al. (2012) is extremely good, with all the values compatible within 1σ and only in a few cases within 2σ. Similarly to Pérez et al. (2012) we derive larger disks ($R_{\mathrm{T}} \gtrsim 60$ au) at the shorter wavelengths and smaller disks ($R_{\mathrm{T}} \approx 25$ au) at the longer wavelengths, thus confirming the observational result that the size of emitting region is anticorrelated with the observing wavelength. As a further check, we note that the estimates of the uncertainty we obtain from our MCMC fits are similar to those obtained by Pérez et al. (2012).

In Figure C.2 we show the midplane temperature profiles (left panel) and the optical depth profiles $\tau_\nu = \kappa_\nu \Sigma$ (right panel) obtained with the single wavelength fits. We note that both the temperature and the optical depth profiles obtained with our single wavelength modeling are found to be in complete agreement with those computed by Pérez et al. (2012). The agreement occurs at all the fitted wavelengths.

In Table C.2 we present the results of the multiwavelength fit that was performed with the same disk model and dust assumptions as the single wavelength fits with the only difference that in the multiwavelength fit, a_{max} is not constant throughout the disk and its radial profile is constrained from the observations at several wavelengths. In Figure C.2 the multiwavelength results are represented with a dashed black line.

The midplane temperature profile obtained with the multiwavelength fit is an average temperature between the four single wavelength profiles. There is close agreement between the multiwavelength temperature profile and those derived at 0.88 and 2.80 mm throughout the disk, whereas at 8.00 and 9.83 mm some discrepancies arise at $R > 40$ au.

Table C.1 Comparison of the single wavelength fits of AS 209 performed with our analysis and the results reported by Pérez et al. (2012).

λ	γ	Σ_T	R_T	Ref.
(mm)		(g/cm^2)	(au)	
0.88	$0.25^{+0.04}_{-0.05}$	$0.44^{+0.02}_{-0.02}$	60^{+2}_{-2}	1
	$0.20^{+0.03}_{-0.05}$	$0.43^{+0.02}_{-0.01}$	61^{+1}_{-2}	2
2.80	$0.76^{+0.09}_{-0.09}$	$0.38^{+0.07}_{-0.07}$	69^{+6}_{-9}	1
	$0.60^{+0.10}_{-0.05}$	$0.47^{+0.03}_{-0.09}$	60^{+7}_{-3}	2
8.00	$0.364^{+0.14}_{-0.17}$	$1.5^{+0.3}_{-0.3}$	24^{+2}_{-4}	1
	$0.36^{+0.09}_{-0.18}$	$1.75^{+0.39}_{-0.21}$	24^{+1}_{-3}	2
9.83	$0.375^{+0.16}_{-0.17}$	$1.748^{+0.37}_{-0.34}$	27^{+3}_{-4}	1
	$0.31^{+0.15}_{-0.18}$	$1.97^{+0.47}_{-0.31}$	26^{+2}_{-4}	2

Notes. For each parameter, we list the median value with uncertainties given by the 16th and 84th percentiles of its marginalized distribution.
References. (1) This work; (2) Pérez (2013).
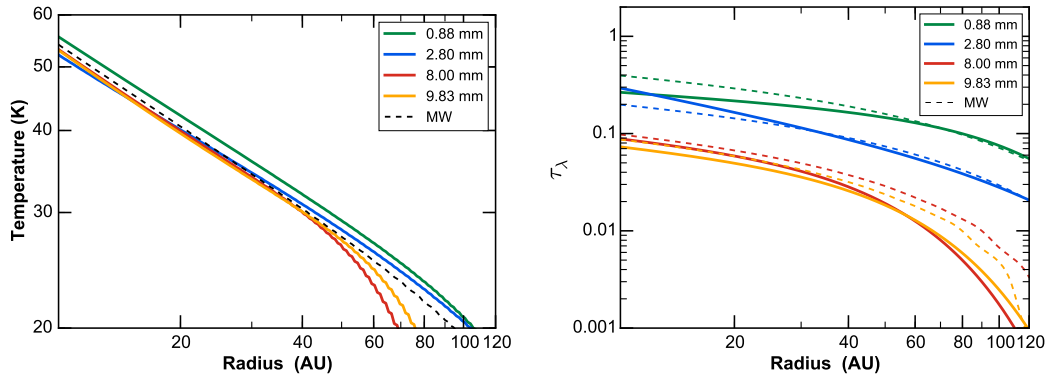
Fig. C.2 *Left panel:* best-fit model midplane temperature obtained from fitting each wavelength separately (solid lines, one line per each wavelength) or from our multiwavelength fit (dashed line). *Right panel:* for the same best-fit models, the optical depth $\tau_\nu = \kappa_\nu \Sigma$ of the disk midplane to its own thermal radiation. *Both panels:* the single-wavelength fits have been performed assuming a constant $a_{\max} = 1.3$ mm (i.e., constant dust opacity) throughout the disk. The dashed lines refer to the best-fit model obtained through multiwavelength modeling.

Table C.2 Parameters derived from the multiwavelength fit of AS 209

γ	Σ_T	R_T	$a_{\max 0}$	$b_{\max}$
	(g/cm^2)	(au)	(cm)	
$0.91^{+0.08}_{-0.04}$	$0.81^{+0.07}_{-0.08}$	48^{+3}_{-4}	$0.37^{+0.04}_{-0.05}$	$-1.3^{+0.1}_{-0.1}$

Notes. For each parameter of the fit, we list the median value; the error bars are given by the 16th and 84th percentiles.

The comparison of the optical depth profiles displays a similar behavior; there is good agreement at 0.88 and 2.80 mm and larger discrepancies at 8.00 and 9.83 mm in the outer disk. The discrepancies in the optical depth can be understood by considering that the $\Sigma(R)$ profiles (and therefore the $\tau_\lambda(R)$ profiles) obtained with the single wavelength fits are totally independent of each other, whereas the multiwavelength fit is defined by a unique $\Sigma(R)$ and produces different $\tau_\lambda(R)$ slopes at different wavelengths through radial variation of $a_{\max}$. In other words, the ability of the multiwavelength fit to produce different $\tau_\lambda(R)$ profiles at different wavelengths depends on the degrees of freedom of the $a_{\max}$ parametrization[1]. That said, the net advantage of using the multiwavelength fit lies in the fact that it provides a unique, self-consistent disk model with a dust radial distribution, as opposed to several single wavelength fits that provide as many different disk structures.

We now compare the $a_{\max}(R)$ and $\beta(R)$ profiles obtained with our multiwavelength fit and those obtained by Pérez et al. (2012). In the left panel of Figure C.3 we compare the $a_{\max}(R)$ profiles, which agree to within a factor of less than 2 in the region where most of the signal comes from (between 40 and 140 au the disk emission is spatially resolved and with signal-to-noise ratio higher than 3). It is reassuring that we both derive the same absolute dust grain size and radial slope throughout the disk. The discrepancy visible at $R < 40$ au our $a_{\max}(R)$ is not a source of concern for two reasons. First, at $R < 40$ au the disk is not spatially resolved at any wavelength. Second, $a_{\max}(R)$ is computed differently. Our $a_{\max}(R)$ profile is by definition a power law; therefore, it cannot become arbitrarily steep since it has to accommodate both the inner and the outer disk simultaneously. Conversely, the $a_{\max}(R)$ profile derived by Pérez et al. (2012) is independent at each radius, but goes to extremely large values $a_{\max} \gtrsim 10$ cm owing to the high degeneracy in the $\beta(a_{\max})$ curve (cf. Figure C.1).

In the right panel of Figure C.3 we compare the radial profile of β between 0.88 and 8.0 mm. The two profiles agree in that they find common evidence of $\beta(R)$ increasing with radius from small values $\beta \sim 0.5$ in the inner disk and $\beta \gtrsim \beta_{\mathrm{ISM}} = 1.7$ in the outer disk. Nevertheless, they also display some important differences that can be understood by recalling the method used to derive them. In our multiwavelength analysis, the constraint is posed on the $a_{\max}(R)$ profile, while $\beta(R)$ is calculated as a post-processing result of the analysis through the Mie theory as explained in Section 3.2.2. It is then natural that a slowly decreasing $a_{\max}(R)$ profile results in a slowly increasing $\beta(R)$ profile. The analysis by Pérez et al. (2012), on the other hand, poses a direct constraint on $\beta(R)$, which is computed substantially as the ratio of the optical depth profiles $\tau_\lambda(R)$ at 0.88 and 8.00 mm obtained from the single-wavelength fits, although the actual procedure they use is more refined since they employ a MCMC to compute a PDF for $\beta(R)$ given the $\tau_\lambda(R)$ profiles and and average temperature $\overline{T}(R)$. For these reasons, the $\beta(R)$ profiles obtained by these two methods are not directly comparable point by point in radius; nevertheless, they show common evidence of an increasing β with radius.

---

[1]This limitation is related to the dust parametrization, not to the multiwavelength approach of the fit: the implementation of more sophisticated $a_{\max}(R)$ parametrizations is not only possible, but is one of the advantages of having a fit architecture that is highly modular.
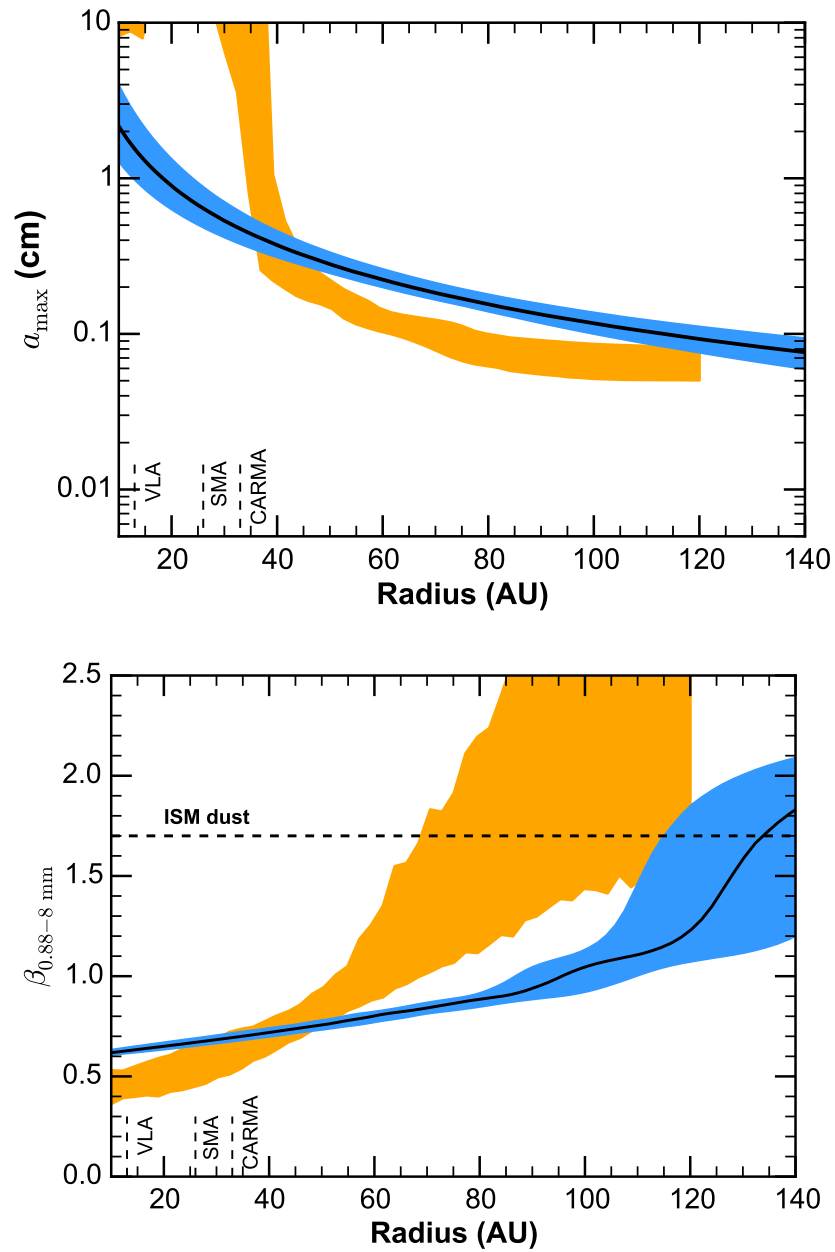
Fig. C.3 *Left panel:* maximum dust grain size a_{max} as a function of the disk radius. *Right panel:* dust opacity spectral index β between 0.88 and 8 mm as a function of the disk radius. *Both panels:* the solid black line with the shadowed blue area represent the best-fit and the 3σ region constrained by our multiwavelength analysis. The yellow shaded area represent the 3σ region obtained by Pérez et al. (2012). The vertical dashed lines represent the spatial resolution of the observations.
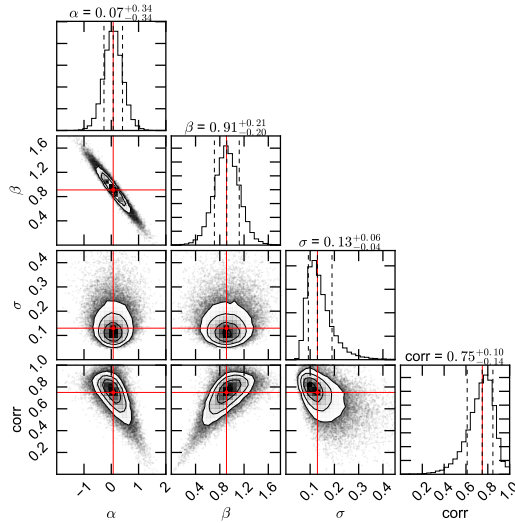
D

Additional material of the Lupus disks analysis

D.1 $M_\mathrm{d} \propto R_c$ correlation

Here we report the results of the bayesian linear regression performed to search for a correlation between the dust mass (M_d) and the disk exponential cut-off radius (R_c).

Fig. D.1   Staircase plot showing the MCMC resulting from the application of the Bayesian regression method by Kelly (2007) to infer a law for M_dust versus R_c (cfr. Figure 5.12). From left to right, the parameters are the intercept (α), the slope (β), the intrinsic scatter of data points (σ) and the correlation degree (corr). The red lines highlight the posterior PDF peak.

D.2   Fits of the individual sources

Following the order in Table 5.3, we report the results of the fits for the individual sources.
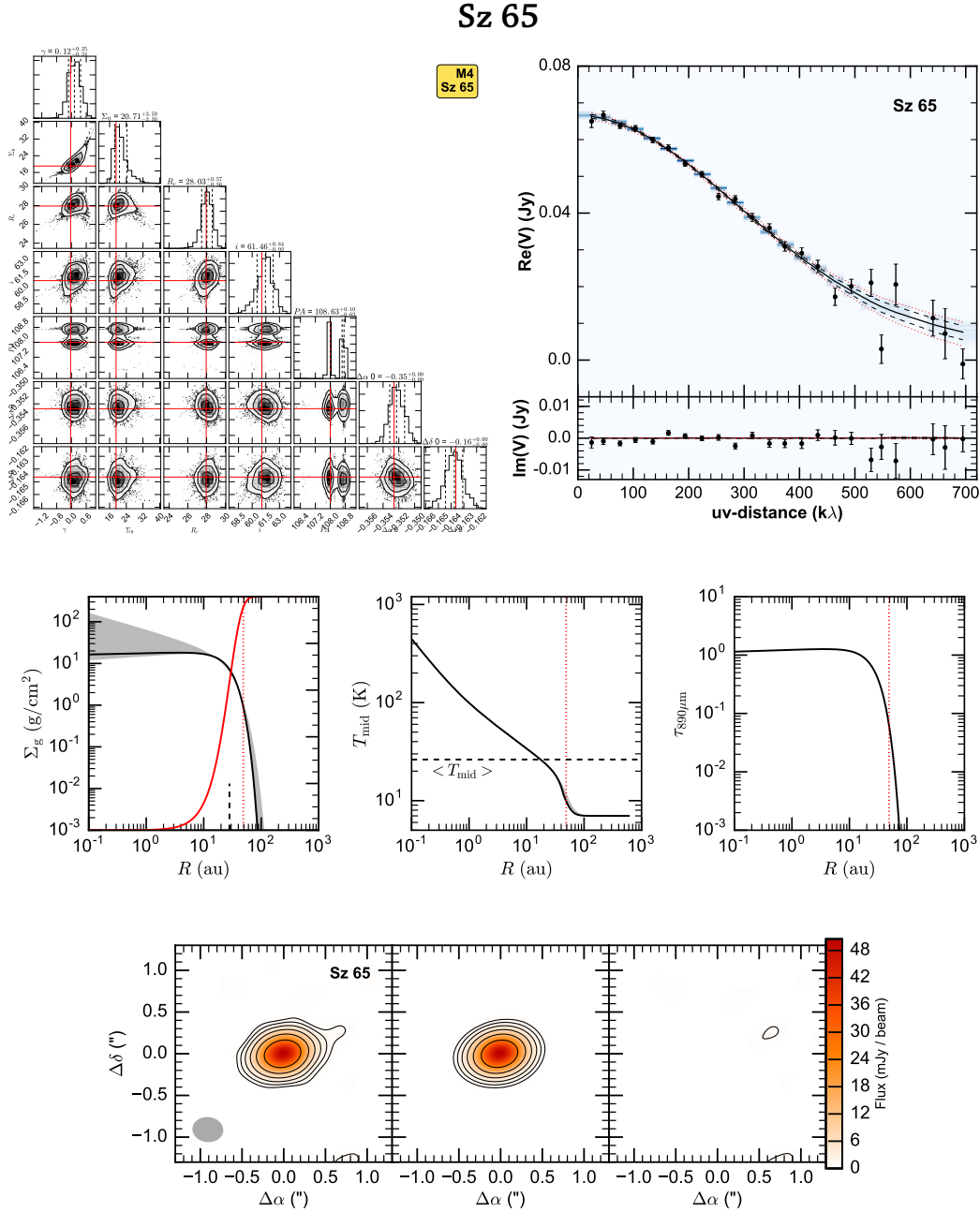
Sz 65

Fig. D.2 Fit results for Sz 65. *Top row:* on the left, the staircase plot showing the MCMC chains as in Figure 5.3; on the right, the comparison of the observations and model deprojected visibilities as a function of $uv-$distance as in Figure 5.5. *Middle row:* plots showing the physical structure of the disk as in Figure 5.4. *Bottom row:* synthesized images of observations, model and residual visibilities as in Figure 5.6. In the images $\sigma = 0.3$ mJy/beam.
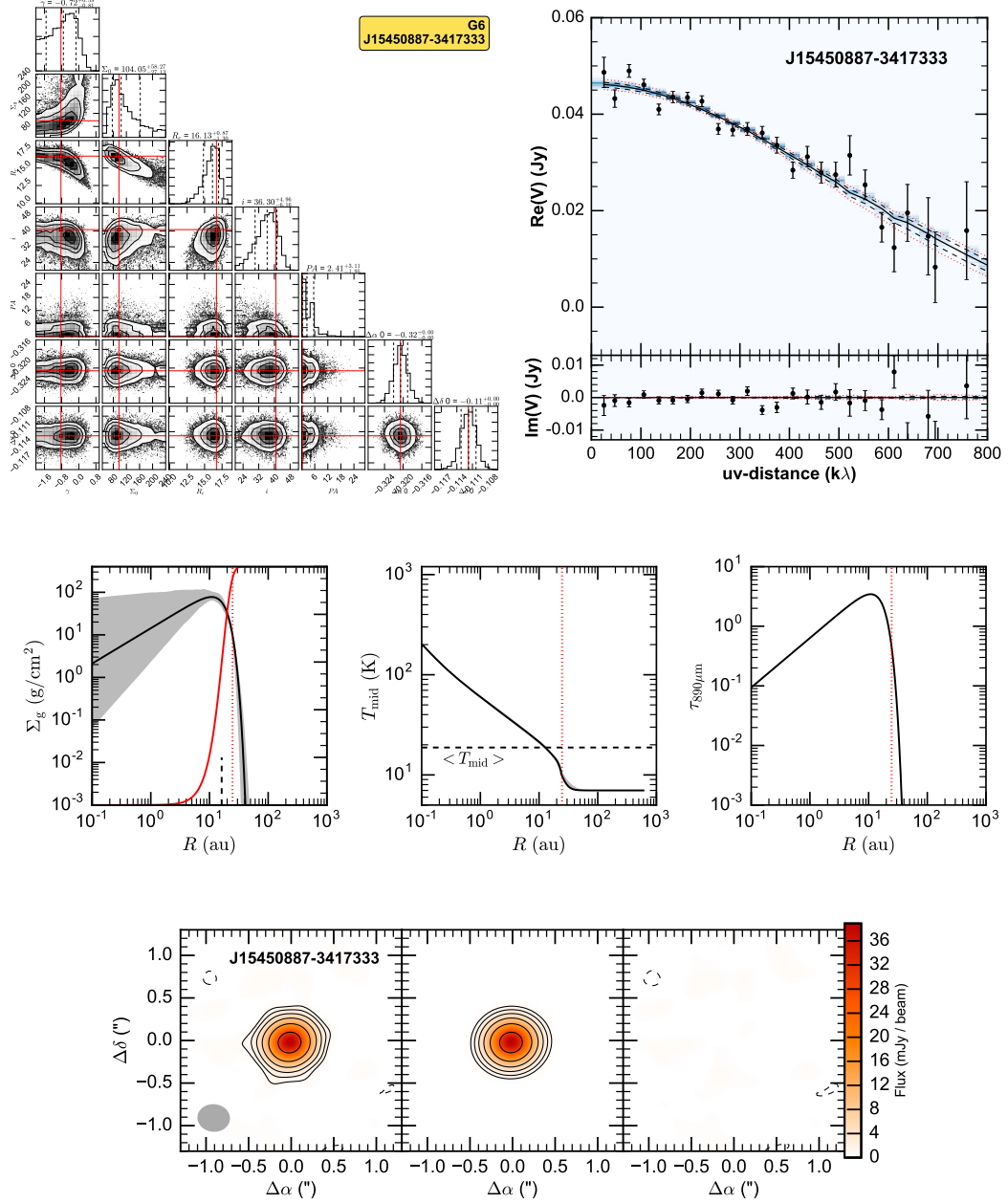
J15450887-3417333

Fig. D.3 Fit results for J15450887-3417333, presented as in Figure D.2. In the images $\sigma = 0.3\,\mathrm{mJy/beam}$.
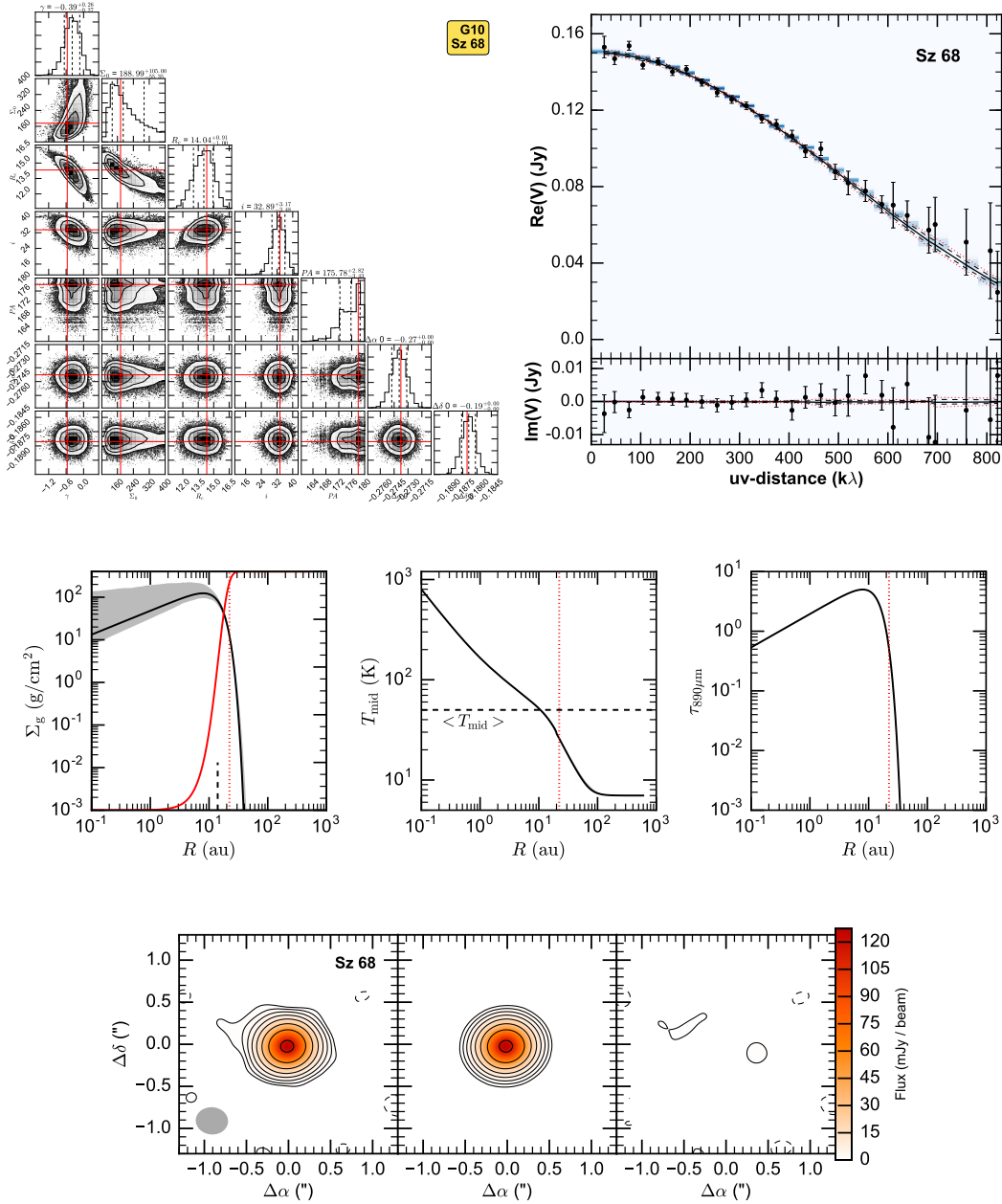
Sz 68

Fig. D.4   Fit results for Sz 68, presented as in Figure D.2. In the images $\sigma = 0.3\,\mathrm{mJy/beam}$.

Sz 69

Fig. D.5 Fit results for Sz 69, presented as in Figure D.2. In the images $\sigma = 0.3\,\mathrm{mJy/beam}$.

Sz 71

Fig. D.6 Fit results for *Sz 71*, presented as in Figure D.2. In the images $\sigma = 0.3\,\mathrm{mJy/beam}$.
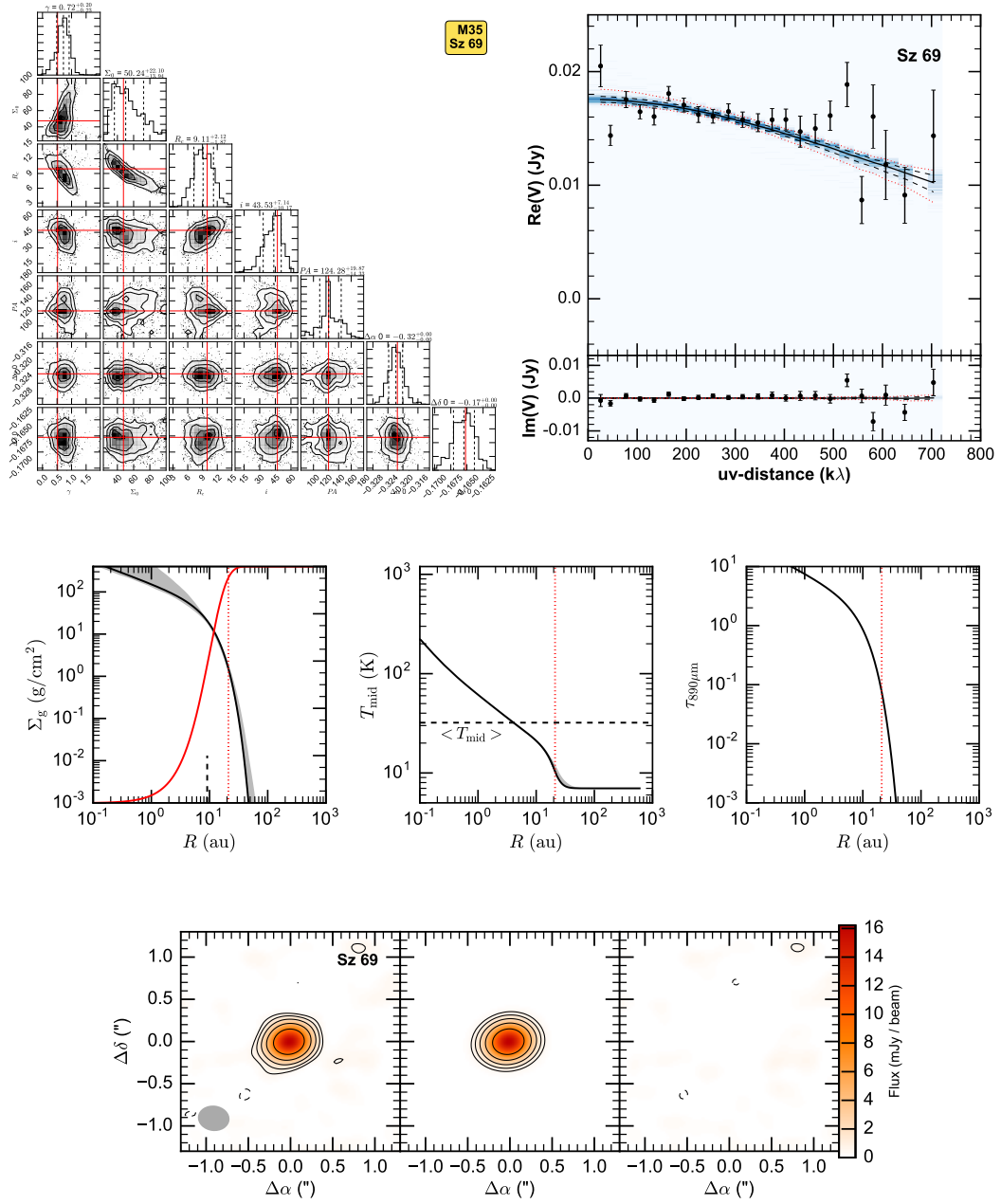
Sz 73

Fig. D.7 Fit results for Sz 73, presented as in Figure D.2. In the images $\sigma = 0.3$ mJy/beam.

IM Lup

Fig. D.8 Fit results for IM Lup, presented as in Figure D.2. In the images $\sigma = 0.3\,\mathrm{mJy/beam}$.

Sz 83

Fig. D.9 Fit results for Sz 83, presented as in Figure D.2. In the images $\sigma = 0.3$ mJy/beam.

Sz 84
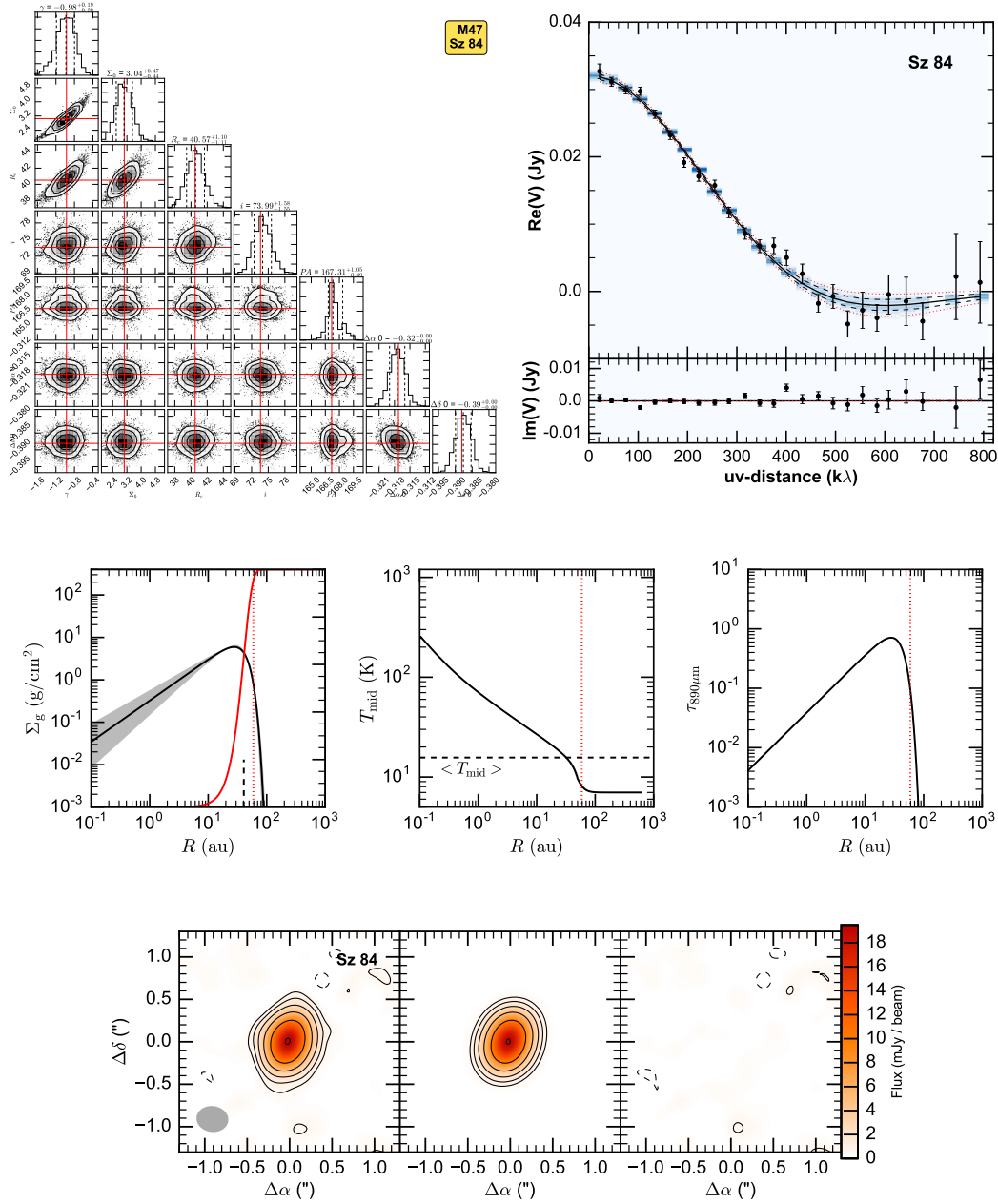
Fig. D.10　Fit results for Sz 84, presented as in Figure D.2. In the images $\sigma = 0.3$ mJy/beam.
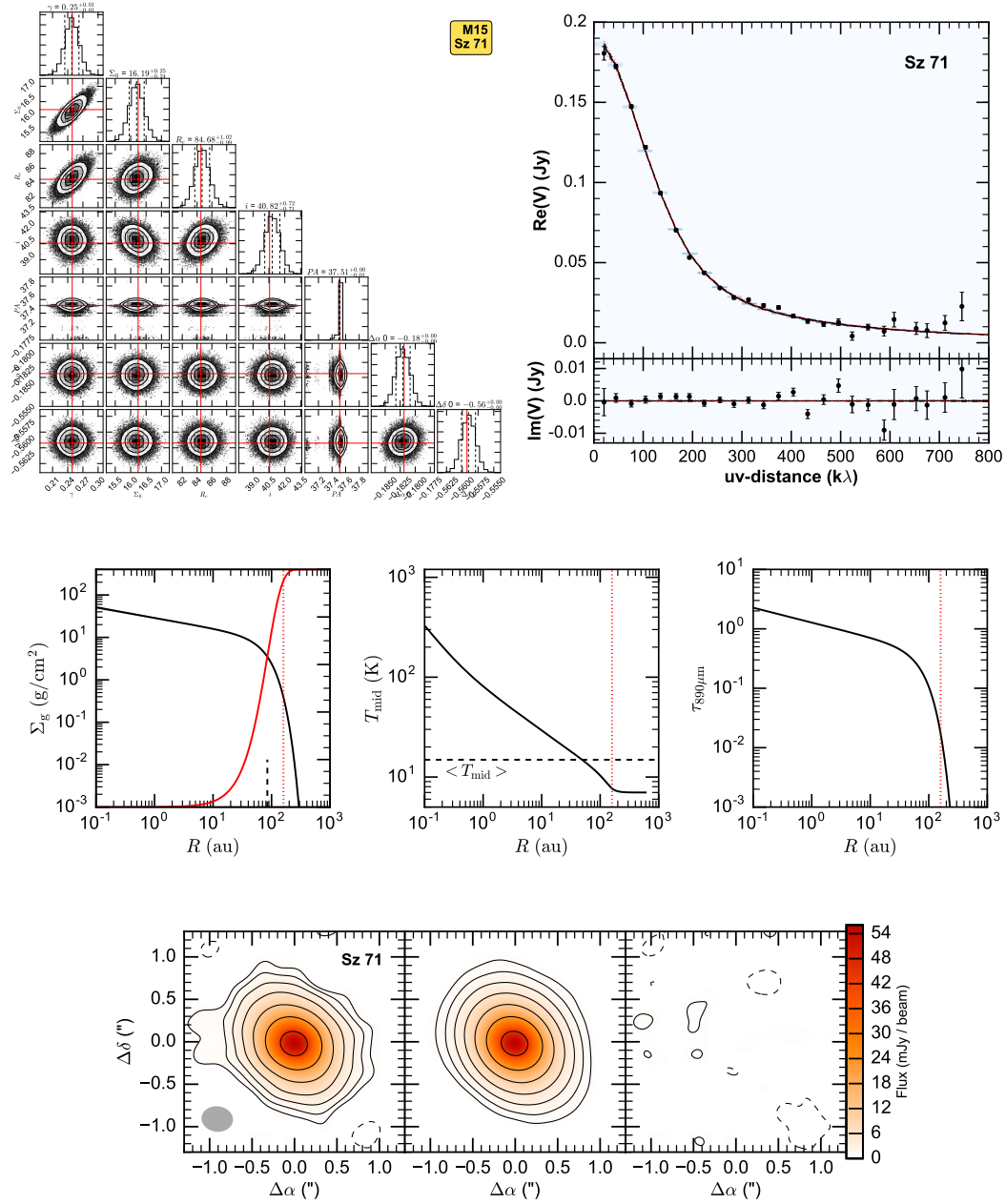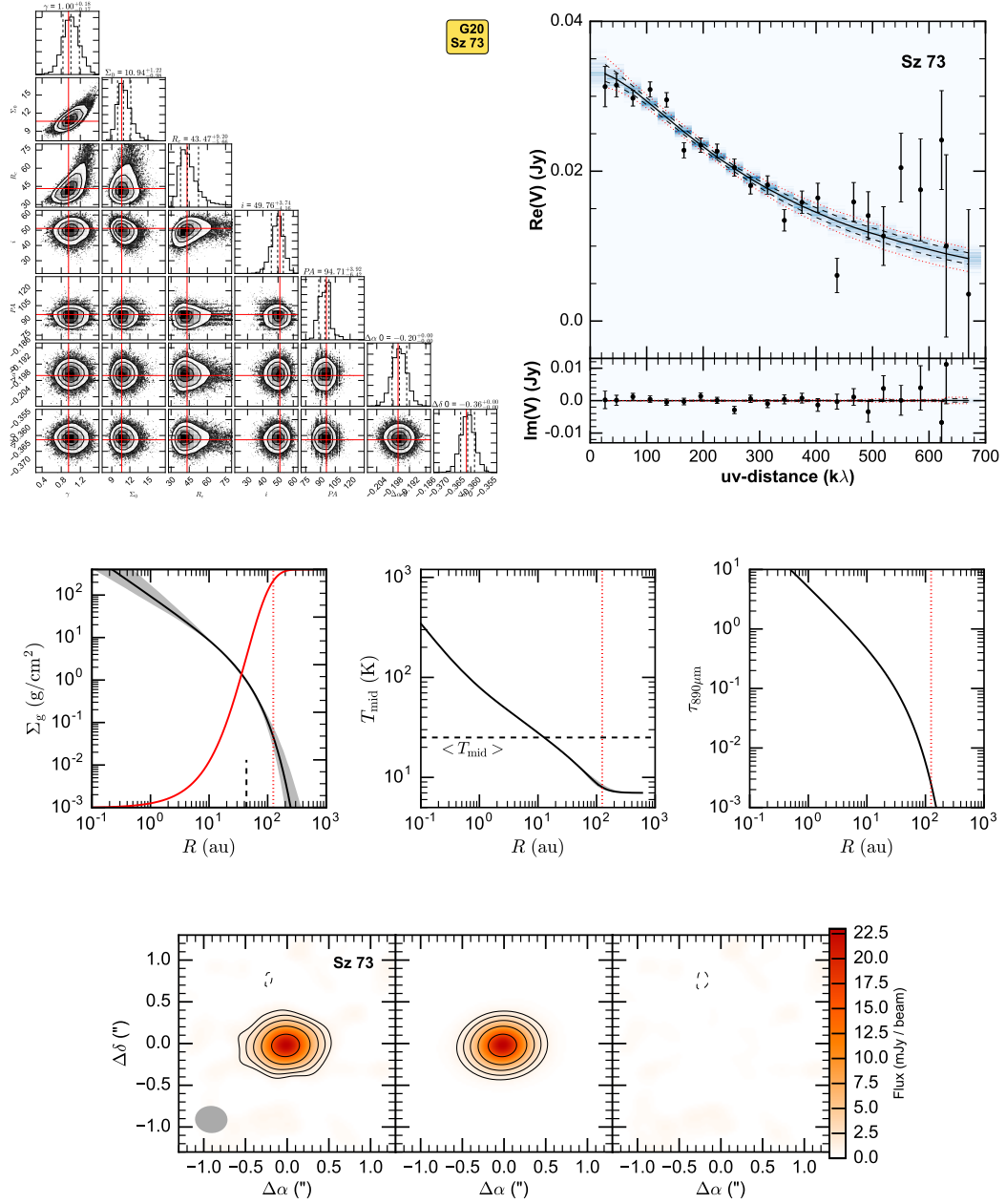
Sz 129
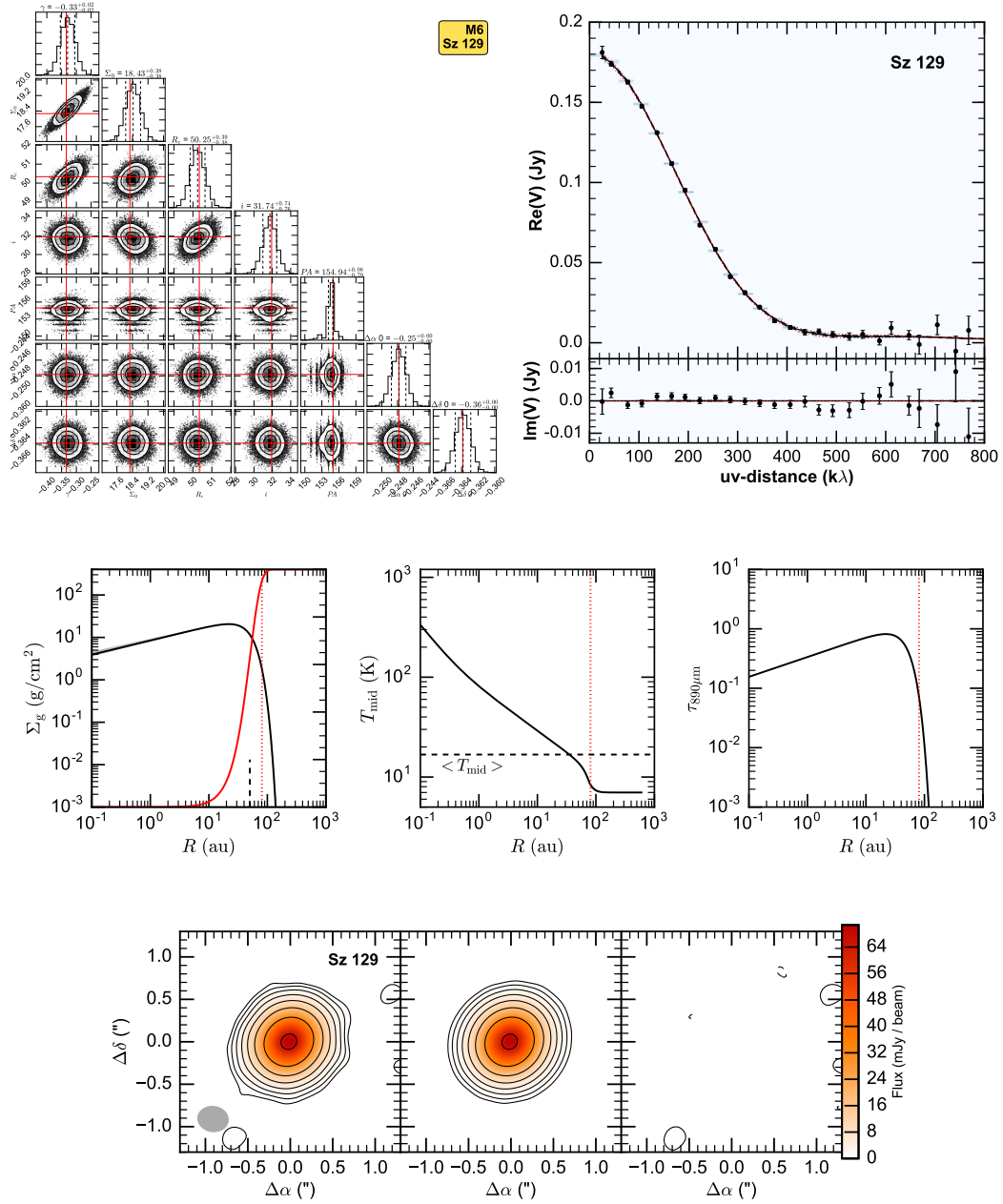
Fig. D.11 Fit results for Sz 129, presented as in Figure D.2. In the images $\sigma = 0.3\,\mathrm{mJy/beam}$.
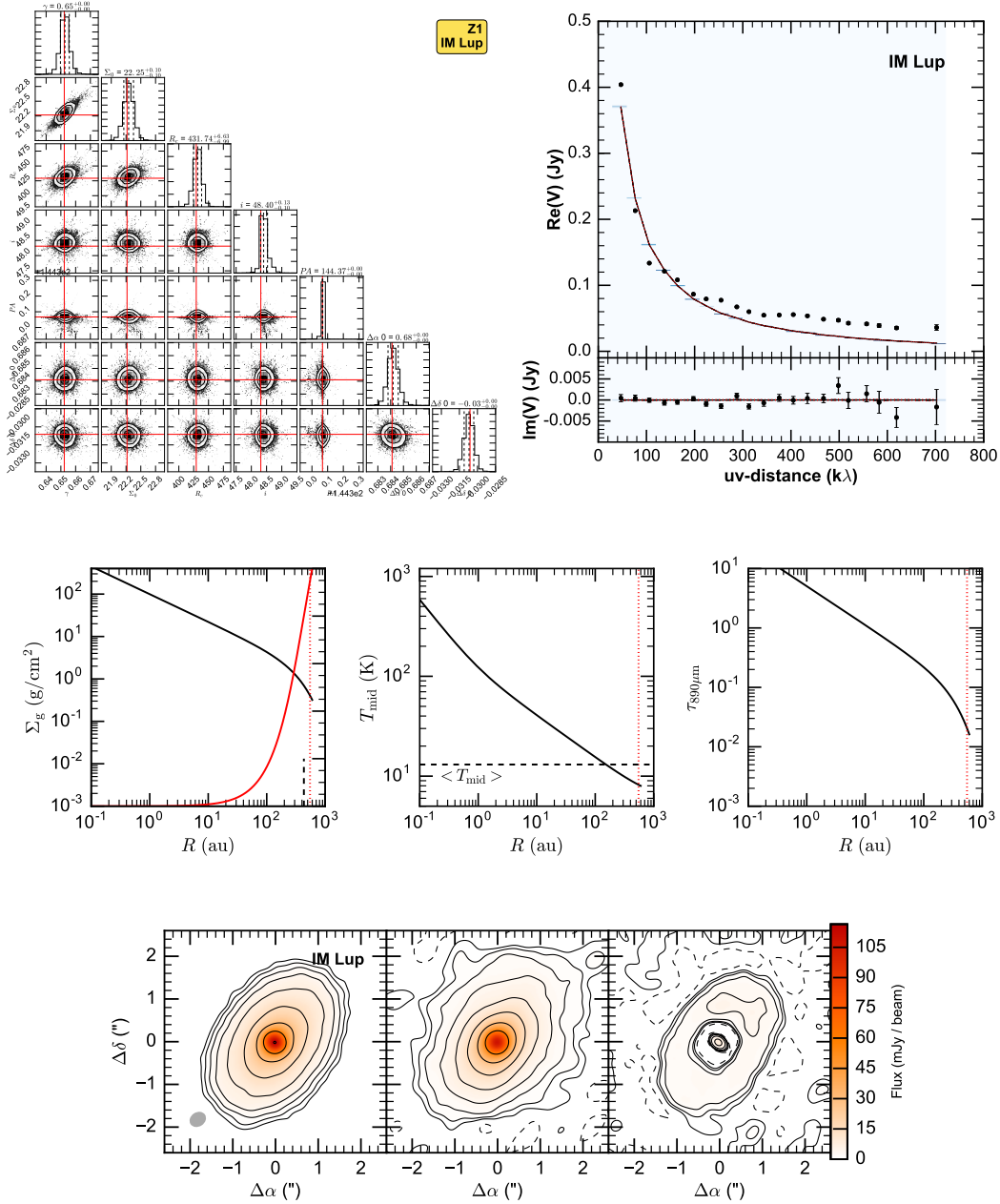
J16000236-4222145
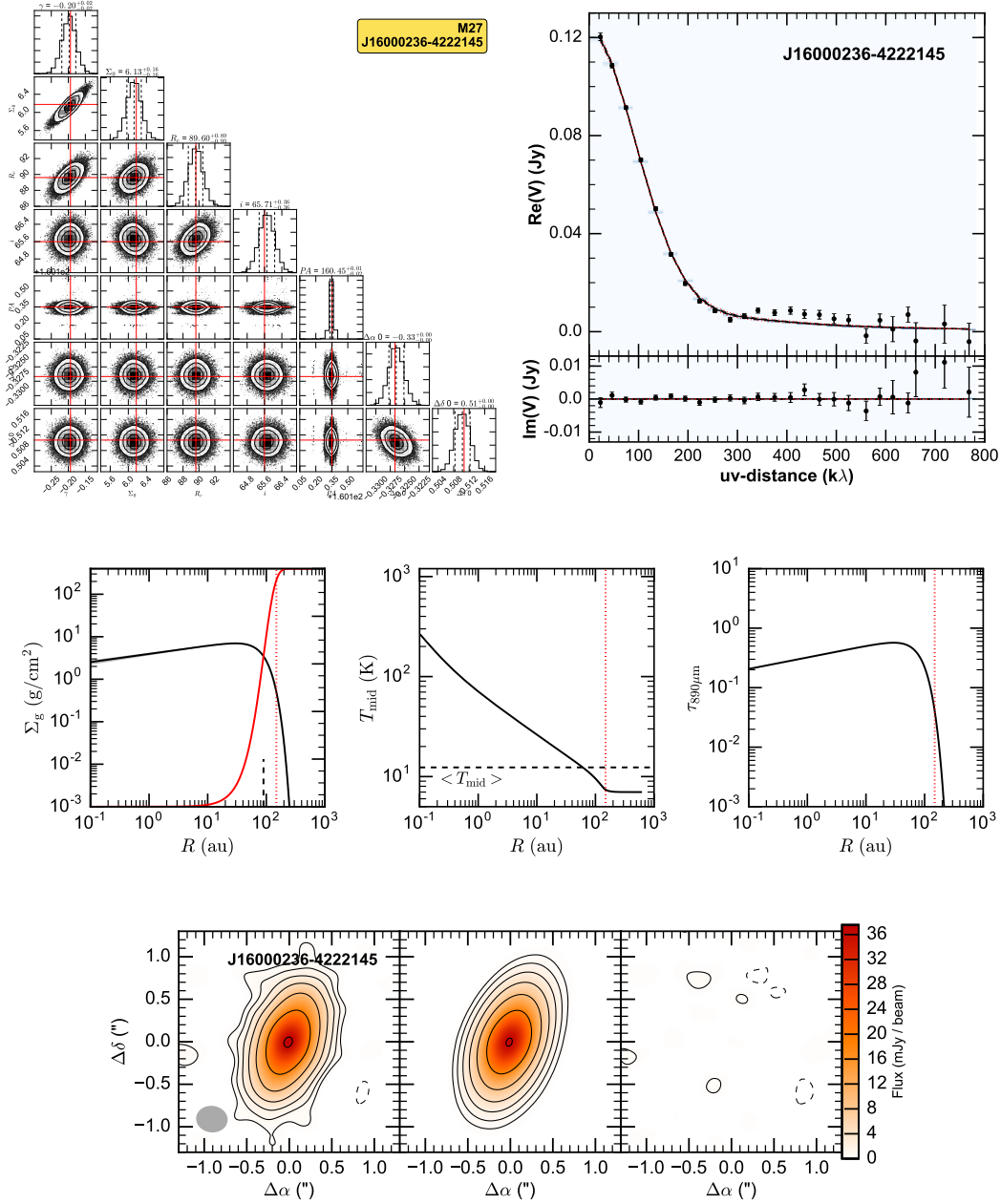
Fig. D.12 Fit results for J16000236-4222145, presented as in Figure D.2. In the images $\sigma = 0.3$ mJy/beam.

MY Lup
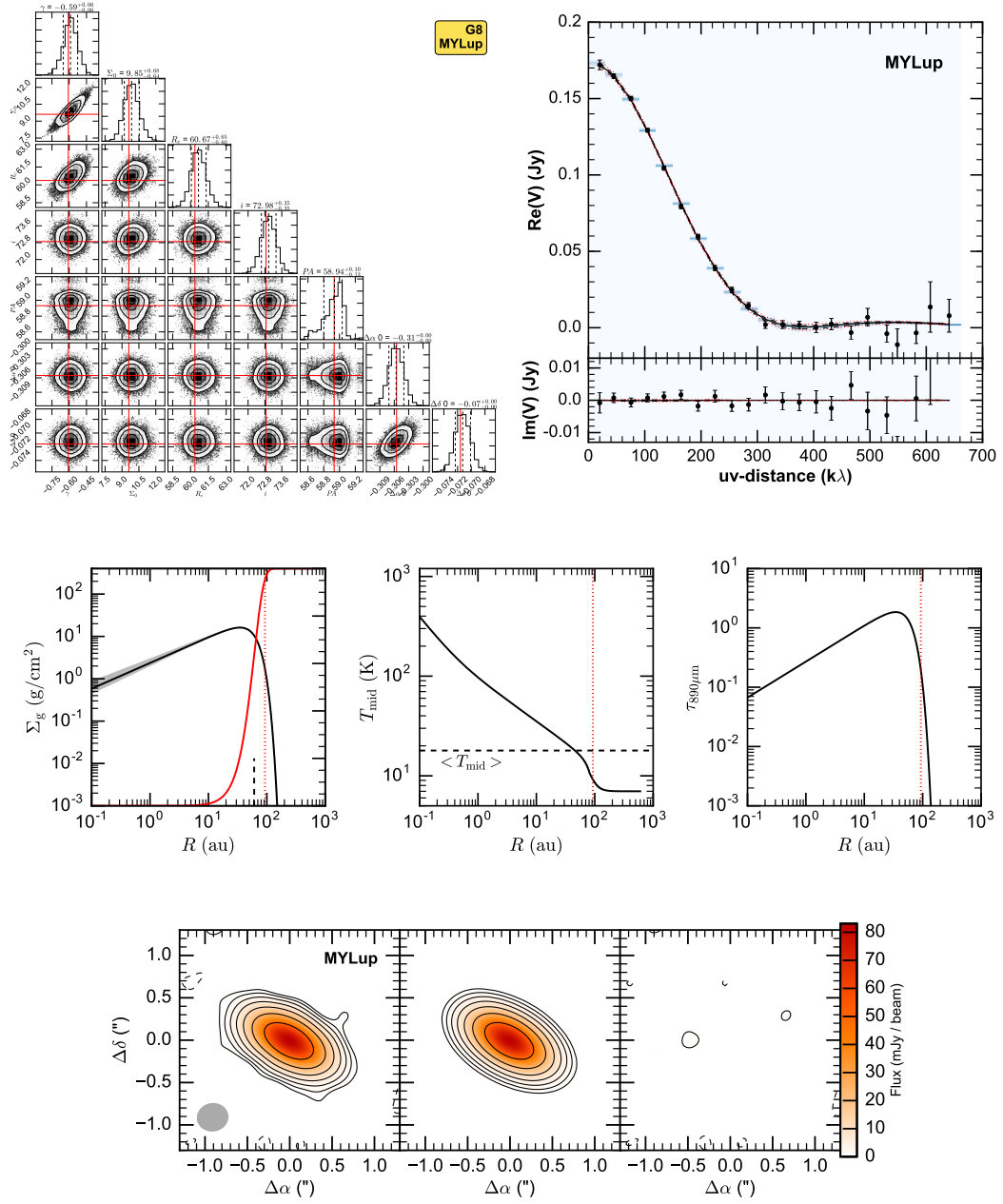
Fig. D.13 Fit results for MY Lup, presented as in Figure D.2. In the images $\sigma = 0.3\,\mathrm{mJy/beam}$.

Sz 133
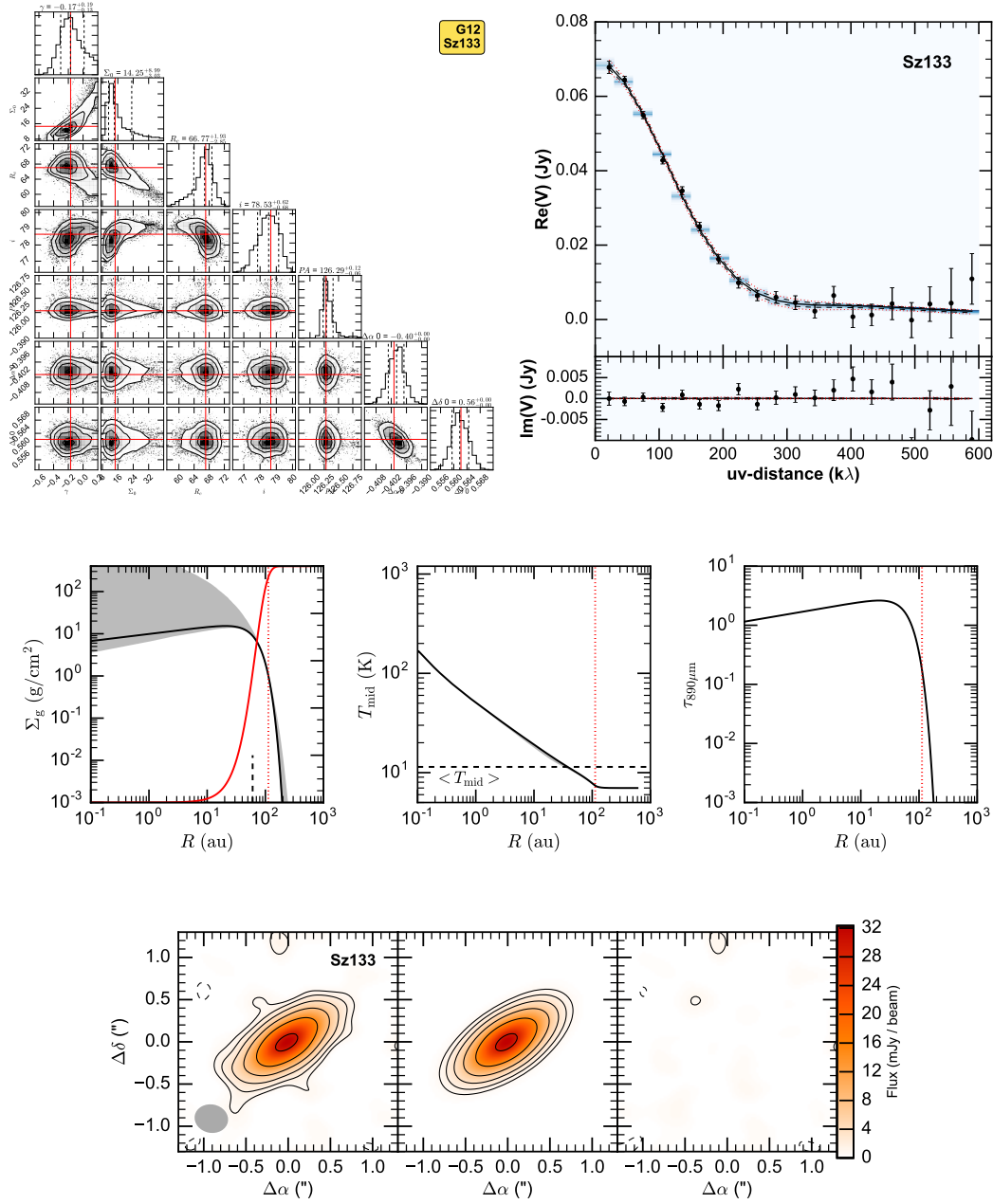
Fig. D.14   Fit results for Sz 133, presented as in Figure D.2. In the images $\sigma = 0.3$ mJy/beam.
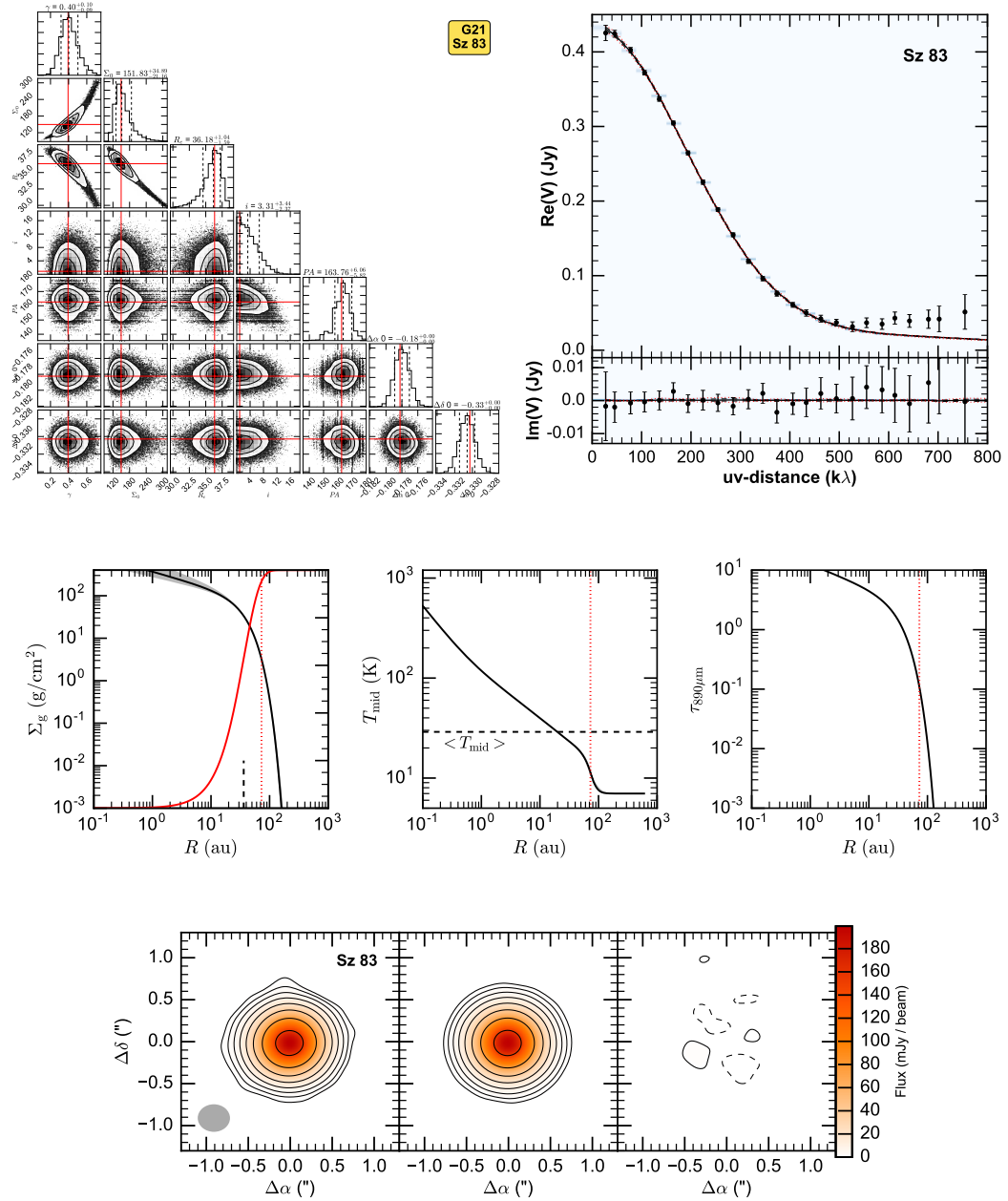
Sz 90
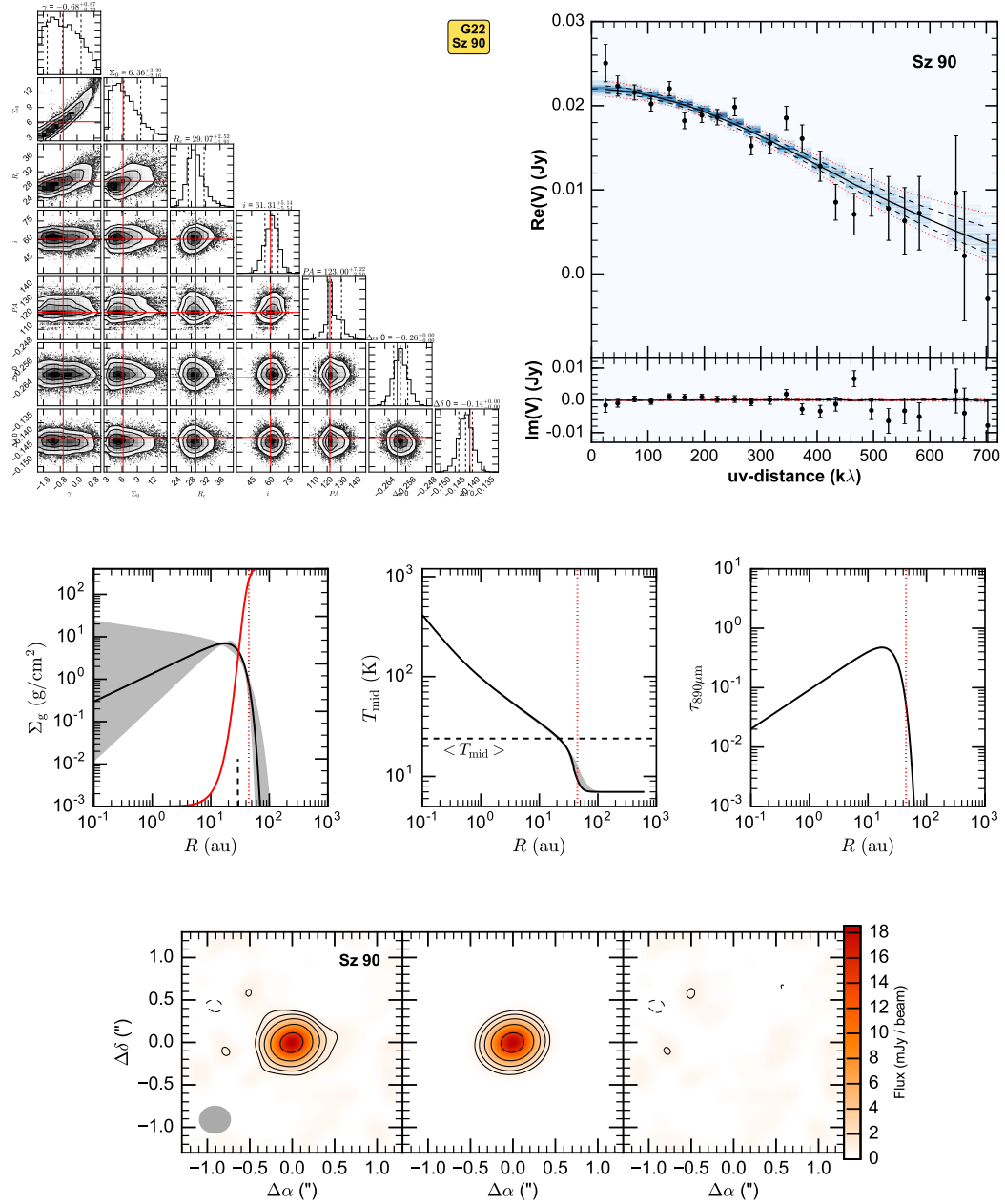
Fig. D.15 Fit results for Sz 90, presented as in Figure D.2. In the images $\sigma = 0.3$ mJy/beam.

Sz 98
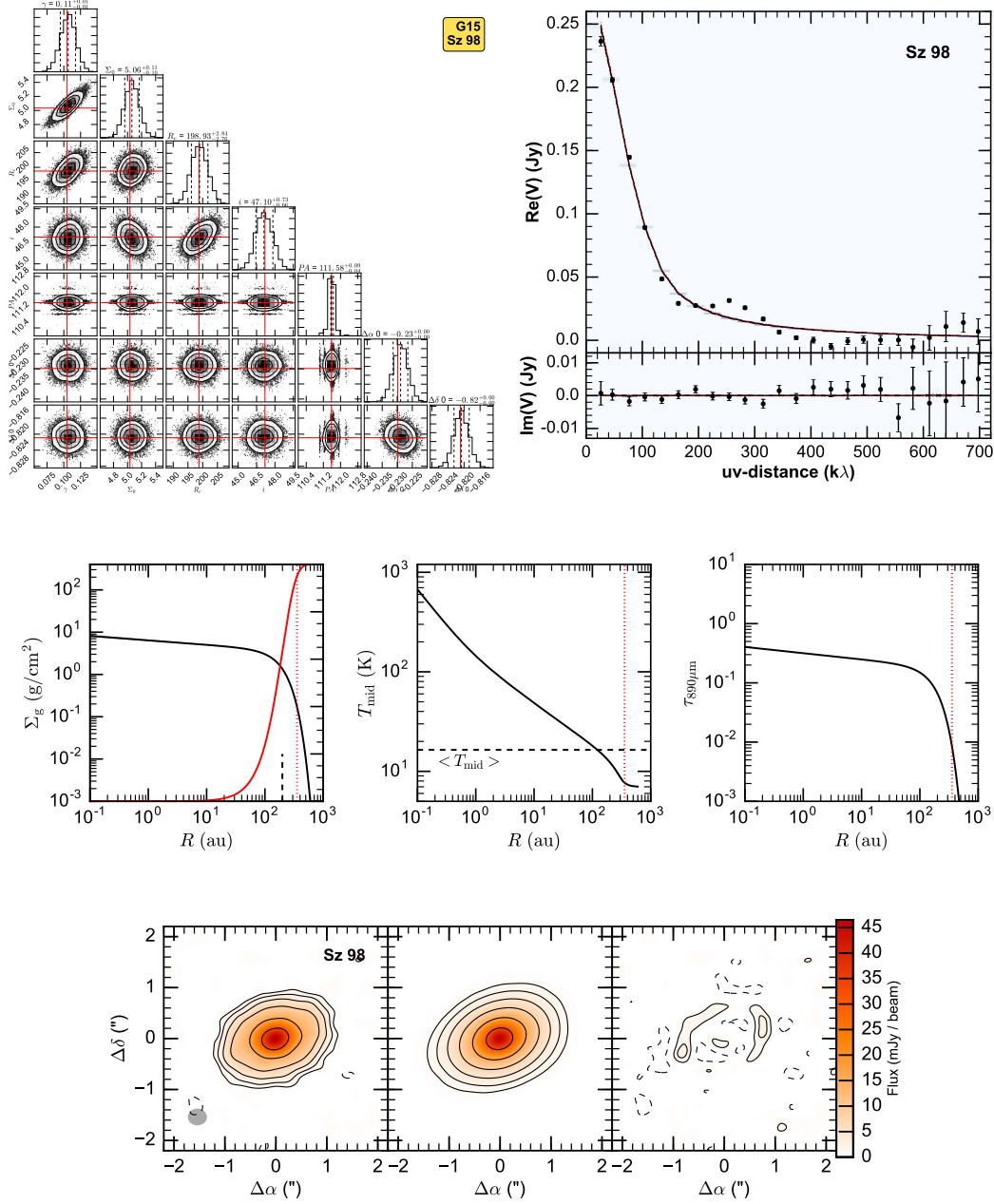
Fig. D.16 Fit results for Sz 98, presented as in Figure D.2. In the images $\sigma = 0.3\,\text{mJy/beam}$.

Sz 100

Fig. D.17 Fit results for Sz 100, presented as in Figure D.2. In the images $\sigma = 0.3$ mJy/beam.

Sz 108B

Fig. D.18 Fit results for Sz 108B, presented as in Figure D.2. In the images $\sigma = 0.3$ mJy/beam.

J16085324-3914401

Fig. D.19 Fit results for J16085324-3914401, presented as in Figure D.2. In the images $\sigma = 0.3\,\mathrm{mJy/beam}$.

Sz 113

Fig. D.20   Fit results for Sz 113, presented as in Figure D.2. In the images $\sigma = 0.3$ mJy/beam.

Sz 114

Fig. D.21 Fit results for Sz 114, presented as in Figure D.2. In the images $\sigma = 0.3$ mJy/beam.
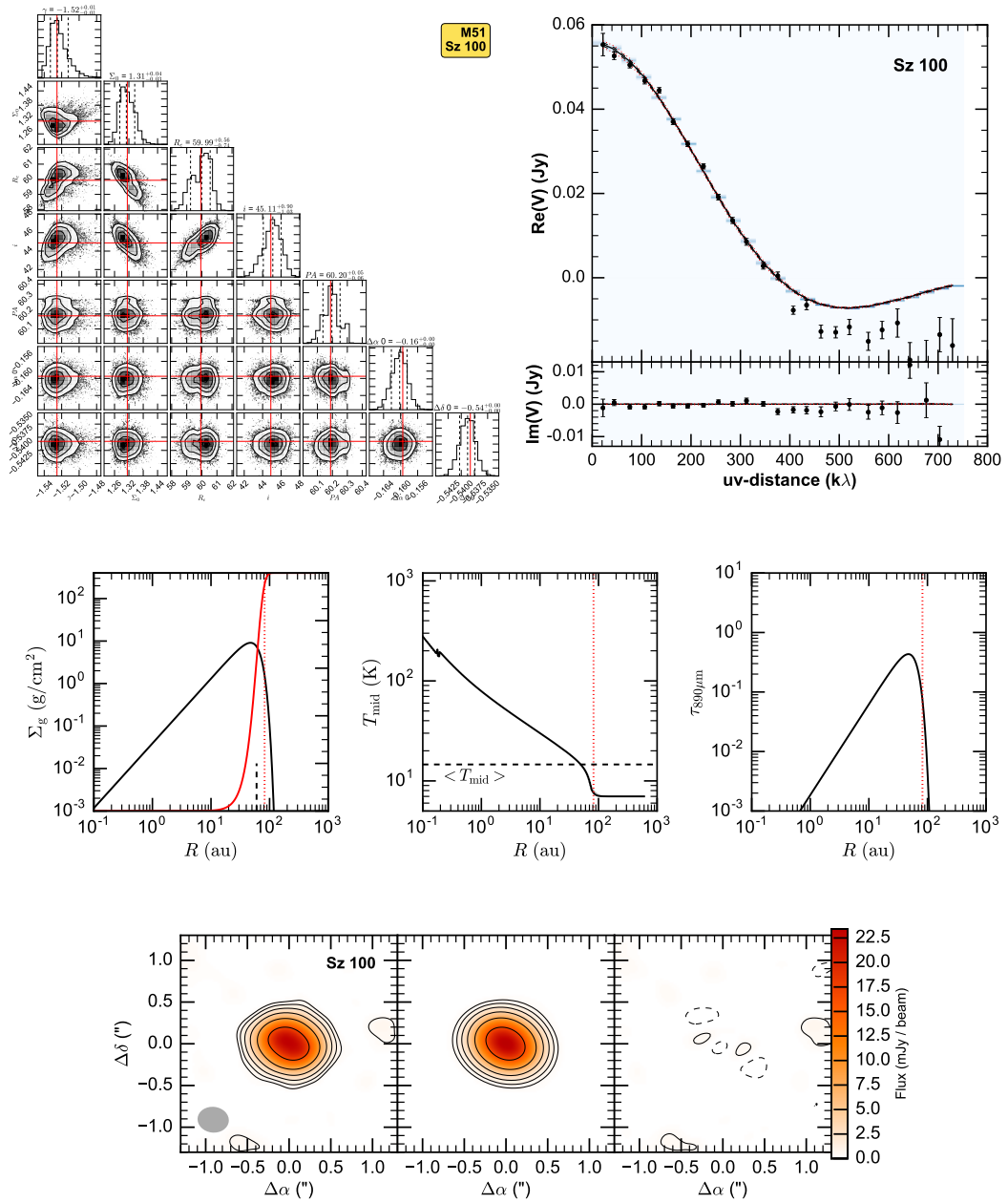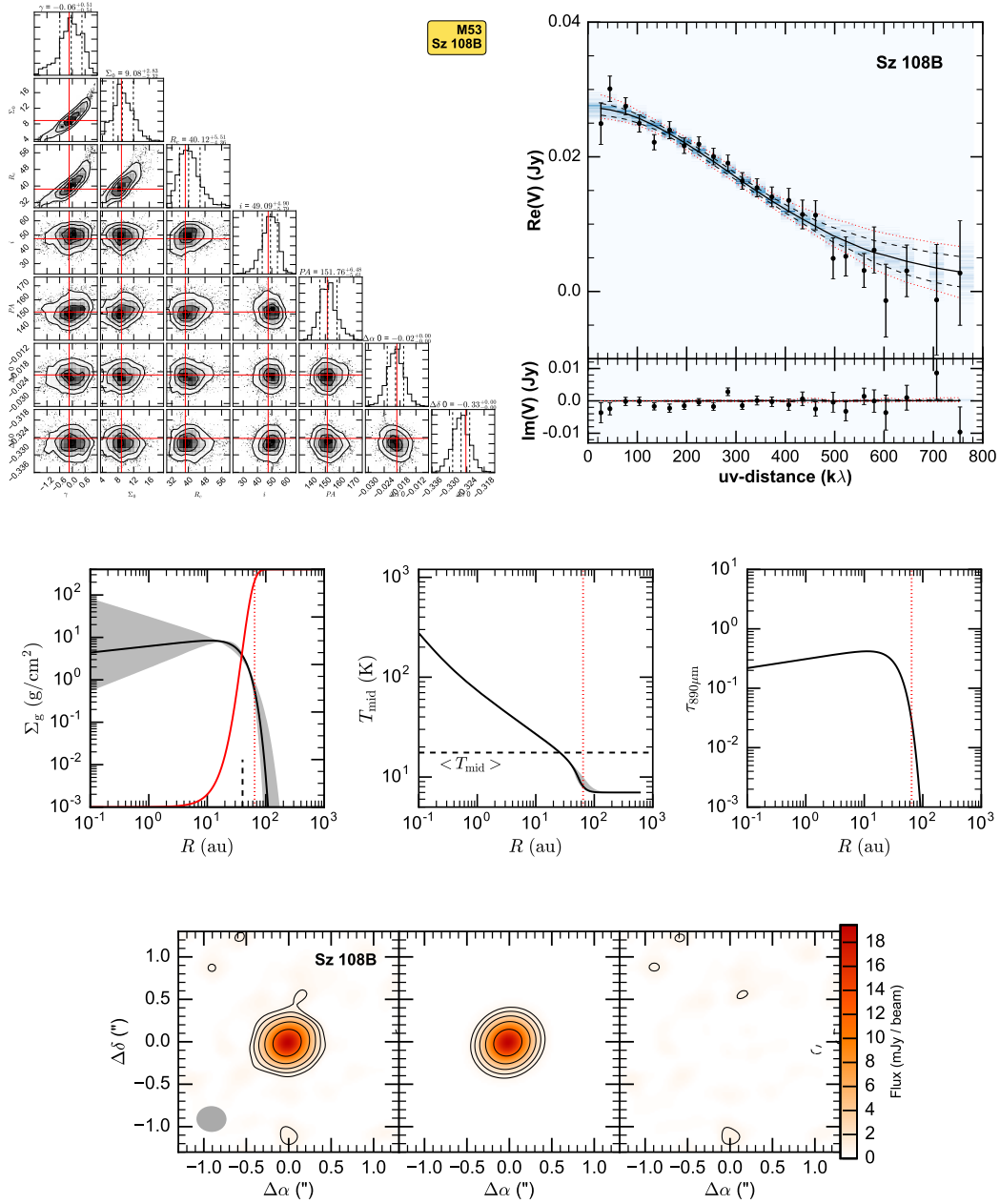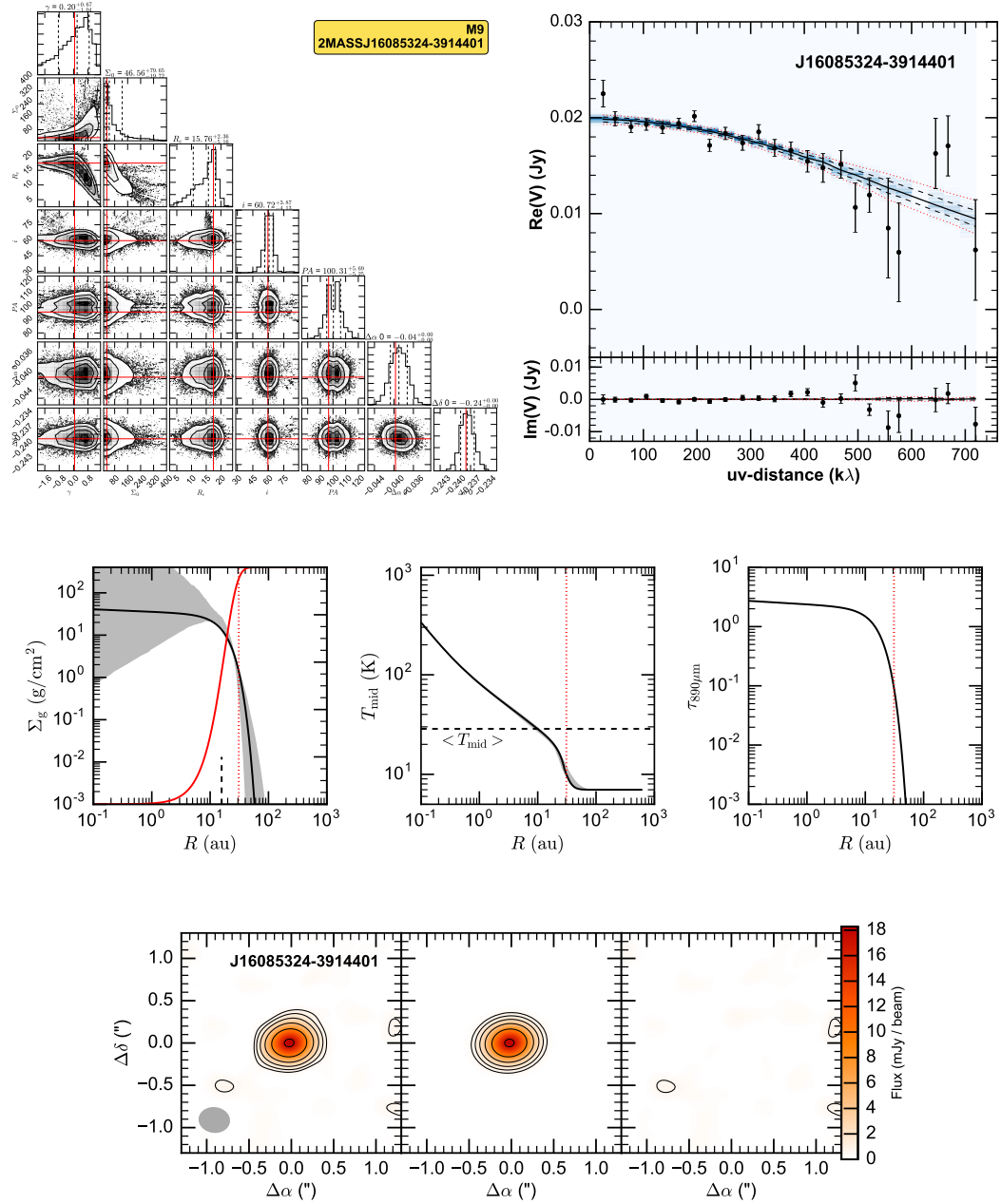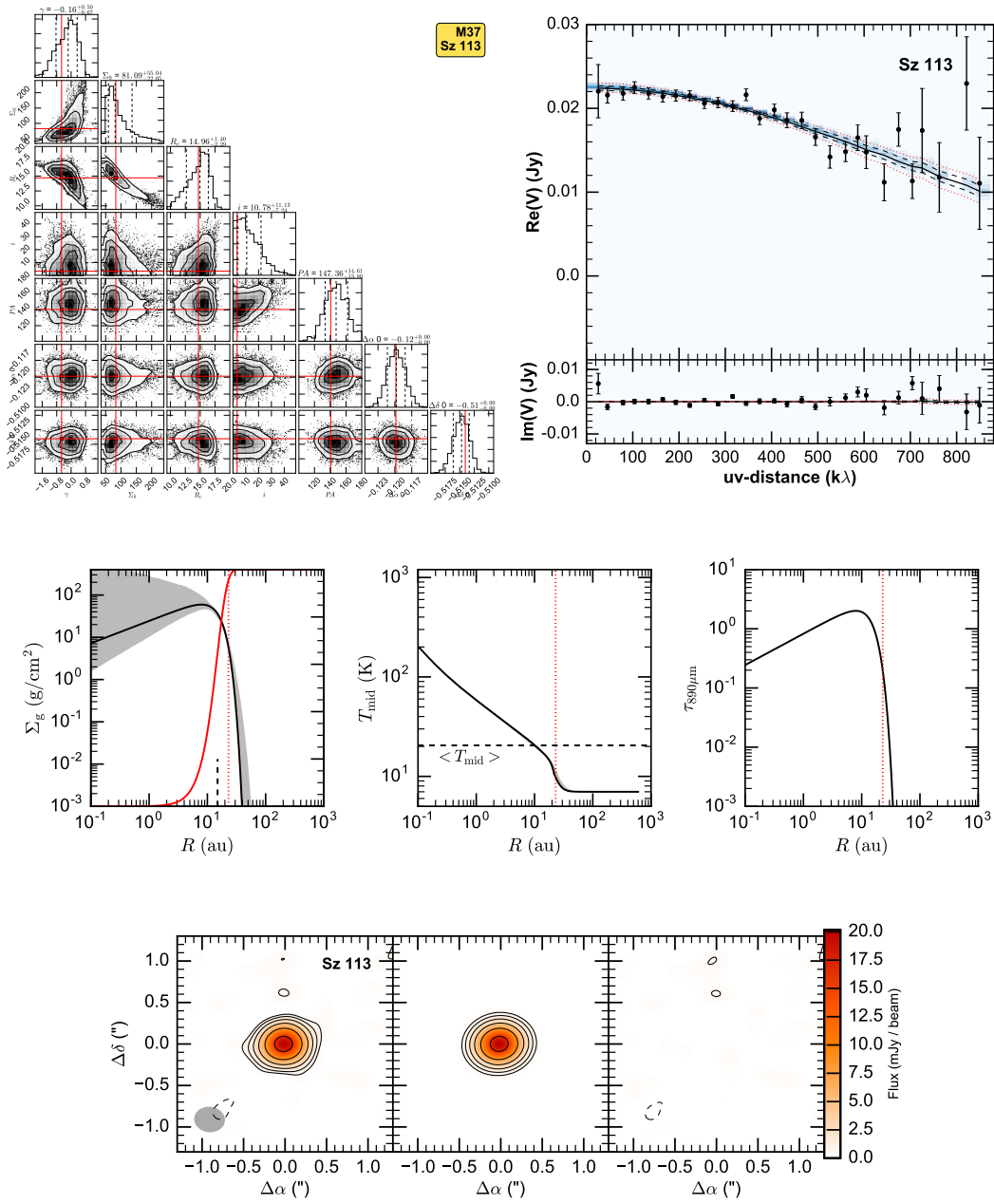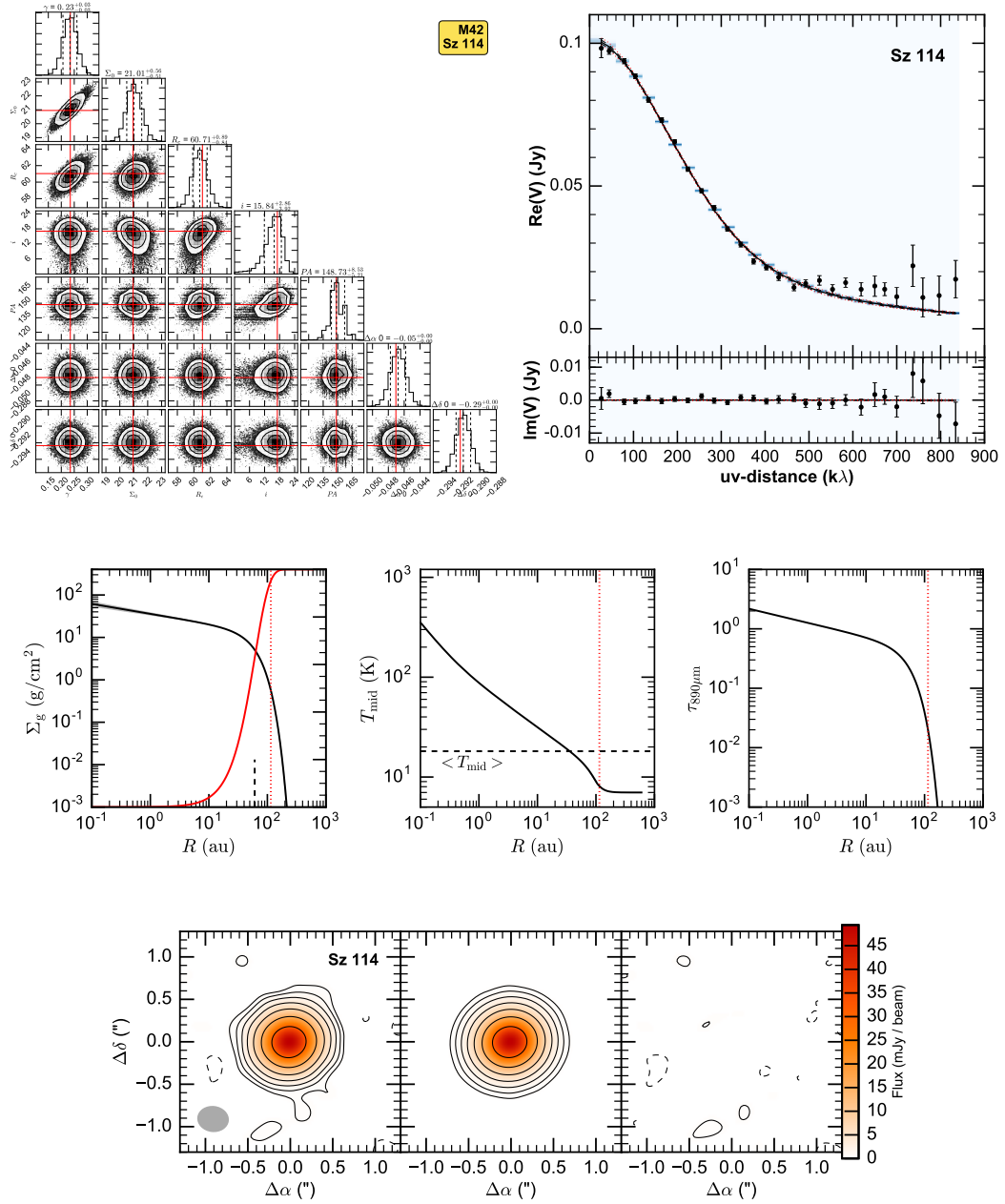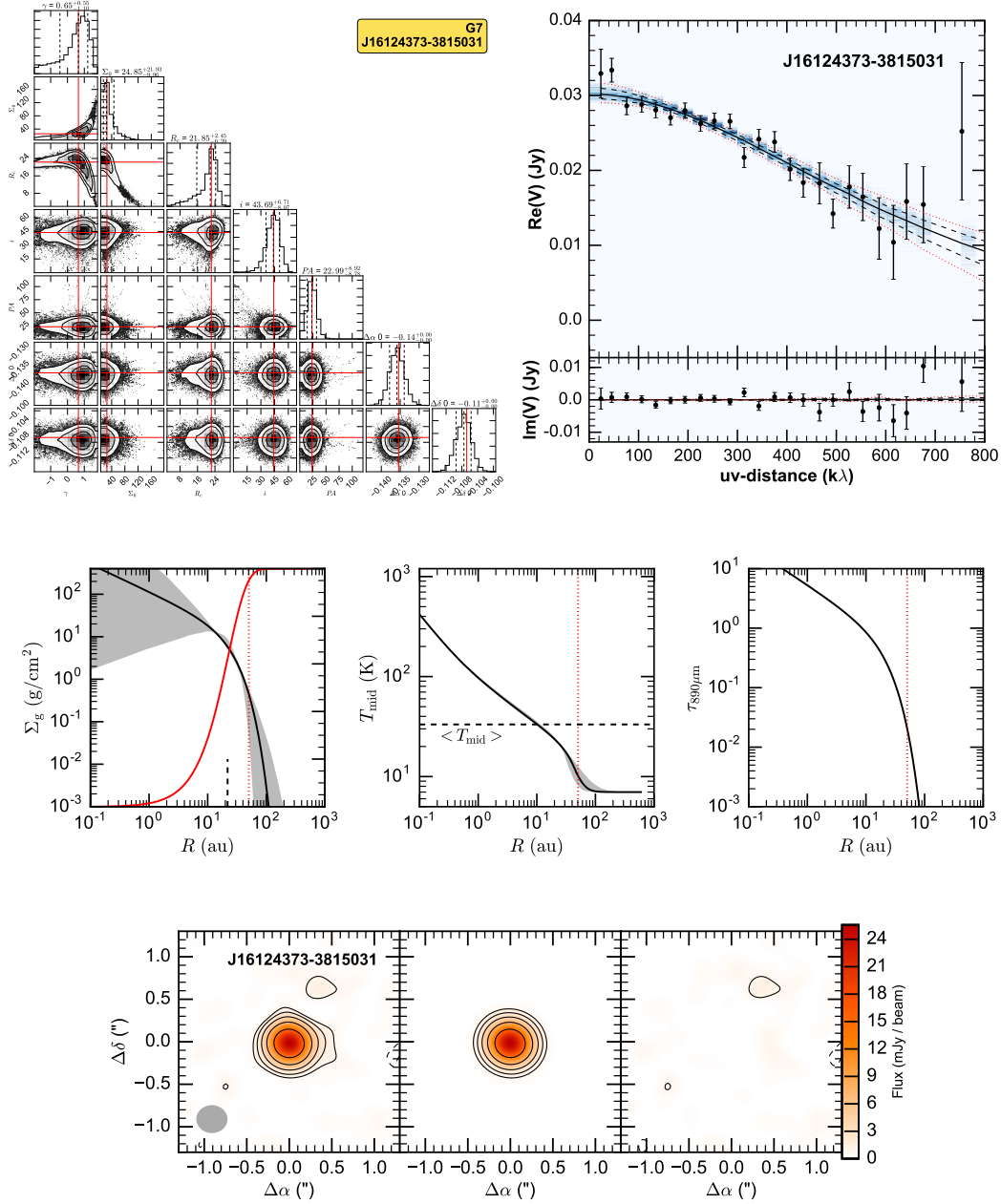
J16124373-3815031

Fig. D.22 Fit results for J16124373-3815031, presented as in Figure D.2. In the images $\sigma = 0.3$ mJy/beam.

E

Details of `pyvfit` implementation

Sample kernels and their implementation

Here we present the implementation of the `shift` algorithm in a CUDA C++ kernel. This example shows how the latest NVIDIA CUDA technologies allows us to write code that is portable, scalable and easily debuggable. In particular, we obtain most of the benefit thanks to the usage of *grid-stride loops*. In the code below we report four functions:

1. `shift_core`: this is the core algorithm. It implements the swap of two matrix elements so that elements of the upper-left quadrant are swapped with those in the lower-right one, and those of the lower-left quadrant with those of the upper-right one. The preprocessor variable `__CUDACC__` used the in the `#ifdef` clauses is used to define the lines that have to be executed only when the GPU version is compiled (i.e. using the NVIDIA nvcc compiler). If the version for CPU is compiled (e.g., with any C++ compiler), the other lines are executed. It is remarkable that for `shift_core`, only the declaration depends on the GPU vs CPU version, and all the instructions are exactly the same both for GPU and CPU execution.

2. `shift_d`: is a wrapper function for the GPU version. It defines the loops over the matrix elements on which the shift is performed. Actually, the loops are done only on *half* of the matrix elements because the `shift_core` function automatically computes the homologous element that should be used for the swap. Moreover, we are using the so called *grid-stride loops*: the stride of the loops is not 1 as usual, but equals the number of threads within the grid of blocks (`blockDim.x` × `gridDim.x`). This allows the `shift_d` kernel to be called without requiring the number of threads to be sufficient to cover all the data at the same time. The data (i.e., the matrix) is processed one grid-size at a time.

3. `shift_h`: this is a wrapper function for the CPU version. It defines the loops on the data (the stride is now 1), and with only one additional line of code on the head of the for loops make the code capable of exploiting the OpenMP technology. Again, the core algorithm of the shift is inlined from the `shift_core` algorithm.

4. `C_acc_shift`: this is the general wrapper that is accessed from Python. If the GPU version is compiled, it performs the memory copy and calls the GPU wrapper `shift_d`. If the CPU version is called, then `shift_h` is executed.

It is apparent from the code above that the usage of grid-stride loops brings several advantages. First, it allows to keep the code readable, and to separate the core algorithm

```
#ifdef __CUDACC__
__host__ __device__ inline void shift_core
#else
inline void shift_core
#endif
(int const idx_x, int const idx_y, int const nx,
 dcomplex* const __restrict__ a) {
  auto const src_ul = idx_x + idx_y*nx;
  auto const src_ll = idx_x + idx_y*nx + nx*nx/2;
  auto const tgt_ul = src_ul + nx/2 + nx*nx/2;
  auto const tgt_ll = src_ll + nx/2 - nx*nx/2 ;

  auto const temp_ul = a[src_ul] ;
  a[src_ul] = a[tgt_ul] ;
  a[tgt_ul] = temp_ul ;

  auto const temp_ll = a[src_ll] ;
  a[src_ll] = a[tgt_ll];
  a[tgt_ll] = temp_ll;
}
```

Fig. E.1 Implementation of the `shift_core()` function.

```
#ifdef __CUDACC__
__global__ void shift_d
(int const nx, dcomplex* const __restrict__ a) {
  // indices
  int const x0 = blockDim.x * blockIdx.x + threadIdx.x
  int const y0 = blockDim.y * blockIdx.y + threadIdx.y

  // stride
  int const sx = blockDim.x * gridDim.x;
  int const sy = blockDim.y * gridDim.y;

  for (auto x = x0; x < nx/2; x += sx) {
    for (auto y = y0; y < nx/2; y += sy) {
      shift_core(x, y, nx, a);
    }
  }
}
#endif
```

Fig. E.2 Implementation of the `shift_d()` function.

```
void shift_h
(int const nx, dcomplex* const __restrict__ a) {
#pragma omp parallel for
  for (auto x = 0; x < nx/2; ++x) {
    for (auto y = 0; y < nx/2; ++y) {
      shift_core(x, y, nx, a);
        }
    }
}
```

Fig. E.3 Implementation of the `shift_h` function.

```
void C_acc_shift(int nx, void* data) {
#ifdef __CUDACC__
    dcomplex *data_d;
  size_t nbytes = sizeof(dcomplex)*nx*nx;
  CCheck(cudaMalloc((void**)&data_d, nbytes));
  CCheck(cudaMemcpy(data_d, data, nbytes,
         cudaMemcpyHostToDevice));

  shift_d<<<dim3(nx/2/32+1, nx/2/32+1),
            dim3(32, 32)>>>(nx, (dcomplex*) data_d);

  CCheck(cudaDeviceSynchronize());
  CCheck(cudaMemcpy(data, data_d, nbytes,
         cudaMemcpyDeviceToHost));
  CCheck(cudaFree(data_d));
#else
    shift_h(nx, (dcomplex*) data);
#endif
}
```

Fig. E.4 Implementation of the C_acc_shift() function.

from the particular calls. Second, it allows to decouple the size of the CUDA grid from the size of the data being processed, thus reducing the overall coupling of the host and device properties. Third, it provides a clear programming pattern to develop portable code for GPU and CPU quickly and in a robust way.

Bibliography

Abdellah M. 2014. "cufftshift: High performance cuda-accelerated fft-shift library". In *Proceedings of the High Performance Computing Symposium*, HPC '14, pages 5:1–5:8. Society for Computer Simulation International, San Diego, CA, USA.

Adams F.C., Lada C.J., Shu F.H. 1987. "Spectral evolution of young stellar objects". *Astrophysical Journal*, **312**:788–806. [ADS].

Alcalá J.M., Natta A., Manara C.F., Spezzi L., Stelzer B., Frasca A., Biazzo K., Covino E., Randich S., Rigliaco E., et al. 2014. "X-shooter spectroscopy of young stellar objects. IV. Accretion in low-mass stars and substellar objects in Lupus". *Astronomy and Astrophysics*, **561**:A2. [ADS].

ALMA Partnership A., Brogan C.L., Pérez L.M., Hunter T.R., Dent W.R.F., Hales A.S., Hills R.E., Corder S., Fomalont E.B., Vlahakis C., et al. 2015. "The 2014 alma long baseline campaign: First results from high angular resolution observations toward the hl tau region". *The Astrophysical Journal Letters*, **808**(1):L3.

André P. 2002. "The Initial Conditions for Protostellar Collapse: Observational Constraints". In *EAS Publications Series*, edited by J. Bouvier, J.P. Zahn, volume 3 of *EAS Publications Series*, pages 1–38. [ADS].

Andre P., Ward-Thompson D., Barsony M. 1993. "Submillimeter continuum observations of Rho Ophiuchi A - The candidate protostar VLA 1623 and prestellar clumps". *Astrophysical Journal*, **406**:122–141. [ADS].

Andrews S.M. 2015. "Observations of Solids in Protoplanetary Disks". *Publications of the ASP*, **127**:961–993. [ADS].

Andrews S.M., Chandler C.J., Isella A., Birnstiel T., Rosenfeld K.A., Wilner D.J., Pérez L.M., Ricci L., Carpenter J.M., Calvet N., et al. 2014. "Resolved Multifrequency Radio Observations of GG Tau". *Astrophysical Journal*, **787**:148. [ADS].

Andrews S.M., Rosenfeld K.A., Kraus A.L., Wilner D.J. 2013. "The Mass Dependence between Protoplanetary Disks and their Stellar Hosts". *Astrophysical Journal*, **771**:129. [ADS].

Andrews S.M., Williams J.P. 2005. "Circumstellar Dust Disks in Taurus-Auriga: The Submillimeter Perspective". *Astrophysical Journal*, **631**:1134–1160. [ADS].

Andrews S.M., Wilner D.J., Hughes A.M., Qi C., Dullemond C.P. 2009. "Protoplanetary Disk Structures in Ophiuchus". *Astrophysical Journal*, **700**:1502–1523. [ADS].

Andrews S.M., Wilner D.J., Hughes A.M., Qi C., Dullemond C.P. 2010. "Protoplanetary Disk Structures in Ophiuchus. II. Extension to Fainter Sources". *Astrophysical Journal*, **723**:1241–1254. [ADS].

Andrews S.M., Wilner D.J., Zhu Z., Birnstiel T., Carpenter J.M., Pérez L.M., Bai X.N., Öberg K.I., Hughes A.M., Isella A., et al. 2016. "Ringed Substructure and a Gap at 1 au in the Nearest Protoplanetary Disk". *Astrophysical Journal, Letters*, **820**:L40. [ADS].

Anglada-Escudé G., Amado P.J., Barnes J., Berdiñas Z.M., Butler R.P., Coleman G.A.L., de La Cueva I., Dreizler S., Endl M., Giesers B., et al. 2016. "A terrestrial planet candidate in a temperate orbit around Proxima Centauri". *Nature*, **536**:437–440. [ADS].

Ansdell M., Williams J.P., van der Marel N., Carpenter J.M., Guidi G., Hogerheijde M., Mathews G.S., Manara C.F., Miotello A., Natta A., et al. 2016. "ALMA Survey of Lupus Protoplanetary Disks. I. Dust and Gas Masses". *Astrophysical Journal*, **828**:46. [ADS].

Armitage P.J. 2010. *Astrophysics of Planet Formation*. Cambridge University Press. [ADS].

Banzatti A., Testi L., Isella A., Natta A., Neri R., Wilner D.J. 2011. "New constraints on dust grain size and distribution in CQ Tauri". *Astronomy and Astrophysics*, **525**:A12. [ADS].

Barenfeld S.A., Carpenter J.M., Ricci L., Isella A. 2016. "ALMA Observations of Circumstellar Disks in the Upper Scorpius OB Association". *Astrophysical Journal*, **827**:142. [ADS].

Beckwith S.V.W., Sargent A.I. 1991. "Particle emissivity in circumstellar disks". *Astrophysical Journal*, **381**:250–258. [ADS].

Beckwith S.V.W., Sargent A.I., Chini R.S., Guesten R. 1990. "A survey for circumstellar disks around young stellar objects". *Astronomical Journal*, **99**:924–945. [ADS].

Birnstiel T., Andrews S.M. 2014. "On the Outer Edges of Protoplanetary Dust Disks". *Astrophysical Journal*, **780**:153. [ADS].

Birnstiel T., Dullemond C.P., Brauer F. 2009. "Dust retention in protoplanetary disks". *Astronomy and Astrophysics*, **503**:L5–L8. [ADS].

Birnstiel T., Dullemond C.P., Brauer F. 2010. "Gas- and dust evolution in protoplanetary disks". *Astronomy and Astrophysics*, **513**:A79. [ADS].

Birnstiel T., Fang M., Johansen A. 2016. "Dust Evolution and the Formation of Planetesimals". *Space Science Reviews*. [ADS].

Birnstiel T., Klahr H., Ercolano B. 2012. "A simple model for the evolution of the dust population in protoplanetary disks". *Astronomy and Astrophysics*, **539**:A148. [ADS].

Birnstiel T., Ormel C.W., Dullemond C.P. 2011. "Dust size distributions in coagulation/fragmentation equilibrium: numerical solutions and analytical fits". *Astronomy and Astrophysics*, **525**:A11. [ADS].

Blum J., Wurm G. 2008. "The Growth Mechanisms of Macroscopic Bodies in Protoplanetary Disks". *Annual Review of Astronomy and Astrophysics*, **46**:21–56. [ADS].

Boss A.P. 1997. "Giant planet formation by gravitational instability." *Science*, **276**:1836–1839. [ADS].

Bouwman J., Meeus G., de Koter A., Hony S., Dominik C., Waters L.B.F.M. 2001. "Processing of silicate dust grains in Herbig Ae/Be systems". *Astronomy and Astrophysics*, **375**:950–962. [ADS].

Brauer F., Dullemond C.P., Henning T. 2008. "Coagulation, fragmentation and radial motion of solid particles in protoplanetary disks". *Astronomy and Astrophysics*, **480**:859–877. [ADS].

Bruggeman D.A.G. 1935. "Berechnung verschiedener physikalischer Konstanten von heterogenen Substanzen. I. Dielektrizitätskonstanten und Leitfähigkeiten der Mischkörper aus isotropen Substanzen". *Annalen der Physik*, **416**:636–664. [ADS].

Cameron A.G.W. 1978. "Physics of the primitive solar accretion disk". *Moon and Planets*, **18**:5–40. [ADS].

Casassus S., Wright C.M., Marino S., Maddison S.T., Wootten A., Roman P., Pérez S., Pinilla P., Wyatt M., Moral V., et al. 2015. "A Compact Concentration of Large Grains in the HD 142527 Protoplanetary Dust Trap". *Astrophysical Journal*, **812**:126. [ADS].

Chiang E., Youdin A.N. 2010. "Forming Planetesimals in Solar and Extrasolar Nebulae". *Annual Review of Earth and Planetary Sciences*, **38**:493–522. [ADS].

Chiang E.I., Goldreich P. 1997. "Spectral Energy Distributions of T Tauri Stars with Passive Circumstellar Disks". *Astrophysical Journal*, **490**:368. [ADS].

Clark B.G. 1980. "An efficient implementation of the algorithm 'CLEAN'". *Astronomy and Astrophysics*, **89**:377. [ADS].

Comerón F. 2008. *The Lupus Clouds*, page 295. [ADS].

Cooley J.W., Tukey J.W. 1965. "An algorithm for the machine calculation of complex Fourier series". **19**(90):297–301.

Cossins P., Lodato G., Testi L. 2010. "Resolved images of self-gravitating circumstellar discs with ALMA". *Monthly Notices of the Royal Astronomical Society*, **407**:181–188. [ADS].

Cuzzi J.N., Dobrovolskis A.R., Champney J.M. 1993. "Particle-gas dynamics in the midplane of a protoplanetary nebula". *Icarus*, **106**:102. [ADS].

Daemgen S., Natta A., Scholz A., Testi L., Jayawardhana R., Greaves J., Eastwood D. 2016. "Brown dwarf disks with Herschel: Linking far-infrared and (sub)-mm fluxes". *ArXiv e-prints*. [ADS].

Dagum L., Menon R. 1998. "Openmp: An industry-standard api for shared-memory programming". *IEEE Comput. Sci. Eng.*, **5**(1):46–55.

de Gregorio-Monsalvo I., Ménard F., Dent W., Pinte C., López C., Klaassen P., Hales A., Cortés P., Rawlings M.G., Tachihara K., et al. 2013. "Unveiling the gas-and-dust disk structure in HD 163296 using ALMA observations". *Astronomy and Astrophysics*, **557**:A133. [ADS].

Debye P. 1909. "Der Lichtdruck auf Kugeln von beliebigem Material". *Annalen der Physik*, **335**:57–136. [ADS].

Dipierro G., Lodato G., Testi L., de Gregorio Monsalvo I. 2014. "How to detect the signatures of self-gravitating circumstellar discs with the Atacama Large Millimeter/submillimeter Array". *Monthly Notices of the Royal Astronomical Society*, **444**:1919–1929. [ADS].

Dipierro G., Pinilla P., Lodato G., Testi L. 2015. "Dust trapping by spiral arms in gravitationally unstable protostellar discs". *Monthly Notices of the Royal Astronomical Society*, **451**:974–986. [ADS].

Dittrich K., Klahr H., Johansen A. 2013. "Gravoturbulent Planetesimal Formation: The Positive Effect of Long-lived Zonal Flows". *Astrophysical Journal*, **763**:117. [ADS].

Dohnanyi J.S. 1969. "Collisional Model of Asteroids and Their Debris". *Journal of Geophysics Research*, **74**:2531–2554. [ADS].

Draine B.T. 2006. "On the Submillimeter Opacity of Protoplanetary Disks". *Astrophysical Journal*, **636**:1114–1120. [ADS].

Draine B.T. 2011. *Physics of the Interstellar and Intergalactic Medium*. [ADS].

Draine B.T., Lee H.M. 1984. "Optical properties of interstellar graphite and silicate grains". *Astrophysical Journal*, **285**:89–108. [ADS].

Drażkowska J., Windmark F., Dullemond C.P. 2014. "Modeling dust growth in protoplanetary disks: The breakthrough case". *Astronomy and Astrophysics*, **567**:A38. [ADS].

Dullemond C.P., Dominik C. 2004. "The effect of dust settling on the appearance of protoplanetary disks". *Astronomy and Astrophysics*, **421**:1075–1086. [ADS].

Dullemond C.P., Dominik C., Natta A. 2001. "Passive Irradiated Circumstellar Disks with an Inner Hole". *Astrophysical Journal*, **560**:957–969. [ADS].

Dullemond C.P., Hollenbach D., Kamp I., D'Alessio P. 2007. "Models of the Structure and Evolution of Protoplanetary Disks". *Protostars and Planets V*, pages 555–572. [ADS].

Durisen R.H., Boss A.P., Mayer L., Nelson A.F., Quinn T., Rice W.K.M. 2007. "Gravitational Instabilities in Gaseous Protoplanetary Disks and Implications for Giant Planet Formation". *Protostars and Planets V*, pages 607–622. [ADS].

Dutrey A., Guilloteau S., Duvert G., Prato L., Simon M., Schuster K., Menard F. 1996. "Dust and gas distribution around T Tauri stars in Taurus-Auriga. I. Interferometric 2.7mm continuum and ^13^CO J=1-0 observations". *Astronomy and Astrophysics*, **309**:493–504. [ADS].

Eisner J.A., Hillenbrand L.A., Stone J.M. 2014. "Constraining the sub-au-scale distribution of hydrogen and carbon monoxide gas around young stars with the Keck Interferometer". *Monthly Notices of the Royal Astronomical Society*, **443**:1916–1945. [ADS].

Ercolano B., Rosotti G.P., Picogna G., Testi L. 2016. "A photo-evaporative gap in the closest planet forming disc". *ArXiv e-prints*. [ADS].

Evans II N.J., Dunham M.M., Jørgensen J.K., Enoch M.L., Merín B., van Dishoeck E.F., Alcalá J.M., Myers P.C., Stapelfeldt K.R., Huard T.L., et al. 2009. "The Spitzer c2d Legacy Results: Star-Formation Rates and Efficiencies; Evolution and Lifetimes". *Astrophysical Journal, Supplement*, **181**:321-350. [ADS].

Fischer D.A., Howard A.W., Laughlin G.P., Macintosh B., Mahadevan S., Sahlmann J., Yee J.C. 2014. "Exoplanet Detection Techniques". *Protostars and Planets VI*, pages 715–737. [ADS].

Foreman-Mackey D., Hogg D.W., Lang D., Goodman J. 2013. "emcee: The MCMC Hammer". *Publications of the ASP*, **125**:306–312. [ADS].

Friesen R.K., Johnstone D., Naylor D.A., Davis G.R. 2005. "Fourier transform spectroscopy of the submillimetre continuum emission from hot molecular cores". *Monthly Notices of the Royal Astronomical Society*, **361**:460–468. [ADS].

Fukagawa M., Tsukagoshi T., Momose M., Saigo K., Ohashi N., Kitamura Y., Inutsuka S.i., Muto T., Nomura H., Takeuchi T., et al. 2013. "Local Enhancement of the Surface Density in the Protoplanetary Ring Surrounding HD 142527". *Publications of the ASJ*, **65**:L14. [ADS].

Gammie C.F. 2001. "Nonlinear Outcome of Gravitational Instability in Cooling, Gaseous Disks". *Astrophysical Journal*, **553**:174–183. [ADS].

Garufi A., Quanz S.P., Schmid H.M., Avenhaus H., Buenzli E., Wolf S. 2014. "Shadows and cavities in protoplanetary disks: HD 163296, HD 141569A, and HD 150193A in polarized light". *Astronomy and Astrophysics*, **568**:A40. [ADS].

Goldreich P., Ward W.R. 1973. "The Formation of Planetesimals". *Astrophysical Journal*, **183**:1051–1062. [ADS].

Goodman J., Weare J. 2010. "Ensemble samplers with affine invariance". *Comm. App. Math. Comp. Sci.*, **5**:65–80.

Greene T.P., Wilking B.A., Andre P., Young E.T., Lada C.J. 1994. "Further mid-infrared study of the rho Ophiuchi cloud young stellar population: Luminosities and masses of pre-main-sequence stars". *Astrophysical Journal*, **434**:614–626. [ADS].

Güdel M., Dvorak R., Erkaev N., Kasting J., Khodachenko M., Lammer H., Pilat-Lohinger E., Rauer H., Ribas I., Wood B.E. 2014. "Astrophysical Conditions for Planetary Habitability". *Protostars and Planets VI*, pages 883–906. [ADS].

Guidi G., Tazzari M., Testi L., de Gregorio-Monsalvo I., Chandler C.J., Pérez L., Isella A., Natta A., Ortolani S., Henning T., et al. 2016. "Dust properties across the CO snowline in the HD 163296 disk from ALMA and VLA observations". *Astronomy and Astrophysics*, **588**:A112. [ADS].

Guilloteau S., Dutrey A., Piétu V., Boehler Y. 2011. "A dual-frequency sub-arcsecond study of proto-planetary disks at mm wavelengths: first evidence for radial variations of the dust properties". *Astronomy and Astrophysics*, **529**:A105. [ADS].

Gundlach B., Blum J. 2015. "The Stickiness of Micrometer-sized Water-ice Particles". *Astrophysical Journal*, **798**:34. [ADS].

Han E., Wang S.X., Wright J.T., Feng Y.K., Zhao M., Fakhouri O., Brown J.I., Hancock C. 2014. "Exoplanet Orbit Database. II. Updates to Exoplanets.org". *Publications of the ASP*, **126**:827–837. [ADS].

Hartmann L., Calvet N., Gullbring E., D'Alessio P. 1998. "Accretion and the Evolution of T Tauri Disks". *Astrophysical Journal*, **495**:385. [ADS].

Hayashi C. 1981. "Structure of the Solar Nebula, Growth and Decay of Magnetic Fields and Effects of Magnetic and Turbulent Viscosities on the Nebula". *Progress of Theoretical Physics Supplement*, **70**:35–53. [ADS].

Helled R., Bodenheimer P., Podolak M., Boley A., Meru F., Nayakshin S., Fortney J.J., Mayer L., Alibert Y., Boss A.P. 2014. "Giant Planet Formation, Evolution, and Internal Structure". *Protostars and Planets VI*, pages 643–665. [ADS].

Henning T., Mutschke H. 2010. "Optical properties of cosmic dust analogs: a review". *Journal of Nanophotonics*, **4**(4):041580. [ADS].

Hernández J., Hartmann L., Megeath T., Gutermuth R., Muzerolle J., Calvet N., Vivas A.K., Briceño C., Allen L., Stauffer J., et al. 2007. "A Spitzer Space Telescope Study of Disks in the Young σ Orionis Cluster". *Astrophysical Journal*, **662**:1067–1081. [ADS].

Hildebrand R.H. 1983. "The Determination of Cloud Masses and Dust Characteristics from Submillimetre Thermal Emission". *Quarterly Journal of the RAS*, **24**:267. [ADS].

Howard A.W. 2013. "Observed Properties of Extrasolar Planets". *Science*, **340**:572–576. [ADS].

Hughes A.M., Wilner D.J., Qi C., Hogerheijde M.R. 2008. "Gas and Dust Emission at the Outer Edge of Protoplanetary Disks". *Astrophysical Journal*, **678**:1119-1126. [ADS].

Isella A., Carpenter J.M., Sargent A.I. 2009. "Structure and Evolution of Pre-main-sequence Circumstellar Disks". *Astrophysical Journal*, **701**:260–282. [ADS].

Isella A., Carpenter J.M., Sargent A.I. 2010. "Investigating Planet Formation in Circumstellar Disks: CARMA Observations of Ry Tau and Dg Tau". *Astrophysical Journal*, **714**:1746–1761. [ADS].

Isella A., Chandler C.J., Carpenter J.M., Pérez L.M., Ricci L. 2014. "Searching for Circumplanetary Disks around LkCa 15". *Astrophysical Journal*, **788**:129. [ADS].

Isella A., Testi L., Natta A., Neri R., Wilner D., Qi C. 2007. "Millimeter imaging of HD 163296: probing the disk structure and kinematics". *Astronomy and Astrophysics*, **469**:213–222. [ADS].

Johansen A., Blum J., Tanaka H., Ormel C., Bizzarro M., Rickman H. 2014. "The Multifaceted Planetesimal Formation Process". *Protostars and Planets VI*, pages 547–570. [ADS].

Johnson J.A., Aller K.M., Howard A.W., Crepp J.R. 2010. "Giant Planet Occurrence in the Stellar Mass-Metallicity Plane". *Publications of the ASP*, **122**:905–915. [ADS].

Juhász A., Bouwman J., Henning T., Acke B., van den Ancker M.E., Meeus G., Dominik C., Min M., Tielens A.G.G.M., Waters L.B.F.M. 2010. "Dust Evolution in Protoplanetary Disks Around Herbig Ae/Be Stars - the Spitzer View". *Astrophysical Journal*, **721**:431–455. [ADS].

Kataoka A., Tanaka H., Okuzumi S., Wada K. 2013. "Fluffy dust forms icy planetesimals by static compression". *Astronomy and Astrophysics*, **557**:L4. [ADS].

Kelly B.C. 2007. "Some Aspects of Measurement Error in Linear Regression of Astronomical Data". *Astrophysical Journal*, **665**:1489–1506. [ADS].

Kenyon S.J., Hartmann L. 1995. "Pre-Main-Sequence Evolution in the Taurus-Auriga Molecular Cloud". *Astrophysical Journal, Supplement*, **101**:117. [ADS].

Klaassen P.D., Juhasz A., Mathews G.S., Mottram J.C., De Gregorio-Monsalvo I., van Dishoeck E.F., Takahashi S., Akiyama E., Chapillon E., Espada D., et al. 2013. "ALMA detection of the rotating molecular disk wind from the young star HD 163296". *Astronomy and Astrophysics*, **555**:A73. [ADS].

Klahr H.H., Henning T. 1997. "Particle-Trapping Eddies in Protoplanetary Accretion Disks". *Icarus*, **128**:213–229. [ADS].

Kobayashi H., Tanaka H. 2010. "Fragmentation model dependence of collision cascades". *Icarus*, **206**:735–746. [ADS].

Kwon W., Looney L.W., Mundy L.G., Welch W.J. 2015. "Resolving Protoplanetary Disks at Millimeter Wavelengths with CARMA". *Astrophysical Journal*, **808**:102. [ADS].

Lada C.J. 1987. "Star formation - From OB associations to protostars". In *Star Forming Regions*, edited by M. Peimbert, J. Jugaku, volume 115 of *IAU Symposium*, pages 1–17. [ADS].

Lada C.J., Wilking B.A. 1984. "The nature of the embedded population in the Rho Ophiuchi dark cloud - Mid-infrared observations". *Astrophysical Journal*, **287**:610–621. [ADS].

Laibe G. 2014. "Growing dust grains in protoplanetary discs - II. The radial-drift barrier problem". *Monthly Notices of the Royal Astronomical Society*, **437**:3037–3054. [ADS].

Laibe G., Gonzalez J.F., Maddison S.T. 2014. "Growing dust grains in protoplanetary discs - I. Radial drift with toy growth models". *Monthly Notices of the Royal Astronomical Society*, **437**:3025–3036. [ADS].

Laplace P.S. 1796. "Exposition du systéme du monde".

Lissauer J.J., Dawson R.I., Tremaine S. 2014. "Advances in exoplanet science from Kepler". *Nature*, **513**:336–344. [ADS].

Luhman K.L., Allen P.R., Espaillat C., Hartmann L., Calvet N. 2010a. "Erratum: "The Disk Population of the Taurus Star-Forming Region" <A href="/abs/2010ApJS..186..111L">(2010, ApJS, 186, 111)</A>". *Astrophysical Journal, Supplement*, **189**:353–354. [ADS].

Luhman K.L., Allen P.R., Espaillat C., Hartmann L., Calvet N. 2010b. "The Disk Population of the Taurus Star-Forming Region". *Astrophysical Journal, Supplement*, **186**:111–174. [ADS].

Lynden-Bell D., Pringle J.E. 1974. "The evolution of viscous discs and the origin of the nebular variables." *Monthly Notices of the Royal Astronomical Society*, **168**:603–637. [ADS].

Mackay D.J.C. 2003. *Information Theory, Inference and Learning Algorithms*. [ADS].

Madhusudhan N., Knutson H., Fortney J.J., Barman T. 2014. "Exoplanetary Atmospheres". *Protostars and Planets VI*, pages 739–762. [ADS].

Makino J., Fukushige T., Funato Y., Kokubo E. 1998. "On the mass distribution of planetesimals in the early runaway stage". *New Astronomy*, **3**:411–417. [ADS].

Marino S., Casassus S., Perez S., Lyra W., Roman P.E., Avenhaus H., Wright C.M., Maddison S.T. 2015. "Compact Dust Concentration in the MWC 758 Protoplanetary Disk". *Astrophysical Journal*, **813**:76. [ADS].

Mathews G.S., Klaassen P.D., Juhász A., Harsono D., Chapillon E., van Dishoeck E.F., Espada D., de Gregorio-Monsalvo I., Hales A., Hogerheijde M.R., et al. 2013. "ALMA imaging of the CO snowline of the HD 163296 disk with DCO$^+$". *Astronomy and Astrophysics*, **557**:A132. [ADS].

Mathis J.S., Rumpl W., Nordsieck K.H. 1977. "The size distribution of interstellar grains". *Astrophysical Journal*, **217**:425–433. [ADS].

Mayer L., Quinn T., Wadsley J., Stadel J. 2004. "The Evolution of Gravitationally Unstable Protoplanetary Disks: Fragmentation and Possible Giant Planet Formation". *Astrophysical Journal*, **609**:1045–1064. [ADS].

McCaughrean M.J., O'dell C.R. 1996. "Direct Imaging of Circumstellar Disks in the Orion Nebula". *Astronomical Journal*, **111**:1977. [ADS].

Menu J., van Boekel R., Henning T., Chandler C.J., Linz H., Benisty M., Lacour S., Min M., Waelkens C., Andrews S.M., et al. 2014. "On the structure of the transition disk around TW Hydrae". *Astronomy and Astrophysics*, **564**:A93. [ADS].

Meru F., Bate M.R. 2011. "Non-convergence of the critical cooling time-scale for fragmentation of self-gravitating discs". *Monthly Notices of the Royal Astronomical Society*, **411**:L1–L5. [ADS].

Meru F., Bate M.R. 2012. "On the convergence of the critical cooling time-scale for the fragmentation of self-gravitating discs". *Monthly Notices of the Royal Astronomical Society*, **427**:2022–2046. [ADS].

Mie G. 1908. "Beiträge zur Optik trüber Medien, speziell kolloidaler Metallösungen". *Annalen der Physik*, **330**:377–445. [ADS].

Miotello A., Robberto M., Potenza M.A.C., Ricci L. 2012. "Evidence of Photoevaporation and Spatial Variation of Grain Sizes in the Orion 114-426 Protoplanetary Disk". *Astrophysical Journal*, **757**:78. [ADS].

Miyake K., Nakagawa Y. 1993. "Effects of particle size distribution on opacity curves of protoplanetary disks around T Tauri stars". *Icarus*, **106**:20. [ADS].

Mizuno H. 1980. "Formation of the Giant Planets". *Progress of Theoretical Physics*, **64**:544–557. [ADS].

Mordasini C., Alibert Y., Benz W. 2009. "Extrasolar planet population synthesis. I. Method, formation tracks, and mass-distance distribution". *Astronomy and Astrophysics*, **501**:1139–1160. [ADS].

Natta A., Testi L. 2004. "Grain Growth in Circumstellar Disks". In *Star Formation in the Interstellar Medium: In Honor of David Hollenbach*, edited by D. Johnstone, F.C. Adams, D.N.C. Lin, D.A. Neufeeld, E.C. Ostriker, volume 323 of *Astronomical Society of the Pacific Conference Series*, page 279. [ADS].

Natta A., Testi L., Calvet N., Henning T., Waters R., Wilner D. 2007. "Dust in Protoplanetary Disks: Properties and Evolution". *Protostars and Planets V*, pages 767–781. [ADS].

Nickolls J., Buck I., Garland M., Skadron K. 2008. "Scalable parallel programming with cuda". *Queue*, **6**(2):40–53.

Öberg K.I., Boogert A.C.A., Pontoppidan K.M., van den Broek S., van Dishoeck E.F., Bottinelli S., Blake G.A., Evans II N.J. 2011. "The Spitzer Ice Legacy: Ice Evolution from Cores to Protostars". *Astrophysical Journal*, **740**:109. [ADS].

O'dell C.R., Wen Z., Hu X. 1993. "Discovery of new objects in the Orion nebula on HST images - Shocks, compact sources, and protoplanetary disks". *Astrophysical Journal*, **410**:696–700. [ADS].

Okuzumi S., Momose M., Sirono S.i., Kobayashi H., Tanaka H. 2016. "Sintering-induced Dust Ring Formation in Protoplanetary Disks: Application to the HL Tau Disk". *Astrophysical Journal*, **821**:82. [ADS].

Okuzumi S., Tanaka H., Kobayashi H., Wada K. 2012. "Rapid Coagulation of Porous Dust Aggregates outside the Snow Line: A Pathway to Successful Icy Planetesimal Formation". *Astrophysical Journal*, **752**:106. [ADS].

Panagia N., Felli M. 1975. "The spectrum of the free-free radiation from extended envelopes". *Astronomy and Astrophysics*, **39**:1–5. [ADS].

Pascucci I., Testi L., Herczeg G.J., Long F., Manara C.F., Hendler N., Mulders G.D., Krijt S., Ciesla F., Henning T., et al. 2016. "A Steeper than Linear Disk Mass-Stellar Mass Scaling Relation". *ArXiv e-prints*. [ADS].

Pérez L.M. 2013. *Phd Thesis*. Ph.D. thesis, Caltech.

Pérez L.M., Carpenter J.M., Chandler C.J., Isella A., Andrews S.M., Ricci L., Calvet N., Corder S.A., Deller A.T., Dullemond C.P., et al. 2012. "Constraints on the Radial Variation of Grain Growth in the AS 209 Circumstellar Disk". *Astrophysical Journal, Letters*, **760**:L17. [ADS].

Pérez L.M., Chandler C.J., Isella A., Carpenter J.M., Andrews S.M., Calvet N., Corder S.A., Deller A.T., Dullemond C.P., Greaves J.S., et al. 2015. "Grain Growth in the Circumstellar Disks of the Young Stars CY Tau and DoAr 25". *Astrophysical Journal*, **813**:41. [ADS].

Pérez L.M., Isella A., Carpenter J.M., Chandler C.J. 2014. "Large-scale Asymmetries in the Transitional Disks of SAO 206462 and SR 21". *Astrophysical Journal, Letters*, **783**:L13. [ADS].

Pérez L.M., Lamb J.W., Woody D.P., Carpenter J.M., Zauderer B.A., Isella A., Bock D.C., Bolatto A.D., Carlstrom J., Culverhouse T.L., et al. 2010. "Atmospheric Phase Correction Using CARMA-PACS: High Angular Resolution Observations of the FU Orionis Star PP 13S*". *Astrophysical Journal*, **724**:493–501. [ADS].

Perley R.A., Butler B.J. 2013. "Integrated Polarization Properties of 3C48, 3C138, 3C147, and 3C286". *Astrophysical Journal, Supplement*, **206**:16. [ADS].

Perri F., Cameron A.G.W. 1974. "Hydrodynamic instability of the solar nebula in the presence of a planetary core". *Icarus*, **22**:416–425. [ADS].

Piétu V., Guilloteau S., Di Folco E., Dutrey A., Boehler Y. 2014. "Faint disks around classical T Tauri stars: Small but dense enough to form planets". *Astronomy and Astrophysics*, **564**:A95. [ADS].

Pinilla P., Birnstiel T., Ricci L., Dullemond C.P., Uribe A.L., Testi L., Natta A. 2012. "Trapping dust particles in the outer regions of protoplanetary disks". *Astronomy and Astrophysics*, **538**:A114. [ADS].

Pollack J.B., Hollenbach D., Beckwith S., Simonelli D.P., Roush T., Fong W. 1994. "Composition and radiative properties of grains in molecular clouds and accretion disks". *Astrophysical Journal*, **421**:615–639. [ADS].

Pollack J.B., Hubickyj O., Bodenheimer P., Lissauer J.J., Podolak M., Greenzweig Y. 1996. "Formation of the Giant Planets by Concurrent Accretion of Solids and Gas". *Icarus*, **124**:62–85. [ADS].

Press W.H., Teukolsky S.A., Vetterling W.T., Flannery B.P. 2007. *Numerical Recipes: The Art of Scientific Computing*. Cambridge University Press, 2007. [ADS].

Pringle J.E. 1981. "Accretion discs in astrophysics". *Annual Review of Astronomy and Astrophysics*, **19**:137–162. [ADS].

Qi C., D'Alessio P., Öberg K.I., Wilner D.J., Hughes A.M., Andrews S.M., Ayala S. 2011. "Resolving the CO Snow Line in the Disk around HD 163296". *Astrophysical Journal*, **740**:84. [ADS].

Qi C., Öberg K.I., Andrews S.M., Wilner D.J., Bergin E.A., Hughes A.M., Hogherheijde M., D'Alessio P. 2015. "Chemical Imaging of the CO Snow Line in the HD 163296 Disk". *Astrophysical Journal*, **813**:128. [ADS].

Qi C., Öberg K.I., Wilner D.J., D'Alessio P., Bergin E., Andrews S.M., Blake G.A., Hogerheijde M.R., van Dishoeck E.F. 2013. "Imaging of the CO Snow Line in a Solar Nebula Analog". *Science*, **341**:630–632. [ADS].

Raymond S.N., Kokubo E., Morbidelli A., Morishima R., Walsh K.J. 2014. "Terrestrial Planet Formation at Home and Abroad". *Protostars and Planets VI*, pages 595–618. [ADS].

Ricci L., Testi L., Natta A., Brooks K.J. 2010a. "Dust grain growth in ρ-Ophiuchi protoplanetary disks". *Astronomy and Astrophysics*, **521**:A66. [ADS].

Ricci L., Testi L., Natta A., Neri R., Cabrit S., Herczeg G.J. 2010b. "Dust properties of protoplanetary disks in the Taurus-Auriga star forming region from millimeter wavelengths". *Astronomy and Astrophysics*, **512**:A15. [ADS].

Rice W.K.M., Armitage P.J., Bate M.R., Bonnell I.A. 2003. "The effect of cooling on the global stability of self-gravitating protoplanetary discs". *Monthly Notices of the Royal Astronomical Society*, **339**:1025–1030. [ADS].

Rodmann J., Henning T., Chandler C.J., Mundy L.G., Wilner D.J. 2006. "Large dust particles in disks around T Tauri stars". *Astronomy and Astrophysics*, **446**:211–221. [ADS].

Ros K., Johansen A. 2013. "Ice condensation as a planet formation mechanism". *Astronomy and Astrophysics*, **552**:A137. [ADS].

Rosenfeld K.A., Andrews S.M., Hughes A.M., Wilner D.J., Qi C. 2013. "A Spatially Resolved Vertical Temperature Gradient in the HD 163296 Disk". *Astrophysical Journal*, **774**:16. [ADS].

Rybicki G.B., Lightman A.P. 1986. *Radiative Processes in Astrophysics*. [ADS].

Safronov V.S. 1972. "Evolution of the protoplanetary cloud and formation of the earth and the planets". *NASA TTF*, **677**.

Sallum S., Follette K.B., Eisner J.A., Close L.M., Hinz P., Kratter K., Males J., Skemer A., Macintosh B., Tuthill P., et al. 2015. "Accreting protoplanets in the LkCa 15 transition disk". *Nature*, **527**:342–344. [ADS].

Sault R.J., Teuben P.J., Wright M.C.H. 1995. "A Retrospective View of MIRIAD". In *Astronomical Data Analysis Software and Systems IV*, edited by R.A. Shaw, H.E. Payne, J.J.E. Hayes, volume 77 of *Astronomical Society of the Pacific Conference Series*, pages 433–+. [ADS].

Shu F.H., Adams F.C., Lizano S. 1987. "Star formation in molecular clouds - Observation and theory". *Annual Review of Astronomy and Astrophysics*, **25**:23–81. [ADS].

Siess L., Dufour E., Forestini M. 2000. "An internet server for pre-main sequence tracks of low- and intermediate-mass stars". *Astronomy and Astrophysics*, **358**:593–599. [ADS].

Stognienko R., Henning T., Ossenkopf V. 1995. "Optical properties of coagulated particles." *Astronomy and Astrophysics*, **296**:797. [ADS].

Stratton J. 1941. *Electromagnetic theory*. International series in pure and applied physics. McGraw-Hill book company, inc.

Supulver K.D., Lin D.N.C. 2000. "Formation of Icy Planetesimals in a Turbulent Solar Nebula". *Icarus*, **146**:525–540. [ADS].

Tanaka H., Himeno Y., Ida S. 2005. "Dust Growth and Settling in Protoplanetary Disks and Disk Spectral Energy Distributions. I. Laminar Disks". *Astrophysical Journal*, **625**:414–426. [ADS].

Tanaka H., Inaba S., Nakazawa K. 1996. "Steady-State Size Distribution for the Self-Similar Collision Cascade". *Icarus*, **123**:450–455. [ADS].

Tazzari M., Testi L., Ercolano B., Natta A., Isella A., Chandler C.J., Pérez L.M., Andrews S., Wilner D.J., Ricci L., et al. 2016. "Multiwavelength analysis for interferometric (sub-)mm observations of protoplanetary disks. Radial constraints on the dust properties and the disk structure". *Astronomy and Astrophysics*, **588**:A53. [ADS].

Terebey S., Shu F.H., Cassen P. 1984. "The collapse of the cores of slowly rotating isothermal clouds". *Astrophysical Journal*, **286**:529–551. [ADS].

Testi L., Birnstiel T., Ricci L., Andrews S., Blum J., Carpenter J., Dominik C., Isella A., Natta A., Williams J.P., et al. 2014. "Dust Evolution in Protoplanetary Disks". *Protostars and Planets VI*, pages 339–361. [ADS].

Testi L., Natta A., Shepherd D.S., Wilner D.J. 2001. "Constraints on Properties of the Proto-planetary Disks around UX Orionis and CQ Tauri". *Astrophysical Journal*, **554**:1087–1094. [ADS].

Testi L., Natta A., Shepherd D.S., Wilner D.J. 2003. "Large grains in the disk of CQ Tau". *Astronomy and Astrophysics*, **403**:323–328. [ADS].

Thompson A.R. 1999. "Fundamentals of Radio Interferometry". In *Synthesis Imaging in Radio Astronomy II*, edited by G.B. Taylor, C.L. Carilli, R.A. Perley, volume 180 of *Astronomical Society of the Pacific Conference Series*, page 11. [ADS].

Tilling I., Woitke P., Meeus G., Mora A., Montesinos B., Riviere-Marichalar P., Eiroa C., Thi W.F., Isella A., Roberge A., et al. 2012. "Gas modelling in the disc of HD 163296". *Astronomy and Astrophysics*, **538**:A20. [ADS].

Toomre A. 1964. "On the gravitational stability of a disk of stars". *Astrophysical Journal*, **139**:1217–1238. [ADS].

Trotta F., Testi L., Natta A., Isella A., Ricci L. 2013. "Constraints on the radial distribution of the dust properties in the CQ Tauri protoplanetary disk". *Astronomy and Astrophysics*, **558**:A64. [ADS].

Ubach C., Maddison S.T., Wright C.M., Wilner D.J., Lommen D.J.P., Koribalski B. 2012. "Grain growth signatures in the protoplanetary discs of Chamaeleon and Lupus". *Monthly Notices of the Royal Astronomical Society*, **425**:3137–3161. [ADS].

van Boekel R., Waters L.B.F.M., Dominik C., Bouwman J., de Koter A., Dullemond C.P., Paresce F. 2003. "Grain growth in the inner regions of Herbig Ae/Be star disks". *Astronomy and Astrophysics*, **400**:L21–L24. [ADS].

van de Hulst H.C. 1981. *Light scattering by small particles*. [ADS].

van den Ancker M.E., de Winter D., Tjin A Djie H.R.E. 1998. "HIPPARCOS photometry of Herbig Ae/Be stars". *Astronomy and Astrophysics*, **330**:145–154. [ADS].

van der Marel N., Pinilla P., Tobin J., van Kempen T., Andrews S., Ricci L., Birnstiel T. 2015. "A Concentration of Centimeter-sized Grains in the Ophiuchus IRS 48 Dust Trap". *Astrophysical Journal, Letters*, **810**:L7. [ADS].

van der Marel N., van Dishoeck E.F., Bruderer S., Birnstiel T., Pinilla P., Dullemond C.P., van Kempen T.A., Schmalzl M., Brown J.M., Herczeg G.J., et al. 2013. "A Major Asymmetric Dust Trap in a Transition Disk". *Science*, **340**:1199–1202. [ADS].

van Leeuwen F. 2007. "Validation of the new Hipparcos reduction". *Astronomy and Astrophysics*, **474**:653–664. [ADS].

Wada K., Tanaka H., Suyama T., Kimura H., Yamamoto T. 2009. "Collisional Growth Conditions for Dust Aggregates". *Astrophysical Journal*, **702**:1490–1501. [ADS].

Warren S.G. 1984. "Optical constants of ice from the ultraviolet to the microwave". *Applied Optics*, **23**:1206–1225. [ADS].

Weidenschilling S.J. 1977. "Aerodynamics of solid bodies in the solar nebula". *Monthly Notices of the Royal Astronomical Society*, **180**:57–70. [ADS].

Weingartner J.C., Draine B.T. 2001. "Dust Grain-Size Distributions and Extinction in the Milky Way, Large Magellanic Cloud, and Small Magellanic Cloud". *Astrophysical Journal*, **548**:296–309. [ADS].

Whipple F.L. 1972. "On certain aerodynamic processes for asteroids and comets". In *From Plasma to Planet*, edited by A. Elvius, page 211. [ADS].

Williams D.R., Wetherill G.W. 1994. "Size distribution of collisionally evolved asteroidal populations - Analytical solution for self-similar collision cascades". *Icarus*, **107**:117. [ADS].

Williams J.P., Cieza L.A. 2011. "Protoplanetary Disks and Their Evolution". *Annual Review of Astronomy and Astrophysics*, **49**:67–117. [ADS].

Wilner D.J., Ho P.T.P., Kastner J.H., Rodríguez L.F. 2000. "VLA Imaging of the Disk Surrounding the Nearby Young Star TW Hydrae". *Astrophysical Journal, Letters*, **534**:L101–L104. [ADS].

Wood J.A., Morfill G.E. 1988. *A review of solar nebula models*, pages 329–347. [ADS].

Wrobel J.M., Walker R.C. 1999. "Sensitivity". In *Synthesis Imaging in Radio Astronomy II*, edited by G.B. Taylor, C.L. Carilli, R.A. Perley, volume 180 of *Astronomical Society of the Pacific Conference Series*, page 171. [ADS].

Wyatt M.C., Dermott S.F., Telesco C.M., Fisher R.S., Grogan K., Holmes E.K., Piña R.K. 1999. "How Observations of Circumstellar Disk Asymmetries Can Reveal Hidden Planets: Pericenter Glow and Its Application to the HR 4796 Disk". *Astrophysical Journal*, **527**:918–944. [ADS].

Youdin A.N., Goodman J. 2005. "Streaming Instabilities in Protoplanetary Disks". *Astrophysical Journal*, **620**:459–469. [ADS].

Zubko V.G., Mennella V., Colangeli L., Bussoletti E. 1996. "Optical constants of cosmic carbon analogue grains - I. Simulation of clustering by a modified continuous distribution of ellipsoids". *Monthly Notices of the Royal Astronomical Society*, **282**:1321–1329. [ADS].

Marco Tazzari

Curriculum Vitae

30 September 2016

▬▬▬ Contact information

European Southern Observatory (ESO)   email:mtazzari@eso.org
Karl-Schwazschild-Straße 2   phone: +49 (0)89 3200 6498
85748 Garching bei München
Germany

▬▬▬ Education

2013 – present	**Ph.D. in Astronomy**, *Ludwig-Maximilians-Universität München (LMU)*
	Thesis: *Observing planet formation: constraints on the spatial distribution and the growth of solids in protoplanetary disks*
	Advisors: Prof. Dr. Barbara Ercolano (USM-LMU), Dr. Leonardo Testi (ESO, INAF-Arcetri).
	Date of PhD Defense: 20 December 2016.
2011 – 2013	**Master's Degree in Astrophysics**, *University of Milan*, Italy, 110/110 cum Laude.
	Thesis: *Evolution of gaseous discs during the merger of SMBH binaries.*
	Advisors: Prof. Giuseppe Lodato (UniMi), Prof. Giuseppe Bertin (UniMi).
2007 – 2011	**Bachelor's Degree in Physics**, *University of Milan*, Italy, 110/110 cum Laude.
	Thesis: *Equilibrium and stability of classical models of self-gravitating fluids in rotation.*
	Advisors: Prof. Giuseppe Bertin (UniMi), Prof. Giuseppe Lodato (UniMi).
2002 – 2007	**High School Diploma**, *Liceo Scientifico A. Oriani*, Ravenna, Italy, 100/100 cum Laude.

▬▬▬ Honors and Awards

2012	**Famiglia Legnanese Scholarship** awarded to the best students of Milan Universities.
2007, 2008	**University of Milan merit-based incentives** for 1st and 2nd year students enrolled in Mathematics, Physics or Chemistry degrees. Earned both years.

▬▬▬ Further Education/Observing experience

03/2015	**45th Saas-Fee Advanced Course**, *From Protoplanetary Disks to Planet Formation*.
11/2014	**Astrostatistics Course** by Prof. Eric Feigelson (Penn State University).
06/2014	**JAC/Mauna Kea Observatory**, *Hawaii*. 5 nights observing with JCMT/HARP, SCUBA-2 instruments
05/2014	**NRAO 14th Synthesis Imaging Workshop**, NRAO Socorro, USA.
04/2014	**Interdisciplinary workshop on GPUs**, Excellence Cluster 'Universe', Garching b. München, Germany.
11/2013	**Monte Carlo Methods in Advanced Statistics Applications and Data Analysis** course, Max Planck for Physics, Munich, Germany.
10/2013	**Scripting with Bash and Python** course, TUM, Garching b. München, Germany.

Research interests

Protoplanetary disks: disc structure and evolution; theoretical and observational planet formation; dust opacity models; observational signatures of grain growth; radio-interferometry observations with ALMA and JVLA.

Black hole mergers: dynamics of black hole binaries; observational signatures of black hole mergers; theoretical modeling of disk-binary evolution.

High Performance Computing: multi-core algorithms; Graphic Processing Units (GPUs) programming; hybrid multi-CPU/multi-GPUs code patterns.

Bayesian analysis: Markov Chains Monte Carlo methods.

Expertise

Interferometry (sub-)mm and cm (e.g., ALMA, JVLA, SMA). Experience in the usage of Common Astronomy Software Applications (CASA).

Programming Python (with Cython and f2py), Fortran, C/C++, NVIDIA CUDA, CERN Root, optimizations for High Performance Computing (HPC).

Computing Parallel computing on large clusters (C2PAP, LRZ, Max-Planck-Gesellschaft Hydra).

Large projects and collaborations

Disks@EVLA collaboration EVLA survey of 66 protoplanetary disks in the nearest star-forming regions aimed at (1) investigating grain growth in disks from spatially resolved millimeter/centimeter observations and (2) studying the dependence of particle populations on properties of the central stars, disk structure, and star-forming environment. PI C. Chandler (NRAO). I am a member since 2013, working on the multi-wavelength analysis of sub-mm, mm and cm observations to study grain growth in the disks in the sample.

ALMA LuPus disks Survey (ALPS) Observing program targeting a complete sample (98 objects; the largest sample so far) of Class II Young Stellar Objects and their host stars in the Lupus star forming region with high spatial resolution sub-mm/mm observations and UV-NIR spectra. PI ALMA J. P. Williams (IfA, Hawaii); PI ESO-VLT/XShooter J. Alcalá (INAF-Naples). The main goal is characterizing the dust distribution and the gas content of disks, and the disk-star interaction through accretion rate measurements. ALMA Band 7 (0.87mm) data have been published and Band 6 (1.3mm) data is incoming. ESO-VLT/XShooter data analysis is complete. Within the collaboration, I am responsible for the analysis of dust continuum, aiming to measure disk masses, sizes and the level of grain growth.

JEts and Disks @ Inaf (JEDI) Collaboration aimed at characterizing protoplanetary disks evolution from the initial stages to the disk dispersal using a comprehensive set of observational techniques (from visible spectroscopy to radio interferometry) and modeling tools (chemical networks, disk and jets modeling). I am a member since 2013, working on the determination of the radial variations of dust properties in disks.

Computational time awarded

C2PAP (LRZ) **700'000 CPU-hours**, PI of the approved projects "Dust evolution in protoplanetary cluster disks" (2015, 2016).

Accepted observing proposals

Observing

ALMA **6 hours** Cycle 4 as *PI*, **43 hours**, Cycle 2, 3 and 4 as Col.

VLA **20 hours** as Col.

Visits and Collaborations

03/2016	GPU Hackathon, Dresden, Germany
01/2016	Science Visitor at Observatoire de Bordeaux, France. Collaborator: Dr. A. Dutrey.
10/2015	Science Visitor at Leiden Observatory, The Netherlands. Collaborator: Prof. E. van Dishoeck.
06/2015	Science Visitor at Harvard-Smithsonian CfA, USA. Collaborators: Sean Andrews, David Wilner.
06/2014	Science Visitor at Caltech, Pasadena, USA. Collaborator: Prof. Andrea Isella (Rice University)
05/2014	Science Visitor at NRAO Socorro, USA. Collaborator: Dr. Claire Chandler.

Other scientific activities

2014 – present	**Organizer of talks and meetings at ESO**: Informal Discussion, Star Formation Coffee.
04/2015	**Organizer of the 2015 Excellence Cluster PhD Event**, ESO, Garching bei Müenchen, Germany.
2014, 2015	**Scientific Assistant**: ESO Observing Proposals Committee, Periods 95, 97.

Public Outreach

11/2015	**Invited lecture** on *"The Beauty of the Universe"*, Darmstadt, Germany.
08/2015	**Invited lecture** on *"What does our life have to do with stars?"*, Hotel Corona, Zoldo, Italy.
04/2015	Cycle of 3 **invited lectures** on *"The adventure of doing research in Astronomy"*, Liceo Classico D. Alighieri, Liceo Scientifico A. Oriani, Scuola San Vincenzo de Paoli, Ravenna, Italy.
01/2013	**Invited lecture** on *"Reflections on scientific research"*, Verbania, Italy.
03/2008	**Invited lecture** on *"Light, Eyes, Meaning, the human experience of sight"*, Liceo Scientifico A. Oriani, Ravenna, Italy.
03/2007	**Invited lecture** on *"The Milky Way amid Science, History, and Art"*, Liceo Scientifico A. Oriani, Ravenna, Italy.

Conference contributions

Talks

06/2016   *"A new tool for generic multi-wavelength uv-plane model fitting"*
Workshop "Origins of Habitable Planets", Gothenburg Center for Advanced Studies, Sweden.

01/2016   *"A multi-wavelength view of planet-forming regions"*
"ESO Science Day 2016", ESO, Garching bei München, Germany.

01/2016   *"A multi-wavelength analysis tool to constrain protoplanetary disk properties"*
Workshop "Astrochemistry with ALMA Cycle 4", Observatoire de Bordeaux, France.

10/2015   *"A multi-wavelength analysis for interferometric sub-mm observations of protoplanetary disks"* Poster prize talk at the conference "From clouds to protoplanetary disks: the astrochemical link", Max-Planck Gesellschaft Harnack House, Berlin, Germany.

09/2015   *"Constraining the dust grain size distribution in protoplanetary disks with ALMA and JVLA"*
5th Workshop of the Italian Astrobiology Society "Life in a Cosmic context", Trieste, Italy.

07/2015   *"Protoplanetary disk evolution and planet formation: an observational perspective"*
Workshop "Excellence Cluster 'Universe' Research Area Day", MPE, Garching bei München, Germany.

06/2015   *"Constraining the dust grain size distribution in protoplanetary disks with ALMA and JVLA"*
"Radio and Geoastronomy Lunch Talk", Harvard-Smithsonian CfA, Cambridge, MA, USA.

04/2015   *"Constraining the size of dust grains in protoplanetary disks"*
Workshop "2015 Excellence Cluster PhD Event", ESO, Garching b. Müenchen, Germany.

04/2015   *"A new fitting tool to constrain dust grain size distribution and disk properties with ALMA and JVLA"*
"2nd Jets and Disks @ Inaf (JEDI) Workshop", INAF-Naples, Italy.

03/2015   *"A new fitting tool to constrain dust grain size distribution and disk properties with ALMA and JVLA observations "*
"Transition disks Workshop", Lorentz Center, Leiden, the Netherlands.

12/2014   *"Constraining the dust grain size in protoplanetary disks with ALMA and EVLA observations"*
"Milan Christmas Workshop", University of Milan, Milan, Italy.

05/2014   *"Multi-CPU and multi-GPU toolkit for robust statistical inference of dust evolution in protoplanetary disks from ALMA and JVLA datasets"*
Review Committee for "Seed Money Projects", Excellence Cluster 'Universe', Garching bei Muenchen, Germany.

01/2014   *"Dust and gas evolution with ALMA/EVLA data: a new fitting tool"*
"II Star and Planet formation Workshop", ESO, Garching bei Muenchen, Germany.

12/2013   *"Dust and gas evolution with ALMA/JVLA observations"* at the
"1st JEDI Workshop: disks, jets and the dawn of planets", INAF-Rome, Italy.

Posters

11/2015   *"Excellence Cluster 'Universe' 2015 Science Week"*, MPE, Garching bei Muenchen, Germany.

10/2015   *"From clouds to protoplanetary disks: the astrochemical link"* Conference, Berlin, Germany. **Award: Poster prize.**

07/2015   *"Origins of Solar Systems"*, Gordon Research Conference, South Hadley, USA.

01/2015	*"Chemical diagnostics of star and planet formation with Cycle 3 ALMA"*, MPE, Garching bei Müenchen, Germany.
09/2014	*"Planet Formation and Evolution 2014"*, Kiel University, Kiel, Germany.
12/2013	*"Excellence Cluster 'Universe' 2013 Science Week"*, MPE, Garching bei Muenchen, Germany.
07/2013	*"Mind the gap: from microphysics to large-scale structure in the Universe"*, Institute of Astronomy, University of Cambridge, UK.

Publications

Here you can find my ADS publication list: [Link]

Highlighted papers
(i.e., first author papers or works in which I was significantly involved at all stages)

[6] **Tazzari M.**, Testi, L., Beaujean, **to be submitted**.
"pyvfit: a GPU-accelerated library for the analysis of interferometric observations".

[5] **Tazzari M.**, Testi, L., Williams, J. P., van Dishoeck, E., Ansdell, M., Manara, C., Miotello, A., Natta, A., et al., **to be submitted**.
"ALMA Survey of Lupus Protoplanetary Disks II: structure of disks".

[4] Testi, L., Natta, A., Scholz, A., **Tazzari M.**, Ricci, L., de Gregorio Monsalvo, I., *"Brown dwarf disks with ALMA: evidence for truncated dust disks in Ophiuchus"*, **A&A in press**, **arXiv**:1606.06448 (2016). [ADS]

[3] Guidi, G., **Tazzari M.**, Testi, L., de Gregorio-Monsalvo, I., Chandler, C.J., Pérez, L.M., Isella, A., Natta, A., Ortolani, S., Henning, Th., Corder, S.A., Linz, H., Andrews, S., Wilner, D.J., Ricci, L., Carpenter, J.M., Sargent, A.I., Mundy, L., Storm, S., Calvet, N., Dullemond, C. P., Greaves, J. A., Lazio, J.A., Deller, A.T., Kwon, W., **A&A**, 588, 112 (2016). [ADS]
"Dust properties across the CO snowline in the HD 163296 protoplanetary disk from ALMA and JVLA observations".

[2] **Tazzari M.**, Testi, L., Ercolano, B., Natta, A., Isella, A., Chandler, C.J., Pérez, L.M., Andrews, S., Wilner, D. J., Ricci, L., Henning, T., Linz, H., Kwon, W., Corder, S. A., Dullemond, C. P., Carpenter, J.M., Sargent, A. I., Mundy, L., Storm, S., Calvet, N., Greaves, J.A., Lazio, J., Deller, A.T., **A&A**, 588, 53 (2016). [ADS]
"Multi-wavelength analysis for interferometric (sub-)mm observations of protoplanetary disks".

[1] **Tazzari M.**, & Lodato, G. **MNRAS**, 449, 1118 (2016). [ADS]
"Estimating the fossil disc mass during supermassive black hole mergers: the importance of torque implementation".

Refereed papers as co-author

[3] Manara, C. F., Rosotti, G., Testi, L., Natta, A., Alcalá, J. M., Williams, J. P., Ansdell, M., Miotello, A., van der Marel, N., **Tazzari M.**, Carpenter, J., Guidi, G., Mathews, G. S., Oliveira, I., Prusti, T., van Dishoeck, E. F., **arXiv**:1605.03050 (2016). [ADS]
"Evidence for a correlation between mass accretion rates onto young stars and the mass of their protoplanetary disks".

[2] Ansdell, M.; Williams, J. P.; van der Marel, N.; Carpenter, J. M., Guidi, G., Hogerheijde, M., Mathews, G. S., Manara, C. F., Miotello, A., Natta, A., Oliveira, I., **Tazzari M.**, Testi, L.; van Dishoeck, E. F., van Terwisga, E., **arXiv**:1604.05719 (2016). [ADS]
"ALMA Survey of Lupus Protoplanetary Disks I: Dust and Gas Masses".

[1] Pérez, L.M., Chandler, C.J., Isella, A., Carpenter, J.M., Andrews, S., Calvet, N., Corder, S.A., Deller, A.T., Dullemond, C. P., Greaves, J. A., Harris, R.J., Henning, Th., Kwon, W., Lazio, J.A., Linz, H., Mundy, L., Ricci, L., Sargent, A.I., Storm, S., **Tazzari M.**, Testi, L., Wilner, D.J. 2015, **ApJ**, 813, 41. [ADS]
"Grain growth in the circumstellar disks of the young stars CY Tau and DoAr 25".

Non-refereed papers

[2] Alcala', J. M., Antoniucci, S., Biazzo, K., Bacciotti, F., Bianchi, E., Bonito, R., Codella, C., Fedele, D., Fontani, F., Frasca, A., Giannini, T., Manara, C. Nisini, B., Podio, L., Rigliaco, E., **Tazzari M.** 2015. [ADS]
"Disks, Jets and the dawn of planets, Proceedings of the 2nd JEDI meeting".

[1] Andreatta, F., Colombo, E., **Tazzari M.**, Gerosa, D., 2008. [Link]
"Lecture Notes on Linear Algebra", textbook for Physics undergraduate studies, CUSL Press 2008, Milan, Italy.

Journal abbreviations:

MNRAS | *Monthly Notices of the Royal Astronomical Society*
A&A | *Astronomy & Astrophysics*
ApJ | *The Astrophysical Journal*